To the Graduate Council:

I am submitting herewith a dissertation written by Luis Edgardo Cuéllar entitled "Circular Dichroism And Photoelectron Angular Distributions of Excited States of Cesium and Rubidium Using Resonantly Enhanced Multiphoton Ionization Techniques." I have examined the final copy of this dissertation for form and content and recommend that it be accepted in partial fulfillment of the requirements for the degree Doctor of Philosophy, with a major in Physics.

Robert N. Compton, Major Professor

We have read this dissertation
and recommend its acceptance:

Joseph Macek

Charles Feigerle

Marianne Breinig

Accepted for the Council:

Associate Vice Chancellor
and Dean of The Graduate School

Circular Dichroism And Photoelectron Angular Distributions Of Excited States of Cesium And Rubidium Using Resonantly Enhanced Multiphoton Ionization Techniques

A Dissertation
Presented for the
Doctor Of Philosophy
Degree
The University of Tennessee, Knoxville

Luis Edgardo Cuéllar

August 1993

In memory of my father

Juan Francisco Cuéllar

ACKNOWLEDGEMENTS

I would like to gratefully acknowledge my two advisors, Dr. Robert Norman Compton and Dr. Charles Stephen Feigerle. Their assistance and patience for the last five years have been most helpful getting me through graduate school.

I also would like thank Dr. Howard Carman, Jr. for his assistance getting me started with the research work; and Dr. Bruce Thomas and Dr. James Park, for their help while finishing my graduate work.

I take this opportunity to thank Dr. Stanley J. Bajic for his assistance and friendship; Dr. Dajun Ding and Kevin Patterson for their help in my research work.

I would also like to thank discussions with Dr. Vince McKoy, Dr. Richard Dubs, Dr. Fred Grimm, Dr. Roger Hegstrom, and Dr. Joseph H. Macek for their assistance to help me to understand the fine points of angular momentum physics.

I would like to thank the personnel of the Electronics and Machine Shops of the Chemistry Department for their assistance whenever my apparatus broke down. It would have been impossible to "keep the ball rolling" without their help.

I would like to thank my parents for their love, which they have expressed in innumerable ways.

Finally, but never last, I would like to thank my wife Melanie for her patience and love during these demanding years of graduate school.

ABSTRACT

Resonantly enhanced multiphoton ionization (REMPI) techniques are used to study spin-orbit effects in the photoelectron angular distributions (PEAD) of excited ns ($n = 8-13$) states of cesium. The asymmetry parameters are shown to exhibit an energy dependence in the region of the Cooper minimum of the photoionization cross section, supporting predictions made by inclusion of relativistic coupling in the continuum.

REMPI is also used to study the photoelectron angular distribution of excited $n^2P_{3/2}$ and $n^2P_{1/2}$ states of cesium and rubidium. The measured asymmetry parameters for the PEADs of $n^2P_{3/2}$ states are found to deviate significantly from theoretical predictions. The difference is attributed to depolarization of the angular momentum polarization due to hyperfine coupling.

Circular dichroism effects in the photoelectron angular distributions (CDAD) are used to measure alignment of the excited $n^2P_{3/2}$ states of cesium and rubidium. Angular distributions of the $n^2P_{1/2}$ states are used to show that isotropic states do not exhibit CDAD.

TABLE OF CONTENTS

LIST OF FIGURES

LIST OF TABLES

CHAPTER I

INTRODUCTION

The dynamics of photoionization is of great interest in many branches of science and has broad applications in technology. Knowledge of ionization energies, atomic structures, photoionization cross sections, and transition energies helps astrophysicists to identify the composition and structure of distant stars, material scientists to develop new materials for use in industry, as well as aids in the development of new research tools for the laboratory and medicine. Photoionization processes are of considerable practical importance in mass spectrometry and detection of pollutants. The results of this dissertation find direct application in isotope detection and isotope separation (*e.g.*, the atomic vapor laser isotope separation program), by providing insight into the dynamics of resonant multiphoton ionization and on the importance of considering hyperfine coupling effects in resolving the angular distribution of photoelectrons.

The experimental study of photoionization received an enormous boost with the relatively new invention of the laser. Early studies of photoionization had been limited to the use of broad spectral sources, such as discharge and arc lamps, and had been restricted mainly to studies of the ground and unresolved excited states of atoms and molecules.

With the invention of the laser in the 1950's, it became possible to resolve spectrally the fine structure of atoms and to carry out experimental studies of state-selected excited states. More recent developments in laser technology have improved the wavelength resolution (bandwidth) of lasers, and have therefore enabled the study of hyperfine levels of atoms.

Studies of multiphoton absorption and ionization became feasible with the advent of high power lasers, enabling the study of high-angular-momentum bound states of simple atomic systems. Control of the polarization of the laser to excite selectively magnetic sublevels makes possible the study of orientation and alignment characteristics of atoms and molecules.

This dissertation involves experimental studies of photoelectron angular distributions of state-selected excited and aligned atoms. For these studies, one or more plane polarized photons are used to selectively excite and align atoms in an atomic beam, and one more photon, either plane or circularly polarized, is used to photoionize the excited atom. In particular we will consider the resonant excitation of an atom

$$A + nh\nu \rightarrow A^* \tag{1-1}$$

followed by the photoionization of the excited atom

$$A^* + h\nu' \rightarrow A^+ + e^-$$

where ν and ν' represent two photons of the same or different energy and polarization. Other process related to REMPI are shown in Figure 1.1.

In these experiments, the fine structure levels of the intermediate excited state are resolved. However, a superposition of hyperfine levels is excited due to the broad

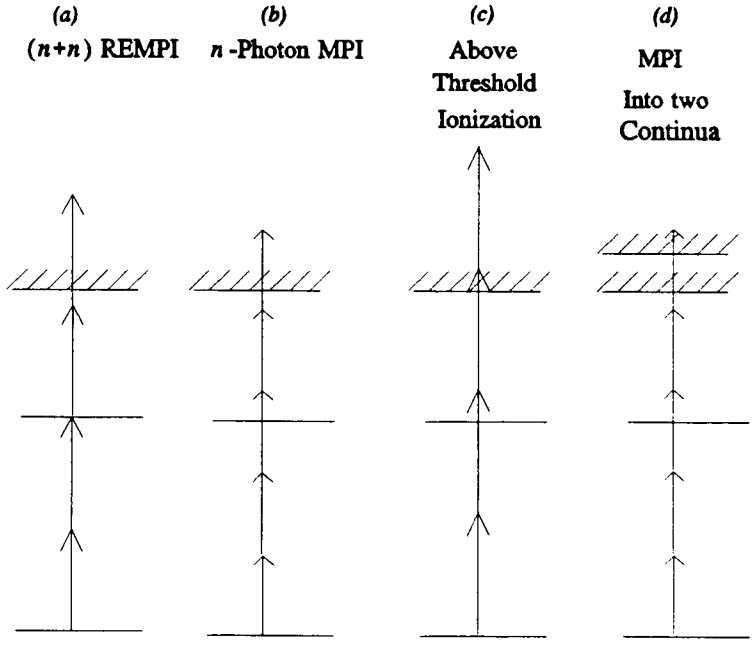

Fig. 1.1. Multiphoton processes. (a) (2 + 2) REMPI; (b) 5-photon MPI; (c) above threshold ionization (ATI); (d) MPI into two continua.

bandwidth of the pulsed laser (~ 1 cm^{-1}, or 30000 MHz), and therefore one must consider hyperfine coupling in the interpretation of the experiments. Typical coupling times for the states studied vary, but are as short as 5 ns (the $5^2P_{3/2}$ state of rubidium has a hyperfine splitting as high as 213 MHz). The observed hyperfine depolarization therefore depends on the pulse length of the laser used for the experiments. Laser pulse widths depend upon the specific wavelength used for the excitation process, but are around 6 to 8 ns. We examine in this dissertation the consequences of hyperfine coupling on the photoelectron angular distribution.

In this study, the angular distributions of the outgoing electrons are measured by recording the number of ejected electrons as a function of angle with respect to the plane of polarization of the photons. In these experiments, the detector is held fixed while the laser polarization is rotated from 0 to 2π using a double Fresnel rhomb. We will use the process described by equation (1-1), with $n = 2$ for the s states and d states and $n = 1$ for the p states.

The theory of multiphoton ionization angular distributions is discussed in chapter II, giving a general discussion of existing theory, as well as some innovative ideas developed for this dissertation. The chapter includes a theoretical discussion of spin-orbit coupling and circular dichroism effects expected to be observed in the photoelectron angular distributions, as well as a discussion of alignment and hyperfine coupling.

Chapter III introduces the experimental apparatus used for this dissertation, including a brief description of the laser and optics used to define the polarization of the photons. Short descriptions are given for the vacuum system, the alkali beam source, the time-of-flight detector, and the data acquisition system. A short discussion of the data analysis process is included.

Experimental results are given in chapter IV for the measurement of the photoelectron angular distributions for the ns (n = 8-13) and np (n = 7-17) states of cesium, np (n = 6-7) states of rubidium, as well as for the measurement of circular dichroism photoelectron angular distributions for the $7p$ and $8p$ states of cesium, and for the $5p$ and $6p$ states of rubidium.

There exists an extensive body of work on photoionization processes of atoms. Among these, worth noting are the books by Berkowitz[1] and Chin and Lambropoulos[2] dealing, respectively, with photoionization and multiphoton ionization of atoms. In addition, Cooper and Zare[3] give an excellent summary on the theory of one photon ionization photoelectron angular distributions in the absence of spin-orbit coupling. An expanded review on the topic of photoelectron angular distributions using multiphoton ionization is provided by Smith and Leuchs[4], giving in addition a review of applications of one and multiphoton ionization to atomic structure and dynamics. Greene and Zare[5] treat in detail the alignment and orientation in photofragmentation (including photoionization) and fluorescence studies of atoms and molecules. Circular dichroism in photoelectron angular distribution (CDAD) is treated in detail by Dubs, *et al.*,[6-8] suggesting CDAD can be used as a probe of molecular and atomic alignment.

Despite the wealth of articles on the photoelectron angular distribution (PEAD) of atoms, only one experimental measurement of the photoelectron angular distribution of an *ns* state of an alkali atom existed previously to this work,[9] and none existed for the alignment of atoms. The PEADs of the *ns* states and the CDAD angular distributions reported in this dissertation are the first experimental results. However, recently Yi-Yian and Elliot[10] have reported measurements of the PEADs of one photon ionization of the ground state ($6^2S_{1/2}$) of cesium at different photon energies.

CHAPTER II

THEORY OF MULTIPHOTON PHOTOELECTRON ANGULAR DISTRIBUTIONS

A. SINGLE PHOTON IONIZATION

The differential cross section, or angular distribution, for a one photon ionization process is proportional to the norm squared of the transition matrix element coupling the initial and final states through a dipole interaction, and averaged over all the (magnetic) projections of the initial state[3]

$$\frac{d\sigma}{d\Omega}(\theta,\phi) = const\ |\langle \psi_f | \vec{r}\cdot\vec{E} | \psi_i \rangle|^2_{\substack{averaged\ over \\ projections}} . \qquad (2\text{-}1)$$

The state $|\psi_i\rangle$ is considered to be the initial ground state, and the final state $|\psi_f\rangle$ is considered to lie in the continuum. The constant takes different values, depending upon the system of units chosen. $\bar{E}$ denotes the electric field of the incident photon, and $\bar{r}$ is the position vector in an arbitrary coordinate system. Once a coordinate system is chosen, typically using the polarization vector $\hat{\epsilon}$ of the electric field and the linear momentum $\bar{\kappa}$ of the photon, the integral in equation (2-1) can be carried out, and all coordinate variables of the wavefunctions are eliminated. The only remaining variables are θ and ϕ, which denote the spherical polar coordinates between the polarization vector $\hat{\epsilon}$ and the direction $\hat{k} = \bar{k}/k$ of the momentum vector of the outgoing photoelectron. In particular, when $\hat{z}\cdot\hat{\epsilon} = 1$, *i.e.*, $\hat{z}$ is chosen parallel to $\hat{\epsilon}$, we have $\cos\theta = \hat{k}\cdot\hat{\epsilon}$. If $|\psi_i\rangle$ is taken to be in a definite energy state with good quantum numbers n, l, and m, then the state may be described in the "length" formulation by the function[4]

$$\langle \vec{r} | \psi_i \rangle = \psi_{nlm}(\vec{r}) = R_{nl}(r)\, Y_{lm}(\theta,\phi) , \qquad (2\text{-}2)$$

where the functions $R_{nl}(r)$ and Y_{lm} are the solutions of the Schrödinger equation for the atomic system in spherical polar coordinates. The functions Y_{lm} are the spherical

harmonics, and can be decomposed into the associated Legendre polynomials $P_l^m(\cos\theta)$ (times a normalization factor and the phase factor $e^{im\phi}$). The final state $|\psi_f\rangle$ can be represented in asymptotic form by a superposition of an incoming spherical wave and an outgoing plane wave,[3]

$$\langle \vec{r} | \psi_f \rangle = \psi_{\vec{k}}^{-}(\vec{r}) \xrightarrow[r\to\infty]{} \frac{1}{(2\pi)^{3/2}}\left[e^{i\vec{k}\cdot\vec{r}} + \frac{f^{-}(\vartheta)}{r} e^{-ikr} \right] . \qquad (2\text{-}3)$$

Here the angle ϑ is measured between $\hat{k}$ and $\vec{r}$, *i.e.*: $\cos\vartheta = \hat{k}\cdot\hat{r}$, and the function $f^{-}(\vartheta)$ denotes the scattering amplitude. This wave function satisfies the time reversed Lippman-Schwinger equation, and reflects that the stationary states corresponding to the final state must tend to a free packet in the *future* instead of the past, and the step function $\theta(t'-t)$, instead of $\theta(t-t')$, must be incorporated into the Green's functions.[11] The function (2-3) has axial symmetry with respect to the electron momentum $\vec{k}$, and may be expanded into a Legendre polynomials series[4]

$$\psi_{\vec{k}}^{-}(\vec{r}) = \sum_{l'=0}^{\infty} a_{l'} P_{l'}(\cos\vartheta) R_{kl'}(r) , \qquad (2\text{-}4)$$

with the following asymptotic behavior for large values of the distance r

$$\psi_{\vec{k}}^{-}(\vec{r}) \xrightarrow[r\to\infty]{} \sum_{l'=0}^{\infty} a_{l'} P_{l'}(\cos\vartheta)(2ikr)^{-1}\left\{ e^{i[kr-l'\pi/2]} \cdot e^{i\delta_{l'}} - c.c. \right\} , \qquad (2\text{-}5)$$

where *c.c.* represents the complex conjugate of the first term in brackets. In similar fashion, the term $e^{i\vec{k}\cdot\vec{r}}$ in equation (2-3) may be expanded[4]

$$e^{i\vec{k}\cdot\vec{r}} \xrightarrow[r\to\infty]{} \sum_{l'=0}^{\infty} i^{l'}(2l'+1) P_{l'}(\cos\vartheta)(2ikr)^{-1}\left\{ e^{i[kr-l'\pi/2]} - c.c. \right\} . \qquad (2\text{-}6)$$

By substituting equation (2-6) into (2-3), and comparing the coefficients of the outgoing spherical wave with those in equation (2-5), we find that $a_{l'} = i^{l'}(2l'+1)e^{-i\delta_{l'}}$, thus

$$\psi_{\vec{k}}^{-}(\vec{r}) \propto \sum_{l'=0}^{\infty} i^{l'}(2l'+1)e^{-i\delta_{l'}}P_{l'}(\cos\vartheta)R_{kl'}(r). \tag{2-7}$$

By use of the spherical harmonic addition theorem,

$$P_{l'}(\cos\vartheta) = \frac{4\pi}{2l'+1}\sum_{m'=-l'}^{+l'} Y^{*}_{l'm'}(\hat{k})Y_{l'm'}(\hat{r}) , \tag{2-8}$$

we can represent the final state wavefunction with the expression[12]

$$\psi_{\vec{k}}^{-}(\vec{r}) = \frac{1}{k^{1/2}}\sum_{l'=0}^{\infty}\sum_{m'=-l'}^{+l'} i^{l'}e^{-i\delta_{l'}}R_{kl'}(r)Y_{l'm'}(\hat{r})Y^{*}_{l'm'}(\hat{k}), \tag{2-9}$$

in which the coordinates of $\hat{r}$ and $\hat{k}$ are now referenced with respect to the axis of quantization. Equation (2-9) is often called a partial wave expansion.

The matrix element to be used in equation (2-1) can thus be written

$$\langle \psi_{nlm}|\vec{r}\cdot\vec{\mathrm{E}}|\,\psi_{\vec{k}}^{-}\rangle \propto \int R_{nl}(r')Y^{*}_{lm}(\hat{r}')\vec{r}'\cdot\vec{\mathbf{E}}\,\frac{1}{k^{1/2}}\sum_{l'=0}^{\infty}\sum_{m'=-l'}^{+l'} i^{l'}e^{-i\delta_{l'}}R_{kl'}(r')Y_{l'm'}(\hat{r}')\,Y^{*}_{l'm'}(\hat{k})\,d^{3}r', \tag{2-10}$$

$$\propto \frac{\mathrm{E}_0}{k^{1/2}}\sum_{l'=0}^{\infty}\sum_{m'=-l'}^{+l'} i^{l'}e^{-i\delta_{l'}}\int R_{nl}(r')\,r'^{3}R_{kl'}(r')\,dr' \times \int Y^{*}_{lm}(\hat{r}')\hat{r}'\cdot\hat{\epsilon}Y_{l'm'}(\hat{r}')\,d\Omega'\;\; Y^{*}_{l'm'}(\hat{k}) , \tag{2-11}$$

where radial and angular integrals are explicitly separated, and $\vec{\mathbf{E}}=\mathrm{E}_0\hat{\epsilon}$. The integrations are carried out over all space in the variables r', θ', ϕ', and the matrix element will depend strictly only on the angular coordinates of the photoelectron momentum.

The occurrence of minima in the differential cross section as a function of both the photoelectron energy ϵ (Cooper minima) and of the angular variables θ and ϕ

(angular minima) becomes possible due to the nodes of the radial and angular momentum wavefunctions. The Cooper minima occur as the result of zeros in the radial dipole integral, and can occur in single continuum ionization channels due to vanishing of the reduced matrix element[13]

$$P^{(1)}_{nl,\epsilon l'} = \langle nl||P^{(1)}||\epsilon l'\rangle = \int_0^\infty r'^3 R_{nl}(r')R_{\epsilon l'}(r')dr', \qquad (2\text{-}12)$$

where $R_{nl}(r)$ and $R_{\epsilon l'}(r)$ are the bound electron radial wavefunction and the free electron continuum function, respectively, and the kinetic energy of the electron is given by $\epsilon = \hbar^2k^2/2m_e$ (where $k = |\vec{k}|$ and m_e is the reduced mass of the electron). The radial wavefunctions can have both positive and negative portions if $n > l+1$, thus the cancellation may be almost 100 percent in some circumstances.[13] Cooper minima should not be confused with Fano minima, which occur as the result of interchannel destructive interference.[13]

The angular minima are a consequence of zeros in the norm of the angular integral

$$\int P_{l'}(\cos\vartheta)\,\hat{\epsilon}\cdot\hat{r}'\,Y_{lm}(\Omega')d\Omega' = \frac{4\pi}{(2l'+1)}\sum_{l'm'} Y^*_{l'm'}(\hat{k})\int Y_{l'm'}(\hat{r}')\,\hat{\epsilon}\cdot\hat{r}'\,Y^*_{lm}(\hat{r}')d\Omega' \ , \qquad (2\text{-}13)$$

where the angle ϑ is the angle between $\vec{k}$ and $\vec{r}'$, *i.e.*, $\cos\vartheta = \hat{r}'\cdot\hat{k}$; $Y^*_{l'm'}(\hat{k})$, $Y_{l'm'}(\hat{r}')$ and $Y^*_{lm}(\hat{r}')$ are the spherical harmonic functions corresponding to the outgoing photoelectron, the final unbound and initial bound states, respectively, of the electron. The integrals are carried out over the coordinates θ' and ϕ', and the direction $\hat{k}$ of the outgoing electron is represented in terms of the spherical polar coordinates θ and ϕ. For the specific case that the photon is plane polarized, *i.e.*, the electric field of the photon is parallel to the axis of quantization $\hat{z}$ of the system, the scalar product $\hat{\epsilon}\cdot\hat{r}'$ leads to the dipole coupling operator $\cos\theta'$, and the integral vanishes identically for $l' \neq l\pm1$ and $m' \neq m$. Angular minima as a function of θ will be treated in more detail in the section treating angular distributions.

B. MULTIPHOTON IONIZATION

For a multiphoton ionization process we have to include the coupling of the initial state with all the intermediate (bound) angular momentum states, resonant and non-resonant alike. We first consider the simplest case of two photon ionization of the ground state using photons of the same wavelength and polarization. The differential cross section may be written[3,4]

$$\frac{d\sigma}{d\Omega}(\theta,\phi) = const \left| \sum_j \langle \psi_f | \vec{r}\cdot\vec{\mathrm{E}} | \psi_j \rangle \frac{\langle \psi_j | \vec{r}\cdot\vec{\mathrm{E}} | \psi_i \rangle}{E_i - E_j + h\nu_1 + i\Gamma_j/2} \right|^2_{\substack{Averaged\,over \\ initial\,state \\ projections}}, \quad (2\text{-}14)$$

where E_i - E_j is the difference in energy between the initial state and the jth excited state, $h\nu_1$ is the energy of the photon used to excite the ground state, and Γ_j is the natural width of the intermediate state j. The constant of proportionality, again, will depend on the particular system of units chosen to study the process. Due to the dipole transition selection rules we need to consider only those states that are coupled with the ground state through a dipole transition. Equation (2-14) can be rewritten (for simplicity we can drop the "averaged over initial state projections" subscript)

$$\frac{d\sigma}{d\Omega}(\theta,\phi) = const \left| \sum_j \langle \psi_f | \vec{r}\cdot\vec{\mathrm{E}} | \psi_j \rangle (\vec{r}\cdot\vec{\mathrm{E}})_{ij} \right|^2, \quad (2\text{-}15)$$

where $(\vec{r}\cdot\vec{\mathrm{E}})_{ij}$ is used to denote the transition probability from the ground state to the jth excited state. The sums are carried over all the intermediate angular momentum states, resonant and nonresonant, coupled by each and all the photons used. In this viewpoint, we see that equation (2-15) is just the norm of a linear combination of terms like those in equation (2-1), modified by the coefficients $(\vec{r}\cdot\vec{\mathrm{E}})_{ij}$. Similarly, the differential cross section for a $n + 1$ photon process can be written

$$\frac{d\sigma}{d\Omega}(\Omega) = const\left|\sum_{j_1\cdots j_n}\langle\psi_f|\vec{r}\cdot\vec{\mathbf{E}}|\psi_{j_n}\rangle\frac{\langle\psi_{j_n}|\vec{r}\cdot\vec{\mathbf{E}}|\psi_{j_{n-1}}\rangle}{E_{j_{n-1}}-E_{j_n}+h\nu_1+i\Gamma_{j_n}/2}\cdots\frac{\langle\psi_{j_1}|\vec{r}\cdot\vec{\mathbf{E}}|\psi_i\rangle}{E_i-E_{j_1}+h\nu_1+i\Gamma_{j_1}/2}\right|^2,$$

$$= const\left|\sum_{j_1\cdots j_n}\langle\psi_f|\vec{r}\cdot\vec{\mathbf{E}}|\psi_{j_n}\rangle(\vec{r}\cdot\vec{\mathbf{E}})_{j_{n-1}j_n}\cdots(\vec{r}\cdot\vec{\mathbf{E}})_{ij_1}\right|^2, \qquad \textbf{(2-16)}$$

where the sums are carried out over all the intermediate states, resonant and non-resonant, and include all the possible paths for photoionization. This enables us to consider resonantly enhanced multiphoton ionization as an extension of single photon ionization processes.

An advantage of using multiphoton ionization (MPI) techniques is the ability to study the differential cross section for photoionization of resonant excited states of atoms. By varying the photon frequency, and hence the photon energy, multiphoton absorption can be used to resonantly excite the electron from the ground state to any of the bound states. In addition, due to the dependence of the factor $(\vec{r}\cdot\vec{\mathbf{E}})_{ij}$ on the photon energy, this factor becomes large for resonant transitions, and is comparatively small for nonresonant transitions. The allowed resonant transitions are determined by both the parity and the angular momentum of the states, as well as the number of photons absorbed by the electron in transit between bound states. These transitions give rise to angular momentum polarization of the intermediate state, which are discussed in better detail in the section dealing with angular momentum considerations.

Although the factor $(\vec{r}\cdot\vec{\mathbf{E}})_{i\,j}$ is relatively small, nonresonant multiphoton ionizations can still be observed if the electron absorbs the photons within a narrow period of time, *i.e.*, within the lifetimes of the intermediate virtual states. This requirement can be satisfied by using a high power, pulsed laser as the light source, since this type of laser can provide a large number of photons within a narrow pulse. Nonresonant multiphoton ionization will exhibit a large dependence on the power density of the light source. In particular, the total cross section for $(n + 1)$ multiphoton ionization will be inversely proportional to the power density of the laser raised to the

$n + 1$ power, thus requiring strong light sources. In other words, the nonresonant multiphoton ionization of an atom can be considered as the photoionization of the ground state using a composite photon, made up of the addition of $n + 1$ photons.

C. STARK EFFECTS

A consequence of using an intense coherent light source is that, due to superposition, the electric field strength $\bar{\mathbf{E}}$ of the photon may become quite large, making the linear and the quadratic Stark effects more significant. Furthermore, due to the oscillatory behavior of the electric field, it is also possible to observe the optical (or a.c.) Stark effect.[14] The linear Stark effect can be larger than fine structure effects, and is given to first order by the perturbation[15]

$$H' = ez\mathbf{E}_0, \tag{2-17}$$

where e is the charge of the electron, z is the component of the position vector $\bar{r}$, and the magnitude of the electric field is denoted by $\mathbf{E}_0 = |\bar{\mathbf{E}}|$. This perturbation couples the orbital quantum levels of different parity of the atom, and the eigenstates of the perturbed Hamiltonian are neither eigenstates of the parity nor of the orbital angular momentum $\bar{\mathbf{L}}^2$ operators, thus the orbital quantum numbers l (and parity) are no longer good quantum numbers (in contrast with fine structure effects that make only the magnetic projections m_l not good quantum numbers). From equation (2-17) we see that the energy shift for the linear Stark effect is, to first order, proportional to the electric field strength $\mathbf{E}_0$. The linear Stark effect is of consequence whenever the atomic (or molecular) system under observation is placed in an external electric field, causing shifts in the energy levels of the atom (or molecule). The linear Stark effect requires a true degeneracy of the energy level, as those in the hydrogen atom. For other atomic energy levels where there are no true degeneracies, the quadratic Stark effect will be more dominant.

It is also possible to observe energy shifts due to the a.c. or optical Stark effect. The shift in energy of an atomic level i induced by the plane polarized electric field $\vec{E}(\vec{r},\omega)=\mathrm{Re}E_0e^{-i(\kappa z-\omega t)}\hat{z}$ is given by[16]

$$\Delta E_j = \frac{1}{4}\sum_{i\neq j}\left\{\frac{|\vec{P}_{ij}\cdot\vec{E}_0|^2}{E_j-E_i-h\nu_1}+\frac{|\vec{P}_{ij}\cdot\vec{E}_0|^2}{E_j-E_i+h\nu_1}\right\}, \qquad \textbf{(2-18)}$$

where $\bar{P}_{ij}$ is the transition dipole moment from the state i to j; $\nu_1=\omega/2\pi$ is the frequency of the time dependent electric field $\bar{E}$; and E_i and E_j are the energies of the unperturbed levels. The optical Stark effect is treated in some detail by Hanna, *et al.*,[17] where the effect is described as an irreversible energy flow from the electromagnetic field of the photon to the atomic system at any instant. The above equation can also be written as[17]

$$\Delta E_i = \alpha_i(\omega)\,|\vec{E}(\omega)|^2, \qquad \textbf{(2-19)}$$

where $\alpha_i(\omega)$ is the frequency-dependent polarizability for the state. When the electric field is static (*i.e.*, $\omega = 0$) we recover the familiar quadratic d.c. Stark effect, with the average optical field strength $\frac{1}{2}\,|\,\bar{E}(\omega)\,|^2$ replaced by E_{DC}^2. In practice, when a pulsed laser is used, the light intensity will rise from zero to a maximum and then decrease back to zero. Thus the atom experiences different energy shifts during the laser pulse and the observed shift will depend on the presence of near resonances[16] and on the pulse shape.

D. ANGULAR MOMENTUM CONSIDERATIONS

In this section we will consider the angular momentum of the photon and how it affects the electron and the ionization process. The photon particle carries one unit of angular momentum, $\bar{u}$, which can be arbitrarily "lined up" with respect to the electron's total angular momentum $\bar{J}$ (made up of orbital angular momentum $\bar{L}$ and electron spin

angular momentum $\bar{S}$). Note that, due to the intrinsic spin, the electron always has at least ½ unit of total angular momentum.

In a multiphoton ionization process using p photons, with an initial (ground state) total angular momentum j_i, the final (continuum) electron total angular momentum j_f may be less than $(j_i - p)$, more than $(j_i + p)$, or any value between these two limits one unit of angular momentum apart. The angular momentum is a vector quantity, and the vector sum of the initial total angular momentum is conserved by the photoionization process. The final angular momentum state will be best described by a linear combination of the unbound angular momentum states, or partial waves, as described by equation (2-9).

In a resonant multiphoton process, the population of the projections m_j (onto the axis of quantization z, as defined by the polarization $\hat{\epsilon}$ of the photons) of the total angular momentum j of the intermediate resonant state (as compared to the initial total angular momentum j_i) will depend on the polarization of the photons used in the excitation process. Plane polarized photons ($\hat{\epsilon} = \hat{e}_z$) will not change the ground state projections, *i.e.*, $\Delta m_j = 0$, whereas circularly polarized photons ($\hat{\epsilon} = \hat{e}_\pm = (\hat{e}_x \pm i\hat{e}_y)/\sqrt{2}$) can change the projections by $\Delta m_j = +1$ (for right, $\hat{\epsilon} = \hat{e}_+$) or by $\Delta m_j = -1$ (for left $\hat{\epsilon} = \hat{e}_-$). This selection rule operates in addition to the other electric dipole transition selection rules $\Delta l = \pm 1$ and $\Delta j = \pm 1,0$. These rules give rise to angular momentum polarization of the intermediate excited state. This polarization can be described by making an expansion of the angular momentum distribution into multipole moments. Depending on the population distribution of the electrons, given by the occupation probabilities $\rho(m_j)$ of the $2j+1$ magnetic sublevels, an atom or molecule can be said to be isotropic (if all sublevels are equally populated, and the monopole term is proportional to the total population), to be oriented (if the distribution can be characterized fully by only the odd power multipole moments, *i.e.*, dipole, octupole, etc.), or to be aligned (if the distribution can be characterized fully by only the even power multipole moments, *i.e.*, quadrupole, hexadecapole, etc.). Figure 2.1 provides examples of population distributions of magnetic sublevels for a system with $j = 2$. Part (a) shows a pure isotropic distribution obtained from a pure monopole moment, part (b) shows a pure oriented distribution (obtained

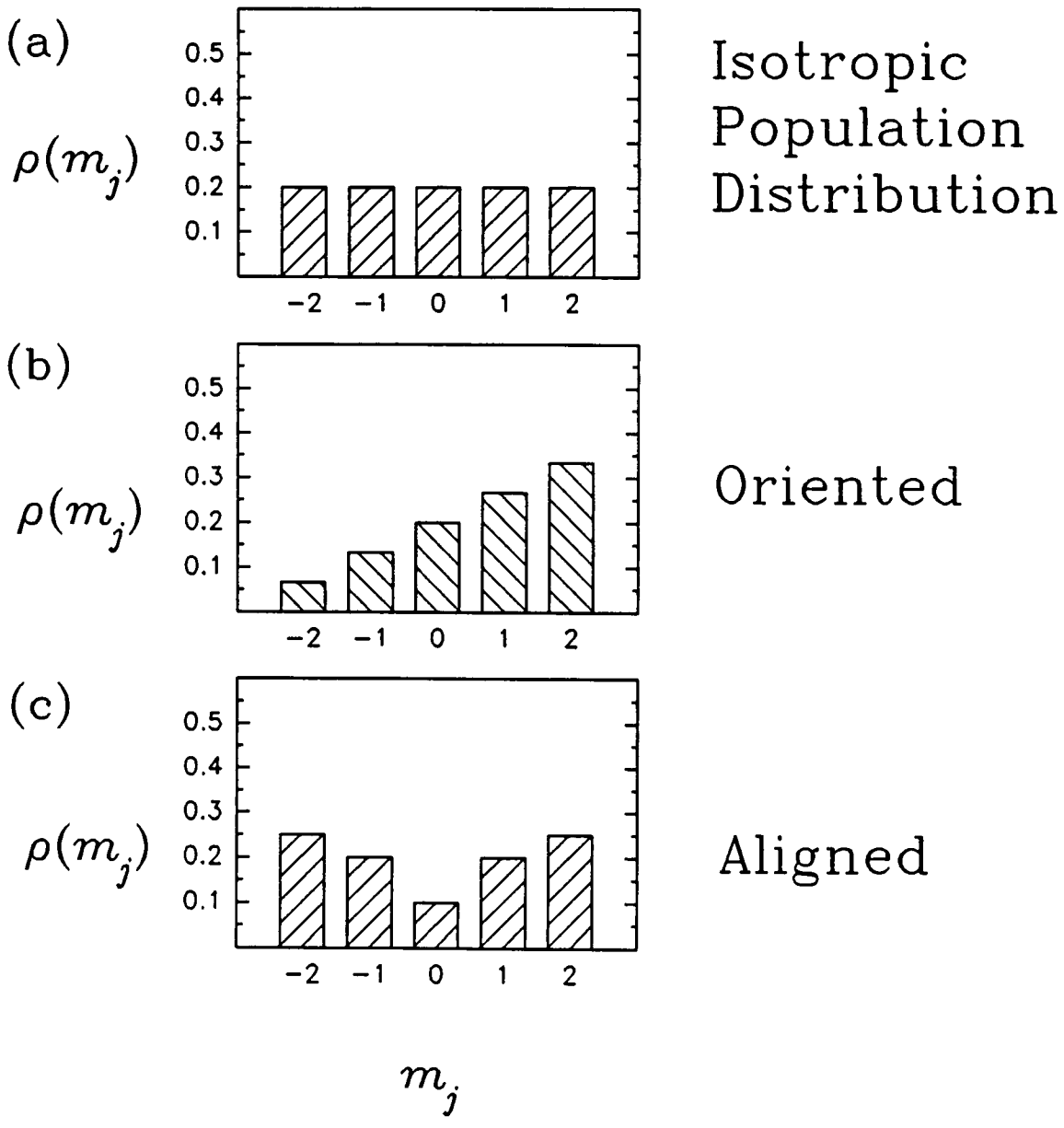

Fig. 2.1. Examples of electron population distributions of magnetic sublevels for the case $j = 2$: (a) isotropic (pure monopole); (b) oriented (a combination of a monopole and a dipole); (c) aligned (a combination of monopole and quadrupole). *Adapted from Greene and Zare, Am. Rev. Phys. Chem, 1982, 33, pp. 119-150.*

from the combination of a monopole and a dipole moments), and part (c) shows a pure aligned distribution (obtained from the combination of a monopole and a quadrupole moments).[5] It is possible for a system to exhibit both orientation and alignment.[18]

Mathematically, these multipole moments can be written as expectation values of the tensor harmonics, or Wigner and Racah operators $T(J)^k_\mu$,[5] and these, by using the Wigner-Eckart theorem, in terms of the spherical tensor operators $J^{(L)}_q$,[18] which are expressed as linear combinations of the powers of the components of the angular momentum operator $\bar{\mathbf{J}}$. The low order tensor harmonic operators are listed in Table II-1 in terms of the components of $\bar{\mathbf{J}}$, *i.e.*, J_+, J_-, J_3, and of $\bar{\mathbf{J}}^2$.[19] The multipole moments are consequently given by[18]

$$n_L = \langle T(J)^{L\dagger}_0 \rangle = \langle J^{(L)}_0 \rangle \frac{\langle J || T^L || J \rangle}{\langle J || J^{(L)} || J \rangle} . \qquad \textbf{(2-20)}$$

In terms of the magnetic projections m_j and total angular momentum j the low order multipoles may be written[18]

$$n_0 = \frac{1}{\sqrt{2j+1}} \sum_{m_j} \rho(m_j) , \qquad \textbf{(2-21.a)}$$

$$n_1 = \left[\frac{3}{j(j+1)(2j+1)}\right]^{\frac{1}{2}} \sum_{m_j} m_j \, \rho(m_j) , \qquad \textbf{(2-21.b)}$$

$$n_2 = \left[\frac{30}{j(j+1)(2j-1)(2j+1)(2j+3)}\right]^{\frac{1}{2}} \sum_{m_j} (3m_j^2 - j(j+1)) \, \rho(m_j) , \qquad \textbf{(2-21.c)}$$

$$n_3 = \left[\frac{70}{(j-1)j(j+1)(j+2)(2j-1)(2j+1)(2j+3)}\right]^{\frac{1}{2}} \times \sum_{m_j} (5m_j^2 - 3j(j+1) + 1) \, m_j \, \rho(m_j) , \qquad \textbf{(2-21.d)}$$

Table II-1 Low order tensor harmonic operators. *Adapted from Biedenharn, et. al., "Angular Momentum In Quantum Physics", pp. 656-657 (1981).*

k	μ	T^k_μ
0	0	1
1	± 1	$\mp\sqrt{2}J_\pm$
	0	$2J_3$
2	± 2	$\sqrt{6}J_\pm^2$
	± 1	$\mp\sqrt{6}J_\pm(2J_3 \pm 1)$
	0	$2(3J_3^2 - \vec{J}^2)$
3	± 3	$\mp 2\sqrt{5}J_\pm^3$
	± 2	$2\sqrt{30}J_\pm^2(J_3 \pm 1)$
	± 1	$\mp 2\sqrt{3}J_\pm(5J_3^2 - \vec{J}^2 \pm 5J_3 + 2)$
	0	$4(5J_3^2 - 3\vec{J}^2 + 1)J_3$
4	± 4	$\sqrt{70}J_\pm^4$
	± 3	$\mp 2\sqrt{35}J_\pm^3(2J_3 \pm 3)$
	± 2	$2\sqrt{10}J_\pm^2(7J_3^2 - \vec{J}^2 \pm 14J_3 + 9)$
	± 1	$\mp\sqrt{5}J_\pm(28J_3^3 - 12\vec{J}^2J_3 \pm 42J_3^2 \mp 6\vec{J}^2 + 38J_3 \pm 12)$
	0	$70J_3^4 - 60\vec{J}^2J_3^2 + 6J^4 + 50J_3^2 - 12\vec{J}^2$

where $\rho(m_j)$ is the population of the magnetic sublevel m_j, corresponding to the intermediate resonant j level; and n_L represents the 2^L multipole moment of the state atom or molecule: the $L=0$ moment is the monopole moment, $L=1$ is the dipole moment, the $L=2$ is the quadrupole moment, and so on. The population of the m_j states is completely described by these multipole moments. For a state with angular momentum j there are in general $2j+1$ different multipole moments. In the large j limit we approach the correspondence principle with classical mechanics, and the multipole moments become the average value of the Legendre Polynomials[5]

$$\lim_{j\to\infty} n_L = \langle P_L(\hat{J}\cdot\hat{z})\rangle \,, \tag{2-22}$$

and the orientation and alignment are proportional to[5]

$$O_0 = \langle P_1(\hat{J}\cdot\hat{z})\rangle = \frac{\langle J_z\rangle}{|\vec{J}|} \,, \tag{2-23.a}$$

$$A_0 = \langle P_2(\hat{J}\cdot\hat{z})\rangle = \left\langle \frac{3J_z^2 - \vec{J}^2}{2\vec{J}^2} \right\rangle, \tag{2-23.b}$$

respectively for all j. However, the correspondence given by equation (2-22) only holds for $L \geq 3$ in the high j classical limit.[5]

These multipole moments can be interpreted as the coefficients in a linear expansion of the density operator in the basis of the spherical tensor operators[10]

$$T(J)_{k\mu} = \sum_{M,M'} (-1)^{J-M} (JM', J-M' \,|\, k\mu) |JM'\rangle \langle JM| \,, \tag{2-24}$$

where $(JM', J\text{-}M' \,|\, k\mu)$ are the Clebsch-Gordan coefficients, and k ranges from 0 to $2J$ and μ ranges in unit steps from $-k$ to k. These operators behave under rotation like the spherical harmonic functions $Y_{k\mu}(\theta,\phi) = N_{k\mu}P_{k\mu}(\cos\theta)e^{-i\mu\phi}$ and constitute an orthonormal basis, since they satisfy the orthonormality conditions[5]

$$Tr[T(J)^{\dagger}_{k\mu}\ T(J)_{k'\mu'}] = T(J)^{*}_{k\mu} \cdot T(J)_{k'\mu'} = \delta_{kk'}\delta_{\mu\mu'} \ . \qquad \text{(2-25)}$$

The density matrix may be written in this basis as[5]

$$\rho = \sum_{k,\mu} \rho_{k\mu}\ T_{k\mu} \qquad \text{(2-26)}$$

with the expansion coefficients given by[5]

$$\rho_{k\mu} = Tr[T^{\dagger}_{k\mu}\rho] = T^{*}_{k\mu} \cdot \rho = \langle T^{\dagger}_{k\mu} \rangle Tr[\rho] \ . \qquad \text{(2-27)}$$

The coefficients ρ_{L0} are the multipole moments n_L given by equation (2-20). In a matrix representation, these multipole moments correspond to the diagonal elements. A complete description of the photoionization process based on density matrices is given by Laplanche, *et al.*,[20] using density matrix descriptions for the initial and final states, as well as using a density matrix description of the radiation field. This formalism allows dealing with multiphoton processes in a more concise manner without being overwhelmed by the calculation of the angular parts related to the different possible ionization channels, whose number becomes prohibitive if the initial state is the excited one.[20]

Finally, we remark that since (to first order) the photon induces only an electric dipole transition, the photon does not couple any of the spin eigenfunctions, and neither the total electron spin nor its projection can be altered significantly by the excitation process.

E. PHOTOELECTRON ANGULAR DISTRIBUTIONS

The goal of this dissertation is to describe the measurements of photoelectron angular distributions (PEAD), or more specifically, differential cross sections for

resonantly enhanced multiphoton ionization (REMPI), and to relate them to existing theory. The angular distribution of photoelectrons from an arbitrary distribution of states, using $n + 1$ photons of arbitrary polarization is given by[4,21]

$$I(\theta,\phi) = \sum_{k=0}^{n+1} \sum_{m=-2k}^{+2k} \beta_{2k,m} Y_{2k,m}(\theta,\phi) \qquad \text{(2-28)}$$

where the $Y_{2k,m}$ are the spherical harmonics, and the expansion coefficients $\beta_{2k,m}$ contain information about the dynamics of excitation and ionization. The actual number of terms in the expansion depends on the possible final total angular momentum j_f of the electron, *i.e.*, that for which the index k is one greater than the difference between the number of $\Delta j = +1$ and $\Delta j = -1$ transitions in the spectroscopically selected route to the resonance state.[4] However, this difference is just the net total angular momentum added to the electron through absorption of n photons, thus we may write

$$k_{max} = |\Delta j_+ - \Delta j_-| + 1 = |j - j_i| + 1, \qquad \text{(2-29)}$$

where j is the total angular momentum of the resonant intermediate state, and j_i is the total angular momentum of the initial state. The "+ 1" term reflects the fact that n photons are used to excite the atom, and one more photon is required to carry out the photoionization of the electron. Equation (2-28) may be also used to describe the angular distributions of $n + n'$ resonant, and of $n + 1$ nonresonant multiphoton ionizations, with the limits now given by $k_{max} = |\Delta j_+ - \Delta j_-| + n'$, and by $k_{max} = n + 1$, respectively.

In the specific case that the photons are plane polarized, resulting in the interaction operator $r\cos\theta$, there is no ϕ dependence, and all terms on the right hand side of equation (2-11) will vanish except those for which $\Delta m = m - m' = 0$.[4] We may then expect the angular distribution to be given only by the $Y_{2k,0}$ functions. Furthermore, in the particular case $l_i = 0$, *i.e.*, the electron is initially in a pure s state, all the initial angular momentum of the electron is given by spin, and the upper limit for the sum is obtained from the total angular momentum j of the intermediate resonant state, and use

of equation (2-29) with $j_i = 1/2$. The angular distribution for the $n + 1$ resonant multiphoton ionization starting from an isotropic population distribution, and using plane polarized light may then be described by the equation

$$\frac{d\sigma}{d\Omega} = \frac{\sigma(\epsilon)}{4\pi} [1 + \sum_{i=1}^{j+1/2} \beta_{2i} P_{2i}(\cos\theta)] \qquad (2\text{-}30)$$

where $\sigma(\epsilon)$ is the total cross section for photoionization as a function of the outgoing electron energy, ϵ, and is factored out so that the leading term of the Legendre expansion is 1; β_{2i} are the asymmetry parameters; P_{2i} are the even order Legendre polynomials; and the angle θ is measured with respect to the plane of polarization of the electric field of the photon. Equation (2-30) in addition to considering the dipole moment of the distribution also considers the higher multipole moments of the distribution through the asymmetry parameters β_{2n}.

The asymmetry parameters β_{2n} depend on the radial matrix elements corresponding to transition probabilities between the intermediate (bound) state and all of the possible final angular momentum partial waves of the expansion (2-9) of the continuum state, as well on the phase shifts of these partial waves. These matrix elements must satisfy the selection rules $\Delta l = \pm 1$, $\Delta j = \pm 1, 0$. Equation (2-30) also assumes that the initial bound state is in a definite state of angular momentum, and also takes into consideration that the intermediate state may not be isotropically populated, but rather has some alignment or orientation.

A modified form of equation (2-30)

$$I(\theta) = a_0 + \sum_{i=1}^{j+1/2} a_{2i} P_{2i}(\cos\theta) \ , \qquad (2\text{-}31)$$

will be used to fit the experimental measurements, and the asymmetry parameters will be calculated as the ratio $\beta_{2i} = a_{2i}/a_0$. This allows us to handle the experimental data independently of any weighing or scaling factors, such as detector gain or efficiency, and to consider all data within the same scale.

Cooper and Zare[3] have made theoretical calculations for the asymmetry parameters for the case of LS coupling of nonrelativistic single-particle wave functions, and single photon ionization from an initial state with orbital angular momentum l, and with an isotropic distribution of substates. In this instance, β is given by[3]

$$\beta_2(\epsilon,l) = \frac{l(l-1)R_{l-1}^2+(l+1)(l+2)R_{l+1}^2-6l(l+1)R_{l-1}R_{l+1}\cos\Delta}{(2l+1)[lR_{l-1}^2+(l+1)R_{l+1}^2]}, \qquad \text{(2-32)}$$

where $R_{l\pm1}$ are the radial matrix elements between the bound and the continuum wave functions for the $l \pm 1$ partial waves; and $\Delta=\delta_{l+1} - \delta_{l-1}$ is the difference in the phase shifts for the two possible continuum wavefunctions. Several special cases are worth noting, but in particular we note that for ionization from a pure *ns* orbital ($l=0$), equation (2-32) produces a β parameter independent of the energy and of the phase shifts, and identically equal to 2. Deviations from this result, have been shown to occur when anisotropic electron-ion interactions are important[22-25] or when relativistic (spin-orbit) interactions are appreciable.[26-31] Anisotropic electron-ion interactions are absent for photoionization from the *s* states of alkali-metal atoms, and deviations from $\beta = 2$ provide a direct test of relativistic interactions. Inclusion of spin-orbit effects will be treated in greater detail in section H.

Compton, *et al.*[32] give specific formulas for the lower order β parameters for excitation of a $n^2S_{1/2}$ ground state to the $n'^2P_{1/2}$ or to the $n'^2P_{3/2}$ states, and subsequent ionization from the excited state using plane polarized light[32]

$$\beta'_2(^2P_{1/2}) = \frac{3\chi^2-6\chi\cos(\delta_0-\delta_2)}{1+\chi^2+2\chi\cos(\delta_0-\delta_2)}, \qquad \text{(2-33.a)}$$

$$\beta'_2(^2P_{3/2}) = \frac{-3[5\chi^2+8\chi\cos(\delta_0-\delta_2)]}{4[1+\chi^2+2\chi\cos(\delta_0-\delta_2)]}, \qquad \text{(2-33.b)}$$

$$\beta'_4(^2P_{3/2}) = \frac{27\chi^2}{4[1+\chi^2+2\chi\cos(\delta_0-\delta_2)]} . \qquad \text{(2-33.c)}$$

Here $\chi = R_D(\epsilon)/R_S(\epsilon)$ is the ratio of the ionization radial matrix elements (given by equation (2-12)), and δ_l is the phase shift of the lth partial wave. These are the coefficients for the case in which equation (2-31) is expressed explicitly as an expansion of powers of cosines. They can be easily transformed to the case, in which equation (2-31) is expressed as an expansion of the Legendre polynomials. The transformation equations are, for $\beta_2(^2P_{1/2})$

$$\beta_2(^2P_{1/2}) = \frac{2\beta'_2(^2P_{1/2})}{3+\beta'_2(^2P_{1/2})} , \qquad \text{(2-34)}$$

and for $\beta_2(^2P_{3/2})$ and $\beta_4(^2P_{3/2})$ we have

$$\beta_2(^2P_{3/2}) = \frac{10}{7}\,\frac{7\beta'_2(^2P_{3/2})+6\beta'_4(^2P_{3/2})}{15+5\beta'_2(^2P_{3/2})+3\beta'_4(^2P_{3/2})} , \qquad \text{(2-35.a)}$$

$$\beta_4(^2P_{3/2}) = \frac{24}{7}\,\frac{\beta'_4(^2P_{3/2})}{15+5\beta'_2(^2P_{3/2})+3\beta'_4(^2P_{3/2})} . \qquad \text{(2-35.b)}$$

In the formalism used in equation (2-31), these parameters take the form:

$$\beta_2(^2P_{1/2}) = \frac{2\chi^2 - 4\chi\cos(\delta_0-\delta_2)}{1+2\chi^2} , \qquad \text{(2-36.a)}$$

$$\beta_2(^2P_{3/2}) = \frac{5}{7}\,\frac{19\chi^2 - 56\chi\cos(\delta_0-\delta_2)}{10+11\chi^2} , \qquad \text{(2-36.b)}$$

$$\beta_4(^2P_{3/2}) = \frac{108}{7}\,\frac{\chi^2}{10 + 11\chi^2}\,. \qquad \textbf{(2-36.c)}$$

Equations (2-36.a-c) are obtained by transforming the expressions given by Compton, *et al.*[32] (equations (2-33.a-c)) using equations (2-34) and (2-35) into the more convenient formalism used in equation (2-31). Equation (2-36.a) can also obtained by using equation (2-32) with $l = 1$ (since the intermediate state is isotropically populated by the excitation process). Equations (2-36.b) and (2-36.c) cannot be obtained from equation (2-32), since the intermediate resonant $n^2P_{3/2}$ state is aligned. Equations similar to (2-36) have been obtained in more elegant fashion by Smith and Leuchs.[4]

The bounds and ranges for the values of the β parameters can be obtained from the condition

$$1 + \sum_{i=1}^{j+1/2} \beta_{2i} P_{2i}(\cos\theta) \geq 0\,, \qquad \textbf{(2-37)}$$

i.e., the differential cross section must be nonnegative for all values of the asymmetry parameters β_{2i}, and it must also hold for all angles θ, specifically at the angular minima. For states with total angular momentum $j = 1/2$, we have

$$1 + \beta_2 P_2(\cos\theta) \geq 0 \qquad \textbf{(2-38)}$$

which after differentiating with respect to θ (in order to identify extrema), setting the derivative equal to zero and solving for β_2, yields the well known result:

$$-1 \leq \beta_2 \leq 2\,. \qquad \textbf{(2-39)}$$

This result is also applicable for all angular distributions from states with an isotropic distribution of magnetic sublevels.

For angular distributions of states with total angular momentum $j = 3/2$, we have from condition (2-37)

$$1 + \beta_2 P_2(\cos\theta) + \beta_4 P_4(\cos\theta) \geq 0\,. \qquad \textbf{(2-40)}$$

Again, by using calculus we find that the inequality has up to three extrema conditions

$$\cos\theta = 0 , \qquad \text{(2-41.a)}$$

$$\cos\theta = 1 , \qquad \text{(2-41.b)}$$

$$\cos^2\theta = \frac{6\beta_2 - 15\beta_4}{35} . \qquad \text{(2-41.c)}$$

We remark that the third extremum only occurs if the condition

$$0 \le 6\beta_2 - 15\beta_4 \le 35 \qquad \text{(2-42)}$$

is also met, *i.e.*, θ is actually an angle. Thus by requiring that the angular distribution be positive, or nonnegative, at the extrema we obtain the inequalities

$$1 - \frac{1}{2}\beta_2 + \frac{3}{8}\beta_4 \ge 0 , \qquad \text{(2-43.a)}$$

$$1 + \beta_2 + \beta_4 \ge 0 , \qquad \text{(2-43.b)}$$

$$1 + \frac{1}{2}\beta_2\left[\frac{-18\beta_2 + 10\beta_4}{35\beta_4}\right] + \frac{1}{8}\beta_4\left[\frac{36\beta_2^2 - 120\beta_4^2}{35\beta_4^2}\right] \ge 0 . \qquad \text{(2-43.c)}$$

This results are shown in Figure 2.2. Note that when $\beta_4 = 0$, we obtain the same result as for the case $j = 1/2$, *i.e.*, inequalities (2-39). Due to the presence of β_4 in the expression for the angular distribution, the range for β_2 is no longer restricted to be between -1 and 2. From the figure we note that the range for β_2 is reduced for negative values of β_4 and extended for some positive values of β_4. All combinations of values for β_2 and β_4 that lie within the boundaries of the "teardrop" yield valid expressions for the

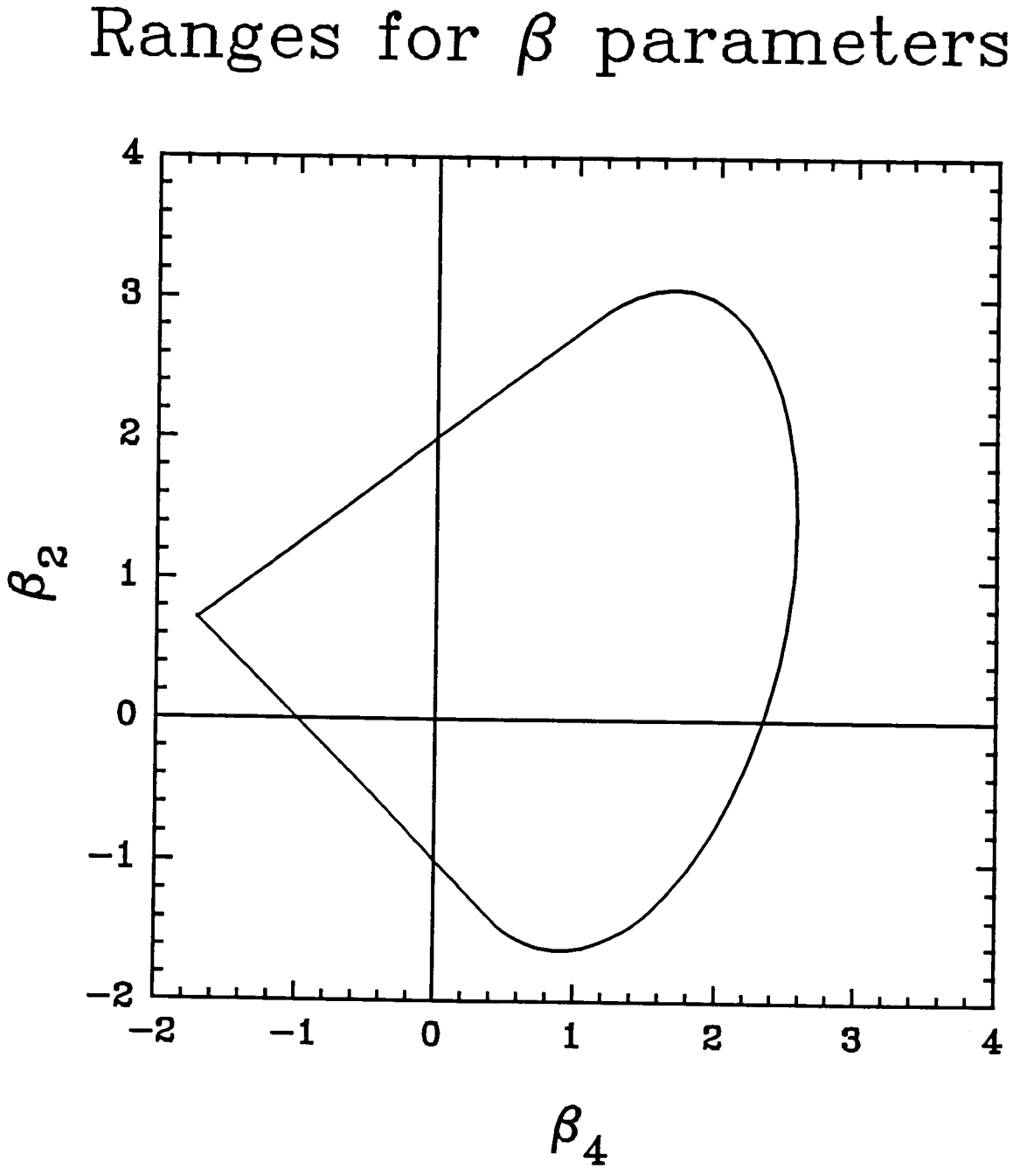

Fig. 2.2. Ranges for β_2 and β_4 using the nonnegative probability condition and the results of equation (2-43).

angular distribution. Different pairs of the asymmetry parameters result from different alignment of the resonant state, which results from using different light polarizations to excite the electron.

More exact bounds for the specific case of resonant photoionization using $n + 1$ plane polarized photons are obtained by varying the parameter χ and the phase shift difference (δ_0 - δ_2) in equations (2-36.a-c). In this case the plane polarized photons couple only the states with the same angular momentum projections m_j, resulting in alignment of the intermediate resonant state, and on the asymmetry parameters given by equations (2-36). We obtain for $j = 1/2$ the same result as before, namely equation (2-39), and for $j = 3/2$ we obtain the family of curves depicted in Figure 2.3 by some selected values of the difference of the phase shifts, $\Delta = \delta_0 - \delta_2$. The perimeter of each curve is obtained by varying the value of χ from $-\infty$ to $+\infty$. From the figure, we remark that β_4 is zero only if β_2 is zero as well. Furthermore, equations (2-36) limit the range of values of the β parameters to a smaller region than that restricted by condition (2-37). This is due to the fact that equations (2-36.a-c) take into account the particular population distributions that result from using plane polarized light. It is interesting to observe that the results of figure 2.3 exclude the result found previously for PEADs from $j = 1/2$ states, implying that for PEADs through a resonant $j = 3/2$ state, there always is a nonzero quadrupole moment in the angular distribution whenever plane polarized light is used. The β_4 parameter serves as an indicator of the alignment of the intermediate state. The greater this alignment, *i.e.*, the quadrupole moment of the distribution, then the larger this parameter will be.

More restricting ranges can be obtained by using a specific model for ionization based on the particular process and the specific atomic state being measured. Calculations using these models will be carried out as part of this dissertation in a forthcoming chapter as part of the analysis of the experimental results.

Finally, the general ranges for the β parameters corresponding to resonantly enhanced photoelectron angular distributions through higher j levels can be obtained from condition (2-37) by using a similar procedure. These results are given in Appendix A,

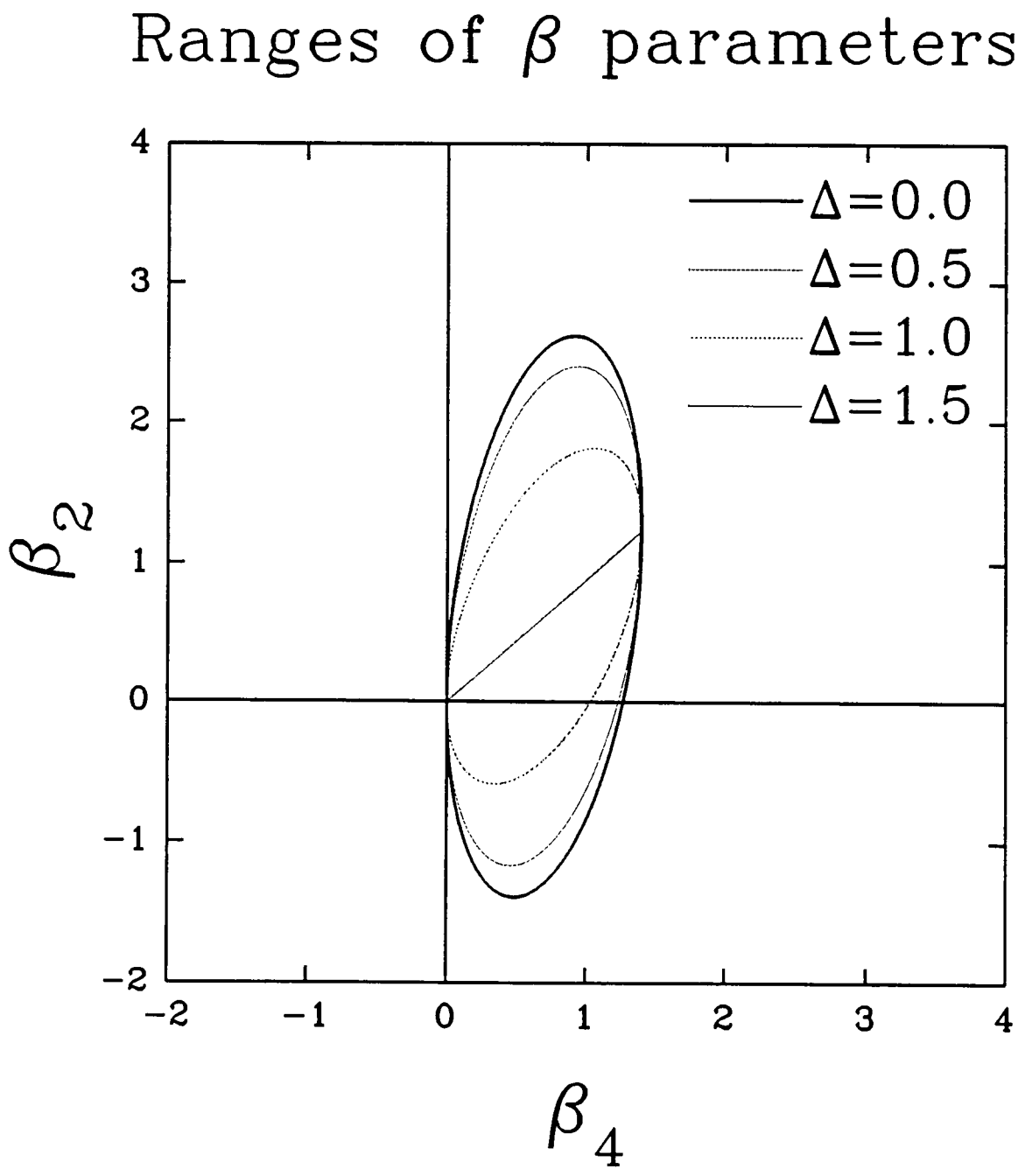

Fig. 2.3. Ranges for the β parameters as given by the equations from Compton, *et al.*, and as adapted for this dissertation. Here, $\Delta = \delta_0 - \delta_2$ is the difference in the phase shifts of the continuum wavefunctions, and $\chi = R_D/R_S \in (-\infty, \infty)$.

outlining some of the details of the calculations using Maple V (University of Waterloo, Maple V Release 2 for MS Windows) for the case $j=3/2$.

F. HYPERFINE STRUCTURE AND ANGULAR DISTRIBUTIONS

The alignment, or orientation, of a state created by the excitation is given entirely by the population distribution $\rho(m_j)$ of the magnetic sublevels. However, due to coupling of the total angular momentum of the electrons with the nuclear spin $\bar{\mathbf{I}}$, the magnetic quantum numbers m_j are no longer constants of the system. The time dependent alignment and orientation of the intermediate state are given by Greene and Zare[5]

$$\begin{aligned} A(t) &= A(0)g^{(2)}(t), \\ O(t) &= O(0)g^{(1)}(t), \end{aligned} \tag{2-44}$$

where the time dependent factor is given by

$$g^{(k)}(t) = \sum_{F,F'} \frac{(2F+1)(2F'+1)}{(2I+1)} \begin{Bmatrix} F & F' & k \\ J_i & J_i & I \end{Bmatrix}^2 \cos\omega_{F'F}t. \tag{2-45}$$

In this expression, $\omega_{F'F}$ is the frequency splitting between the two hyperfine sublevels of total angular momenta $\bar{\mathbf{F}}'$ and $\bar{\mathbf{F}}$; J_i is the angular momentum quantum number of the intermediate excited state, and I is the nuclear spin quantum number. The factor in brackets is a Wigner 6-j symbol which can be obtained from tables (see for example the tables in Cowan[13]).

Arimondo, *et al.*[33] give a complete and detailed treatment of the calculation of the hyperfine structure for alkali atoms, with formulas for the hyperfine energy contributions due to the electric dipole and quadrupole. As long as J can be considered a good

quantum number for the states with $J = l \pm 1/2$, the hyperfine energy shift can be written[33]

$$W^{eff} = hA\vec{I}\cdot\vec{J} + hB\frac{6(\vec{I}\cdot\vec{J})^2 + 3(\vec{I}\cdot\vec{J}) - 2I(I+1)J(J+1)}{2I(2I-1)2J(2J-1)}, \qquad \textbf{(2-46)}$$

where the magnetic dipole constant A and the electric quadrupole constant B are defined by[33]

$$A = \left(1 \mp \frac{1}{2l+1}\right)a_o \pm \frac{1}{2l+1}a_c + 3\left[\frac{5(2J+1)(2l+1)l(l+1)}{J(J+1)(2l+3)(2l-1)}\right]^{1/2}\begin{Bmatrix} 1/2 & 1/2 & 1 \\ l & l & 2 \\ J & J & 1 \end{Bmatrix} a_d , \qquad \textbf{(2-47)}$$

$$B = \frac{2J-1}{2J+2}b_q , \qquad \textbf{(2-48)}$$

where the $+$ is used for $j = l + 1/2$, and the $-$ is used for $j = l - 1/2$. The quantity in braces is a Wigner 9-j symbol, and can be obtained from tables[34,35] or from its definition in terms of 6-j or in terms of 3-j symbols[13]

$$\begin{Bmatrix} j_{11} & j_{12} & j_{13} \\ j_{21} & j_{22} & j_{23} \\ j_{31} & j_{32} & j_{33} \end{Bmatrix} = \sum_j (-1)^{2j}(2j+1)\begin{Bmatrix} j_{11} & j_{21} & j_{31} \\ j_{32} & j_{33} & j \end{Bmatrix}\begin{Bmatrix} j_{12} & j_{22} & j_{32} \\ j_{21} & j & j_{23} \end{Bmatrix}\begin{Bmatrix} j_{13} & j_{23} & j_{33} \\ j & j_{11} & j_{12} \end{Bmatrix},$$

$$= \sum_{all\ m}\begin{pmatrix} j_{11} & j_{12} & j_{13} \\ m_{11} & m_{12} & m_{13} \end{pmatrix}\begin{pmatrix} j_{21} & j_{22} & j_{23} \\ m_{21} & m_{22} & m_{23} \end{pmatrix}\begin{pmatrix} j_{31} & j_{32} & j_{33} \\ m_{31} & m_{32} & m_{33} \end{pmatrix}$$

$$\times \begin{pmatrix} j_{11} & j_{21} & j_{31} \\ m_{11} & m_{21} & m_{31} \end{pmatrix}\begin{pmatrix} j_{12} & j_{22} & j_{32} \\ m_{12} & m_{22} & m_{32} \end{pmatrix}\begin{pmatrix} j_{13} & j_{23} & j_{33} \\ m_{13} & m_{23} & m_{33} \end{pmatrix}, \qquad \textbf{(2-49)}$$

The coupling constants $a_{o,d}$, a_c, and b_q represent the different contributions to the dipolar and quadrupolar splitting defined as[33]

$$a_{o,d} = -2\frac{\mu_0}{4\pi}\frac{1}{h}\mu_B^2 g_I \langle 1/r^3\rangle_{o,d} , \qquad \textbf{(2-50.a)}$$

$$a_c = -\frac{\mu_0}{3\pi}\frac{1}{h}\mu_B^2 g_I \langle 1/r^3\rangle_{10}, \qquad \text{(2-50.b)}$$

$$b_q = \frac{e^2}{4\pi\epsilon_0}\frac{Q}{h}\langle 1/r^3\rangle_q, \qquad \text{(2-50.c)}$$

where μ_0 and ϵ_0 are the vacuum magnetic susceptibility and electric permeability; μ_B is the Bohr magneton; g_I is related to the nuclear Landé g factor by $g_I = \mu_N g/\mu_B$, and its sign is chosen opposite to the sign of the associated magnetic moment; and Q represents the nuclear quadrupole moment. These constants indicate the radial parameters in the effective hyperfine splitting Hamiltonian, and the subscripts are used to indicate the origin of each constant: o for 01, d for 12 (dipole), and q for 02 (quadrupole). The radial averages $<r^{-3}>_{ij}$ are taken using the relativistic wavefunctions of the electronic states ij.

The frequency splittings can be calculated using the tabulated data for the dipole constant A and the quadrupole constant B given by Arimondo, *et al.*[33] and by use of equation (2-46). For instance, cesium has only one stable isotope, ^{133}Cs, having nuclear spin $I = 7/2$. For the ground state of cesium $6^2S_{1/2}$, we employ $A = 2298.16$ MHz, and $B = 0$, calculating an hyperfine separation between the $F = 3$ and the $F = 4$ levels of $\Delta E_{34} = 9{,}192.7$ MHz. For the $7^2P_{1/2}$ state of cesium, $A = 94.35$ MHz, $B = 0$, giving $\Delta E_{34} = 377.4$ MHz. The $7^2P_{3/2}$ state is more complex, involving four hyperfine sublevels, $F = 2,3,4,5$. Using the values $A = 16.605$ MHz, and $B = -0.15$ MHz, we calculate a splitting of $\Delta E_{25} = 199.281$ MHz between the $F = 2$ and the $F = 5$ hyperfine levels of the $7^2P_{3/2}$ state of cesium. We may then expect the population distribution of sublevels, and thus the alignment, created by using plane polarized light to resonantly excite the ground state of cesium to the $7^2P_{3/2}$ state, to exhibit the time dependence indicate by equation (2-45). Fig. 2.4 shows the time dependence of the alignment of the $7^2P_{3/2}$ state of cesium created by exciting the ground state of cesium using plane-polarized light. The population distribution $\rho(m_j)$ changes rapidly, and within 5 ns it has been destroyed. It oscillates, reaching several local maxima and minima, an effect often referred to as quantum beats. It does not approach the original alignment until about 60 ns after the

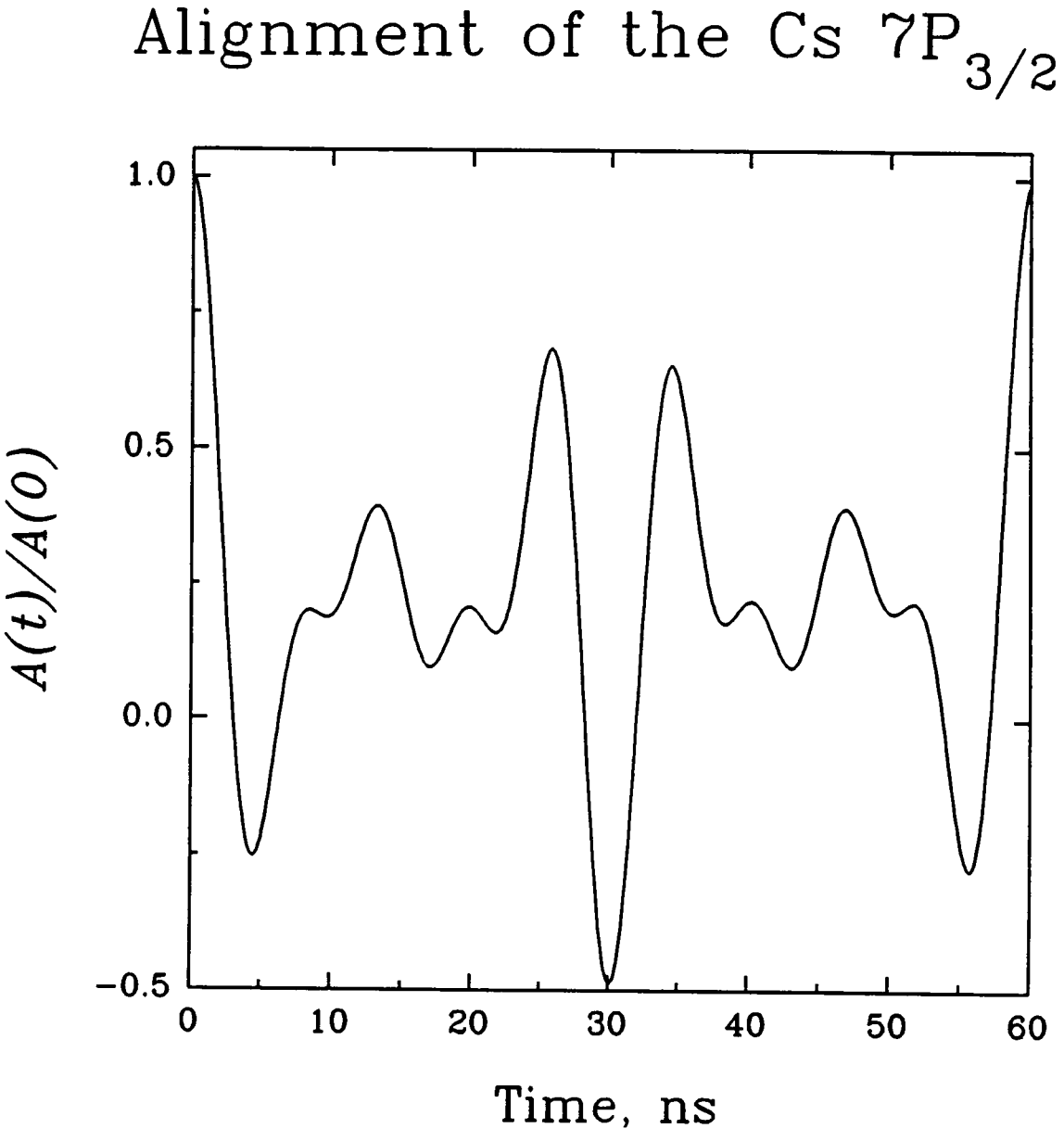

Fig. 2.4. Time dependence of the alignment of the $7^2P_{3/2}$ state of cesium created using plane polarized light. Depolarization occurs due to hyperfine coupling.

initial alignment was formed.

Few experiments achieve the time resolution required to observe the oscillations indicated by equation (2-44), and normally only a time-averaged effect is observed. To include this effect, we integrate over all time and include a exponential time decay factor, $\exp(-t/\tau)$, to reflect the finite lifetime τ of the intermediate state, due to both photoionization and fluorescence. The time averaged value of the $g^{(k)}(t)$ is then given by[5]

$$\bar{g}^{(k)} = \sum_{F,F'} \frac{(2F+1)(2F'+1)}{(2I+1)} \begin{Bmatrix} F & F' & k \\ J_i & J_i & I \end{Bmatrix}^2 \frac{1}{1+\omega_{F'F}^2 \cdot \tau^2}, \qquad \text{(2-51)}$$

where each factor $\cos\omega_{F'F}t$ has been replaced by $(1+\omega_{F'F}^2\tau^2)^{-1}$. This depolarization factor lies between two extremes:[5]

1. $|\omega_{F'F}| \ll \tau^{-1}$: precession of $\bar{\mathbf{J}}$ about $\bar{\mathbf{F}}$ is so slow that little precession occurs before photoionization. Then the depolarization factor $\bar{g}^{(k)} \approx 1$, and hyperfine coupling has little effect on the angular distribution.

2. $|\omega_{F'F}| \gg \tau^{-1}$: precession is rapid and $\bar{\mathbf{J}}$ precesses about $\bar{\mathbf{F}}$ many times before photoionization takes place. In this instance, all terms with $F' \neq F$ vanish and the alignment, or orientation, of the intermediate state is then reduced by the factor

$$\bar{g}^{(k)} \approx \sum_{F} \frac{(2F+1)^2}{(2I+1)} \begin{Bmatrix} F & F & k \\ J_i & J_i & I \end{Bmatrix}^2 . \qquad \text{(2-52)}$$

In some instances, when the lifetime τ of the intermediate state is short, or when photoionization occurs almost instantaneously, as in multiphotoionization of atoms using a strong, single pulse of the laser, very little depolarization occurs, and hyperfine effects are not observed in the angular distribution. In practice, the multiphoton absorption process can be considered as occurring instantaneously, with the total cross for ionization being enhanced by resonances that lie near any of the steps taken in the ionization path. If a time delay is allowed between the excitation and the ionization steps, then it becomes

possible for the alignment created by the excitation step to evolve, and quite likely to depolarize the angular momentum distribution. We must then consider depolarization due to hyperfine coupling in our treatment of multiphoton ionizations, in particular where we create an aligned or oriented intermediate state, and allow for the time evolution of the system. For a complete treatment, we must also include a full description of the exact time-dependent laser pulses used for the excitation and ionization steps.

If the bandwidth, *i.e.*, $\Delta\nu$, of the excitation photon is large compared to the natural width Γ_j of the intermediate level, then the excitation process will coherently excite all of the hyperfine sublevels of the state, and the angular distribution will depend on the transition probabilities between the hyperfine sublevels corresponding to the initial and intermediate energy levels. The observed photoelectron angular distribution will then consist of a coherent superposition of the angular distribution from all the resonant hyperfine sublevels. If on the other hand, the bandwidth of the laser used to excite the atom is relatively narrow, then we must consider the selection rules for transitions between hyperfine sublevels. These selection rules follow right out of the Wigner 6-j coefficients, and are similar to the selection rules for dipole transitions: $\Delta F = \pm 1, 0$; and $\Delta m_F = \pm 1, 0$. We must remark that due to the triangle condition of vector addition, the selection rule $\Delta F = 0$ only holds if $F \neq 0$.

Further modeling of hyperfine coupling depolarization for specific states will be deferred to later chapters as part of the analysis of the results of the experiments carried out as part of this dissertation.

G. CIRCULAR DICHROISM IN ANGULAR DISTRIBUTIONS

Circular dichroism (CD) is a phenomenon associated with the difference of the responses of a molecular or atomic system to left and to right circularly polarized light. This can come about from the dependence of the coefficients of absorption on the

polarization of light, due to asymmetries or multipole moments considerations. Circular dichroism is often associated with the chirality (the handedness) of molecules, although recent studies[36-42] have shown that dichroism effects can also occur in resonantly enhanced multiphoton ionization from atomic systems due to the alignment or the orientation of the intermediate states, arising out of the selection rules for dipole transitions. Historically, circular dichroism has been associated only with chiral molecules which lack a plane of symmetry and an inversion center. Previous studies of CDAD[36-40] had assumed strong spin-orbit coupling or high multipole interactions, however, more recent analyses[6,42] have shown that a proper choice of electron collection and of the photon propagation direction can break the cylindrical symmetry of the target and give rise to dichroic effects in the electric-dipole approximation. CDAD cannot exist if the target is isotropic (because of symmetry reasons), and its very existence implies alignment of the target. Thus the shape of the CDAD spectrum provides details about the alignment of the target.[6]

Figure 2.5 depicts the Dubs, *et al.*[7] method for experimentally observing CDAD. Alignment of an intermediate state is created by pumping an isotropic population of states to a resonant state using plane polarized light. Due to the dipole selection rules, only the sublevels of the intermediate state satisfying $\Delta m_j = 0$ are populated, thus giving rise to an aligned state. The alignment is then probed using circularly polarized light in the second step of photoionization. The angular distribution for such pump-probe multiphoton process is also given by equation (2-28). The specific form of the angular distribution will depend on the particular alignment A_o, as given by the multipole moments of the population distribution produced by the excitation process. This alignment in turn can be modified by any depolarization due to atomic collisions, coupling with other states, or with the nuclear spin (hyperfine coupling, $\vec{F} = \vec{J} + \vec{I}$). As discussed in the previous section, hyperfine coupling introduces a time dependence to the alignment or orientation, and this in turn, causes the photoelectron angular distributions to depend on the relative time between the excitation (pump) and ionization (probe) steps.

To formally consider CDAD, we start by rewriting the dipole moment operator (for the ionizing photon) to include the circular polarization of the photon[8]

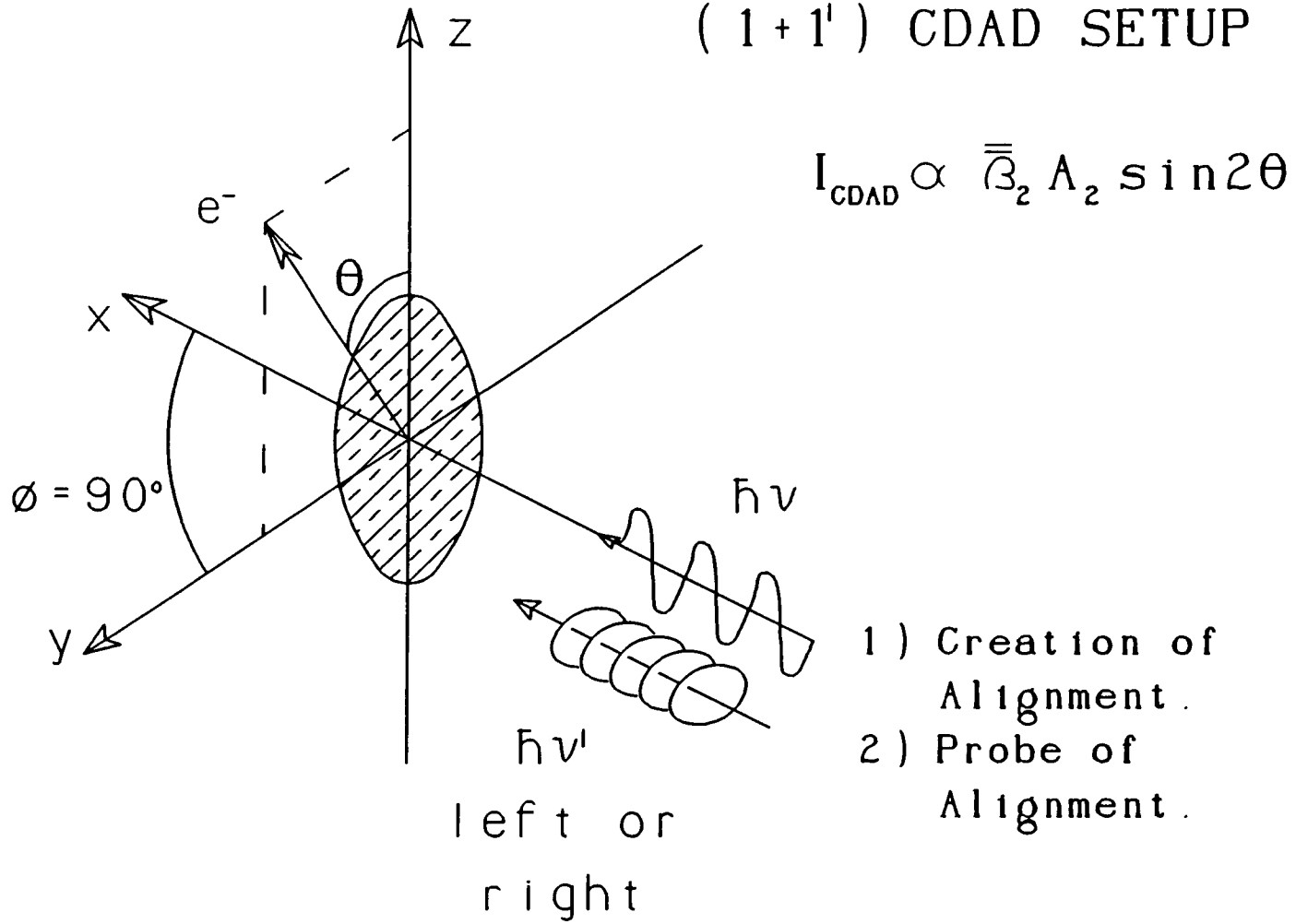

Fig. 2.5. Dubs, *et al.*[7] basis for CDAD. Alignment of the state is created using plane polarized light in step 1, and then probed using circularly polarized light in step 2.

$$D_\mu = \left(\frac{4\pi}{3}\right)^{1/2} r \sum_{\mu'} D^1_{\mu',\mu} Y_{1\mu'}(\hat{r}) \ . \qquad \text{(2-53)}$$

Here μ denotes the polarization index, 0 for linear and ± 1 for circular polarization, and the coefficients $D^1_{\mu',\mu}$ are used to transform the dipole operator from the frame of the ionizing photon to the frame of the exciting photon, since the two frames may not coincide.

The bound and continuum wavefunctions are written in the exciting photon frame[43]

$$|\psi_i^{jm}\rangle = R_{nlj}|lsjm\rangle, \qquad \text{(2-54)}$$

$$|\psi^-_{f,\hat{k}}\rangle = 4\pi\left(\frac{\pi}{2k}\right)^{1/2} \sum_{l'=0}^{\infty} \sum_{m'=-l'}^{l'} i^{l'} e^{-i\delta_{l'}} Y^*_{l'm'}(\hat{k}) \sum_{j'm'} R_{el'j'}(r)\langle l'sm'm_s|j'm'\rangle |l'sj'm'\rangle, \qquad \text{(2-55)}$$

and the kets are given by

$$|lsjm\rangle = \sum_m \sum_{m_s} \langle lsmm_s|jm\rangle Y_{lm}(\hat{r})|sm_s\rangle \ . \qquad \text{(2-56)}$$

The radial wavefunctions $R_{\epsilon lj}(r)$ and the phase shifts δ_l can be calculated as in Ref. 43. We will omit the details of the calculation, and cite the final result given by Dubs, *et al.*[43] for the photoelectron matxix element[8]

$$I^{jm}_{l'm'\mu} = (-i)^{l'} e^{i\delta_{l'}} \bar{r}_{fi} (-1)^{j+l+1/2} \sqrt{\frac{3}{4\pi}} [(2j+1)(2l+1)]^{1/2}$$
$$\times \sum_{j'm'} \langle l'sm'm_s|j'm'\rangle \begin{Bmatrix} l' & j' & s \\ j & l & 1 \end{Bmatrix} \langle j1m\mu|j'm'\rangle \langle l100|l'0\rangle, \qquad \text{(2-57)}$$

where

$$\bar{r}_{fi} = \langle R_{\alpha' j'}(r) | r | R_{nlj}(r) \rangle \ . \qquad \textbf{(2-58)}$$

In the absence of any depolarization effect, the angular distribution for a $(n + n')$ pump-probe multiphoton process, starting from an isotropic distribution, is given by the equation

$$I^{\pm}(\theta,\phi) = 1 + \sum_{i=1}^{n+n'} \beta_{2i,0} P_{2i}^{0}(\cos\theta) \pm \beta_{2i,\pm 1} P_{2i}^{\pm 1}(\cos\theta) e^{\pm i\phi} + \ldots + \beta_{2i,\pm 2i} P_{2i}^{\pm 2i}(\cos\theta) e^{\pm i(2j+1)\phi} \ , \qquad \textbf{(2-59)}$$

where the sum indicates any trace of a photoelectron angular distribution obtained using the first type (plane) of photons, and the remaining terms are obtained from using the circularly polarized photons. These can be separated using different energy photons, or by making the laser beam used for excitation relatively weak compared to the laser beam used in the ionization step. In practice, we are interested in the difference between the left and the right circularly polarized photoelectron distributions, and if the same laser intensities are used for both experiments, the trace of a PEAD will be canceled out. From equation (2-59) we obtain for a $(1 + 1')$ process (for brevity, constants of proportionality are omitted)

$$I_{CDAD}(\theta,\phi) = I^{-}(\Omega) - I^{+}(\Omega) = (\beta_{2,-1} e^{-i\phi} + \beta_{2,1} e^{i\phi}) \sin\theta\cos\theta. \qquad \textbf{(2-60)}$$

By symmetry, the coefficients $\beta_{2,\pm 1}$ are identical, and the coefficients may then be combined. Normally, we will measure the photoelectron angular distributions by either holding the detector fixed and rotating the plane of polarizations of the photons, or by rotating the detector while maintaining the plane polarization fixed. In either case, the angle ϕ will be held constant, and the above angular distribution is simplified to[44]

$$I_{CDAD}(\theta,\phi=fixed\equiv 0) = (\beta_{2,-1}+\beta_{2,1})\sin\theta\cos\theta, \qquad (2\text{-}61)$$
$$= A_0\,\bar{\bar{\beta}}_2\sin\theta\cos\theta.$$

This result is exactly that which has been obtained by a more detailed theoretical analysis by Dubs, *et al.*[7] All the constants can be factored out by normalizing the data using the normalization scheme

$$S_{CDAD}(\theta) = \frac{I^{-}(\theta)-I^{+}(\theta)}{\frac{1}{2}[I^{(\pm)}(0)+I^{(\pm)}(\frac{\pi}{2})]}. \qquad (2\text{-}62)$$

where $I^{(\pm)}(0)$ and $I^{(\pm)}(\pi/2)$ are the values of the distributions at 0° and at 90°. This normalization scheme in effect factors out all the scaling factors that do not depend on the angular variables, including the dependence on the total cross section $\sigma(\epsilon)$. The angular distribution will then depend strictly on the dynamics of excitation and ionization.

An isotropic angular distribution has no quadrupole moment, as can be seen from equation (2-21.c), and it does not have an alignment. Thus, the photoelectron angular distributions from states with $j = 1/2$ will not exhibit circular dichroism effects. We can expect to observe circular dichroism effects in the angular distributions from states that are either aligned or oriented, either naturally or by preparation using plane polarized light.

If there are depolarizing effects, such as hyperfine coupling, the population distribution and the ensuing alignment of the resonant state will be time dependent, making the observed CDAD to exhibit time dependent effects. As pointed out in the section of hyperfine coupling, this time dependence will depend largely on the states involved in resonant multiphoton ionization, and for most experiments only a time averaged effect will be observed.[44]

H. RELATIVISTIC EFFECTS IN THE PHOTOELECTRON ANGULAR DISTRIBUTIONS

The asymmetry parameters given by equation (2-32) considered only the coupling of the orbital angular momentum of the bound states with the continuum partial wave functions. However, studies have shown that it possible to observe spin orbit effects in the angular distributions if *LS* coupling is taken into account in the calculation of the photoelectron angular distributions.[22-31] These effects are formally included if spin-orbit (relativistic) wave functions are used in the calculation of the β parameters. These spin-orbit wavefunctions are given by[27]

$$\chi_{j m_j}(\theta,\phi) = \sum_{\sigma} (-1)^{l-\frac{1}{2}+m_j}(2j+1)^{\frac{1}{2}} \begin{pmatrix} l & \frac{1}{2} & j \\ m_j-\sigma & \sigma & m_j \end{pmatrix} Y^{l}_{m_j-\sigma}(\theta,\phi)\,\Phi_{\sigma}\,, \qquad \textbf{(2-63)}$$

The functions Φ_σ are the two component Pauli spinors, and the sum is carried over the projections of the spin. It is useful to define the quantum number κ, related to the total angular momentum j and spin projection σ by[27]

$$\begin{aligned} |\kappa| &= (j+\tfrac{1}{2}) && , \\ \text{"}\textit{parallel}\text{"}\ \vec{L}\vec{S}\text{:}\quad \kappa &= -(j+\tfrac{1}{2}) = -(l+1) && , \\ \text{"}\textit{antiparallel}\text{"}\ \vec{L}\vec{S}\text{:}\quad \kappa &= (j+\tfrac{1}{2}) = l && , \\ \kappa &= -(2j+1)\,\sigma && . \end{aligned} \qquad \textbf{(2-64)}$$

The wavefunctions can therefore be represented (in Euclidean-spin space, $\mathscr{E}_r \otimes \mathscr{E}_s$) by the 2x1 spinor matrix[27]

$$\psi_{n\kappa m_j}(\vec{r}) = \langle \vec{r}|n\,\kappa m_j\rangle = \begin{bmatrix} \langle \vec{r}|n\,\kappa m_j,\zeta=-1\rangle \\ \langle \vec{r}|n\,\kappa m_j,\zeta=+1\rangle \end{bmatrix}, \qquad \textbf{(2-65)}$$

where each matrix entry corresponds to a projection of the spin of the electron. Because of the dependence of κ on both j and σ, the radial part of the relativistic wavefunction also reflects a spin dependence. The radial part of the wavefunction is thus given by[27]

$$\langle r\,|n\kappa\zeta\rangle = \begin{cases} \frac{1}{r}P_{n\kappa}(r), & \zeta = -1 \\ \frac{i}{r}Q_{n\kappa}(r), & \zeta = +1 \end{cases}, \tag{2-66}$$

where $P_{n\kappa}(r)$ and $Q_{n\kappa}(r)$ are respectively the large and small components of the wavefunction,[27] and the angular part is given by equation (2-63).

Continuum orbitals are written in similar fashion as a sum over partial waves[27,45]

$$\psi_{\vec{k}}(\vec{r}) = 4\pi \sum_{\kappa m_j} e^{i\delta_\kappa}(\chi_{\kappa m_j}(\hat{k})\Phi)\begin{bmatrix}\langle\vec{r}|k\kappa m_j,\zeta=-1\rangle \\ \langle\vec{r}|k\kappa m_j,\zeta=+1\rangle\end{bmatrix}. \tag{2-67}$$

As r goes to infinity, the wavefunction behavior is given by[46,47]

$$\frac{P_\kappa(r)}{r} \xrightarrow[r\to\infty]{} j_l(kr)\cos\delta_\kappa - n_l(kr)\sin\delta_\kappa \tag{2-68}$$

where $j_l(kr)$ and $n_l(kr)$ are the spherical Bessel and Neumann functions, respectively; and δ_κ is the phase shift of the κth partial wave.

The angular distribution is again given by equation (2-1) for a one photon ionization, or by equation (2-16) for a $n + 1$ multiphoton ionization. The dipole interaction gives rise to the same selection rules as before, *i.e.*, $\Delta l = \pm 1$ and $\Delta j = \pm 1$, 0, but now they act between the relativistic wavefunctions given by equations (2-63) and (2-67). There is no coupling between the spin wavefunctions, so the spin selection rules are still $\Delta s = 0$ and $\Delta m_s = 0$. Depending on the polarization of the photon, the selection rule for the projection of angular momentum of the electron being ejected is $\Delta m_j = \pm 1$ (for right and left circular polarization), 0 (for plane polarized photons).

We will skip the tedious details of the calculations, and give the result for the β

parameter for the photoelectron angular distribution from a state with total angular momentum j and an isotropic population of sublevels using unpolarized light[27]

$$\beta_2 = \left(\frac{(2j-3)(2j-1)}{48j^2}R_{j-1}^2 - \frac{(2j-1)(2j+3)}{48j^2(j+1)^2}R_j^2 + \frac{(2j+3)(2j+5)}{48(j+1)^2}R_{j+1}^2 \right.$$
$$\left. + \frac{(2j-1)}{8j^2(j+1)}|R_j R_{j-1}^*| + \frac{(2j+3)}{8j(j+1)^2}|R_j R_{j+1}^*| + \frac{(2j-1)(2j+3)}{8j(j+1)}|R_{j-1}R_{j+1}^*|\right)$$
$$\Big/\left(\frac{(2j-1)}{12j}|R_{j-1}^2| + \frac{1}{12j(j+1)}|R_j^2| + \frac{(2j+3)}{12(j+1)}|R_{j+1}|\right) . \qquad \textbf{(2-69)}$$

Here the matrix elements $R_{j'}$ are given by the bound state of angular momentum j, and the continuum orbital of angular momentum j'. They are defined by the radial integral[27]

$$R_{j'} = i[(\kappa - \kappa' - 1)\langle Q_{j'}|P_j\rangle + (\kappa - \kappa' + 1)\langle P_{j'}|Q_j\rangle]e^{i\delta_{j'}} . \qquad \textbf{(2-70)}$$

where $\delta_{j'}$ is the phase shift of the continuum orbital, and the quantum numbers κ, κ' were defined in equation (2-64). The large component P_j, and small component Q_j functions are solutions to the coupled first order differential equations[27]

$$\frac{dP}{dr} + \frac{\kappa P}{r} - \left(2c + \frac{V-E}{c}\right)Q = 0$$
$$\frac{dQ}{dr} - \frac{\kappa Q}{r} + \left(\frac{V-E}{c}\right)P = 0 . \qquad \textbf{(2-71)}$$

The matrix elements (2-70) depend on the energy ϵ of the photoelectron through the dependence of the continuum wavefunction on the momentum $\vec{k}$ of the photoelectron. Due to nodes in the wavefunctions and to interference between the wavefunctions, the matrix elements can vanish as a function of energy. Thus the matrix elements can exhibit Cooper minima, occurring at slightly different energy for each photoionization channel

($j \pm 1$, or j).

For the photoelectron angular distribution from an $n^2S_{1/2}$ (or from a state with total angular momentum $j = 1/2$) that is isotropically populated, equation (2-70) predicts[27,28,31]

$$\beta_2 = \frac{2R_{3/2}^2 + 4R_{1/2}R_{3/2}\cos(\delta_{3/2} - \delta_{1/2})}{R_{1/2}^2 + 2R_{3/2}^2}, \qquad (2\text{-}72)$$

where now the phase shift dependence is explicitly written, and $R_{1/2}$ and $R_{3/2}$ denote the radial matrix elements. This result is in sharp contrast to the result predicted by equation (2-32). It has been shown[27-30,48] that the phase shift difference $\delta_{3/2}$ - $\delta_{1/2}$ is generally close to zero. Under this condition, we observe that when the matrix elements $R_{1/2}$ and $R_{3/2}$ are equal, the asymmetry parameter β_2 is again equal to 2. In the energy region where the two matrix elements differ significantly, *i.e.*, when one or the other radial matrix element goes through a minima, β_2 is expected to differ from the value 2. Since the minima of the radial matrix elements occur at slightly different energies this region can be relatively broad. Other specific cases worth noting are:[27] if $R_{3/2} = 0$, $\beta_2 = 0$ (isotropic angular distribution); when $R_{1/2} = 0$, $\beta_2 = 1$ (this and the former are single channel ionizations); and when $R_{1/2} = -R_{3/2}$, $\beta_2 = -\frac{2}{3}$.

It is convenient to redefine the ratio $\chi = R_{3/2}/R_{1/2}$, and to define $\Delta = \delta_{3/2} - \delta_{1/2}$ and to rewrite equation (2-72) as

$$\beta_2 = \frac{2\chi^2 + 4\chi\cos\Delta}{1 + 2\chi^2}. \qquad (2\text{-}73)$$

This enables us to study the variation of the β_2 parameter as a function of χ and of the difference of the phase shifts $\delta_{3/2}$ - $\delta_{1/2}$. These results are shown in Figure 2.6. We observe again that the asymmetry parameter ranges from -1 to 2. As the value of χ is varied from $-\infty$ to ∞ we see from the figure that (for $\Delta = 0$) β_2 takes on all the values between -1 and 2, reaching a local minimum of -1 at $\chi = -\frac{1}{2}$, and a local maximum of

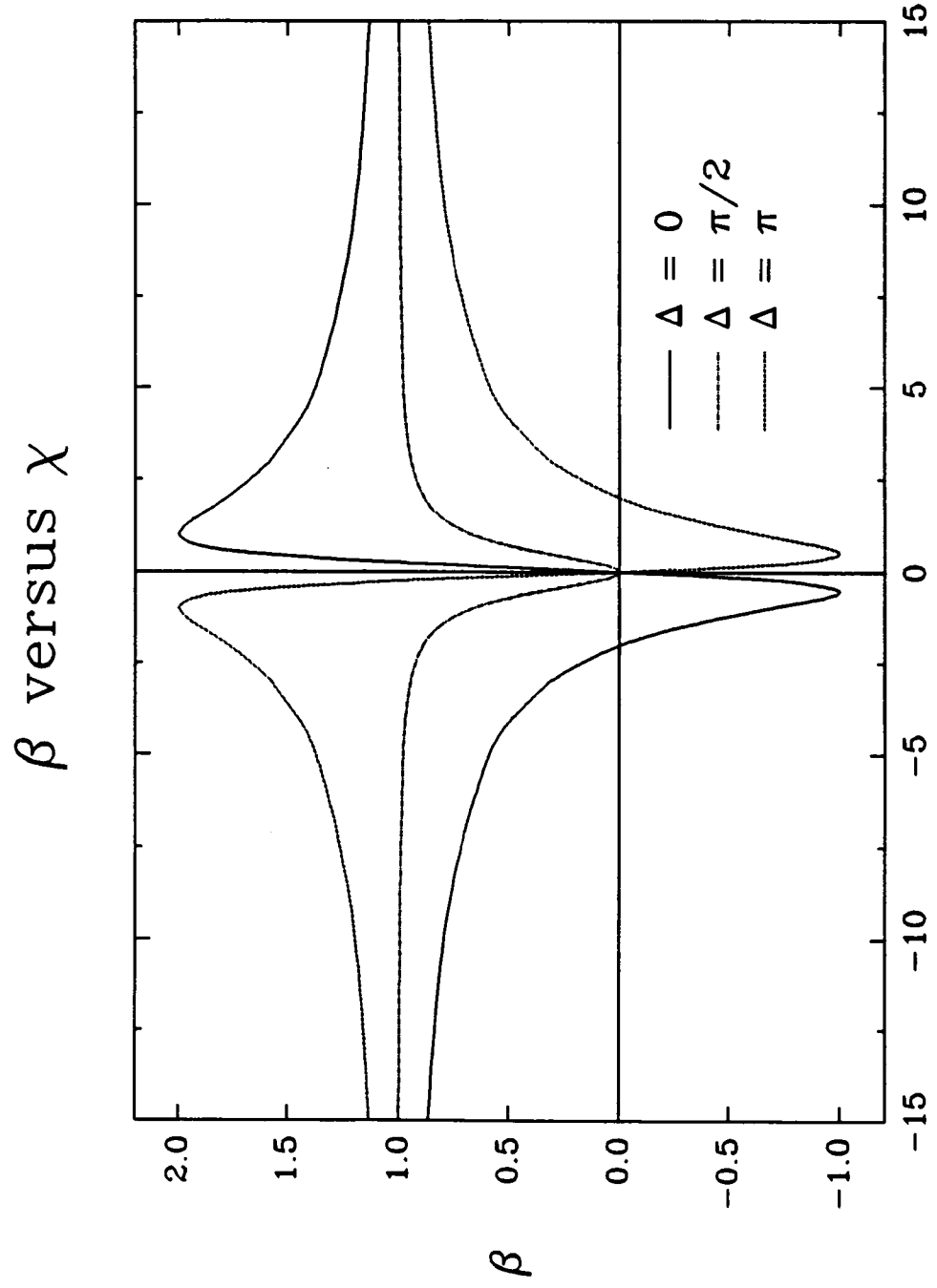

Fig. 2.6. Asymmetry parameter β_2 for an isotropic angular distribution versus the ratio of the radial matrix elements, $\chi = R_{3/2}/R_{1/2}$, and $\Delta = 0,\ \pi/2,\ \pi$.

2 at $\chi = 1$. We also see that β_2 has an asymptotic value of 1 as $R_{1/2} \rightarrow 0$, and that when $\chi = 0$, β_2 becomes 0 too.

Marr,[28] Ong and Manson,[29] and Huang and Starace[30] have calculated the energy dependence of β_2 as a function of the photon energy for the photoelectron angular distributions from the ground state of cesium, and Yi-Yian and Elliot[10] converted the results of Norcross[49] for the Fano parameter into β_2 in order to compare their experimental results to theory. Marr calculated β_2 by introducing the spin orbit perturbation function (or Fano parameter)[48]

$$X(\epsilon) = \frac{R_0}{\Delta R} = \frac{2R_{3/2} + R_{1/2}}{R_{3/2} - R_{1/2}}, \tag{2-74}$$

where R_0 is the total radial matrix element. Then β_2 is given by[28]

$$\beta_2(\epsilon) = \frac{2(X^2 - 1)}{X^2 + 2}. \tag{2-75}$$

From this equation we see that $\beta_2 = 2$ only in the limit $X \rightarrow \infty$. In the region where there is a large spin-orbit interaction, $X = 0$, and $\beta_2 = -1$. Data on the spin orbit perturbation function X are available from the polarization studies of the Fano effect.[28]

Ong and Manson performed *ab initio* calculations, which placed the location of the Cooper minima relatively high. Huang and Starace carried out their calculation in both in the length and velocity gauges and using both frozen and relaxed ionic core wavefunctions. However, these calculations placed the Cooper minima at different energies, the length model placing it high, while the velocity model placed it low relatively to experimental results.[10] Yi-Yian and Elliot obtained excellent agreement with the results of the calculations by Norcross.[10]

The photoelectron angular distribution for the 8^2S, 9^2S, 10^2S, and 12^2S states of cesium using (2 + 1) resonantly enhanced photoionization were measured as part of this

dissertation. The analysis and results of these experiments are included in Chapter IV. Photoelectron angular distributions from the 7^2S state of cesium could not be measured using a (2 + 1) technique because the resonant state (at 18535.51 cm^{-1}) lies below two thirds of the way between the ground state and the continuum (binding energy of cesium is 31406.71 cm^{-1}), and it is not possible to resonantly excite and ionize the atom using three photons of the same wavelength.

Finally, relativistic β parameters for angular distributions from aligned or oriented states can be calculated by using equation (2-16) and the relativistic wavefunctions (2-63) and (2-67). At the time of this writing, these results have not been found in the literature, and it is the belief of the author that none were available.

CHAPTER III

EXPERIMENTAL MEASUREMENT OF PHOTOELECTRON ANGULAR DISTRIBUTIONS

A. GENERAL OVERVIEW

Atomic photoionization can be visualized as a collision process in which the incident photon (projectile) collides with an atom (target) to produce an ion-electron final state. Multiphoton ionization represents the interaction of more than one photon with a single atom giving rise to an electron-ion pair in the continuum. The ionization process is enhanced by the presence of an allowed energy level near the absorption of one or more of the photons, or greatly enhanced in the case of resonantly enhanced, stepwise multiphoton ionization. The energy of the photon can be varied by using light of different wavelengths, and hence frequencies, in order to excite the electron to different excited bound states of the atom. The excitation can be done stepwise using one or more photons to populate states with distinct angular momentum and parity, allowing for studies of ionization of excited states of atoms by single photon absorption from resonant states.

This stepwise excitation of bound states requires photons with a wide range of energies. The photons can be obtained using a tunable light source like a pumped dye laser (PDL), and the ranges provided by different dyes extended using nonlinear doubling and mixing techniques. Photons are then easily available with wavelengths ranging from 800 nm (12500 cm^{-1}) to 210 nm (40000 cm^{-1}). Thus, the energy of the photons can be varied almost continuously by using different dyes in conjunction with different doubling, or mixing, crystals in a wavelength extender (WEX-1).

The output polarization of dye lasers and wavelength extenders is typically 95-100% plane polarized, and the degree of polarization can further be defined using an optical polarizer. The polarization of the laser can be used to define the axis of quantization in the laboratory frame, and the angular distribution of the outgoing electron can then be determined relative to the polarization of the laser.

In order to determine the angular distribution, the target atom must be relatively isolated in order to keep the outgoing electron from colliding with some other atom or molecule. This is accomplished by using targets in the gas phase at very low pressure and isolated using a vacuum chamber, since then the long mean free present under high vacuum conditions ensures a low probability of collisions between the outgoing electron and some other target in the vicinity of the target. For our experiments, the target atoms were obtained using an atomic beam originating from a thermal oven. The atomic beam was crossed with a beam of polarized photons, thus defining a plane of interaction, an interaction region, and an axis of quantization.

Fig. 3.1 provides an illustration of the geometry used for the measurement of photoelectron angular distributions for our studies on the photoionization of selected states of cesium and rubidium. In order to determine the photoelectron angular distribution, electrons are counted as a function of the angle θ between the axis of quantization $\hat{z}$ and the direction of observation. The axis of quantization is chosen to be parallel to the plane polarization of the photons, and hence, a single detector can be

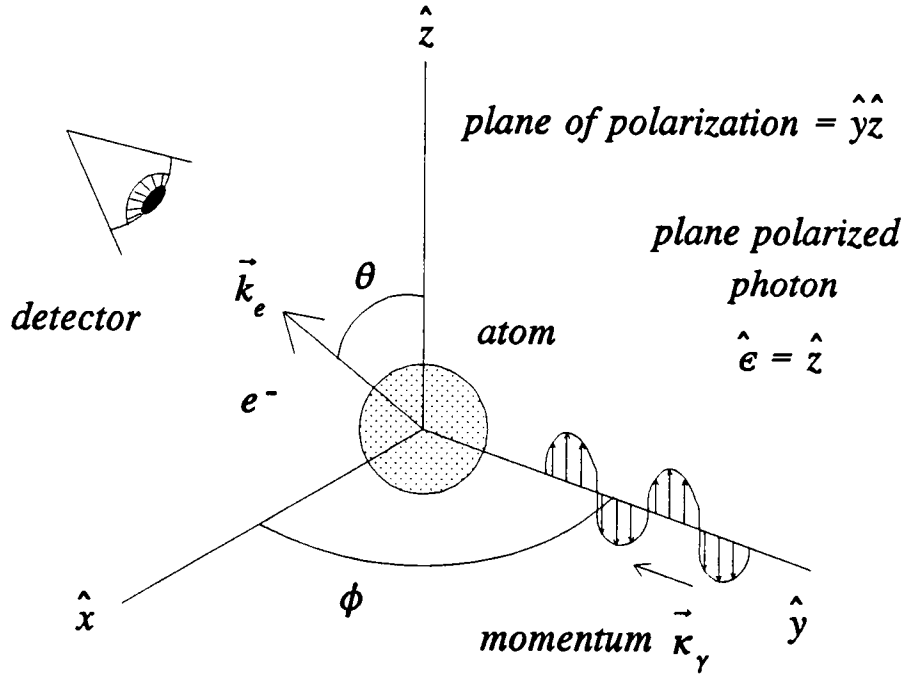

Fig. 3.1. Geometry for the measurement of photoelectron angular distributions. Electrons are detected as a function of the angle θ for the particular case of $\phi = \pi/2$.

placed along the normal of the plane of interaction and above the interaction region. The detector is held fixed and the polarization of the photons is rotated through 360° using a double Fresnel rhomb. A time-of-flight (TOF) mass spectrometer is chosen as a detector for its simple requirements and ease of use. The only way to distinguish electrons in a time-of-flight spectrometer is by their time of flight, and often it is hard to differentiate fast photoelectrons. Typically, since we can expect all photoelectrons from the same atomic state to have similar kinetic energies, we expect the photoelectrons to reach the detector at the same time in a pulse comparable to the pulse of the laser beam.

An overview of the experimental apparatus used in this dissertation is given in figure 3.2. The different components of the apparatus used will be described in detail in subsequent sections. Several photoionization experiments were carried out using this apparatus, but we will focus on the measurement of photoelectron angular distributions using resonantly enhanced multiphoton ionization (REMPI) of the ground state of cesium and rubidium employing (2 + 1) and (1 + 1′) photoabsorption.

The two different excitation schemes used to study PEAD and CDAD in cesium and rubidium are depicted in figure 3.3. In ionization scheme (a), two plane polarized photons (labeled π) of same frequency ν_1 excite the ground state of the atom to the resonant $n^2S_{1/2}$ state, and a third photon, also of frequency ν_1, ionizes the atom. In the second scheme (b), one plane polarized photon of frequency ν_3 is used to excite the ground state to either the resonant $n^2P_{1/2}$ or $n^2P_{3/2}$ state, and a photon of circular polarization, ϵ_+ or ϵ_- (labeled $\sigma^\pm$ in the figure), and of frequency ν_4 is used to ionize the atom. The photoelectron angular distributions obtained using scheme (a) will be referred as PEADs, and the difference between the distributions obtained using ϵ_- and ϵ_+ polarizations in scheme (b) will be referred as CDAD.

The PEADs from resonant n^2D_J using (2+1) photoabsorption, as well as the PEADs from resonant n^2P_J using (1+1) photoabsorption, were also measured for this dissertation for diagnostic purposes, and the results are included for comparison with previous measurements by Compton, *et al.*[32] and Kaminski, *et al.*[51]

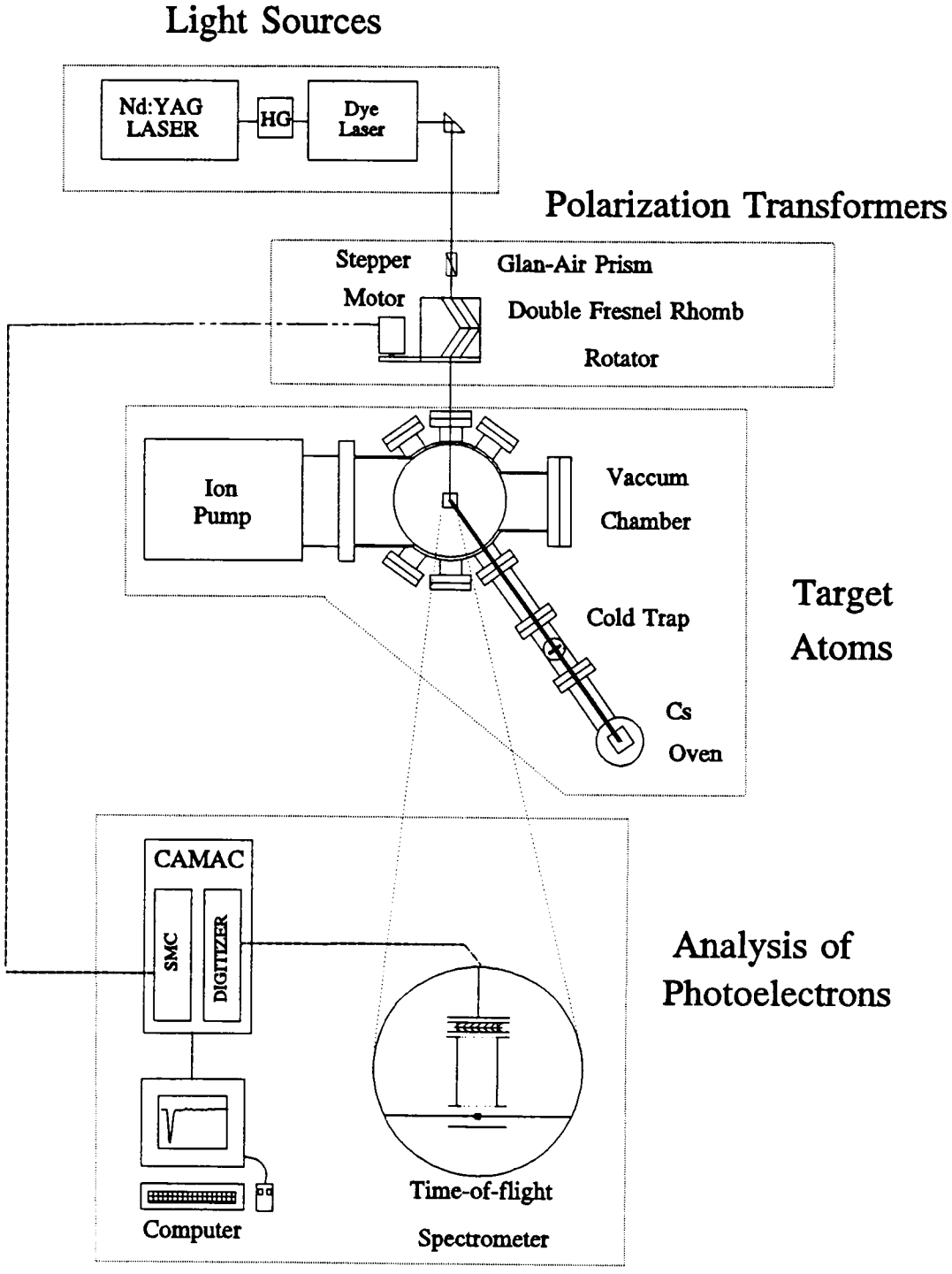

Fig. 3.2. An overview of the experimental procedure used in this dissertation. The output of a light source is polarized and used to ionize target atoms, and the photoelectrons are then measured.

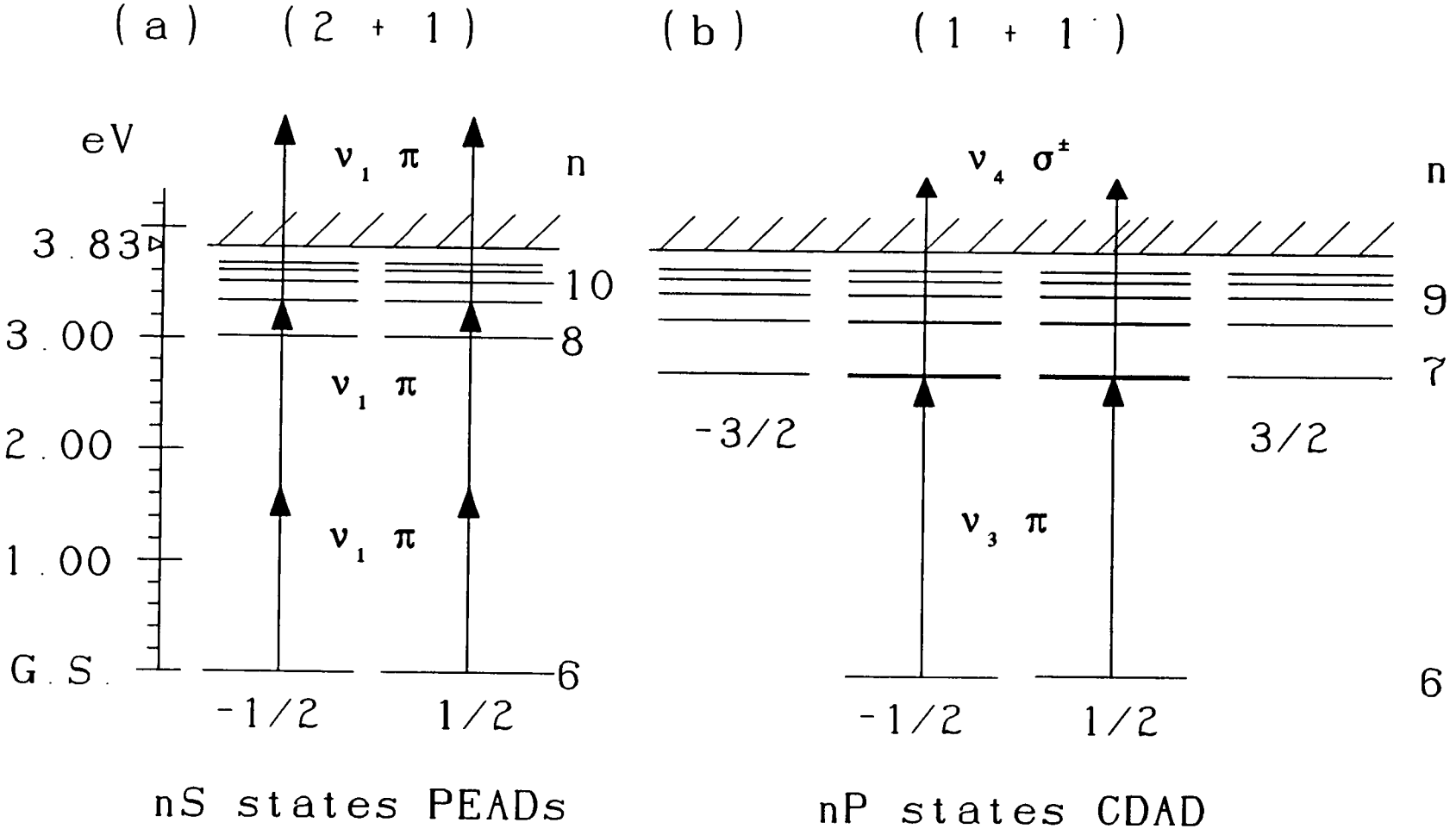

Fig. 3.3. Excitation and ionization schemes used for this dissertation. (a) 2 photon resonant, 1 photon ionization (2+1); (b) 1 photon resonant, 1 photon ionization (1+1').

B. APPARATUS HARDWARE

B-1. LASER SYSTEMS

The laser system consisted of a neodymium yttrium aluminum garnet (Nd:YAG), Quanta Ray DCR-2A (10) laser system (fundamental wavelength line at 1064nm) with variable power output, ranging from 5 mJ/pulse up to 800 mJ/pulse. The Nd:YAG is a solid state laser, consisting of both oscillator and amplifier sections each containing an yttrium aluminum garnet crystal rod doped with neodymium atoms. The ends of the rods are cut at Brewster's angles in order to increase transmission and to define the polarization of the laser beam. Electrons are excited across the solid state band gap using two flash lamps in the oscillator section, and two flash lamps in the amplifier section, with their axes placed parallel to the axes of the rods. When the electrons decay down to the ground state, fluorescence is emitted in all directions, but only the fluorescence along the axis of the rod is reflected back through the rod by use of reflecting mirrors placed at each end of the rod. The reflected light stimulates emission by coupling the electromagnetic fields of the photons with other excited electrons in the rod. Further amplification of the emitted light occurs in the amplifier section of the Nd:YAG. As the photons travel through the amplifier rod they are also coupled with excited electrons in the amplifier section of the laser. Light amplification occurs due to the coupling of the electromagnetic field of the photon with the electrons.

The pulse rate of the Nd:Yag is variable from 1 to 20 Hz, and the pulse width of the laser is controlled using a piezoelectric transducer, which changes the polarization of the end mirrors at the chosen pulse rate. The polarization is changed by using a Q-switch to maintain the end mirrors at an electric potential of 32 kV. When the Q-switch is triggered, the mirrors are discharged, momentarily becoming transparent by rotation of their optical axis. Thus, the output of the Nd:YAG is emitted in a pulse about 10 ns wide every second to one fifth of a second. The triggering sequence is timed to optimize the power output of the laser, and could be manually "tweaked" using the

Q-switch delay and bias controls. A reference synchronization output of the Q-switch with a 12 volt threshold is available that can be used to trigger other electronic equipment synchronously with the laser. All experiments were carried out using a fixed pulse rate of 10 Hz and the data acquisition was synchronized using the Q-switch synchronization output.

The harmonics of the Nd:YAG laser fundamental were produced using a harmonic generator (Quanta Ray HG-2), consisting of doubling and mixing crystals. The second harmonic (532 nm) was generated by mixing two 1064 nm photons using a Type II SHG crystal, and the third harmonic (355 nm) was generated by mixing the second harmonic beam with the fundamental 1064 nm using a THG-type crystal. Nominal relative power efficiencies are 45 percent for the second harmonic, and 19 percent for the third harmonic. Nominal pulse temporal widths are 6-7 ns for the 532 nm beam, and 5-6 ns for the 355 nm beam. The harmonics were physically separated using an harmonic separator (Quanta Ray PHS−1), whose main component was a Pellin-Broca prism, cut to separate the laser harmonics by using the principle of refraction of light. The harmonic separator also has another large prism to extend the separation of the harmonics to about 2.5 cm at 0.8 m, and two half-wave plates used to rotate the polarization of either of the two principal harmonics of the Nd:YAG by 90°. The Nd:YAG beams had an optical divergence of less than 0.5 mrad full angle.

The harmonic generator also had two sliding prisms that could be used to choose any of the harmonics to serve as the pump to the dye laser (Quanta Ray, PDL-2). The PDL-2 could be set up to generate an assortment of laser wavelengths using different dye solutions. The laser dyes used for our experiments are listed in Table III-1, along with several important characteristics. Inside the PDL-2 the pump harmonic beam is split using a combination of beam splitters into three distinct beams. One beam is used to pump the dye oscillator cell, while another can be used to pump a pre-amplifier dye cell, depending on the dye used. The third beam is used to pump the amplifier cell either longitudinally (end pumping) or transversely (side pumping), again depending on the dye used. The fluorescence off the oscillator cell also scatters in all directions, but similarly to the Nd:YAG laser, only the radiation at a right angle from the pump beam is reflected

Table III-1. Laser dyes used for (2+1), (1+1), and (1+1′) experiments in this dissertation.

Dye (Trade name)	Solvent	Concentration (osc,amp) mg/l	Wavelength Range, nm	Power, mJ/Pulse (%)	½ Life, Hrs.
Exalite 389	10% p−Dioxane in MeOH	149.62, 58.0	378-395	21 (18)	0.25
Coumarin 440	Methanol	300, 60	425-457	21 (14)	3
Coumarin 460	Methanol	300, 60	446-478	15 (10)	3
DCM	Methanol	175.24	605-672	70 (21)	> 30
LDS 821	Methanol	125, 17	785-851	28 (7)	> 40
LDS 750	Methanol	116, 15	698-743	38 (11)	> 40
LDS 751	Methanol	150, 40	714-792	714-792	> 40
LDS 698	Methanol	225, 28.75	662-730	60 (16)	> 40
Rhodamine 6G	Methanol	115, 17	553, 577	100 (16)	> 40

inside a resonant cavity using a rotatable diffraction grating at one end, and a fixed, partially reflecting quartz window (oscillator output mirror) at the other end. The grating reflects light back into the dye cell, where lasing occurs by coupling of the photon with excited dye molecules. Unlike the Nd:Yag laser, fluorescence from the dye molecules has a broad wavelength band, Doppler broadened as well by motion of the dye molecules. The diffraction grating provides a means to select the wavelength that is reflected back into the dye cell through rotation of the plane of the grating. This in effect creates a tunable resonant cavity with a selectable resonant wavelength. The diffraction grating reflects the beam through several diffraction orders, and the highest available order was used for the experiments because it provided the best wavelength resolution. A drawback of using the highest order is that the laser intensity is reduced for each higher order.

The output wavelength of the dye laser can be frequency doubled or mixed with the fundamental or an harmonic of the Nd:YAG laser by using a wavelength extender (Quanta Ray WEX-1), which acts as a tunable harmonic generator for the output of the dye laser. The WEX-1 can be configured in several ways by combinations of a reflecting mirror, and a doubling and/or mixing crystal. The WEX-1 used for our experiment has three different SHG crystals for second harmonic generation, *i.e.*, doubling of the dye laser beam. and four different crystals for mixing of the fundamental of the Nd:Yag laser with either the dye laser beam or with the second harmonic of the dye laser. By choosing a different crystal, it was possible to extend the wavelength range well into the ultraviolet. The WEX-1 also had a Pellin-Broca prism used to separate the dye beam from the frequency doubled, or mixed laser output of the WEX-1. With the use of the WEX-1, we had photons available for the experiments in the range from 800 nm to 220 nm. In particular, the WEX-1 was used to double the output wavelength of DCM and Rhodamine 6G dyes to access the near ultraviolet.

The power output of the WEX depended very largely on the power output used for the pumped dye laser, and this in turn depended largely on the power output selected for the Nd:YAG laser. The different laser components of the system needed to be properly aligned and "tweaked" in order to maximize the power output used for the multiphoton ionization studies. Typical maximum power output for our laser system was 300 mJ/pulse for the second harmonic of the Nd:YAG laser. The output of the dye laser could vary greatly depending on the dye laser used. For instance, nominal output for DCM was 60 mW, and for Rhodamine 6G (Rhodamine 590) was 100 mW. This resulted in a typical power output of the WEX-1 of about 1 mJ/pulse.

There was also a time dependence to the pumped dye laser power output due to the finite lifetime of the dye used, some dyes having relatively long lifetimes, *e.g.*, 40 hours for DCM, some others having very short lifetimes, *e.g.*, 15 minutes for Exalite 389. Great care had to be taken to ensure that no damage was made to the pumped dye laser cells due to the high incident power of the harmonics of the Nd:YAG laser.

B-2. Optics

The output beams of the harmonic generator, dye and WEX-1 are very nearly plane polarized. Nevertheless, single Glan-Air prisms (Karl Lambrecht, ARA-12-6) were used to guarantee that the plane of laser polarization was well defined before rotating it or transforming it to a different polarization.

Two different optical layouts were used for measuring the photoelectron angular distributions, both depicted in figures 3.4 and 3.5. The first configuration used either the plane polarized output of the dye or of the WEX laser to resonantly ionize the ground state of cesium, while the second configuration used the plane polarized output of the dye laser to excite the ground state of cesium or rubidium to a resonant state, and then used one of the circularly polarized harmonics of the Nd:YAG to ionize the excited state. The photoelectron angular distributions were then measured by rotating the plane of polarization of the excitation laser beam by using a double Fresnel rhomb rotator (Karl Lambrecht, MFRA2-10-580) and detecting the outgoing photoelectron at a fixed direction in space. The first Fresnel rhomb changed the polarization of the photon by changing the relative phase of the component of the electric field of the photon perpendicular to the optical axis of the rhomb,[52] *i.e.*, it changed the polarization of the photon from plane to elliptical. The second Fresnel rhomb changed the polarization back to planar. The net effect of this combination was to rotate the plane of polarization of the photon by an angle 2θ, where θ is the angle between the plane of polarization of the photon and the optical axis of the double Fresnel rhomb. Thus rotating the double Fresnel rhomb through 180° in effect rotated the plane of polarization through 360°. The double Fresnel rhomb rotator due to the shape and cut of the BK7 (borosilicate glass) material had an effective wavelength range of 330-1000 nm, and another double Fresnel rhomb rotation device (Karl Lambrecht, MFRA2-10-272, made out of fused quartz) was used to span the range of wavelengths used to study photoionization in the UV range of 237-307 nm.

The linear polarization of the harmonics of the Nd:YAG laser was transformed to circular polarization by using the optical setup depicted in figure 3.6(a). The

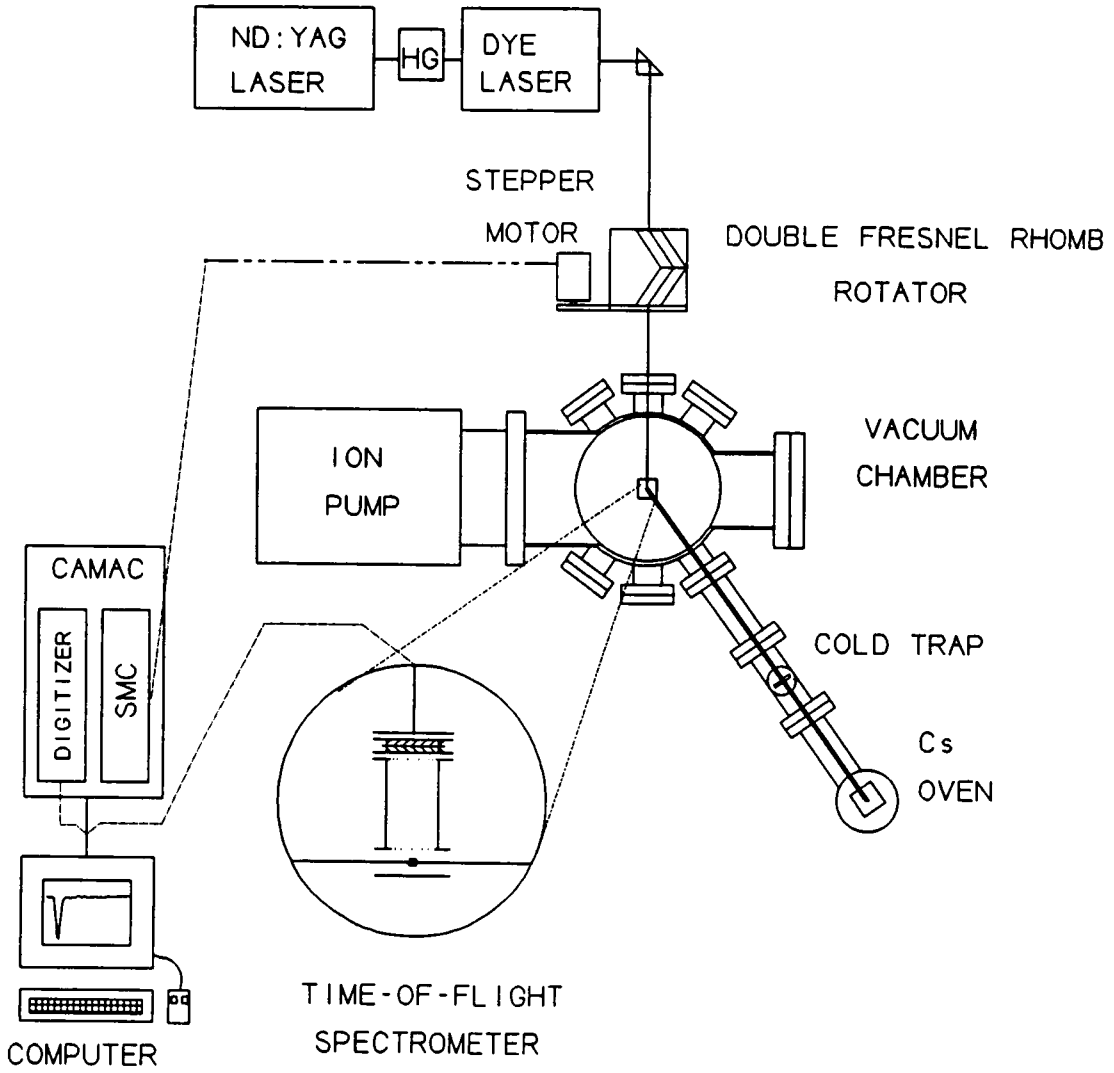

Fig. 3.4. Apparatus and laser arrangements used to study photoelectron angular distributions from excited states in cesium.

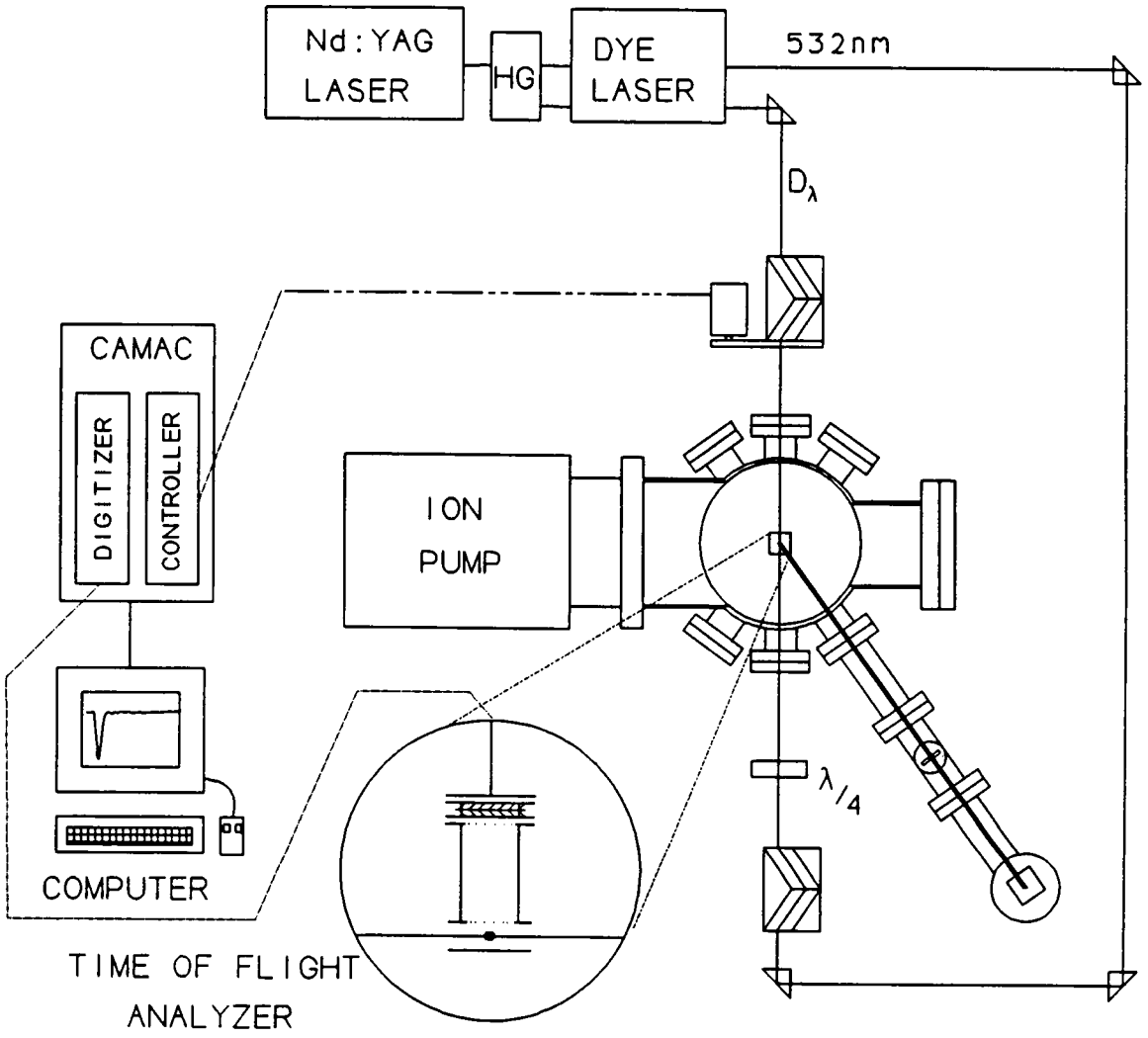

Fig. 3.5. Apparatus and laser arrangements used to study the circular dichroism from the $7^2P_{1/2}$ and $7^2P_{3/2}$ states of cesium.

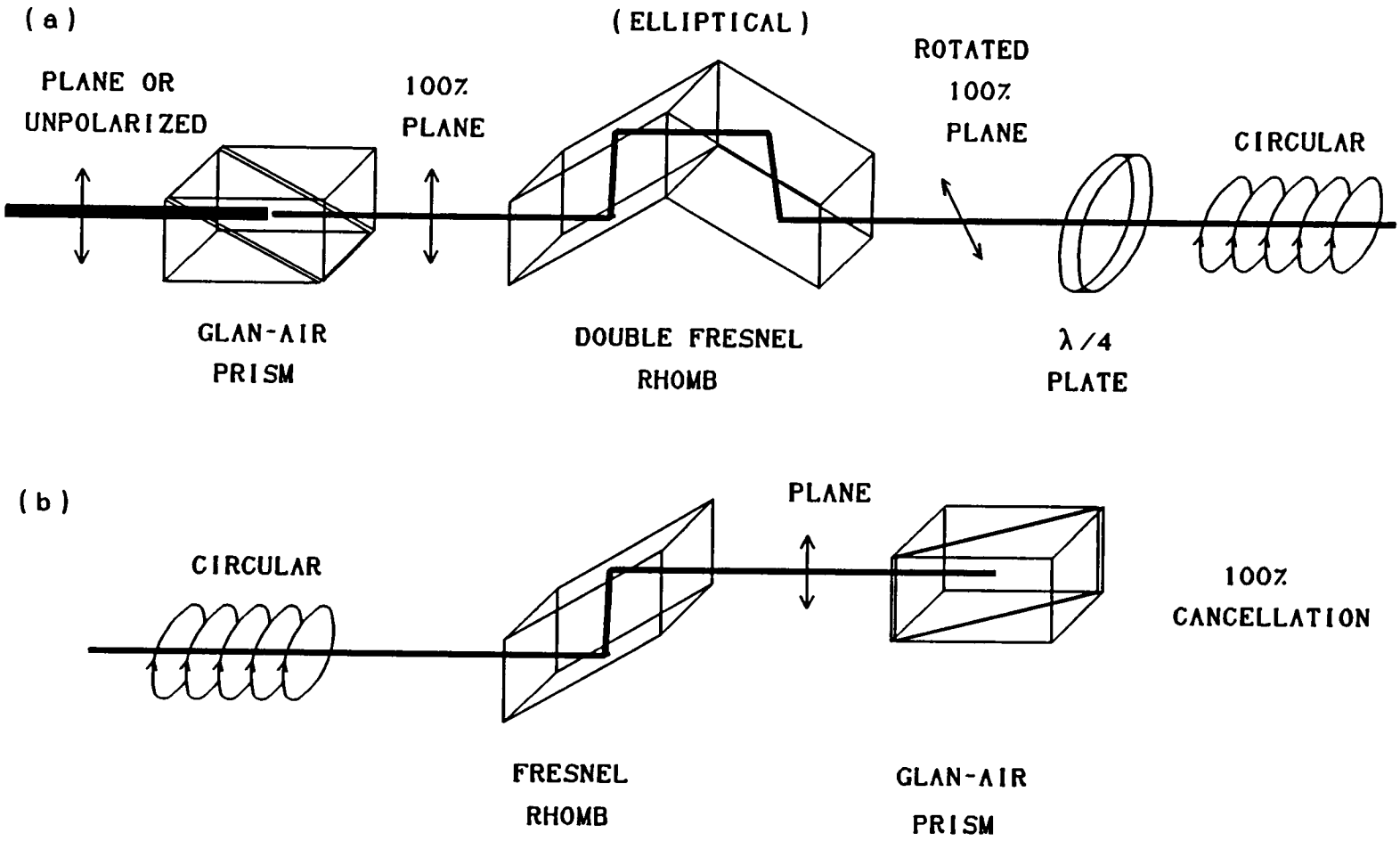

Fig. 3.6. (a) Optical setup used to transform the polarization of a laser beam from plane to either right or left circularly polarized polarization. (b) Setup to analyze the polarization of the laser beam.

polarization of the laser beam was additionally defined using a Glan-Air prism, and its plane of polarization was rotated either 45° ($\pi/4$) to the left or right with respect to the optical axis of the quarter wave plate by using another double Fresnel rhomb (Spectra Physics, 310A-21). Two different quarter wave plates cut for each of the harmonics of the Nd:YAG laser were used to transform the polarization of the harmonic beam from planar to circular. The effectiveness of this setup was confirmed by placing a single Fresnel rhomb (Karl Lambrecht, FRS4-10-580) in the path of the output of the quarter wave plate, as shown in figure 3.6(b), and analyzing the output of the rhomb with a single Glan-Air prism with its optical axis at 90° from the axis of the Fresnel rhomb. Cancellation of the laser beam was nearly 100 percent at cross-polarization. The setup in figure 3.6(a) was assembled by using this technique of cross-polarization to determine the optical axes of each of the optical components.

The polarization of the laser beams inside the interaction chamber was examined by studying the effect of the window ports of the chamber on the polarization of the light on the cross-polarized light. It was determined that synthetic quartz (CVI Laser Corp., suprasil) and sapphire (MDC, VP-100S) windows did not affect the polarization of the laser beam, while fused quartz windows depolarized the light. For the one laser beam experiments (Fig. 3.4) the output window was cut at Brewster's angle to minimize back reflections of the laser beam, that could generate background electrons.

The laser beams were adjusted for maximum spatial overlap with the alkali beam, and in the two color experiments, the overlap of the laser beams was also confirmed by checking the beams on both sides of the chamber. An ultraviolet wavelength plate was used to filter out the 532 nm beam in order to avoid damage to the dye laser optics before it reentered the PDL-1. Damage can occur to the dye laser optics by the high intensity 532 nm beam as a consequence of optimum overlap of the beams throughout their path, allowing the high power second harmonic to enter the dye laser through its output port. In addition to spatial overlap, in experiments using two pulsed laser beams, the temporal overlap of the beams inside the interaction region was varied by placing a delay line in the path of the excitation laser (not shown in figure 3.5). The delay line consisted of 3 to 5 quartz prisms mounted on an optical bench, and their positions were

varied to extend the path of the laser beam, changing the time offset at a rate of approximately 3.3 ns/m.

B-3. Vacuum Chamber and Vacuum Pumps

The experiments were carried out in a vacuum chamber in order to increase the mean free path length of the target atoms and electrons. The vacuum system is shown in figure 3.7. The main chamber consisted of a cylindrical stainless steel body (custom made by Varian Corporation with 304 grade stainless steel) 8.00" O.D., and 10.00" in height, with ten access ports of varying size.

The largest port above the chamber was 7.75" I.D. and closed off with a 10" flange (Varian., ConFlat flange), concentric with the main axis of the cylinder, serving as the main access port to the vacuum chamber. The cover had three 2.75" feedthrough ports (Varian, ConFlat flange), one concentric with the cover, and the other two placed 120° degrees apart in a 6" bolt circle. These three ports were used for a linear motion translator for the time-of-flight spectrometer (section B-4), while the other two ports were used for a high voltage (MDC, MHV−275−4) and for a BNC (MDC, BNC−275−4) feedthroughs for electrical connection.

One of the ports consisted of 6" O.D. tube, centerline placed 5.66" below the top flange and on the side of the chamber, and was used to connect the chamber to the ion pump (Varian, Triode VacIon pump). This relatively large diameter tube was chosen to provide a large conductance for the pumping system.

Two other ports were made up of 4" O.D. tubes. One of these was opposite and below to the 10" cover, and was sealed off using a 6" flange (Varian ConFlat flange), whereas the other tube, centerline 4.00" below the cover flange and opposite to the ion pump feedthrough, was closed using a 7056 glass window (MDC, VP-400), serving as a viewing port into the chamber. This window was used to peer into the chamber to adjust and arrange the laser beams, and to position the time-of-flight mass spectrometer.

There were also six smaller feedthrough ports 1.5" O.D. (with 2-3/4" ConFlat

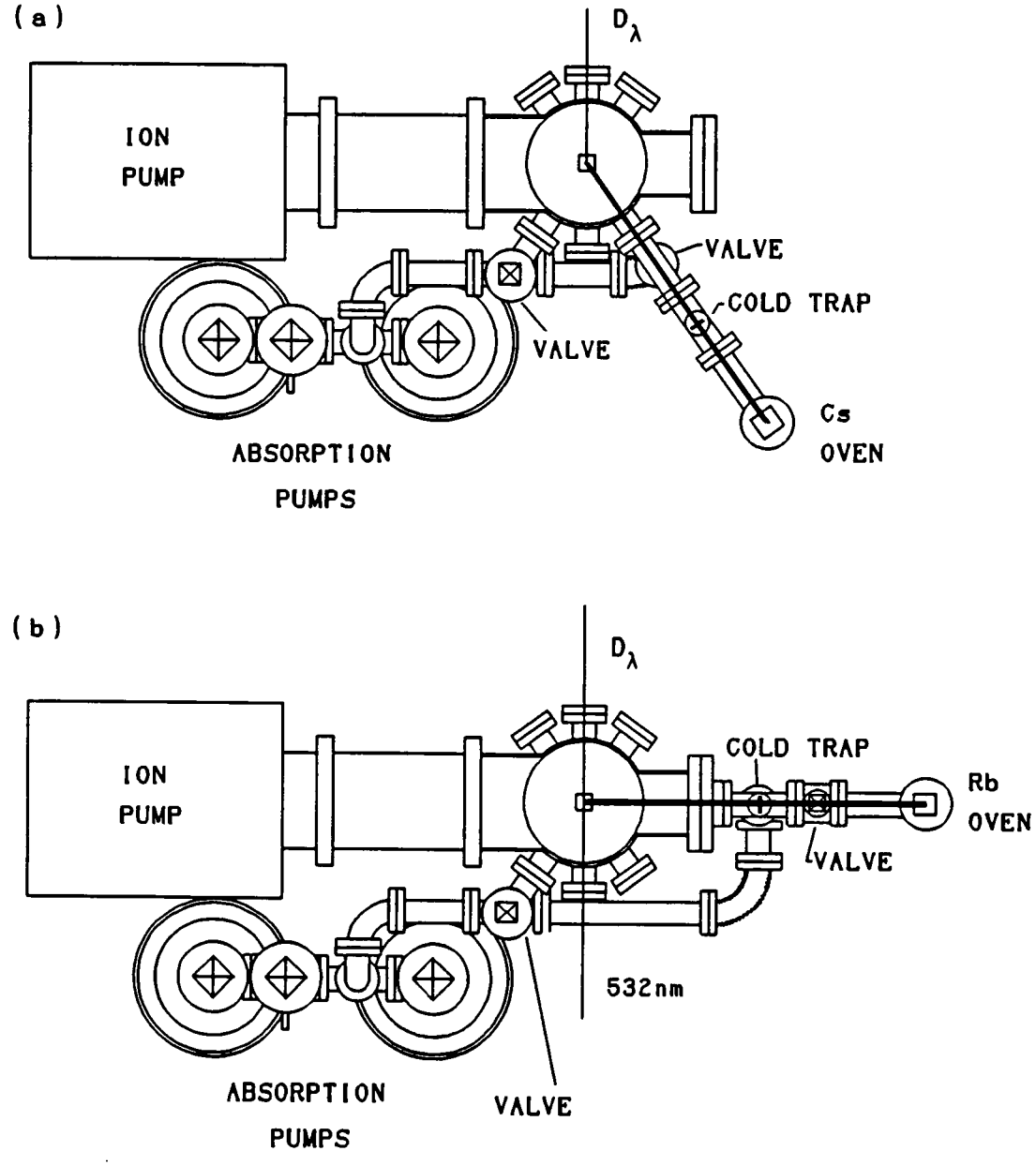

Fig. 3.7. Vacuum chamber and pump configurations used in the photoelectron angular distributions: (a) original setup used for studies of cesium; (b) subsequent configuration used to eliminate the doppler broadening of the resonances in rubidium.

flanges) located around and normal to the cylindrical body of the chamber, at the same height as the viewing port. Two of these smaller ports were at right angles from the larger viewing ports, and the other four at 35.5° from each side of the other two. These ports were used to install the alkali oven assembly (section B-5), the hot-wire detector (section B-5), the laser beam windows, and a rough pump manifold. The one remaining port was used to position a nude ion gauge (MDC, BATT 43200), in order to monitor the pressure inside the vacuum chamber. In later experiments, this port was connected to a variable leak valve (Varian, 951-5106), used to regulate the flow of oxygen into the chamber in an attempt to eliminate the creation of background photoelectrons while using UV laser frequencies.

Two different vacuum pump systems were employed in the experimental apparatus. The rough pump system consisted of a pair of molecular sieve absorption pumps (Varian, VacSorb Pump) used to evacuate the chamber from atmospheric pressure to about $1x10^{-3}$ torr. Each absorption pump consisted of an aluminum chamber with radial fins on the inside surface, filled with molecular zeolite (Varian, Type 5A), functioning as the molecular sieve. The chambers were submerged in liquid nitrogen (LN_2) to below $-195°C$ (77 K), cooling down the molecular zeolite. The molecular sieve is a poor conductor of heat, and the pump had to be chilled for several minutes before it could effectively be used, since maximum capacity of a sorption pump is realized only when the absorbent is completely chilled.[53] As the molecular sieve was cooled down, most gaseous molecules present inside the pump were trapped inside the sieve material, thus reducing the pressure. Pressures of a few millitorrs are obtained when air is pumped with a single stage pump, but better results are obtained by using a two absorption pump system.[53] The first stage can pump out a portion of the residual gases by driving them inside the pump with the other gases during the initial interval of the pumping procedure. Good pumping out of the residual gases is obtained if the pump is then valved off and the second pump used to pump out.

The ion pump (Varian, Triode VacIon Pump 912-7014) was used to further pump down the system to an operational pressure of about $3x10^{-6}$ torr (the limiting value was determined by the vapor pressure of the alkali metal at room temperature). The ion pump

consisted of two titanium electrode pairs inside a stainless steel chamber. One of the electrodes was shaped into a honeycomb-like pattern that maximized the surface area of the electrode, and the other was shaped into a grid-like pattern. The ion pump worked on the principle of ionization of atoms and molecules by the action of a strong electric field. A potential of over 4000 V was present across the titanium electrodes of the ion pump. The entire electrodes were surrounded by a large magnet in order to drive the charged ions to the surfaces of the titanium elements.

The pumping down procedure consisted in using the molecular pump as a rough pump to the chamber. When the pressure reached roughly $10x10^{-3}$ torr using only the absorption pumps, the ion pump was turned on and "baked" for about 30 minutes while continuing to pump down using the absorption pump. Due to the large power dissipated by the ion pump, the entire pump heated up, outgassing the electrodes. The ion pump was turned off and allowed to cool down when the body of the pump reached about 150°C, while continuously pumping down the chamber using the absorption pumps. The titanium elements of the ion pump cooled down after a couple of hours. At this stage, the absorption pumps were taken off-line by closing them, and it became possible to use the ion pump to continue to pump down the vacuum system. After about 15 hours of running the ion pump, the pressure was believed to be low enough (reaching the vapor pressure of the alkali metal in use, about $2x10^{-7}$ torr) and the ion pump to be sufficiently stable to withstand the operation of the heating element of the oven without shutting down the ion pump controller.

B-4. Mass Spectrometer and Electron Analyzer

The photoelectrons were detected and analyzed using a short (5cm) time-of- flight (TOF) spectrometer. The TOF spectrometer is depicted in Fig. 3.8, together with a SIMION (Simion PC/PS2, version 4.02, Idaho National Engineering Laboratory) analysis of typical field lines and electron trajectories for typical operating conditions.

The time-of-flight electron spectrometer was built using standard stainless steel

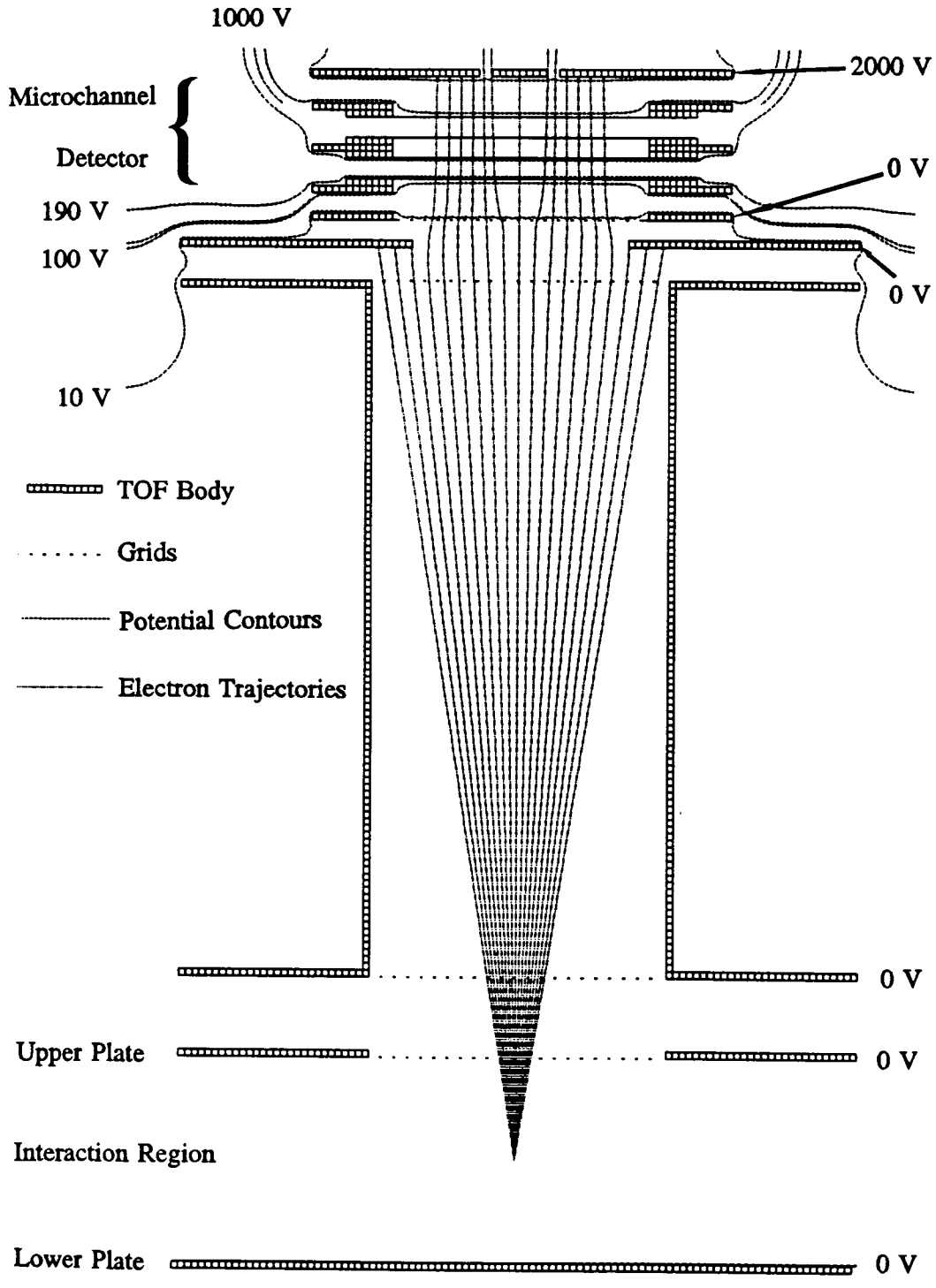

Fig. 3.8. Time-of-flight electron spectrometer used to detect the photoelectrons, with a SIMION analysis electron trajectories under typical conditions. Each electron trajectory is 1° apart.

eV parts (Kimball Physics, Inc.), and the actual flight tube was 1" O.D. and 5 cm long. The tube was spot welded at each end to a 1.5" square plate, with a 1" round hole in the center, and rows of five 3/16" holes along each edge, providing means for connections and aligning with other eV parts. One 90 percent transparency electroform molybdenum mesh grid was attached to each plate, thus covering the 1" hole, in order to minimize the effects of stray electromagnetic fields on the flight path of the photoelectrons. One of the gridded plates was attached to two L-brackets (Kimball Physics, Inc., SS-BR-B2x5) used to link the time-of-flight tube to a custom designed aluminum support bracket, connected to the linear motion feedthrough. This bracket centered and held the time-of-flight assembly firmly in place. The gridded plate at the opposite end was used to hold two additional square plates through four ceramic insulating posts (Kimball Physics, Inc., Alumina tubing, various lengths). One of these plate also had a 1" round hole at the center covered with molybdenum mesh, and was in direct electrical contact with the flight tube. The other plate only had the holes along the edge, and was electrically insulated from the rest of the time-of-flight tube. This plate was used to push either electrons or ions into the flight tube for diagnostics and evaluations of the experimental apparatus. The insulation posts were covered with stainless steel caps and cylindrical spacers (Kimball Physics, Inc., SS-IP-C and SS-SP-C-250) in order to keep the ceramic from charging by stray photoelectrons or ions. The caps and spacers were of two different diameters, and were held apart using an insulating ceramic spacer (Kimball Physics, Inc., Al_2O_3-SP-C-100) that fit inside the larger cap. The plate separation was varied from 0.5 cm up to 2.5 cm by using insulating posts and stainless spacers of different lengths.

The TOF detector evolved through different stages of improvements but the basic design was similar for all experiments. The primary difference between different configurations was that the parallel plates (interaction region) separation was varied, and that for experiments involving short wavelength (ultraviolet) radiation the lower plate was removed in order to reduce the background noise photoelectrons from surfaces inside the chamber. For the experiments where the parallel plates were used, both plates were grounded and kept at zero potential using 0.08 nichrome wire (Pelican Wire Company).

The upper plate was also grounded by physical contact with the support system, and only the lower plate was electrically disconnected from ground, allowing application of a potential across the plates to push either the photoelectrons or the ions into the flight tube.

All metallic surfaces of the flight tube, except for the molybdenum grids, were coated with a thin layer of colloidal graphite (Acheson, Aerodag) in order to reduce localized point charge effects by making all interior and exterior surfaces of uniform potential.

By using the linear motion feedthrough, the flight tube assembly could be placed so that photoionization took place in the region halfway between the two parallel plates when these were employed. Photoelectrons were ejected in all directions, but ions, due to their larger mass and momentum, traveled in the same direction as the alkali beams, unless forced into the flight-tube by applying a "pushing" voltage using the lower parallel plate. The lower plate could alternatively be used to force photoelectrons into the flight tube. However, the lower plate was consistently grounded while measuring the photoelectron angular distributions using a grounding cap on the MHV connector feedthrough.

The photoelectrons, or ions, are detected at the opposite end of the flight tube using two microchannel plates (Varian Electro Optical Sensors Division, 8960), which can be biased using a power supply (Tennelec, TC-952) to detect either negatively or positively charged particles. Fig. 3.9 shows the microchannel assembly, including an electrical diagram depicting the voltage distribution to the assembly used to detect the particles as an electronic pulse. Each microchannel plate has an impedance of roughly 950 MΩ. The applied voltage to the microchannel plates is split across the resistors and microchannel plates, so that the entrance (lower) microchannel plate (B) is slightly biased with respect to ground. To detect photoelectrons the lower microchannel plate is biased using the 15 MΩ resistor to about +100 V (V_2 grounded), and the exit (upper) plate is biased using another 15 MΩ resistor to +1.9 kV ($V_1 \approx +2$ kV). To detect photoions the lower microchannel plate is biased to about −1.9 kV ($V_2 \approx -2$ kV), while the upper microchannel plate is biased to about -100 V (V_1 grounded). This bias provides the

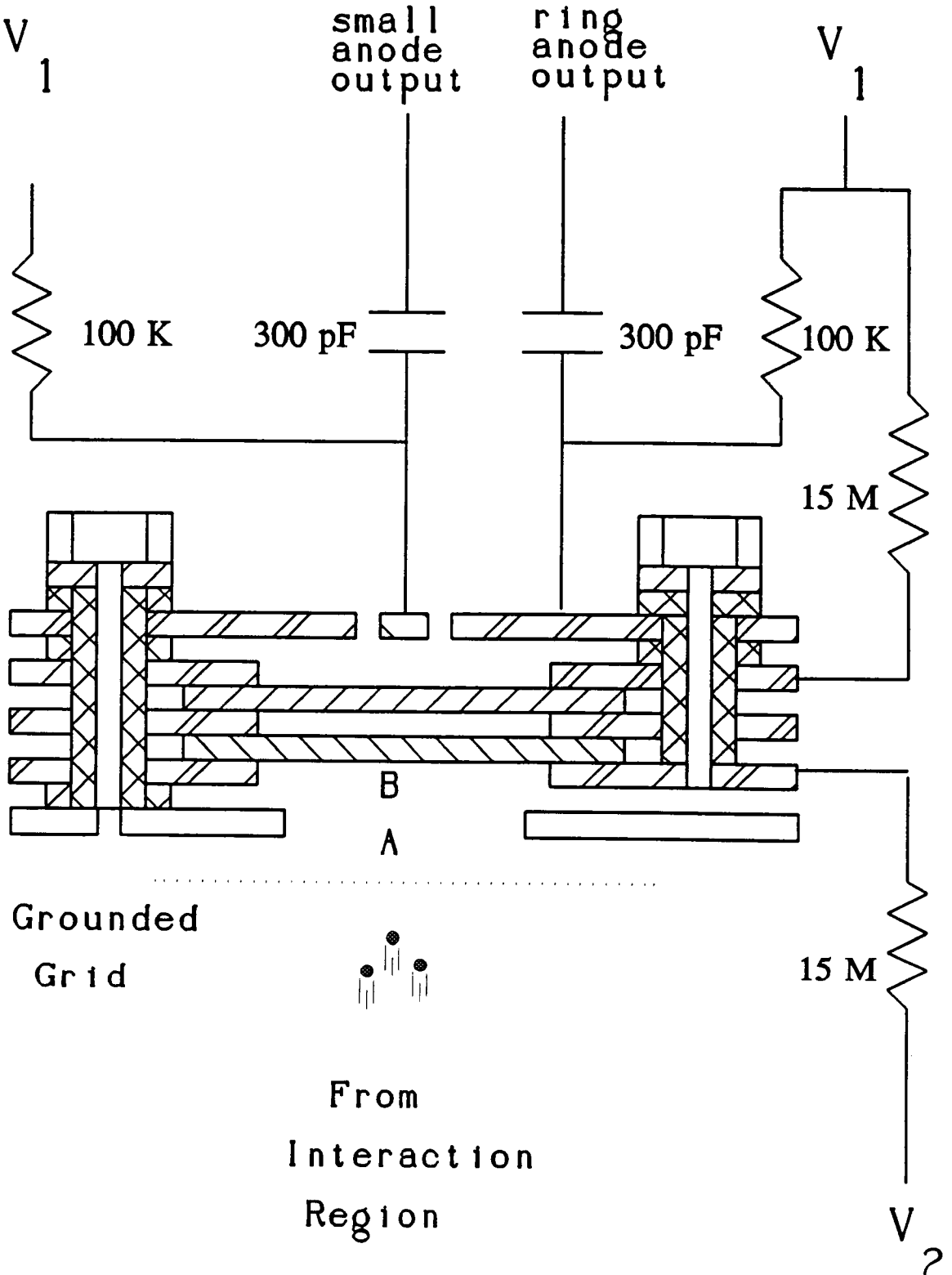

Fig. 3.9. Microchannel assembly and electronic diagram depicting the electronic configuration used to readout the photoelectron pulse.

electrons that are produced when the photoelectrons or ions hit the front microchannel plate. The particles enter the detector through the aperture A and generate secondary electrons upon entrance into the front surface of the microchannel plate B. Multiplication gains at typical applied voltages are in the order of 10^6:1. The secondary electrons are generated at the top of an electric potential gradient, and "fall" to the other end of the microchannel plates, where they are measured using a split anode. For detecting electrons the anode was kept at a fixed potential, typically around +2 kV, and the electrons were detected as a transient pulse using a charged capacitor.

To increase the angular resolution of the time-of-flight detector, a smaller disk anode of 6 mm in diameter was used. The smaller anode was placed inside a circular aperture of about 7 mm in center of the larger ring anode. The larger anode was used for diagnostic and alignment purposes due to its larger acceptance angle, but the actual data was acquired using the smaller anode. Each anode was kept at the same electrical potential by placing them in a parallel circuit, but each had its own readout output port and capacitor so both anodes could be measured separately and simultaneously.

The electrical design used to readout the photoelectron signal is presented also in figure 3.9. The resistors and capacitors are placed inside the vacuum chamber in order to reduce electrical noise, and this requires that special glass-encased resistors and ceramic capacitors be used. The wiring was covered with 100 mil teflon tubing in order to prevent the electrical lines from shorting. Electrical connections were made using 3/16" quick connectors and spotwelding resistors. Two 2−3/4" feedthrough ports (MDC, MHV-275−4 and BNC-275−4) were used to connect the detector with the outside world.

The performance of the time-of-flight spectrometer was investigated with SIMION modeling calculations on a personal computer. Results of this studies are shown in Appendix B. The effects of changing the different applied voltages to the parallel plates and to the microchannel plates were studied using the SIMION fast voltage adjust option. The studies included an analysis of the trajectories and time of flights of the photoelectrons, information which was used to provide an idea of the angular and time resolution of the detector.

Two distinct methods were used to counter the Earth's magnetic field. The first method consisted in placing three pairs of orthogonal Helmholtz coils around the apparatus, and varying each coil current in order to generate a magnetic field equal in magnitude, but opposite in direction to the Earth's magnetic field. Three different power supplies were used to control each axis of the generated magnetic field, and the current for each axis was varied until each component of the Earth's magnetic field was canceled. Proof of cancellation was made by using a Hall probe, showing a residual magnetic field strength of less than $\sim$ 0.05 G. Uniformity of the zero field inside the Helmholtz coil was reasonable good.

The second method of annulling the Earth magnetic field was to enclose the entire interaction region and detector inside a magnetic μ-metal shield. Apertures were included for all the feedthrough ports. The larger apertures were extended with magnetic sleeves in order the reduce penetration of external magnetic fields. The shield was custom made by the Ad-Vance Magnetics, Inc. The manufacturing process involved the machining and molding of the shield, and once put into the shape specified by the design, the annealing of the shield in a field free oven within a vacuum atmosphere at around 2150°F (1450°K) for two to four hours.

The magnetic shield method proved to be more effective than using the Helmholtz coil to counter the Earth's magnetic field, since the shield acted like a variable magnet, responding to all external magnetic fields. Explicit measurements with a Hall probe gave an estimated residual magnetic strength of 4.5 mG. The only noticeable electromagnetic fields could have originated from different metallic parts used inside for the time-of-flight detector. Great care was used in choosing materials that were conducting and non-magnetic for use inside the chamber. Any insulating parts used were carefully shielded using non-magnetic metallic caps and sheaths. Furthermore, in later experiments, the interior of the chamber was divided using a copper plate to reduce the effect of any electric fields due to the anodes of the time-of-flight detector.

B-5. ALKALI AND MOLECULAR BEAM OVEN

The alkali beam was generated by heating a 0.5-1.0 g ampule of cesium, or rubidium, inside an oven chamber. The diagram of the oven is shown in figure 3-10. The interior of the oven was cylindrical in shape, and slightly larger than the ampules used for the experiment. The upper half of the oven was a made out of a 1.25" × 1.25" × 1.5" rectangular block of stainless steel, with one square face bored with a 0.75" I.D. round hole, forming half of the oven cavity. One side wall of the stainless steel block was drilled through to the oven cavity with a 1.0 mm hole, constituting the oven aperture. The lower half of the body was also rectangular, made using an 1.25" × 1.25" × 1.25" oxygen free, high conductivity (OFHC) copper block. One square face was drilled through with a 0.875" round hole. This hole was used to hold a stainless steel cup, forming the other half of the oven cavity. A retaining nut, placed between the cup and the copper block, is used to attach both halves of the oven together. The cup was held in place using a metal screw on one side of the copper block. Each half the oven was drilled through with four 0.125" holes, allowing for the insertion of 1.6 mm heating coils inside alumina tubing (Kimball Physics, Inc., Al_2O_3-TU-C-200). The heating coils were wired to provide independent heating of the lower and upper halves of the oven. Wires covered in fish-eye ceramic tubing were run from the heating coils to the top of the oven, where more wires covered in fish-eye ceramic tubing were used to connect the wires to electrical feedthroughs in a 2-3/4" flange (MDC, MC-153). Electrical connections were made using spotwelding and 3/8" brass connectors. K-type thermocouple wires were used to monitor the temperature of both the top and bottom halves of the oven. The leads of the thermocouple wires were also covered with 100 mil teflon tubing to keep them from shorting, and each was connected to a different thermocouple feedthrough.

The heating procedure consisted in heating the top half of the oven directly by running a 2.5 VAC current through the heating coils. The bottom of the oven was heated by thermal contact, setting a temperature gradient of about 10° C that kept the top half hotter than the bottom half, and kept the alkali gas from condensing and blocking the

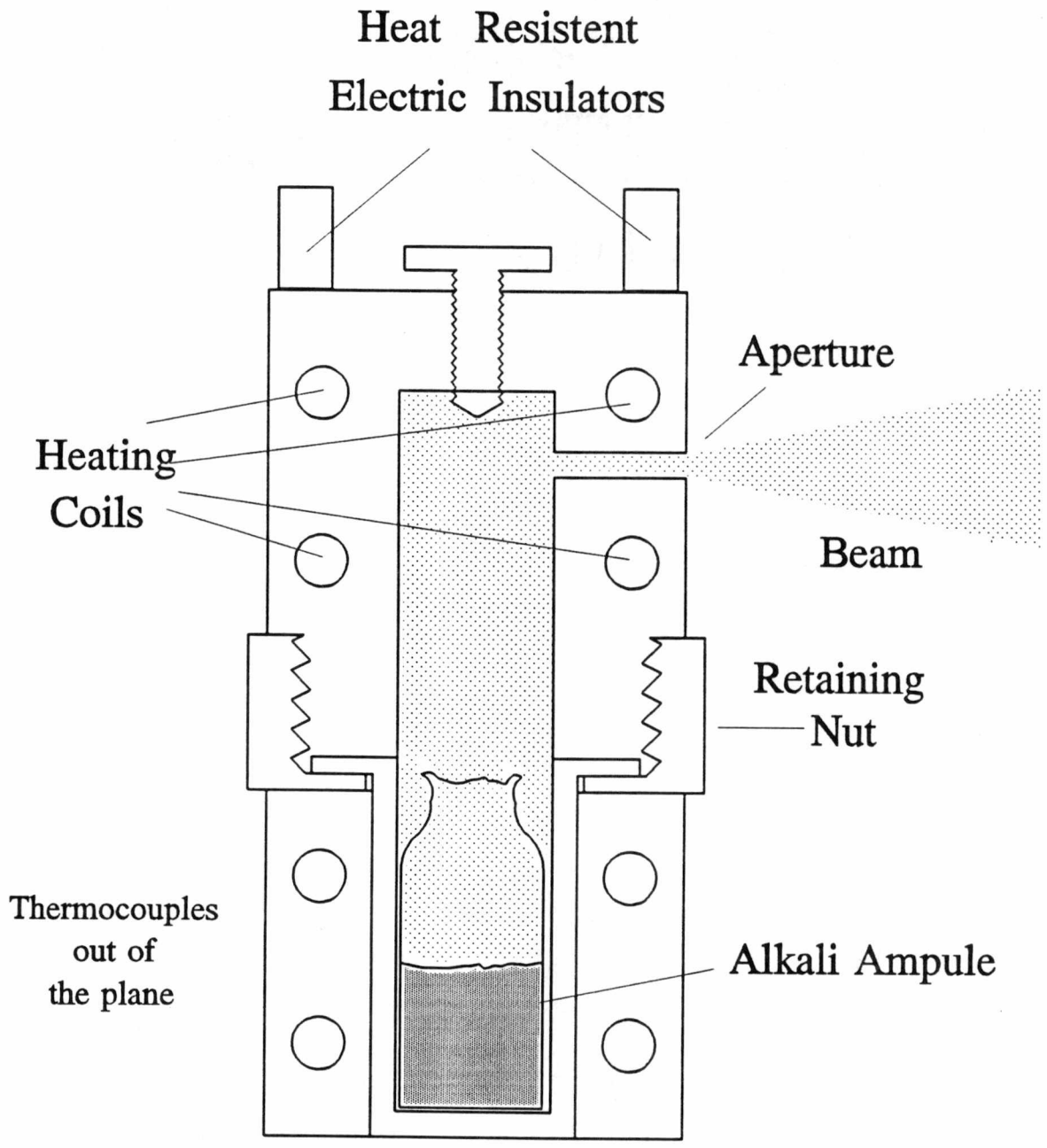

Fig. 3.10. Diagram depicting the alkali beam source. See text for full description.

aperture of the oven. A benefit of this temperature gradient was the dissociation of alkali dimers, which ensured that the alkali beam consisted only of atomic monomers. Standard operating temperatures T for the upper half of the oven were 130° C for cesium, and 170° C for rubidium.

The oven heated the ampule, melting and subliming the alkali metal under vacuum. As the alkali became a gas, it accumulated inside the oven chamber, and escaped through the aperture forming an atomic beam. The atoms in the atomic beam were randomly oriented, and had an average kinetic energy of $3kT/2$. The dispersion of the alkali beam was estimated to be about 10°, with a particle density $\sim 5 \times 10^7$ atoms/cm^2 sec at the interaction region.

The alkali beam was collimated using an 1/4" aperture in a copper plate cooled down with liquid nitrogen and placed about 8" from the oven, and about 10" from the interaction region. In subsequent experiments the collimation system was expanded by placing several 1/4" apertures in aluminum disks 1" apart at about a distance of 10" from the oven and 10" from the interaction region. Fig 3.11 depicts the two collimation schemes used to delineate the alkali metal beam, and their placement in the apparatus. The multi-aperture scheme proved to be the better method at minimizing the deposition of alkali metal onto the TOF. This was verified by observing the creation of noise electrons when using ultraviolet wavelengths. However, even with this system after a long periods of operation the background noise reappeared, as the system equilibrated with alkali in the vacuum chamber.

The beam density could be monitored using a hot wire detector placed at the opposite end of the alkali oven source. A hot wire detector as depicted in Fig. 3.12 was used to detect the alkali beam. A 5 mils tungsten wire shaped into a 2mm coil is heated to about 2400°K using a 1.5 A DC current. As the beam particles strike the wire, they become ionized, and the charged particles are detected using an anode or cathode. These particles are observed as a small current, which was monitored using a picoammeter (Keithley, model 417). The hot wire detector was biased using the variable output voltage from a battery box to measure Cs ions. The density of the beam could be determined by using the equation[54]

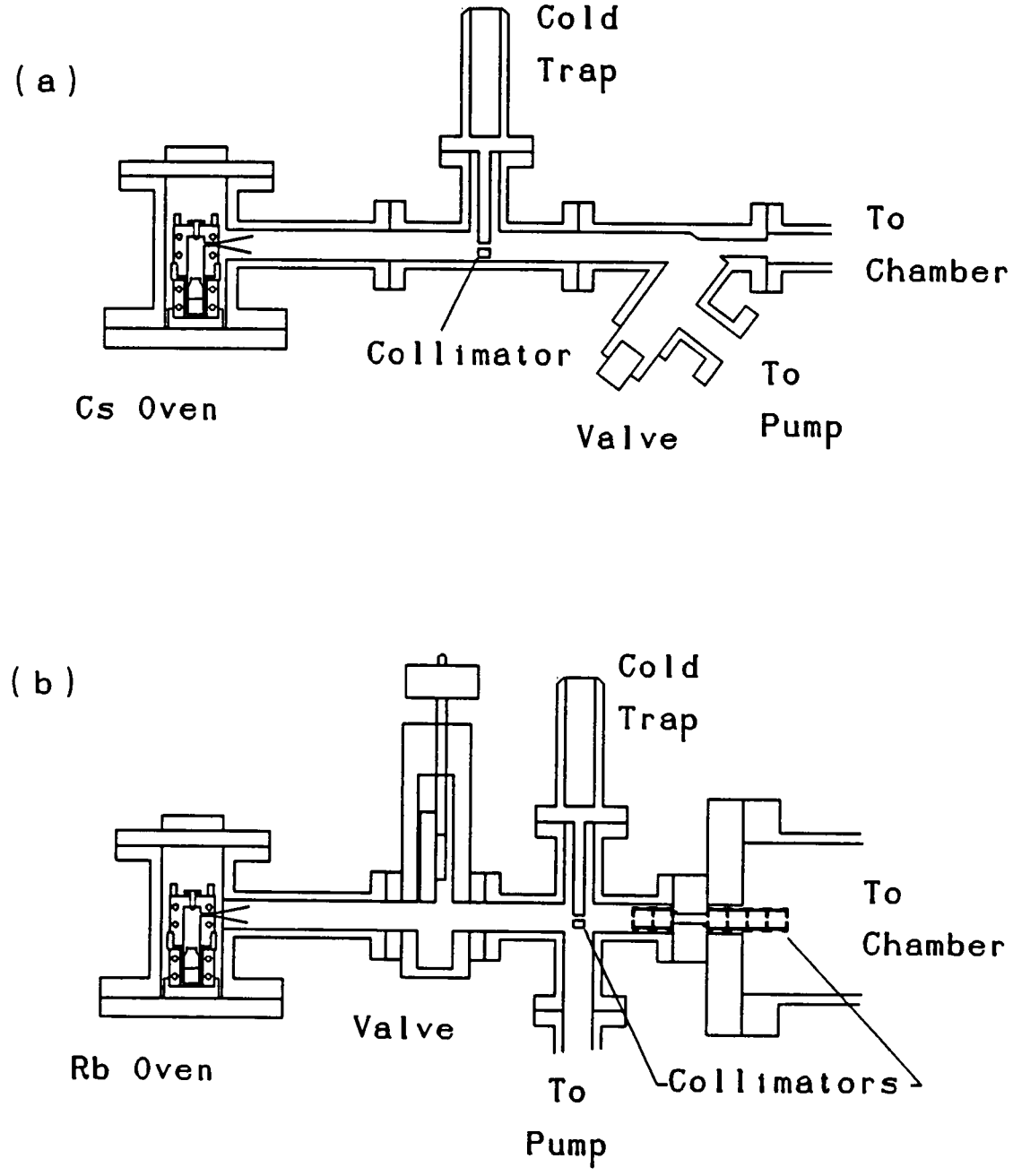

Fig. 3.11. Two different collimation schemes used to define the alkali beams, (a) aperture in a copper plate cooled with liquid nitrogen; (b) series of apertures in aluminum disks.

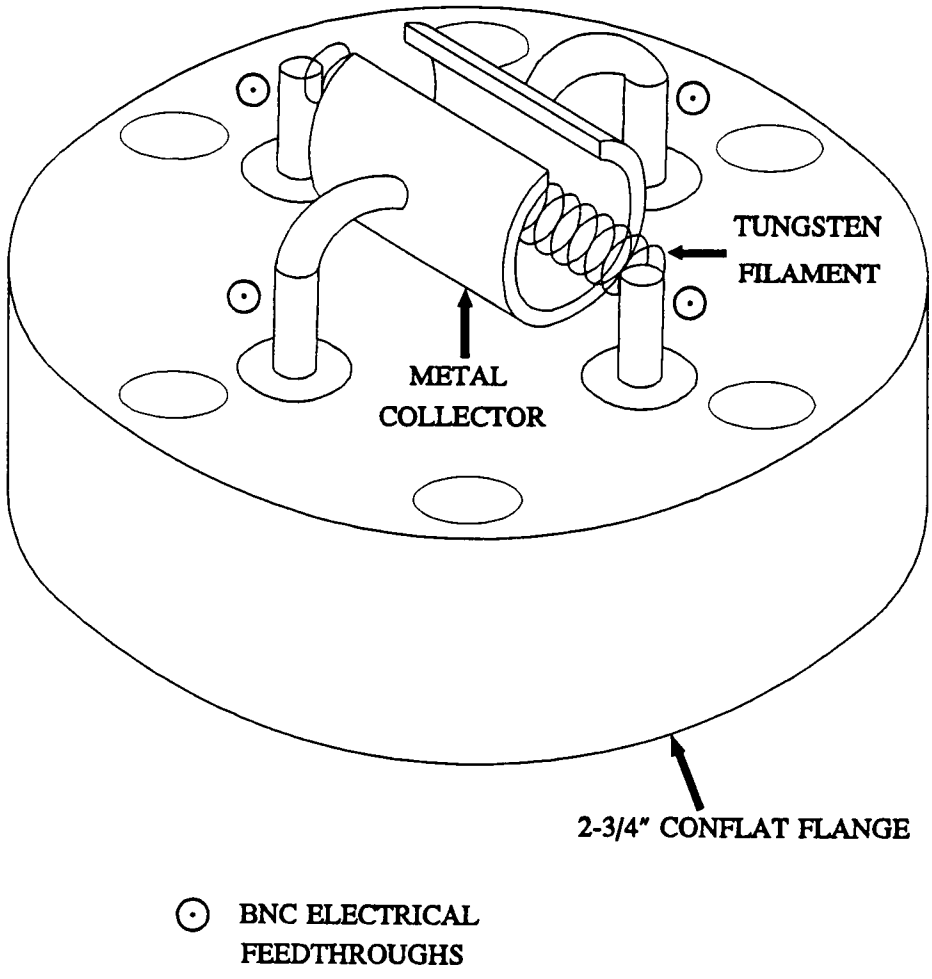

Fig. 3.12. Hot wire detector used to monitor the alkali beam density.

$$\rho = \frac{I_c}{2.3\,nA} \times 10^8 \frac{atoms}{cm^3}, \qquad (3\text{-}1)$$

Typical cesium beam densities were determined to be $3\text{-}6\times10^7$ atoms/cm^3 when the oven temperature was 136°C. The rubidium density could not be measured using the hot wire detector due to geometrical arrangement used for the rubidium experiments.

C. DATA ACQUISITION SYSTEM

C-1. DATA ACQUISITION HARDWARE AND ELECTRONICS

Because a pulsed laser was used as the light source for the experiment, data acquisition was synchronized using the Q-switch synchronization output of the Nd:YAG laser. Photoelectrons or ions were observed as a voltage pulse which were electronically delayed from the Q-switch synchronization trigger as shown in Fig. 3.13. The delay is a composite of the TOF of the photoelectrons or ions as well as the time difference between the Q-switch synchronization pulse and the arrival of the photons to the interaction region. The observed temporal width of the electronic signal stems from the width and pulse shape of the Nd:YAG laser pulse and the RC time constant of the microchannel detector and readout system.

The size of the electronic signal depended on the laser intensity and on the voltage across the microchannel plates, as well as on the intrinsic polarization dependence we sought to observe. Typical signals had a maximum height between 10 and 100 mV. This signal was directly proportional to the number of electrons reaching the microchannel plates. However, our concern was in the fraction of photoelectrons ejected into a direction, or angle, compared to those ejected parallel to the direction of the (plane polarized) electric field of the photons used. For the data analysis, both the height and area under the signal were normalized to the height and area of the signal at 0°, *i.e.*, the

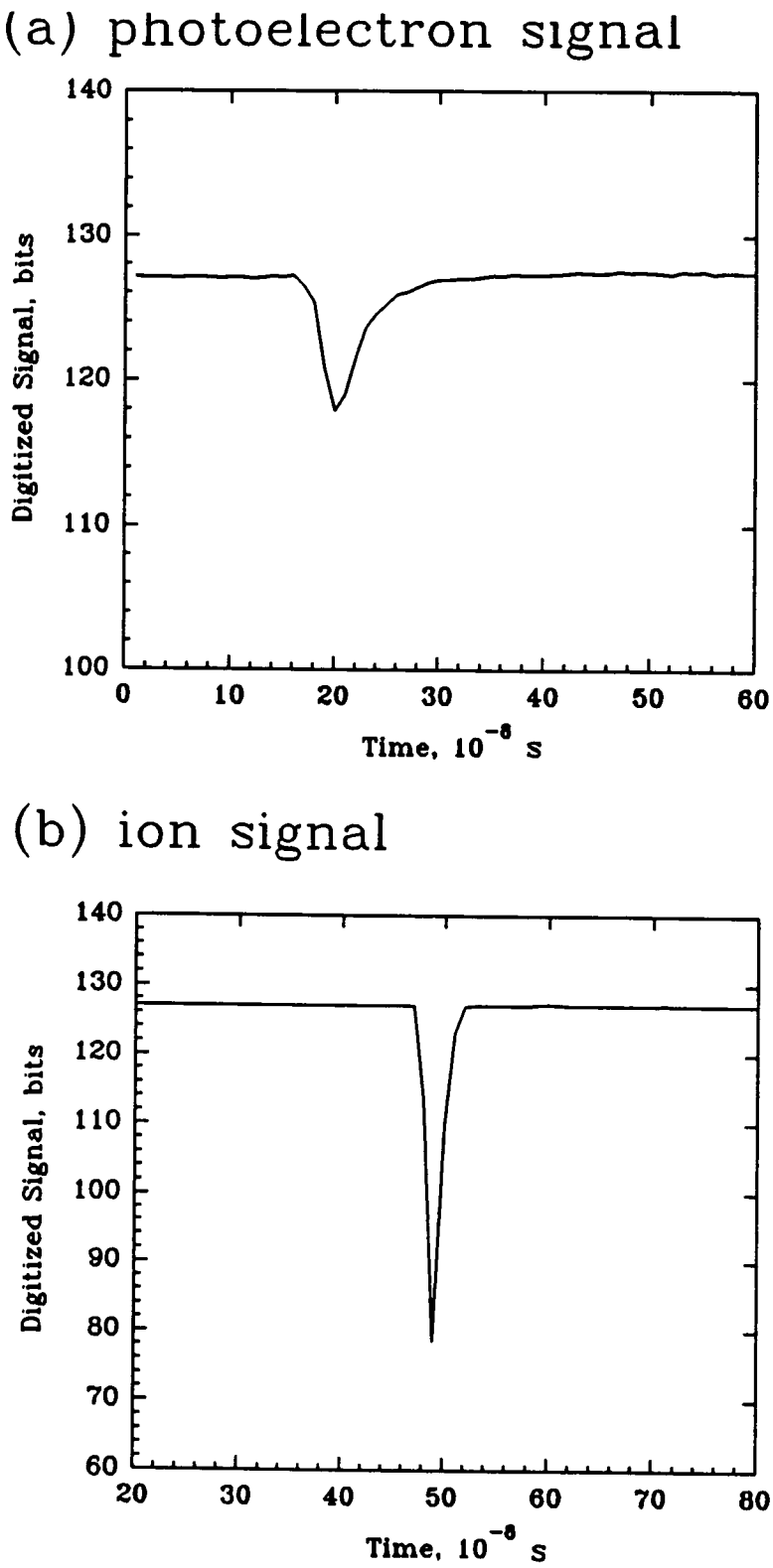

Fig. 3.13. Typical electronic signal as observed using the transient recorder and computer, (a) photoelectrons (lower plate grounded); (b) ions with a +1 kV pushing voltage on the lower plate.

signal corresponding to a direction parallel to the polarization of the electric field.

The electric signal could be measured using an oscilloscope (Tektronix, 2235), a boxcar integrator (Stanford Research Systems, SR-265), or digitized using a transient recorder (DSP Technology, TD-2001A). All three instruments were utilized at various stages of the experiment, but we chose to use the transient recorder in conjunction with a desktop computer (COMPAQ Deskpro 286) to digitize and process the electronic signal. All the experimental data presented in this dissertation were obtained using the 8-bit transient recorder, unless otherwise noted.

The COMPAQ Deskpro 286 computer used an 80286 processor, with 12 MHz clock speed. It featured 640 KB total memory, with 80287 math coprocessor, a Quadram EGA video card, and a NEC Multisync color monitor. Available peripherals were an IBM 6180 Color Plotter, and an EPSON LQ-800 dot matrix printer. Unless otherwise noted, these computer resources were used for the data acquisition, data analysis, generating plots of the data, and SIMION modeling of the apparatus.

Connection between the computer and the transient recorder was accomplished with a Computer-Automated Measurement And Control (CAMAC, ANSI/IEEE Std. No. 583-1975 and updates) interface, a Crate Controller (DSP Technology model 6001) and CAMAC interface card (DSP Technology model PC004) placed inside the computer in one of its ISA expansion slots. The controller had a 24 bit parallel data bus, and provided full control of the transient digitizer. In addition, we were able to control other CAMAC modules with the crate controller, including an analog to digital converter (DSP Technology model ADC E-200), a digital to analog converter (DSP Technology model DAC E-250), as well as a stepper motor controller (DSP Technology model SMC E-406).

The two CAMAC modules most used were the transient recorder and stepper motor controller. The digitizer was used to record and digitize the electronic pulse across the capacitor for each laser pulse, and the stepper motor controller was used to turn the double Fresnel rhomb. The entire procedure was coordinated using the computer, which also was used to average signal pulses recorded at a single angular position of the double Fresnel rhomb. After averaging the data and storing to disk, the stepper motor controller

was used to rotate the double Fresnel rhomb to another angle.

The transient digitizer had a maximum time resolution of 10 ns per channel and a voltage resolution of 2 mV per count (one part in 256, or 8 bits). The TD 2001A featured a variable buffer size from a minimum size of 256 bytes, up to a maximum size of 32768 bytes (32 KWord), used to store the digitized signal, as well as a variable internal clock to adjust the sampling interval from 10 ns up to 10 μs per channel. Both the buffer size and the sampling interval were selectable from the front panel of the digitizer unit, as well as selectable using software commands. This sampling interval could also have been controlled using an external TTL trigger, up to a maximum frequency of 100 MHz. The digitizer would continually digitize any electronic input until it was stopped using an external trigger or its front panel manual trigger. For convenience, the Q-switch synchronization trigger pulse of the Nd:YAG to stop the digitizer and synchronize the data acquisition. The digitizer also featured control to select what fraction of pre-trigger samples were to be considered as part of the signal. Thus, the digitizer would store the signal using the whole memory buffer and keep track which channel corresponded to the stop trigger, *i.e.*, "zero". Once stop triggered, the digitizer set on a look-at-me (LAM) indicator to flag to the controller (and thus the computer) that data was ready for read out from the digitizer buffer.

Typically the photoelectron signal was digitized using the 256 byte buffer and a sampling interval of 10 ns.[1] However, since the photoelectron pulse arrived within 600 ns of the Q-switch trigger, only the first 128 channels (corresponding to 1.28 μs) were kept. The electronic signal was usually sampled 100 times and averaged in order to improve data statistics.

The stepper motor controller was used to turn a dual phase stepper motor (Bodine Electric Company, HY-Sync AC synchronous/DC, 2409). This motor offered a resolution of 200 steps per revolution, but could be also hardwired to step in half-steps by varying the timing sequence of the coils of the motors. In addition, the SMC E-406 was hard-wired using the SMC232 interface port to enable half-step control. A gear ratio

---

[1] This buffer size did not allow for the storage of pre-trigger samples.

of 4:1 was set between the stepper motor and the double Fresnel rhomb. The step resolution was thus 1600 steps per revolution, thus giving a physical angular resolution of 0.225° and an optical resolution of 0.45° per step of the double Fresnel rhomb.

C-2. Data Acquisition Software

The computer software for the data acquisition was developed using TURBO Pascal for IBM and compatible computers (Borland International, Inc., versions 3.0 through 6.0). The main data acquisition and control program originated from one of the sample programs provided with the CAMAC software drivers by DSP Technology, Inc. and evolved through several modifications and versions throughout the research stage.

The first version of the CAMAC driver program code, written using version 3.0 of TURBO Pascal and designated CDRIVER, consisted of a single file that did a little more than provide menu support for choosing CAMAC commands for each of the crate modules available for our experiment. The user was required to provide the setup information, *i.e.*, the location of the distinct modules in the CAMAC crate, and was also required to have an understanding of CAMAC commands by typing the combinations of addresses, functions and numbers for the modules in order to transfer the digitized data from the TD 2001A, to computer memory, and then to disk.

In contrast, version 5.1 of the program code takes advantage of TURBO Pascal version 5.5 unit technology and concepts to include code supporting each of the CAMAC modules, with subroutines for common command sequences typical for each CAMAC module, and other enhancements like online help, reading the crate module configuration by querying each module for its ID, and tools for the realtime graphical display, averaging, and analysis of the digitized signal. A program tree depicting the modular organization of the program is shown in Fig. 3.14. The CRT, Overlay, and DOS units were included with the Turbo Pascal compiler package, and were not modified in any way. The Video, BinU, MouseU, MenuU, and Keybrd units were duplicated from the book "Turbo Pascal: Advanced Programmer's Guide".[55] The MenuU unit was modified

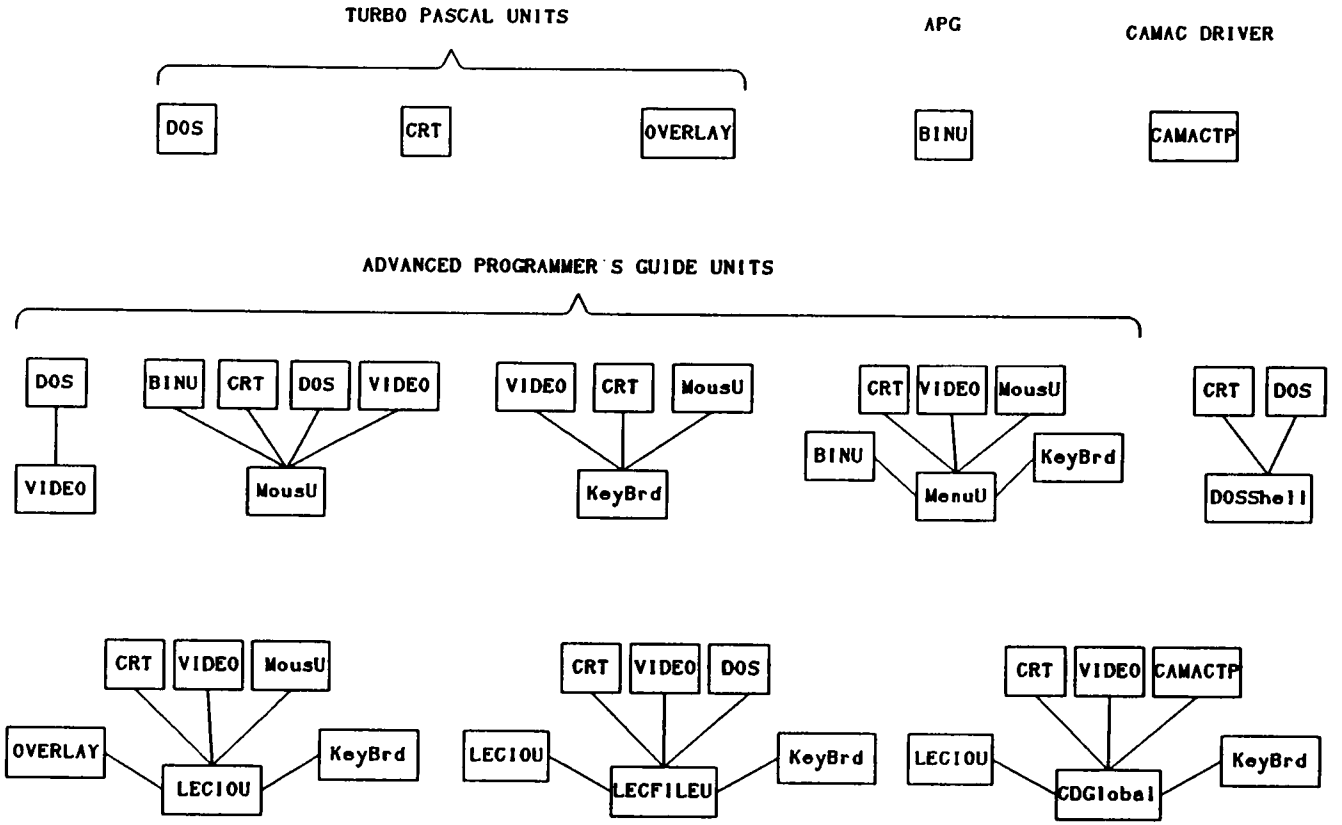

Fig. 3.14. Tree depicting organization of the CAMAC Driver, version 5.1, program. For more details see text.

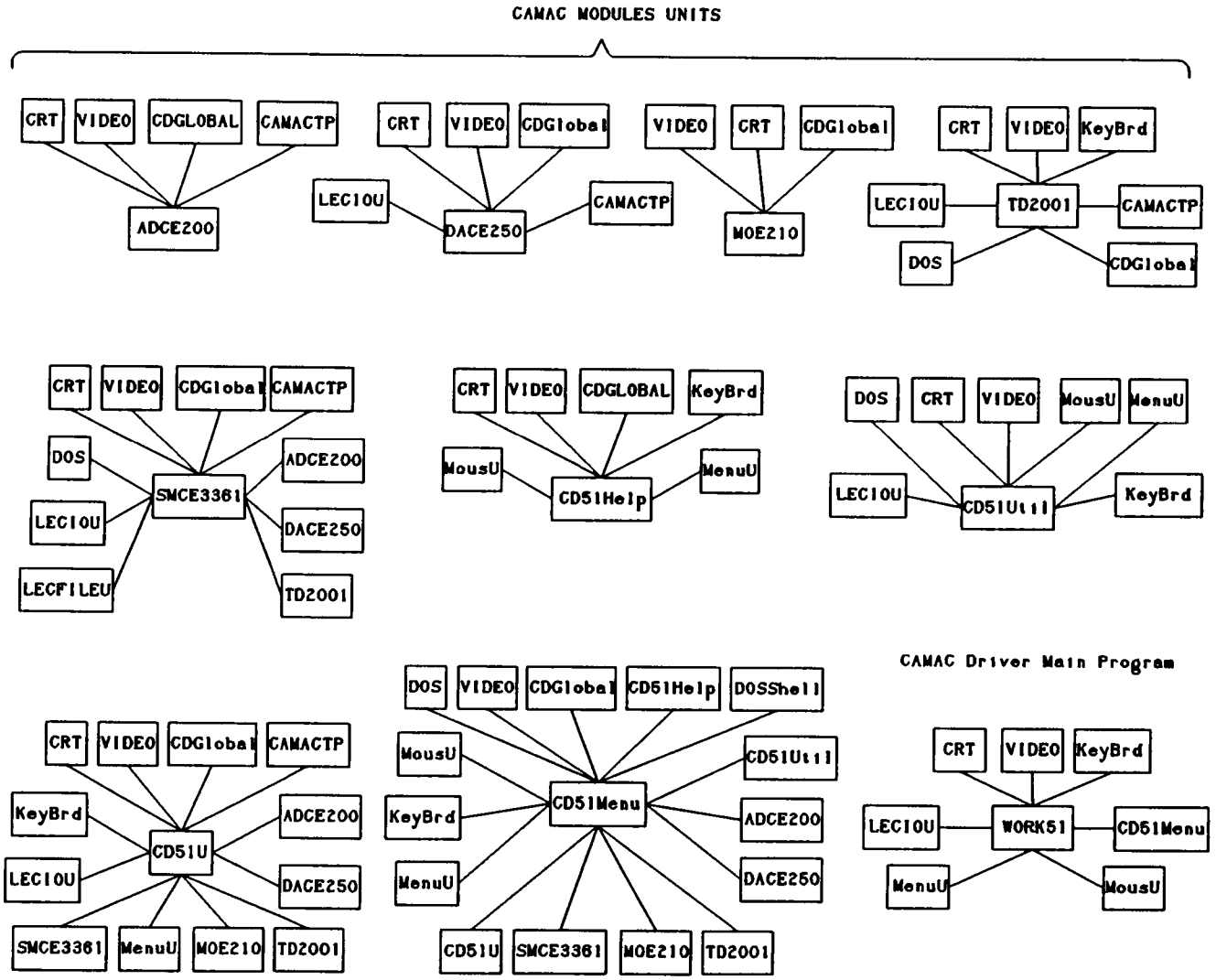

Fig. 3.14. (Continued)

from the original published code to include case sensitive help, "hot keys" and mouse control, while the Keybrd unit was expanded to provide mouse control. The remaining units were written to provide support for each of the CAMAC modules, and to provide the means to share data between units of the program, as well to provide some useful tools for data processing.

The flow control of the program is depicted in Fig. 3.15. After initializing several global variables and the program menus, the program identifies and locates each of the modules supported and loads up the user definable menu for external programs and routines from an ASCII file, as well as providing the user to optionally specify external programs to be used for some of the data acquisition and diagnostics tasks. The user is then presented with the main menu of the program, which is shown in Fig. 3.16.

An important feature of version 5.1 of CDriver is the inclusion of expandability of the program through a user-definable menu table (selections F8 and F9). This enables the execution of external programs such as file and disk managers, and data analysis programs, from a menu of up to 14 items. This limitation can be easily overcome by the use of an external program that extends the menu tree up to any level desired. In addition, access to the DOS command line (selection F6) is provided through the Turbo Pascal Exec procedure (available through the DOS unit).

Three menu options were of vital interest for the data acquisition. One of the menu options used often was "Monitor (REALTIME) [F7]". This option executes the external program defined as MONITOR in the configuration sequence. The program used for the experiments, also written in Turbo Pascal and called NOVOTIME, provides a realtime graphics display of the digitized signal, providing an immediate analysis of the response of the photoelectron signal due to changes to the laser beam, alkali source or applied voltages. Both the time and signal scales can be changed through keyboard commands. The main purpose of the NOVOTIME program is the dynamic display of the digitized signal, emulating a single channel digital oscilloscope, but also provides diagnostic tools like averaging of several digitized sweeps of the electronic signal, and a method to store and display a "snapshot" of the instantaneous or averaged signal under some conditions, which could then be compared with the signal under other conditions.

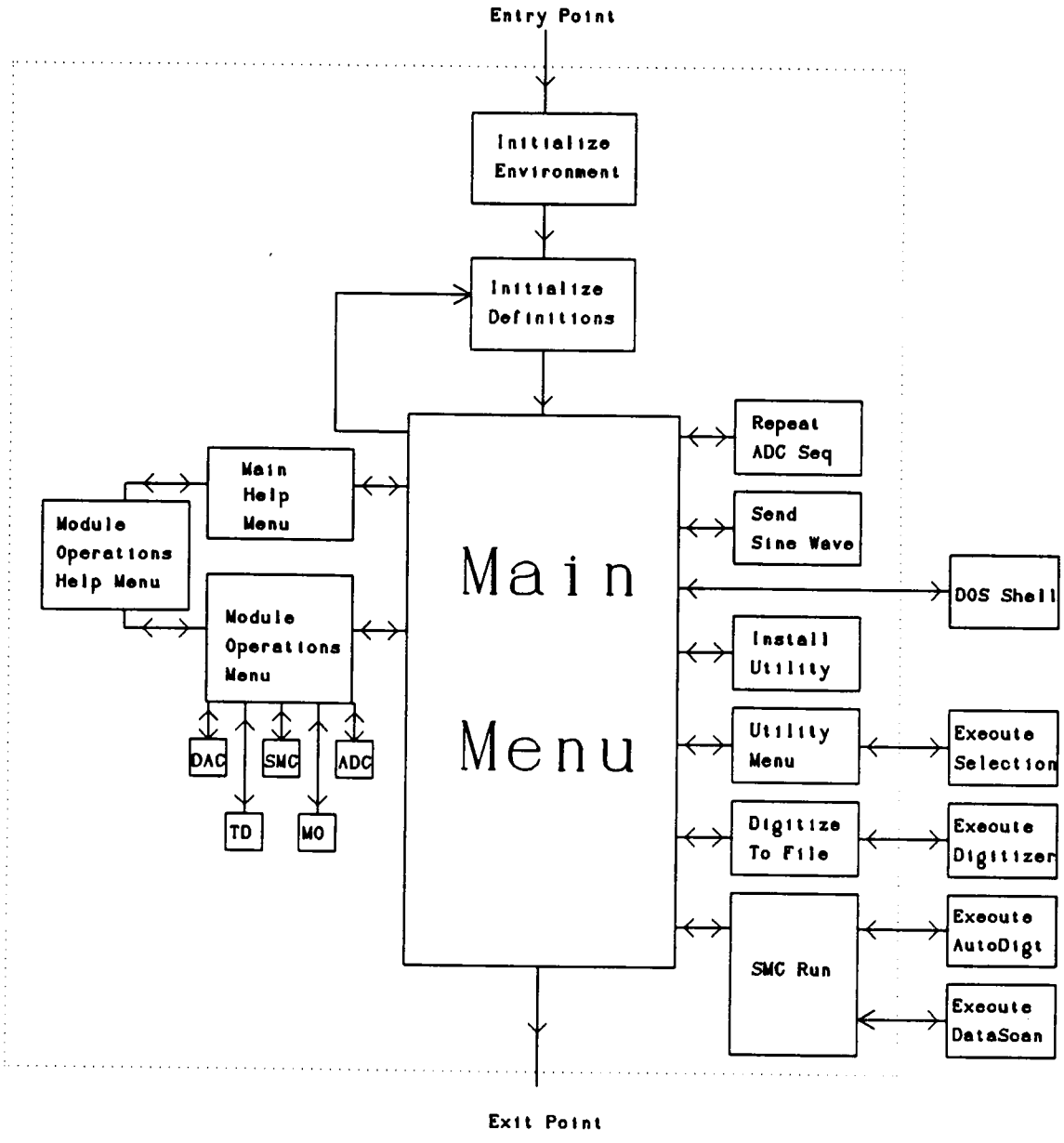

Fig. 3.15. Flow diagram of the CAMAC driver program.

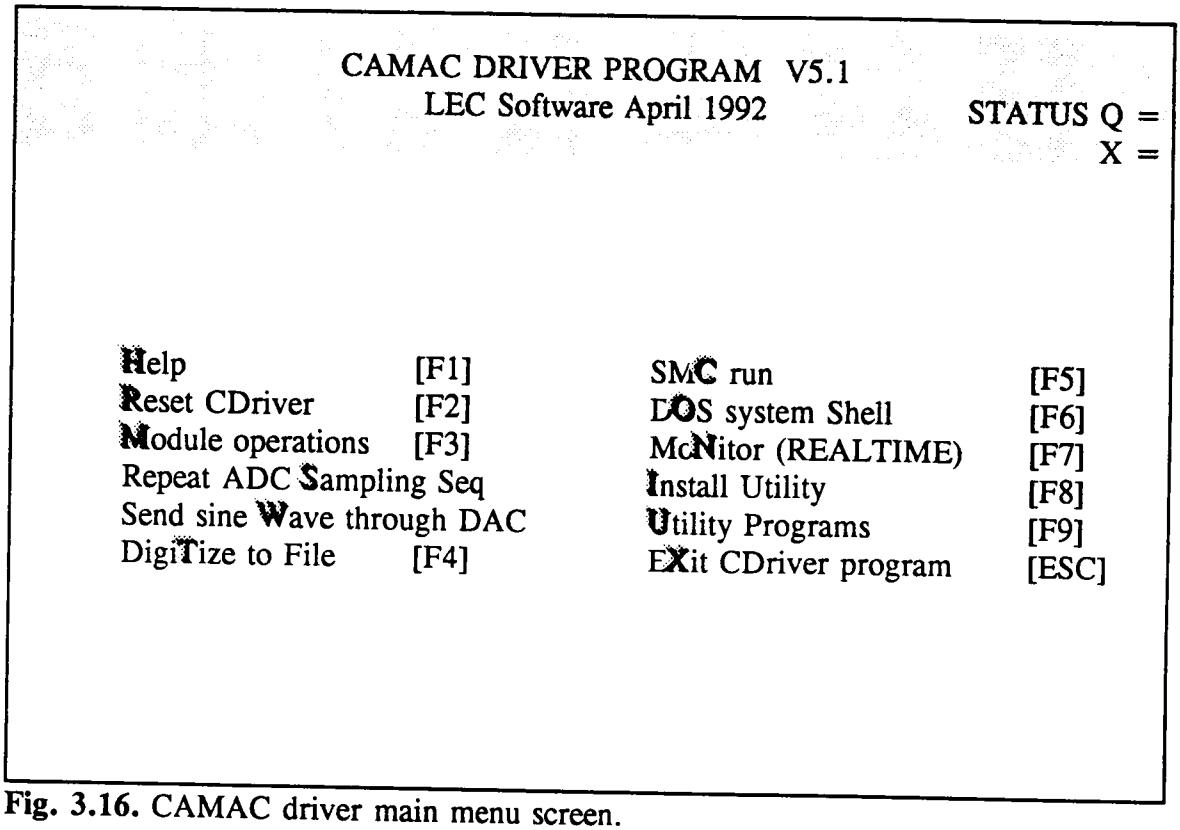

Fig. 3.16. CAMAC driver main menu screen.

NOVOTIME also provides a command to store the averaged signal to disk as an ASCII text file. Averaged signals under different conditions can be saved by specifying different file names. Two weaknesses of the NOVOTIME program are the relatively slow clearing of the graphics display, and lack of any statistical analysis of the signal. Great effort was spent in order to achieve the fastest signal display, determining that the best method to erase the old data was to overwrite it with the background color of the video monitor.

Another useful menu option is the "Digitize To File [F4]" ran the external program defined as the DIGITIZER in the Cdriver configuration sequence (selection F2). The digitizing program used was also written using TURBO Pascal V6.0, and its final rendering was called NEWDIGT. It includes code to determine the location of the DSP Technology TD-2001A module in the CAMAC crate by looking for the module's ID (id number 2001). If the location of the module can not be determined, maybe due to the CAMAC crate being powered off or to improper installation of the module, NEWDIGT halts execution, and indicates that the transient digitizer module can not be found. If

found, NEWDIGT allows the user to choose the output file name, the number of laser sweeps to digitize and to average, as well as to choose which digitized channel range to be saved in the output file, *i.e.*, data clipping, and to choose whether statistics on the averaged signal are to be determined. These parameters can also be defined at the DOS command line. Signal averaging is done by simple addition of each digitized sweep to a buffer array and then division by the total number of sweeps taken. One additional feature of NEWDIGT is the determination of the standard deviation for each point of the averaged digitized signal. This is accomplished by using one more data array to store the sum of the squares for each channel of the digitized signal and by using the formula for the standard deviation for each digitized channel[56,57]

$$\sigma_i = \sqrt{\frac{1}{N-1}\sum_j^N x_{ij}^2 - \frac{N}{N-1}\bar{x}_i^2}\ , \tag{3-2}$$

where the index i is used to refer to each channel, and the index j is used to refer to the jth digitized sweep. N indicates the total number of sweeps averaged, x_{ij} denotes the ith channel of the jth sweep, and $\bar{x}_i$ the represents the average of the ith channel

$$\bar{x}_i = \frac{1}{N}\sum_j^N x_{iJ}\ . \tag{3-3}$$

The square of the standard deviations given by equation (3-2) denote the variance of sampling of the digitized signal due to fluctuations in the laser power, atom densities, and fluctuations in the timing of the laser trigger. These standard deviations were used throughout the data analysis, which consisted in measuring the peak height against the baseline of the data, as well as an integration of the peak channels.

The third useful menu option for the data acquisition is "SMC run [F5]", which is used to measure the photoelectron angular distributions. This option automates the data acquisition by coding an algorithm for the turning of the double Fresnel rhomb (see

section B-2) and the averaging of the digitized signal scans. The averaging is done by an automated, streamlined version of NEWDIGT program, called AUTODIGT, that stores the averaged signal in an ASCII file. This file is then analyzed by the program designated as the SCANNER in the configuration sequence, creating a histogram of the photoelectron angular distribution. This program allows the measurement of a particular channel, termed "peak channel", and integration over a range of channels, referred as "integral". The channel can be locked, or the scanner program allowed to determine the extremum of the data. In order to measure peak heights and integrals the scanner program determines the baseline of the data by averaging the channels at the trailing end of the digitized average. The histogram contains information relating the peak height, integral, the channel corresponding to the maximum of the digitized signal, and the average of the baseline to the total number of steps offset from the starting position.

The "SMC run" routine permits the user to specify by how many steps to rotate the stepper motor (defining the angular separation between measured angles, using 0.45° per step), the number the angles to sample (defining the bounds of the angular scan), the direction and the number of passes over the angular region being scanned, the number of laser sweeps to average, and optionally whether standard deviations for each channel are to be computed. The program also lets the user specify the output file name where the histogram of the photoelectron angular distributions will be kept, and whether the average of the sweeps for each angle will be saved after the angular scan. In order to make the output data files compatible with most data analysis software and packages, all data files are saved in ASCII format, *i.e.*, text format. Data analysis software will be discussed in the following section.

Several modes of operation can be used to improve data acquisition speed. The best mode is to use a disk caching to improve disk access, and to store the data files in a ramdrive, *i.e.*, active memory, since RAM accesses are faster than hard disk accesses. After completion of a run, the histogram file and the files containing the averages of the sweeps for each angle were copied to more permanent magnetic media.

C-3 Data Analysis Software

Data analysis of the photoelectron angular distributions was done initially using programs written for the data analysis, and subsequently using a commercial spreadsheet program (Borland, Quattro Pro, versions 1, 3, and 4). This permitted to analyze the data systematically, and uniformly.

Analysis of the data consisted in rescaling the PEADs corresponding to the same resonant state by normalizing the data to the value of the signal at 90°, *i.e.*, determining the fraction of photoelectrons scattered into a particular angle relative to those scattered parallel to the polarization of quantization. This procedure is equivalent to assigning weights to the data, since then average of the PEADs is given by

$$I_{ave}(\theta) = \sum_{i}^{runs} s_i I_i(\theta), \qquad (3\text{-}4)$$

where the factors s_i are given by the normalization factors for each PEAD and the total number of PEADs averaged.

The average of the PEADs given by equation (3-4) was then fitted to equation (2-31) using linear least squares methods. Fitting of the experimental data and calculation of the asymmetry parameters were done using the spreadsheet program, both by using the built−in regression analysis feature, and by typing formulas to carry out the fitting analysis. The latter was done to make use of the standard deviations for each channel provided by the data acquisition program. The formulas used for fitting the data and calculation of the standard deviations were derived using the principles of data regression and error propagation given by Bevington.[57]

The spreadsheet program permits the creation of a data analysis "template" used to fit the experimental data, making it possible to analyze PEADs from different states by simply importing the ASCII files into the proper cells. Recalculation of the template

is done automatically, except for the built−in linear regression feature that requires that it be recalculated each time the data is modified.

Finally, the fitted data was exported to a scientific graphing system (Jandel Corporation, SigmaPlot 5.0) for graphing the data analysis results. The graphing system also permits the creation of a graphing "template" that can be used to uniformly plot the experimental data.

CHAPTER IV

EXPERIMENTAL RESULTS

A. PHOTOELECTRON ANGULAR DISTRIBUTIONS

A-1. *n*S STATES OF CESIUM

The photoelectron angular distributions for resonantly enhanced multiphoton ionization, using (2 + 1) photons, via the *ns* state, with n = 8, 9, 10, 12, were measured and reported[50] using the experimental setup depicted in figure 3.3. An earlier version of the data acquisition software was used that did not compute the standard deviation for each channel of the averaged signal. The resonant states lie between 24317.17 cm^{-1} (3.01 eV) and 29666 cm^{-1} (3.67 eV). Since the parity of the ground and *ns* states are the same, two photons were needed to excite the ground state to the *ns* state, and one more photon to ionize the atom, *i.e.*, (2 + 1) ionization. In these experiments, three coherent photons from the same laser pulse were used to excite and to ionize the atom. This required choosing the photon energy to be half the energy of the resonance state being studied. The final photoelectron energy that results from using (2 + 1) REMPI through these *ns* states is in the region of the Cooper minimum of the photoionization cross section, enabling the observation of spin-orbit coupling effects in single channel photoionization.

By using the second harmonic of the Nd:YAG laser to pump different laser dyes with wavelength outputs in the range corresponding to the energies of the photons needed for these experiments (see Table III-1), it was possible to excite the ground (6*s*) state and to resolve the resonantly enhanced photoionization signal for several excited *ns* states of cesium, with n=8-14. The (2 + 1) REMPI angular distributions are given by equation (2-30) with j=1/2, and are thus characterized by only one asymmetry parameter, β_2.

Unfortunately, the proximity of the 7*f* (at 29148 cm^{-1}) state to the 11*s* (at 29130 cm^{-1}), compounded by the presence of the 5*d* state (14597 cm^{-1}) about halfway

between the ground state and the 11*s* state introduce complications in resolving the 11*s* state resonance. The $6s \rightarrow 5d$ transition is quadrupole allowed, increasing the probability of a transition to the 7*f* state, as well as increasing the cross section for photoionization through this channel. The spectral resolution of the 13*s* and 14*s* states using (2 + 1) REMPI is made difficult by the presence of the Cooper minimum in the photoionization cross section, making the measured signals very weak. The states were located by tuning the dye laser while applying a −100 V pushing voltage. For the experiments on the 13*s* state, without a pushing voltage, it was necessary to use the laser at maximum power (to increase the photon density), and a fast gain amplifier (to increase the electronic signal). The 14*s* state could not be observed without a pushing voltage. Attempts were made to measure the contribution to the photoionization signal from any other coupled states by measuring PEADs at slightly above and below, as well as at right on the photon wavelengths for the 13*s* state. The average of the measured off-resonance PEADs was subtracted from the measured resonant PEAD in order to single out contributions of the 13*s* states to the measured PEAD. For completion, results are presented for the experimental measurement of the PEADs for the 11*s* and the 13*s* states of cesium, although we emphasize the inconclusiveness of these results.

The results of averaging several experimental measurements for each state measured are shown in figures 4.1 through 4.6. The data for each distribution was fitted to equation

$$I(\theta) = a_0 + \sum_{i=1}^{j+1/2} a_{2i} P_{2i}(\cos\theta) , \qquad (4\text{-}1)$$

with $j = 1/2$ using the linear least squares algorithm presented by Bevington[57] and Quattro Pro. The asymmetry parameters are calculated by the ratio $\beta_2 = a_2/a_0$. Because of the shape of the angular distribution for the 13*s* state, the data was also fitted using equation (4−1) with $j = 3/2$. Both fits are shown in figure 4.6 for comparison.

Ideally, the axis of quantization, given by the axis of polarization, would experimentally be well defined and consistent for all states, and a linear fit of the data

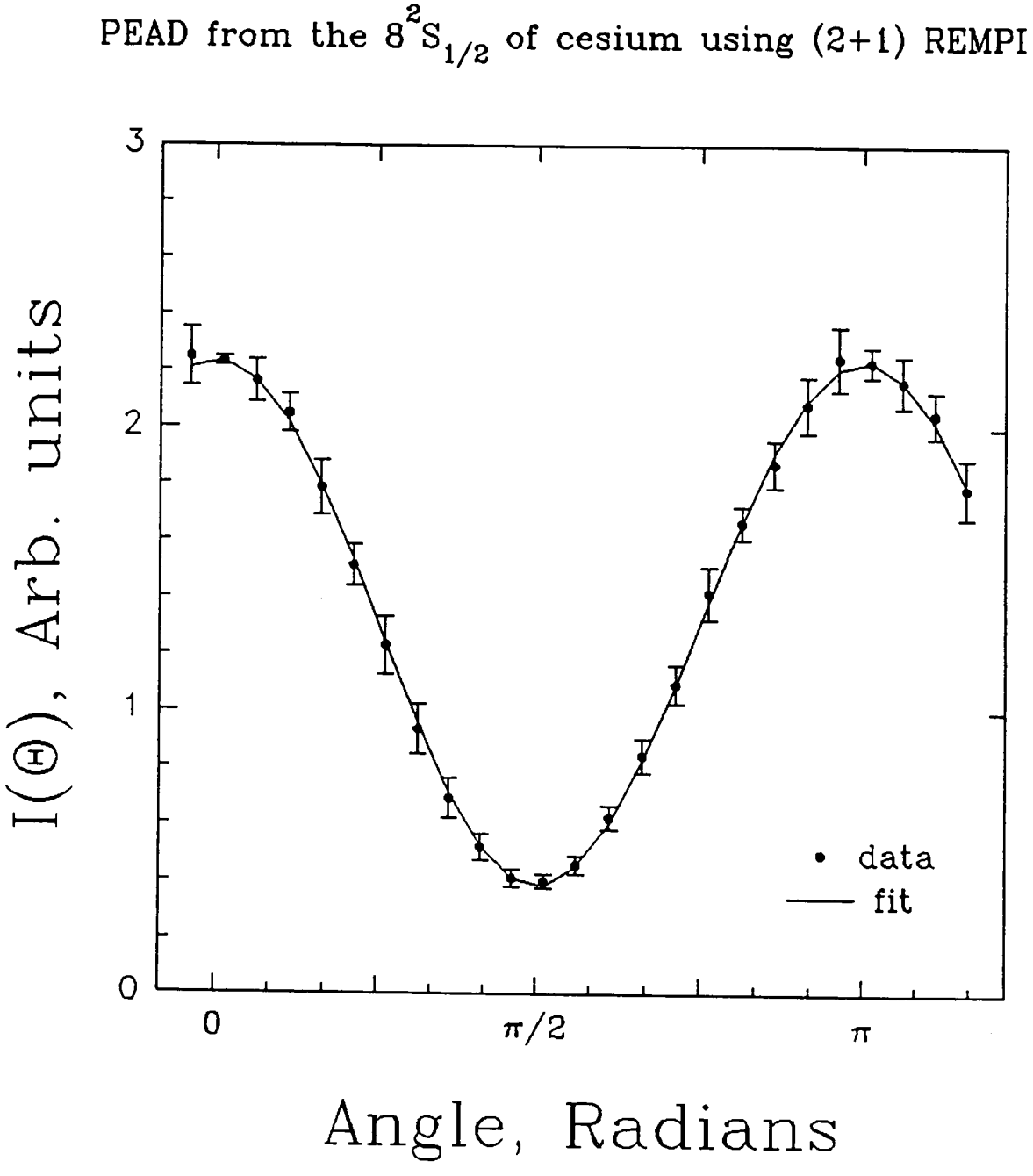

Fig. 4.1 PEAD for the $8^2S_{1/2}$ state of cesium. The uncertainties σ are obtained from averaging 8 measurements of the angular distribution and performing a least squares fit of the data.

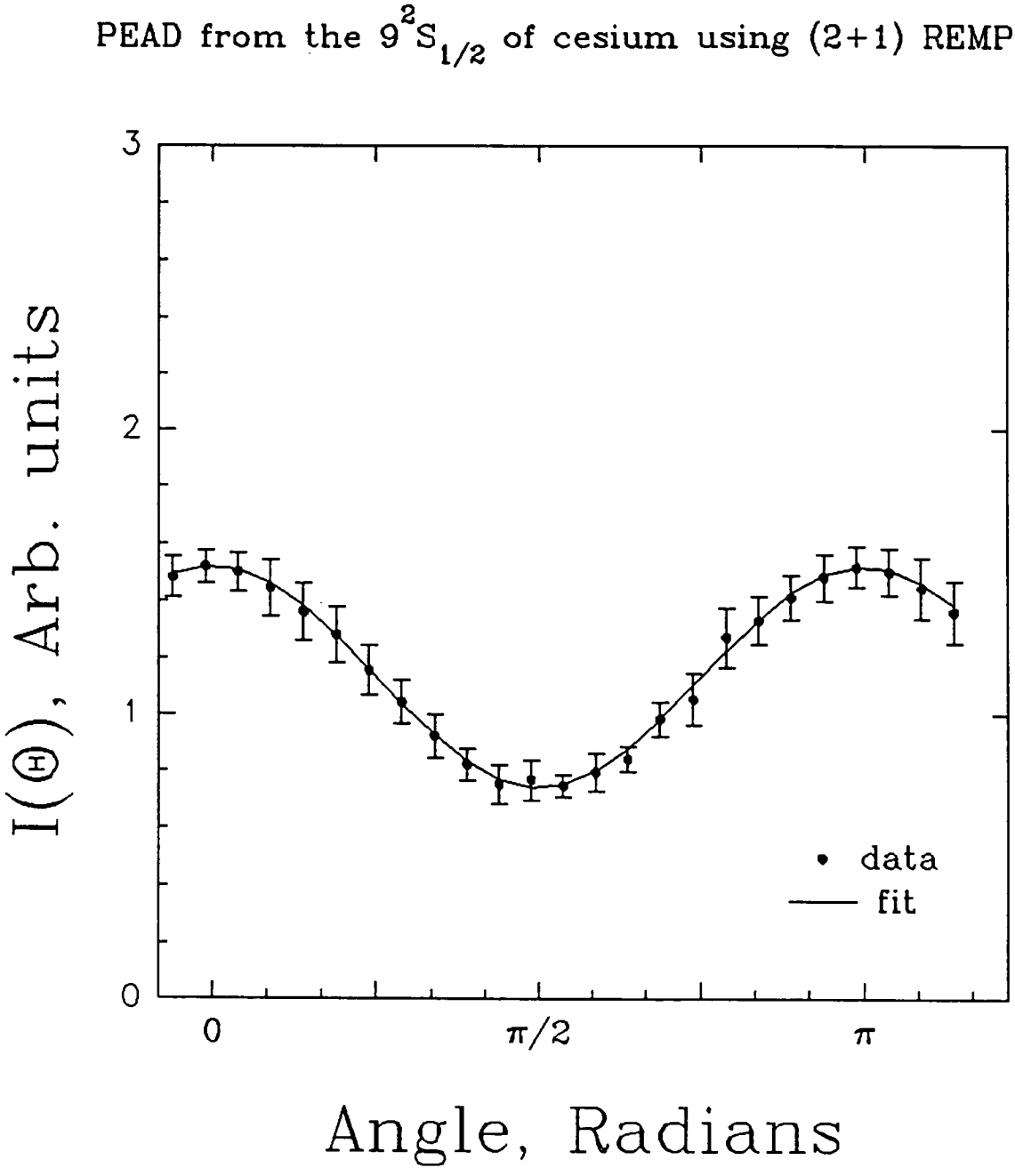

Fig. 4.2 PEAD for the $9^2S_{1/2}$ state of cesium. The uncertainties σ are obtained from averaging 6 measurements of the photoelectron angular distribution and performing a least squares fit of the data.

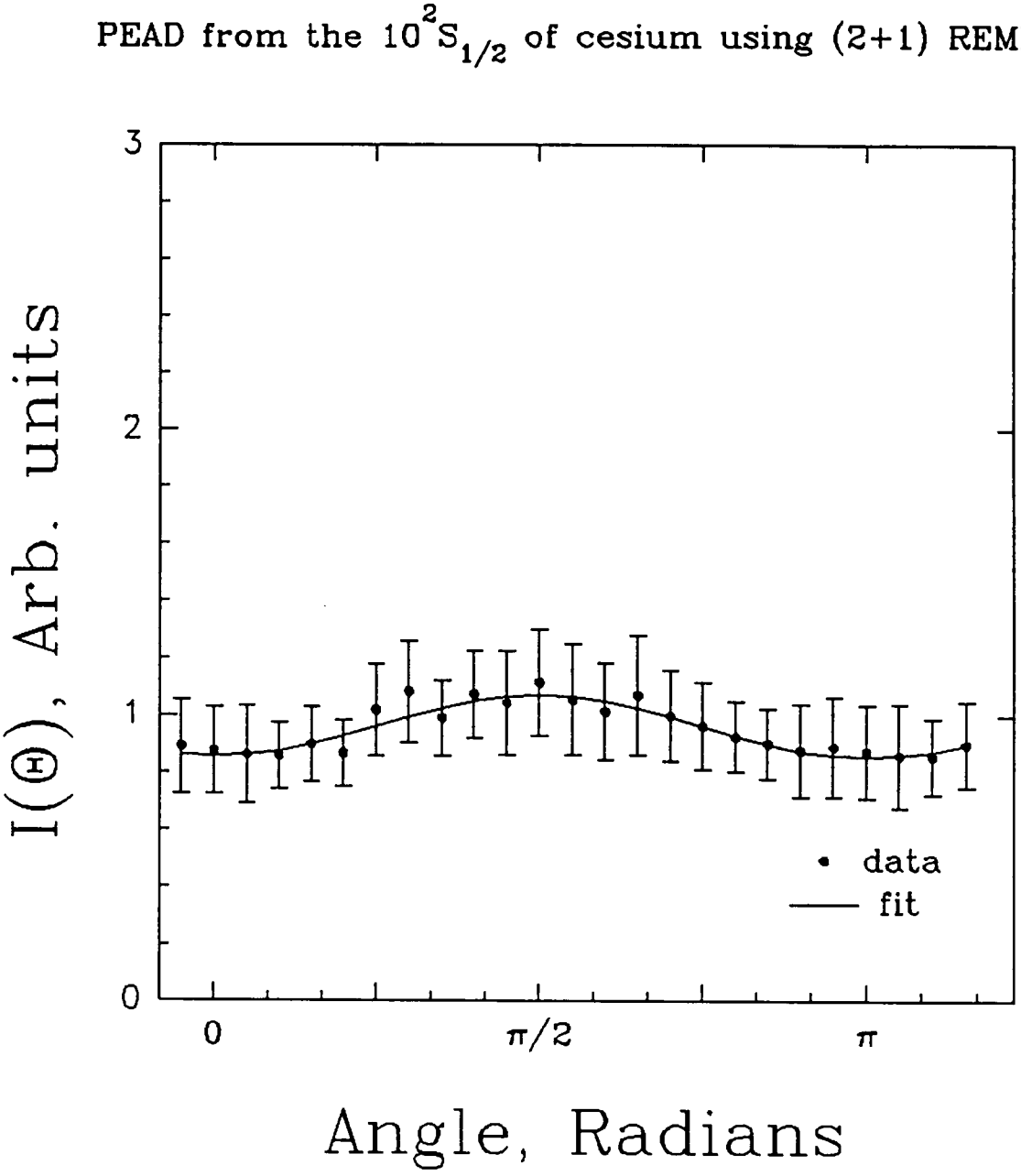

Fig. 4.3 PEAD for the $10^2S_{1/2}$ state of cesium. The uncertainties σ are obtained from averaging 4 measurements of the angular distribution and performing a least squares fit of the data.

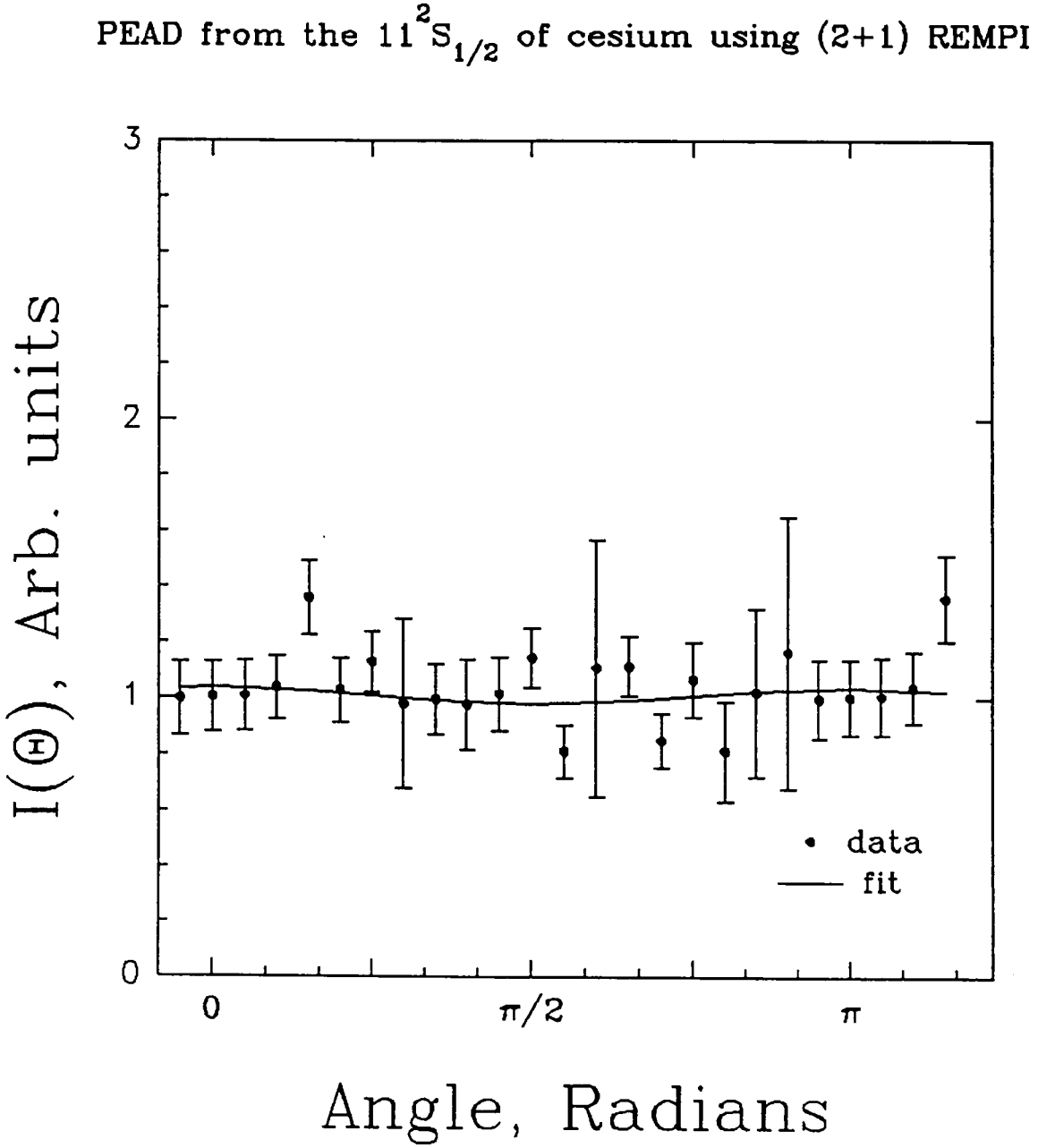

Fig. 4.4. PEAD for the $11^2S_{1/2}$ state of cesium. The uncertainties σ are obtained from averaging two measurements of the angular distribution and performing a least squares fit of the data. The PEAD is affected by the proximity of the $7f$ level, and the presence of the $5d$ level halfway between the ground state and the $11s$ state.

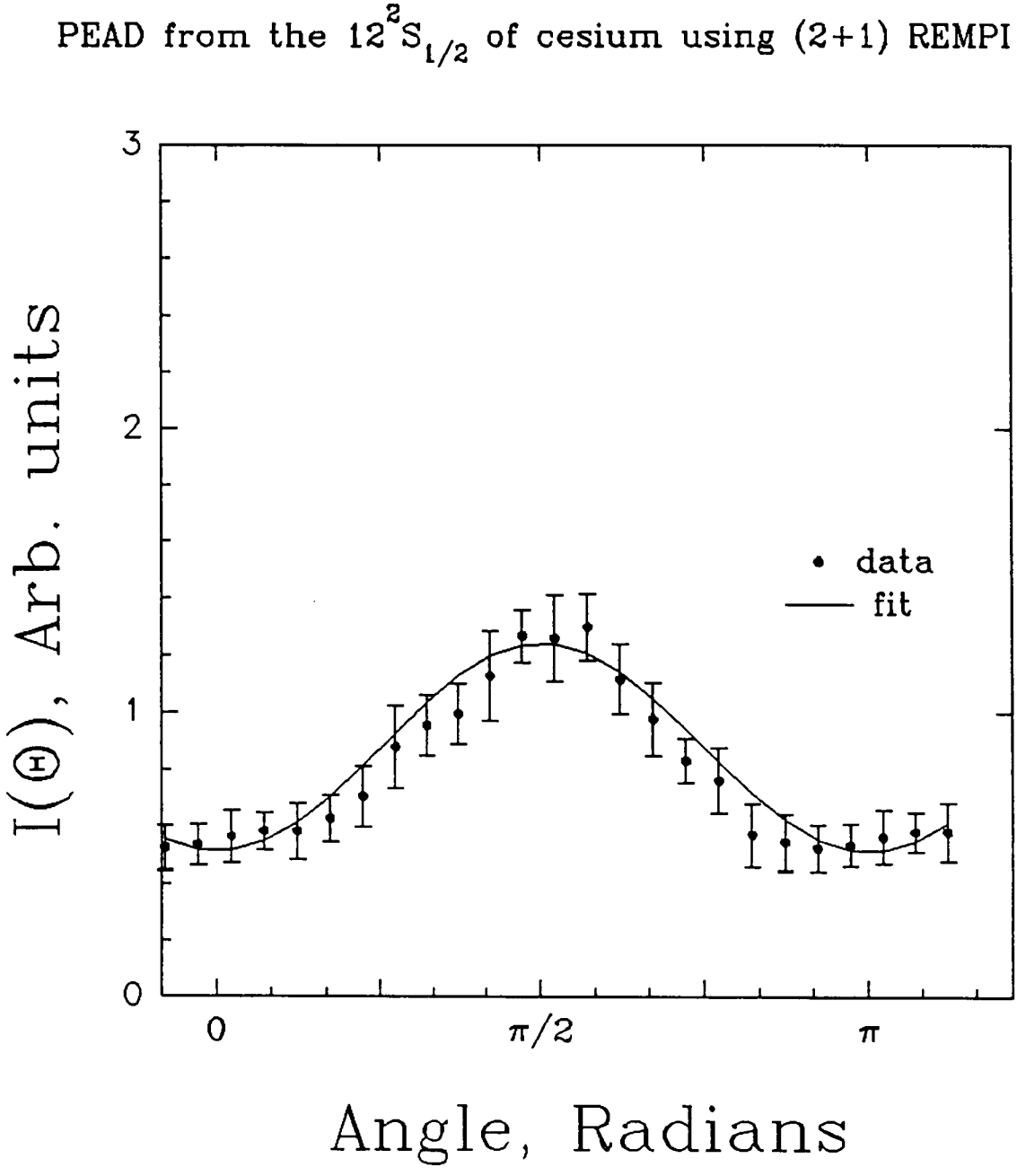

Fig. 4.5 PEAD of the $12^2S_{1/2}$ state of cesium. The uncertainties σ are obtained from averaging 6 measurements of the angular distribution and performing a least squares fit of the data.

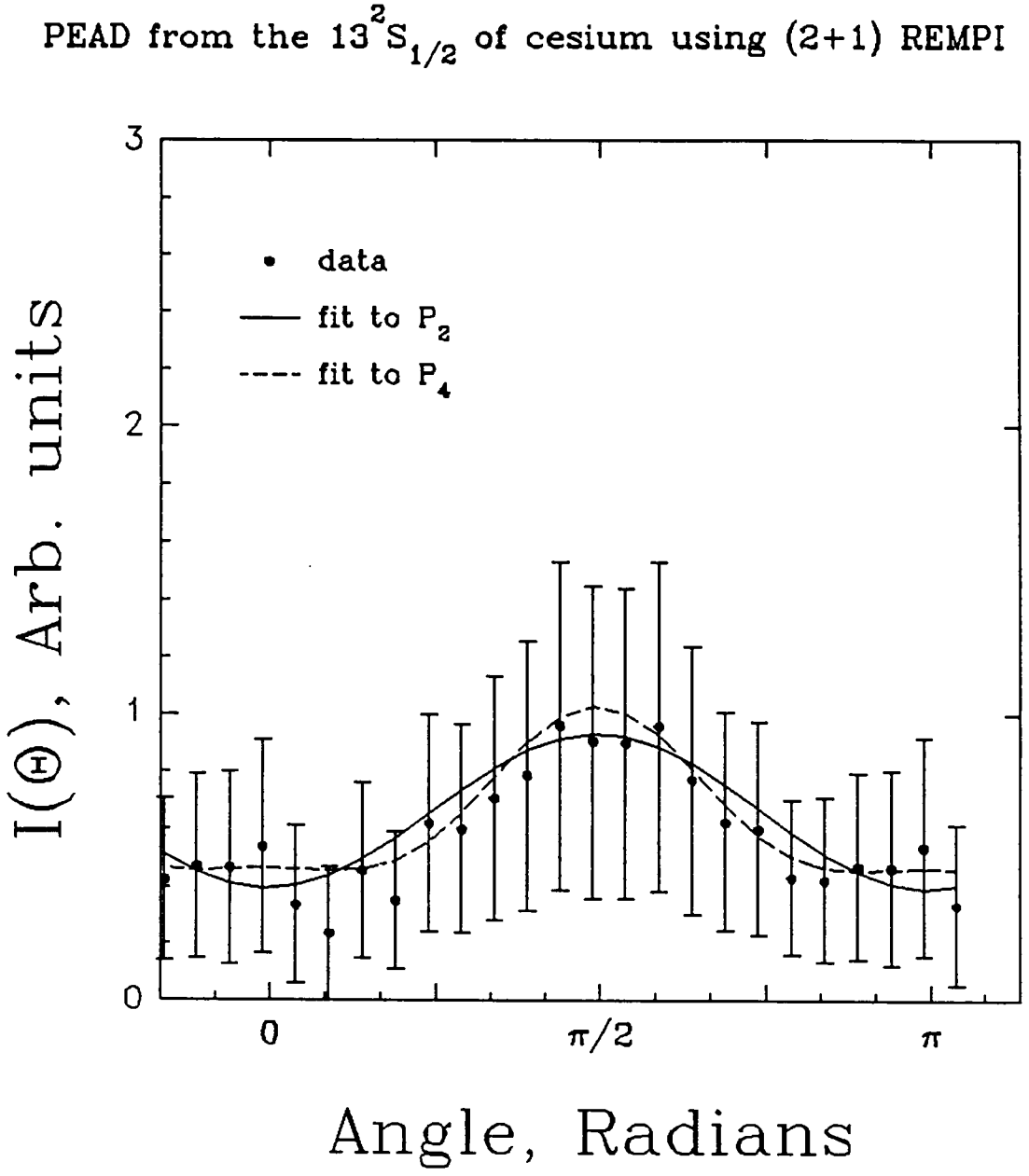

Fig. 4.6 PEAD for the $13^2S_{1/2}$ state of cesium. The uncertainties σ are obtained by averaging 5 measurements of the PEAD and performing a least squares fit to the data.

would suffice. However, since the laser beam typically traversed several optical accessories, small variations of the optical axis were to be expected due to slight misalignment of turning prisms and focusing lenses. Therefore, an angular offset was allowed during the fitting of the data to account for any variations of the optical axis from the starting angular position. The fits were characterized by calculating

$$\chi^2 = \sum_{angles} [I_{fit}(\theta) - I_{exp}(\theta - \theta_{offset})]^2 \ . \qquad (4\text{-}2)$$

The angular offset was varied, and the fitting of the data repeated until the smallest χ^2 was found. This parameter is minimized by the linear least squares method where the only degrees of freedom are given by the asymmetry parameters, acting as coefficients of the fitting functions, in this case, the Legendre Polynomials. The uncertainties of the β_2 were determined using the propagation of error techniques given by Bevington[57] and the standard deviations for the average of several PEAD measurements.

Table IV-1 summarizes the results of the (2+1) REMPI PEAD measurements,

Table IV-1 Summary of experimental results, *n*S states. The energies for the levels were obtained from C. Moore[58] and Weber and Sansonetti.[59]

State	Energy cm^{-1}	Wavelength, nm	Electron energy, cm^{-1}	Time of flight, ns	Asymmetry parameter, β_2
8s	24317	822	5069	106	1.235 ± 0.052
9s	26910	743	8959	80	0.517 ± 0.044
10s	28300	706	11043	72	-0.144 ± 0.081
11s	29130	686	12288	68	NA[a]
12s	29666	674	13092	66	-0.488 ± 0.054
13s	30036	666	13647	65	NA[b]
14s	30298	660	14040	64	NA[b]

[a] PEAD complicated by the one photon quadrupole coupling of the ground state with the $5^2D_{5/2}$ and the proximity of the energy level with the 7^2F level.

[b] PEAD complicated by being in the region of the Cooper minimum and low signal levels.

of flight. The photoelectron kinetic energy is determined by subtracting the binding energy from the total energy absorbed by the electron, which in the case of (2 + 1) absorption is three times the photon energy $h\nu_1$. This energy can also be determined from measurements of the time of flight of the photoelectrons and knowledge of the length of the time-of-flight tube. The electron energies measured from the time-of-flight analysis were in good agreement with those calculated using the ionization potential of cesium, *i.e.*: IP(Cs) $- 3h\nu_1$.

The asymmetry parameters β_2 were found to vary from $+1.23$ for the $8s$ state to about -0.5 for the $12s$ state. The least squares analysis of the data for the $11s$ and $13s$ respectively yielded β_2 values of 0.033 ± 0.099 and -0.475 ± 0.208. A fourth order analysis of the data for the $13s$ state produced $\beta_2 = -0.597 \pm 0.294$ and $\beta_4 = 0.189$.

As was previously noted, in the absence of spin-orbit coupling in the continuum, β_2 is predicted to be energy independent and equal to 2. The observed variation is attributed to relativistic (spin-orbit) effects in the photoionization continuum. Inclusion of relativistic effects results in radial matrix elements which depend upon the total angular momentum j' of the continuum wave function. This allows for more than one photoionization channel into the continuum. From equation (2-72) we have for the asymmetry parameter β_2 of the angular distribution for photoionization of an s state in which the outgoing electron has an $\epsilon p\,\frac{1}{2}$ and $\epsilon p\,\frac{3}{2}$ continuum waves[27,28,31]

$$\beta(\epsilon) = \frac{2R_{3/2}^2 + 4R_{1/2}R_{3/2}\cos(\delta_{3/2} - \delta_{1/2})}{2R_{3/2}^2 + R_{1/2}^2}, \tag{4-2}$$

where $R_{j'}$ is the radial matrix between the bound $n^2S_{1/2}$ and the continuum $\epsilon pj'$ partial wave, and $\delta_{j'}$ is the phase shift of the pj' partial wave. We may rewrite equation (4-3) by defining the ratio of the matrix elements $\chi = R_{3/2}/R_{1/2}$, and the difference of the phase shifts $\Delta = \delta_{3/2} - \delta_{1/2}$

$$\beta(\epsilon) = \frac{2\chi^2 + 4\chi\cos\Delta}{1 + 2\chi^2}. \tag{4-3}$$

We remark that this equation differs from equation (2-36.a) only in the sign of the relative phase of the ratio of the matrix elements χ. This reflects the fact that equation (4-2) includes radial matrix elements of the two relativistic pj ($j=1/2$ and $j=3/2$) partial waves, whereas equation (2-36.a) was defined using nonrelativistic d and s partial waves. Mathematically, these equations can be interpreted as mirror images of each other about $\chi = 0$.

Until recently, deviations from $\beta_2 = 2$ had been observed in only a few cases. Niehaus and Ruf[60] measured angular distributions for ionization of the $6s$ electron in mercury, finding that the asymmetry parameter β_2 was energy dependent, varying from 2 to 1.25. Several experimental and theoretical groups have studied the $5s \rightarrow \epsilon p$ photoionization of xenon[61-69,71] and $4s \rightarrow \epsilon p$ photoionization of krypton.[70] Two of these experiments[67,69] suggested a small "dip" in β_2 at a photon energy of $\sim$32 eV, in the region of the Cooper minimum. Two of the theoretical calculations[63,64] included relativistic effects but only considered single-hole ionization channels and predicted a much larger decrease in β_2 from the value 2 than was found experimentally; a third such calculation[66] predicted a smaller decrease in β_2 than was found experimentally. However, Tulkki[71] calculated asymmetry parameters which were in excellent agreement with experiment. These calculations included double-excitation channels on equal footing with the important single-excitation channels using the multichannel multiconfigurational Dirac-Fock (MMCDF) method. Thus in this case, the relativistic (spin-orbit) effects were obscured by the effects of multielectron excitation which are known to be present from studies of satellite spectra in the region of the xenon $5s$ Cooper minimum.[68]

Surprisingly, until very recently, only one measurement of a photoelectron angular distribution existed for an alkali-metal s state. Chaffee[9] reported in 1931 an asymmetry parameter β_2 approximately equal to 2 for photoionization of the ground state of potassium in the region of $\sim$2400 Å, although he did detect a small residual signal when the light polarization was perpendicular to the electron detection direction. Samson[72] performed a detailed analysis of the data obtained by Chaffee and concluded that β_2 was not 2 but closer to 1.55. The Chaffee data was again analyzed in 1979 by

Ong and Manson,[29] who obtained $\beta_2 = 1.5 \pm 0.3$. More recently, Yi-Yian and Elliot[10] measured the photoelectron angular distribution from the ground state of cesium using single photon ionization at various photon energies, covering the Cooper minimum. Their data agreed very well with the theoretical results of Norcross.[49] For comparison, the results of this work are compared with the experimental results of Yi-Yian and Elliot,[10] and the theoretical calculations by Norcross[49] in figure 4.7. The differences are not surprising, since the radial transition matrix elements between bound and continuum states, and thence the position of the Cooper minimum, depend largely on contributions from the $|\psi_{ns}\rangle$ wavefunction, and this function varies largely from state to state. Comparison of the experimental results of this dissertation with theoretical calculations by Pindzola[31] is made in figure 4.8.

A-2 *n*P States Of Cesium

The (1+1) resonantly enhanced photoelectron angular distribution for the $n^2P_{1/2}$ and $n^2P_{3/2}$ (n = 7 to 17) states of cesium were also measured using a similar experimental arrangement as that depicted in figure 3.3, with the single anode collector. PEAD measurements were taken using the data acquisition software that averaged several digitized signal sweeps and also calculated the standard deviation for each digitized channel. Several of the measurements of the higher *np* states were taken with a variation in the parallel plate separation in order to reduce the generation of background noise due to scattering of the laser beam. We also observed no significant difference in the PEAD measurements between having this plate in place and a grounded plate, as verified by PEAD measurements on the 8^2P_j state.

Typical photon energies for single photon excitation of the *n*P states were in the short wavelength region of the spectrum, ranging from 456 nm for the $7^2P_{1/2}$ level down to 328 nm for the $17^2P_{3/2}$ level. Typical digitized photoelectron signals are shown in figure 4.9. The resolution of the dye laser was not sufficient to resolve the fine structure

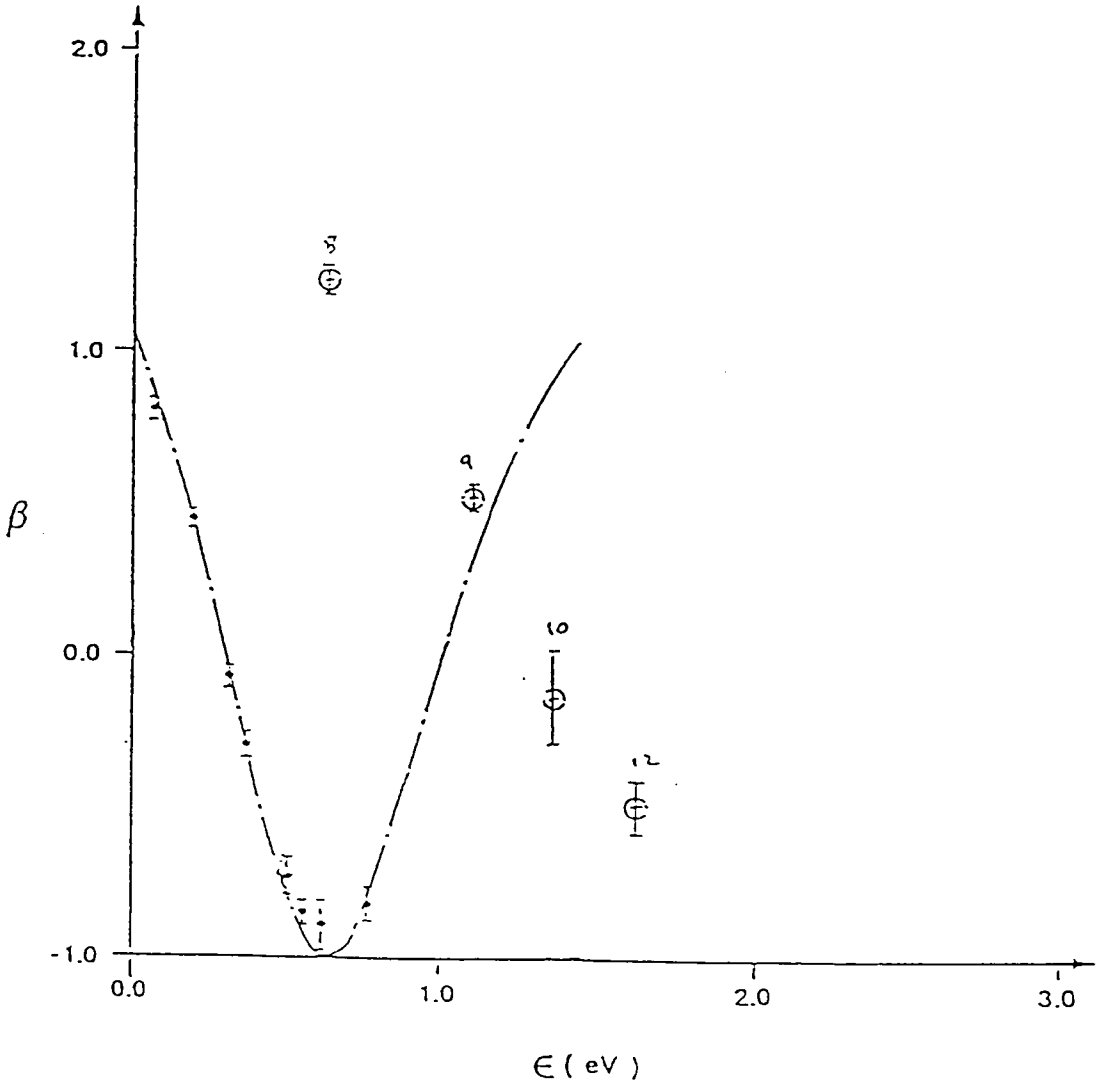

Fig. 4.7. Comparison of the experimental results of this work (open circles) with those of Yi-Yian and Elliot[10] (closed circle) and the theoretical calculations by Norcross[49] converted for the Fano parameter(dot-dashed line). *Graph courtesy of D. S. Elliot.*

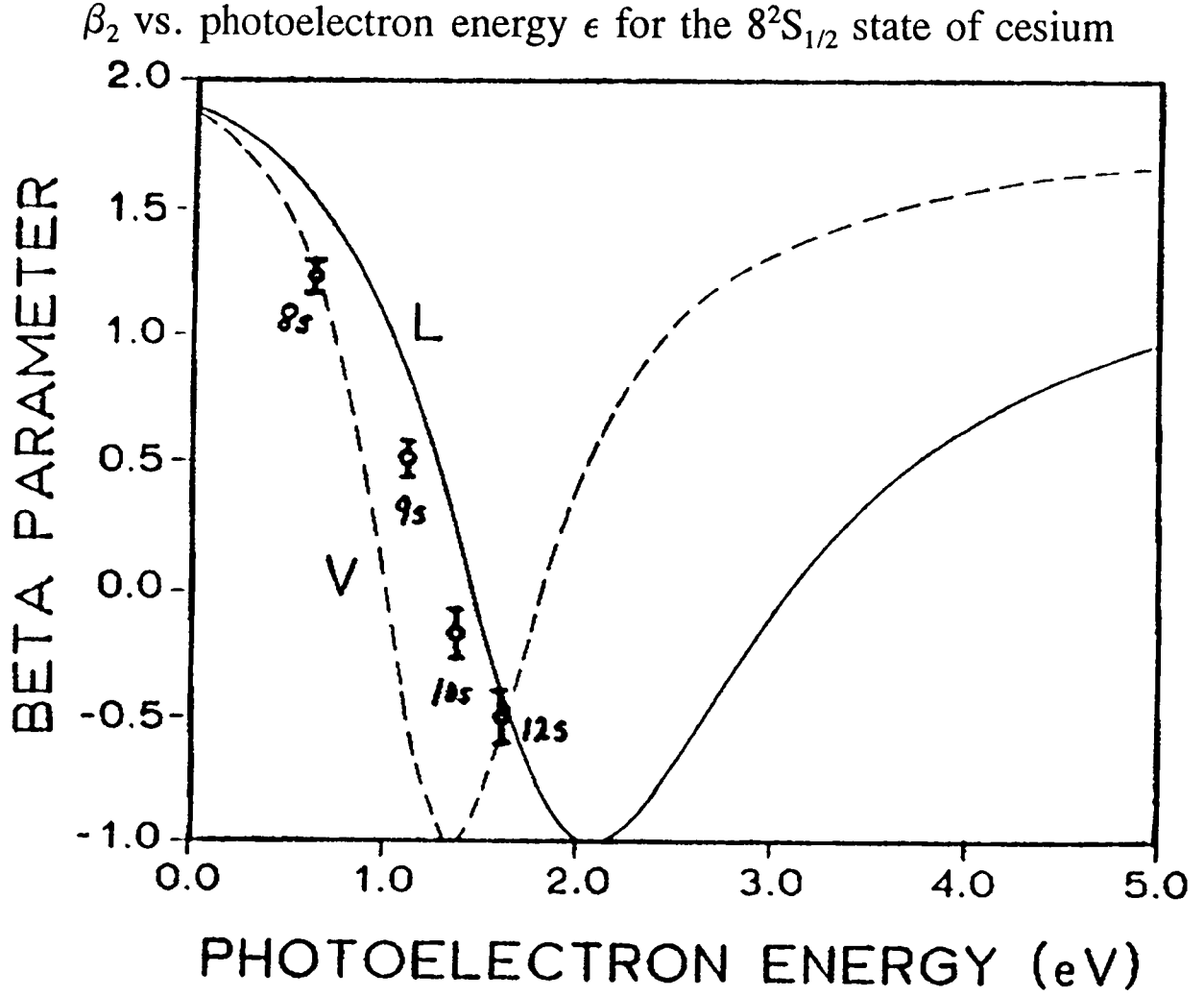

Fig. 4.8. Comparison of the experimental results of this work with theoretical calculations by Pindzola[31] for the 8*s* state of cesium. *Graph courtesy of M. S. Pindzola.*

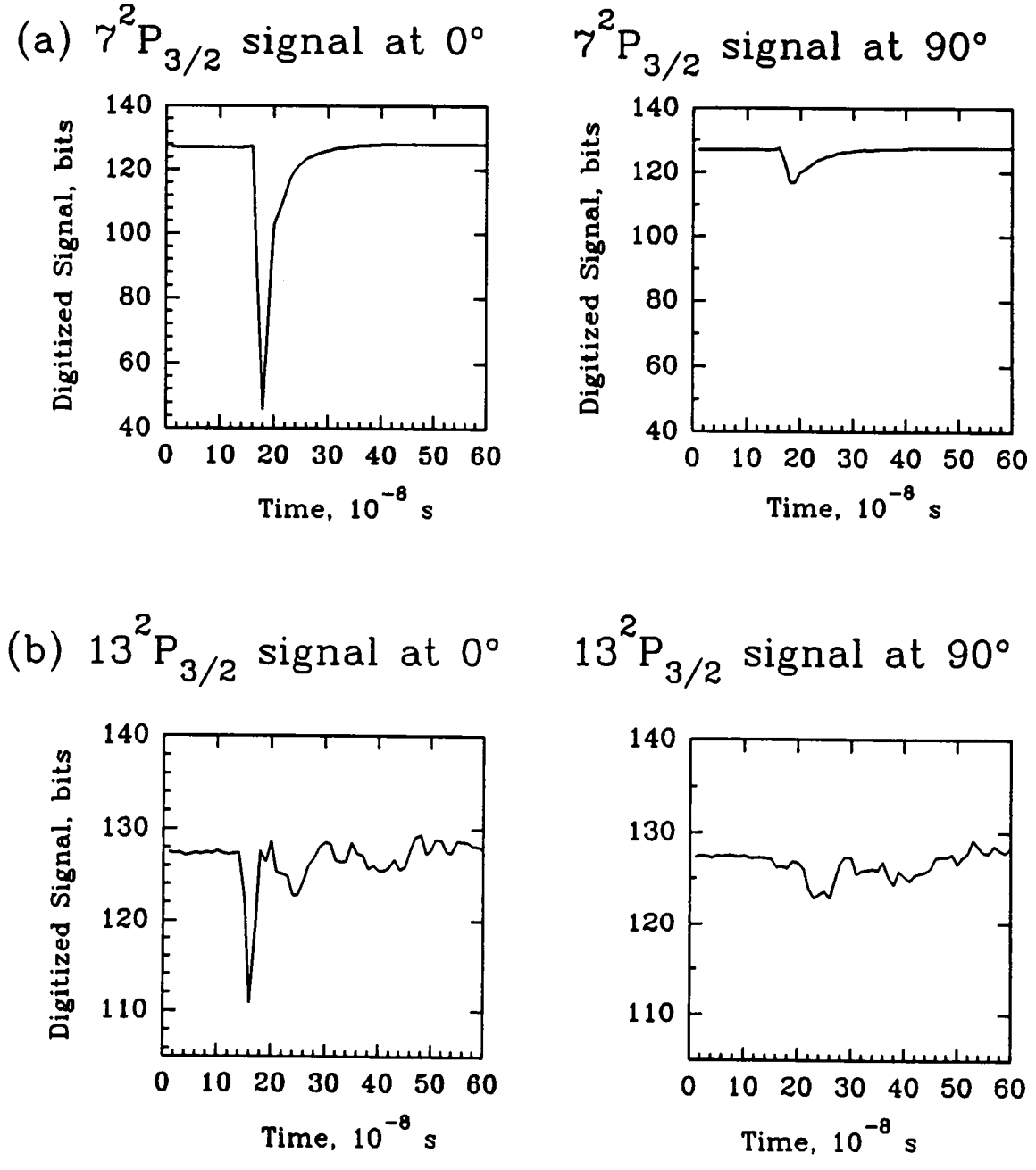

Fig. 4.9. Photoelectron signals from n^2P_j states. (a) $7^2P_{3/2}$, (b) $13^2P_{3/2}$ at 0° and 90°. The large, broad peaks at 40 ns, and 60 ns are due to background noise.

of the higher ($n > 12$) p energy levels. The PEADs shown corresponding to these higher np states therefore consists of a coherent superposition of two levels, although the ratio of the intensities of the resonances greatly favors the $j=3/2$ state.[73] In addition, a further complication in the measurement of these photoelectron angular distributions was due to the fact that cesium accumulated on the internal surfaces of the chamber, lowering the work function of the metals. Any stray near UV radiation striking these surfaces created background noise electrons with energies comparable to the energy of the photoelectrons. The noise was often large enough to overwhelm the photoelectron signal from the resonant state, as depicted in figure 4.9 (b). Since the background noise was not sensitive to small wavelength changes, it was possible to improve the data by subtracting on resonance the off-resonance ionization signal.

The (1+1) REMPI angular distributions from resonant $n^2P_{1/2}$ and $n^2P_{3/2}$ states are expected to be given by equation (2-30) with, respectively, $j = 1/2$ and $j = 3/2$, and are thus characterized by either only a β_2, or by a β_2 and a β_4 asymmetry parameters. The observed photoelectron angular distributions for the n^2P_j ($n = 7-12$) states, and respective fits using equation (4-1), are shown in figures 4.10-4.21. Resonant ^2P_j states of higher n (up to $n = 17$) were also observed and (1 + 1) REMPI PEADs of these states were also measured. However, results from these states were marred by the generation of background noise electrons and the corresponding PEADs were not fitted. Figures 4.22-4.26 show the experimental results for these states. Figure 4.27 shows a plot of the asymmetry parameters β_2 and β_4 versus quantum number n for each of the $n^2P_{3/2}$ and $n^2P_{1/2}$ sublevels measured and fitted in this work.

Photoelectron angular distributions for the np states ($n = 7, 8, 9$) of cesium have previously been measured by Compton, *et al.*[32] They fitted their data to a power series of cosines squares. Their resulting β_4 and β_2 asymmetry parameters were transformed to the β parameters corresponding to an expansion of Legendre polynomials, *i.e.*, equation (2−30), by using the transformation equations (2-34), and are compared with the results of this work in figure 4-28.

The asymmetry parameter β_2 for the (1 + 1) REMPI angular distribution from

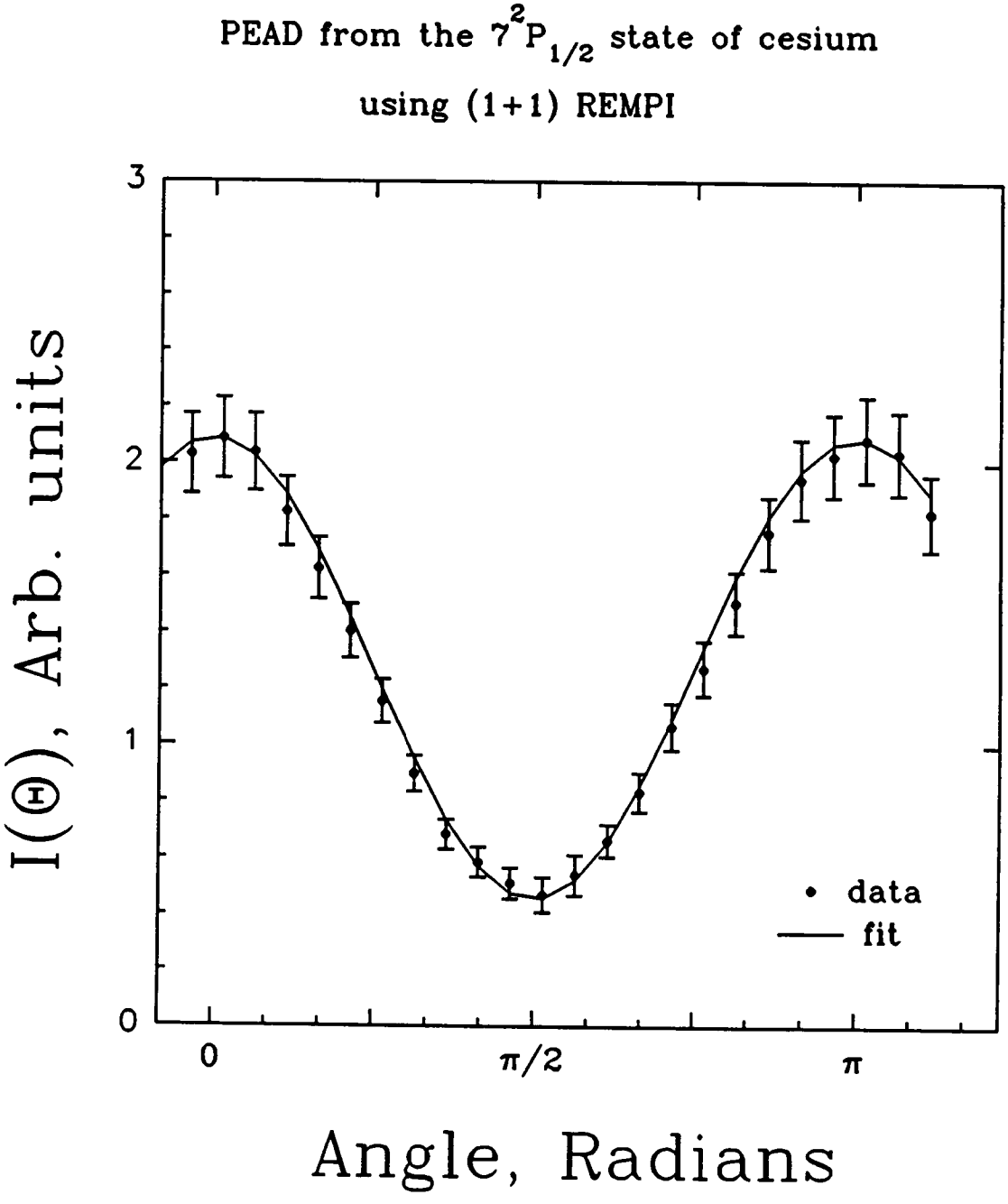

Fig. 4.10 PEAD from the $7^2P_{1/2}$ state of cesium. Standard deviations correspond to the average of 6 scans, each consisting of 100 laser pulses per angle.

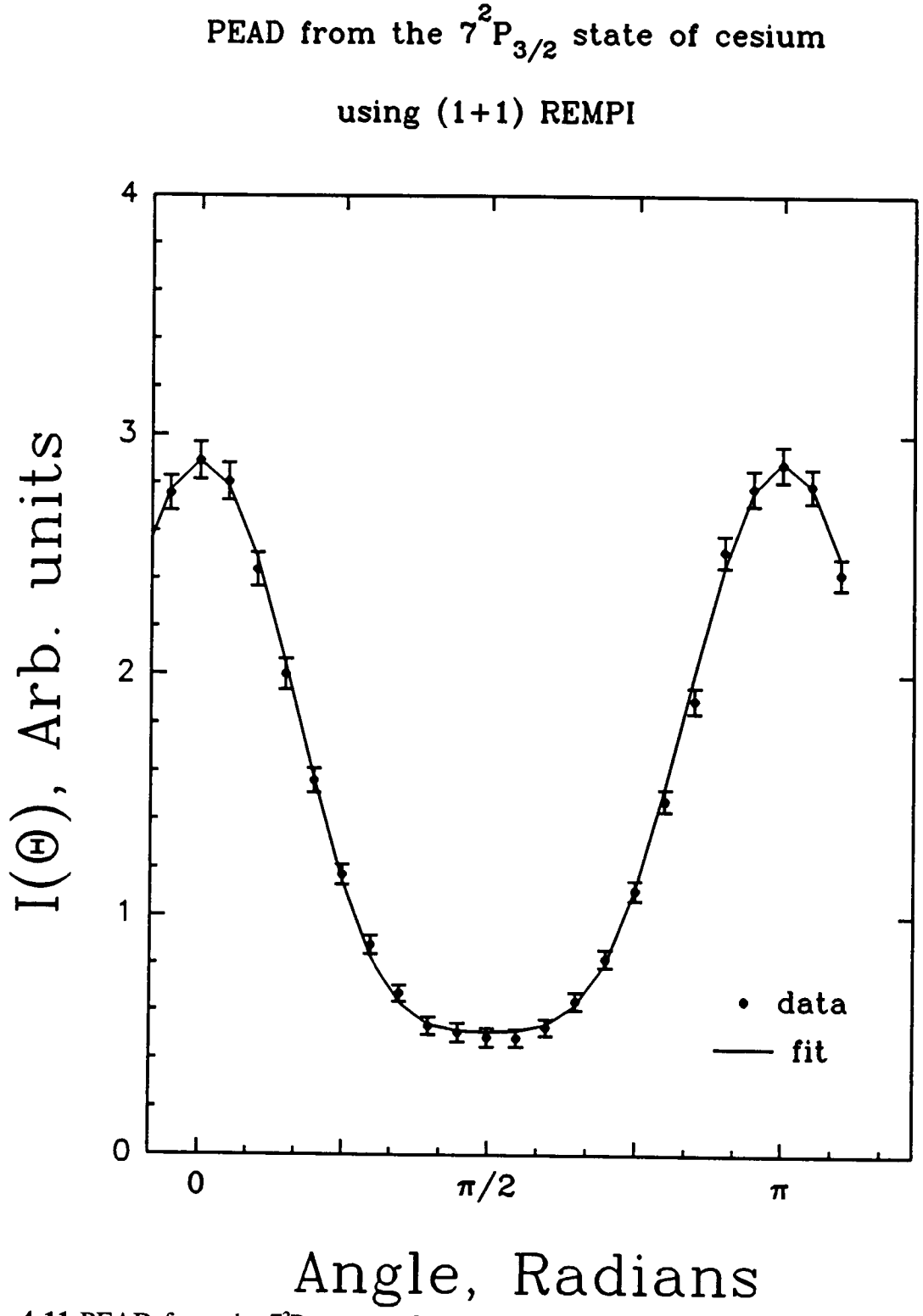

Fig. 4.11 PEAD from the $7^2P_{3/2}$ state of cesium. Standard deviations correspond to the average of 6 scans, each consisting of 100 laser pulses per angle.

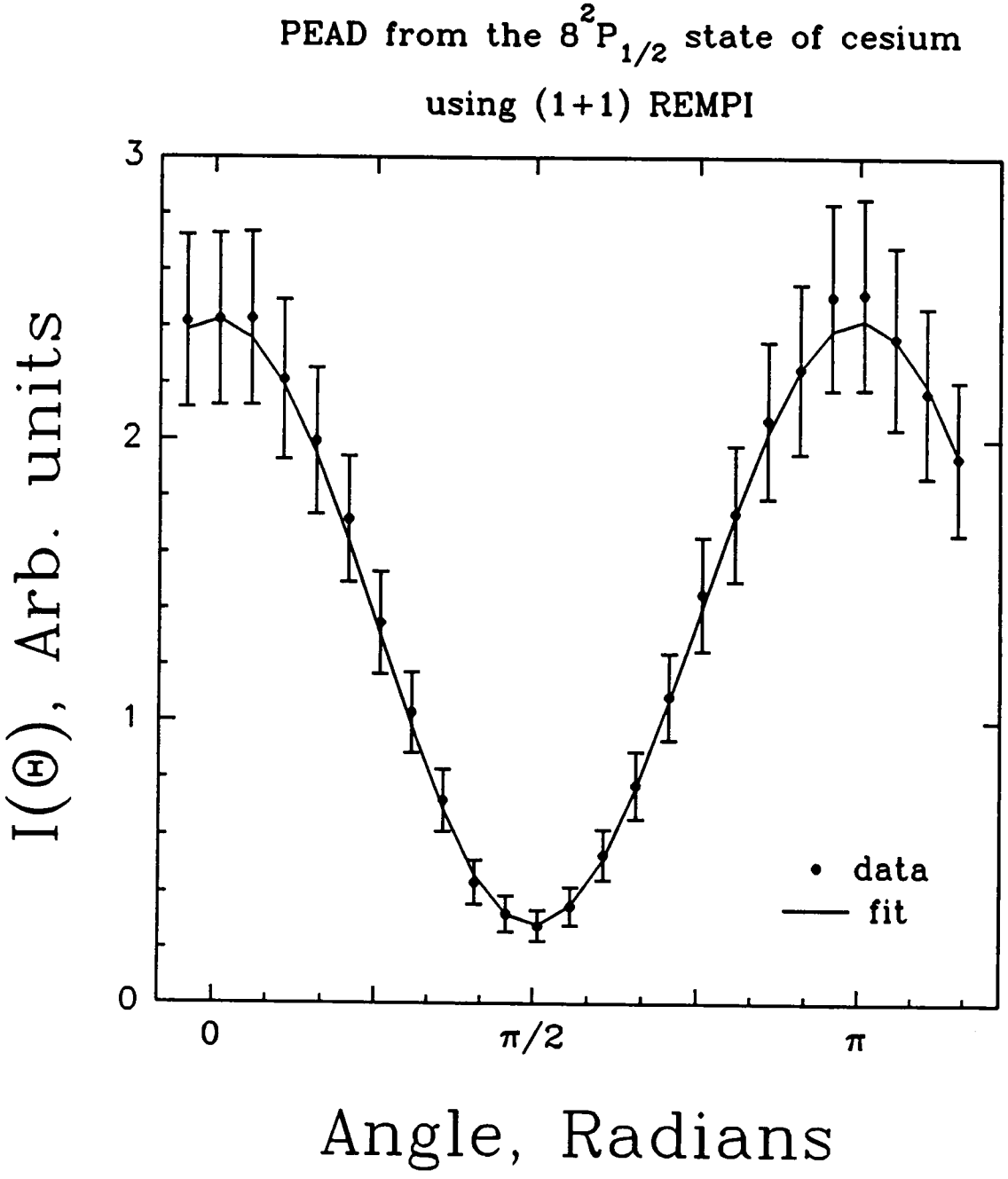

Fig. 4.12 PEAD for the $8^2P_{1/2}$ state of cesium. Standard deviations reflect the averaging of 6 scans, each consisting of 100 laser pulses per angle.

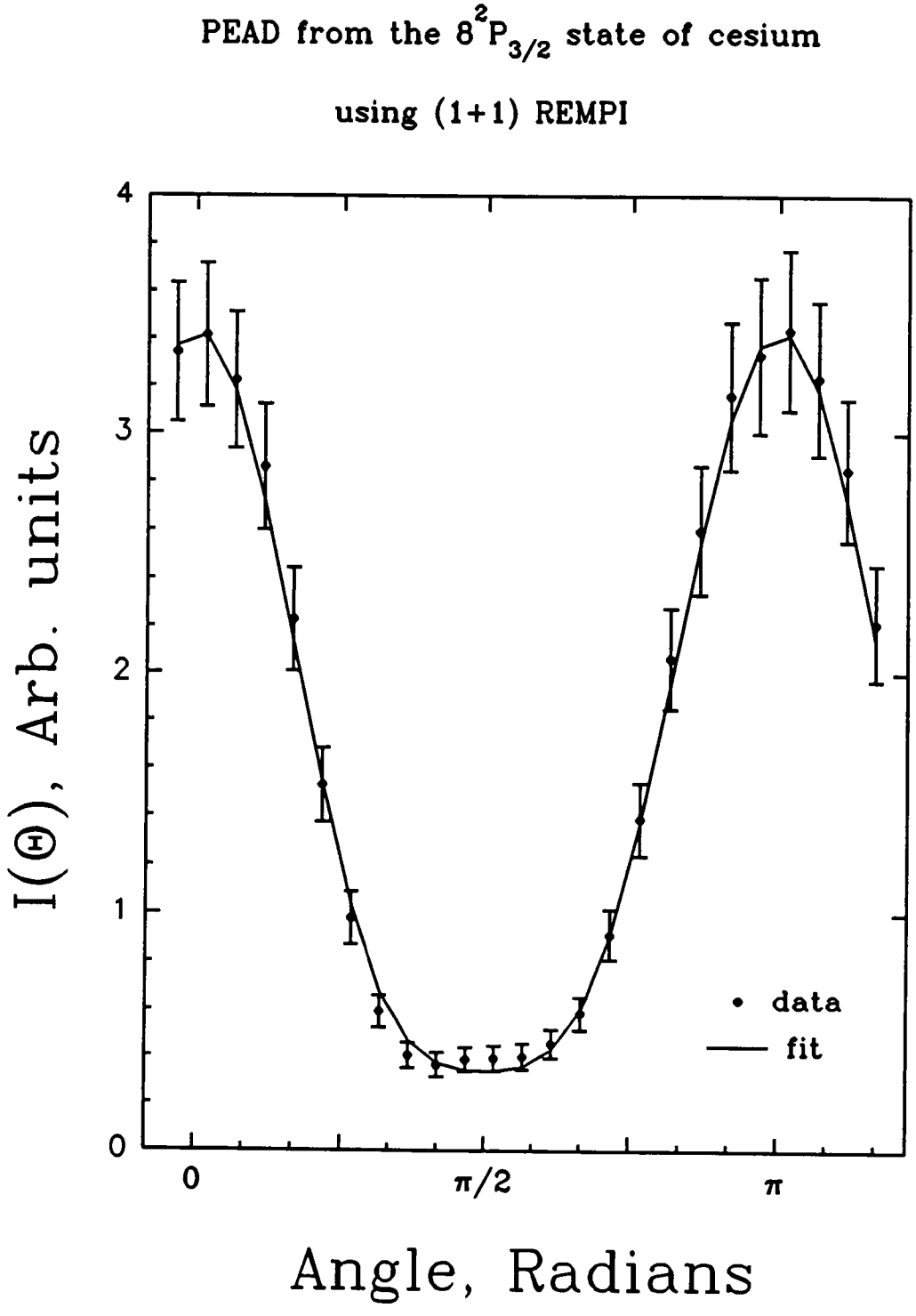

Fig. 4.13 PEAD from the $8^2P_{3/2}$ state of cesium. Standard deviations correspond to the average of 6 scans, each consisting of 100 laser pulses per angle.

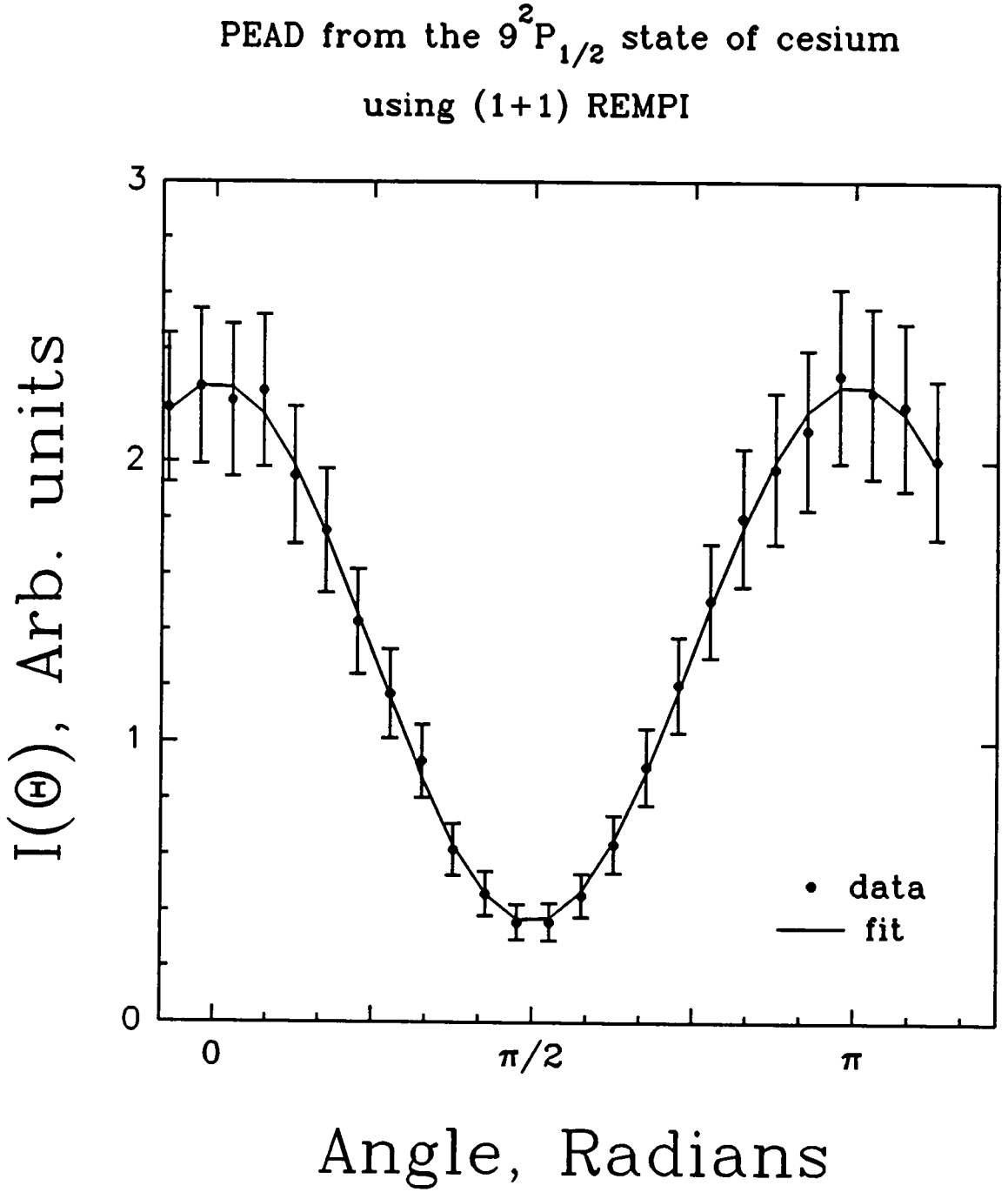

Fig. 4.14 PEAD for the $9^2P_{1/2}$ state of cesium. Standard deviation correspond to the average of 4 scans, each consisting of 100 laser pulses per angle.

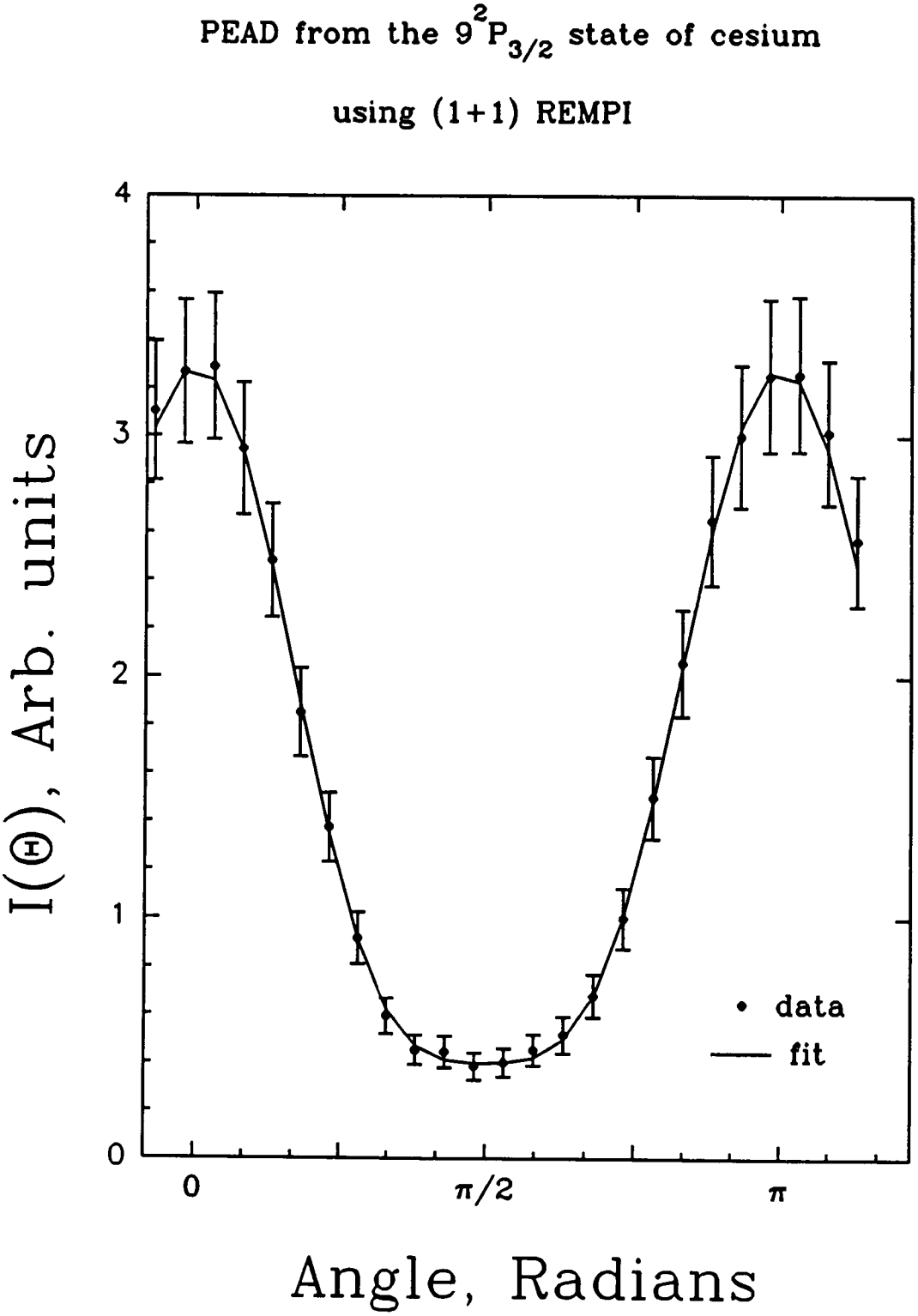

Fig. 4.15 PEAD for the $9^2P_{3/2}$ state of cesium. Standard deviation correspond to the average of 4 scans, each consisting of 100 laser pulses per angle.

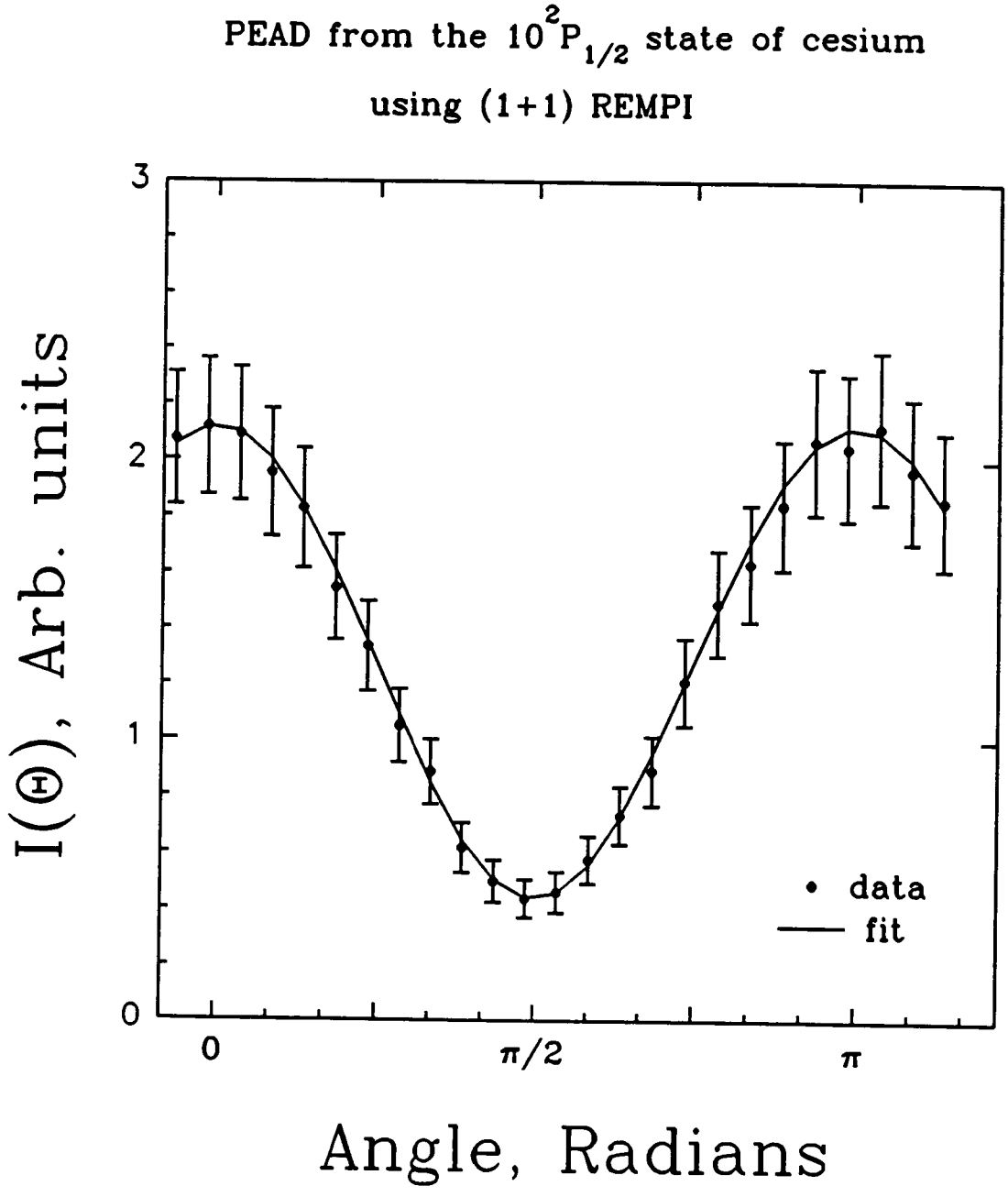

Fig. 4.16 PEAD for the $10^2P_{1/2}$ state of cesium. Standard deviation correspond to the average of 4 scans, each consisting of 100 laser pulses per angle.

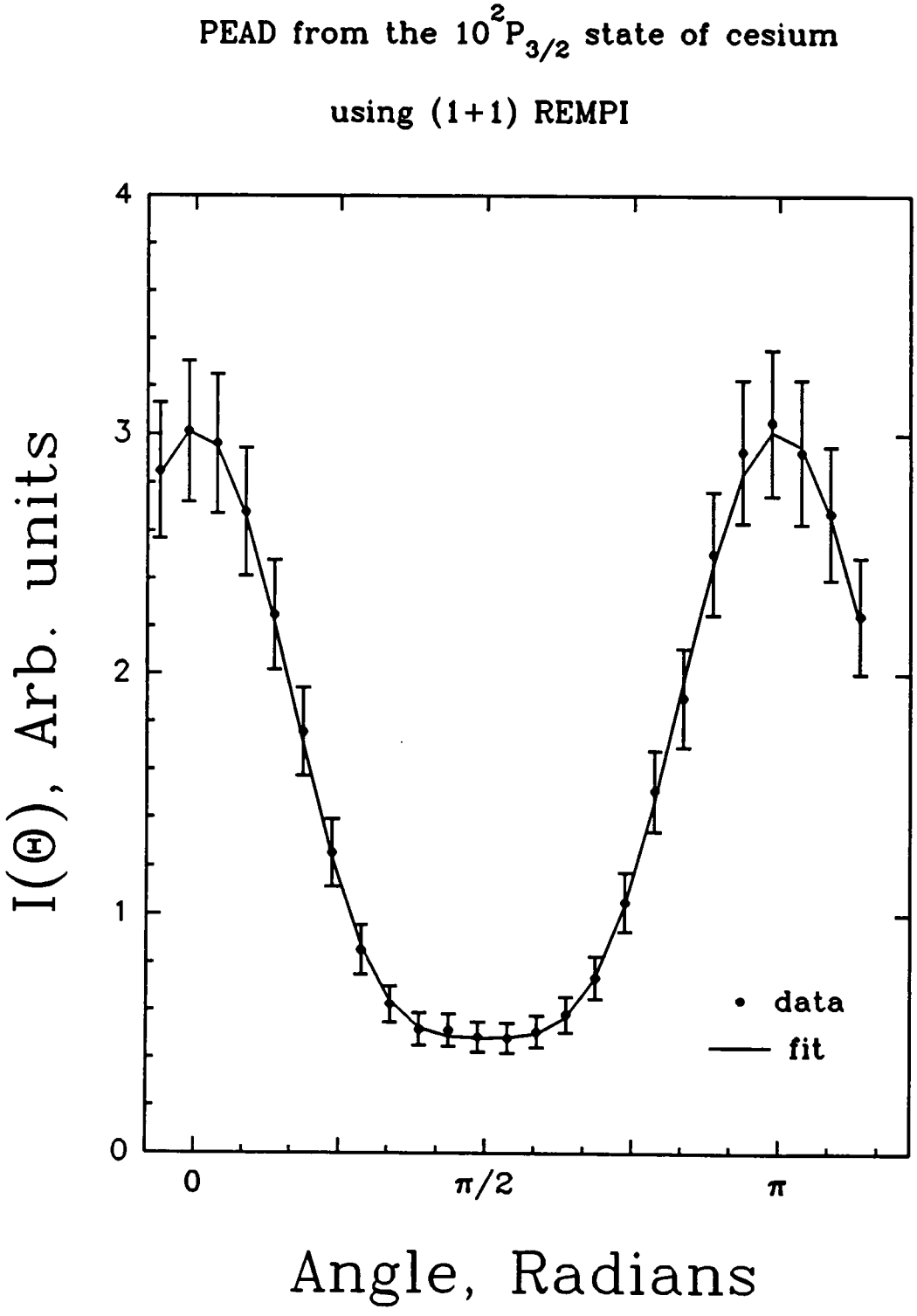

Fig. 4.17 PEAD for the $10^2P_{3/2}$ state of cesium. Standard deviation correspond to the average of 4 scans, each consisting of 100 laser pulses per angle.

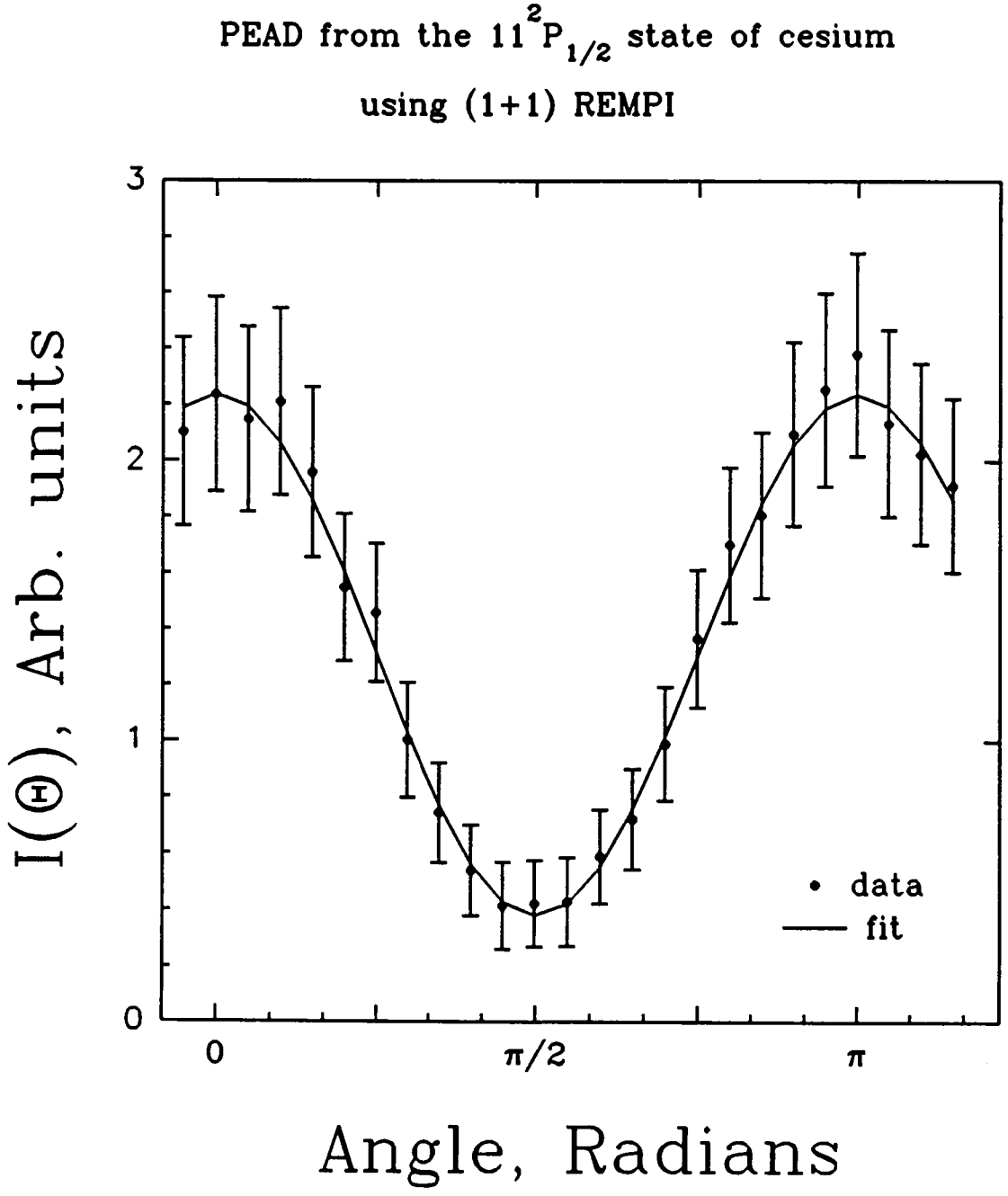

Fig. 4.18 PEAD for the $11^2P_{1/2}$ state of cesium. Standard deviation correspond to the average of 4 scans, each consisting 100 laser pulses for each angle, minus an average of the PEAD of the background noise.

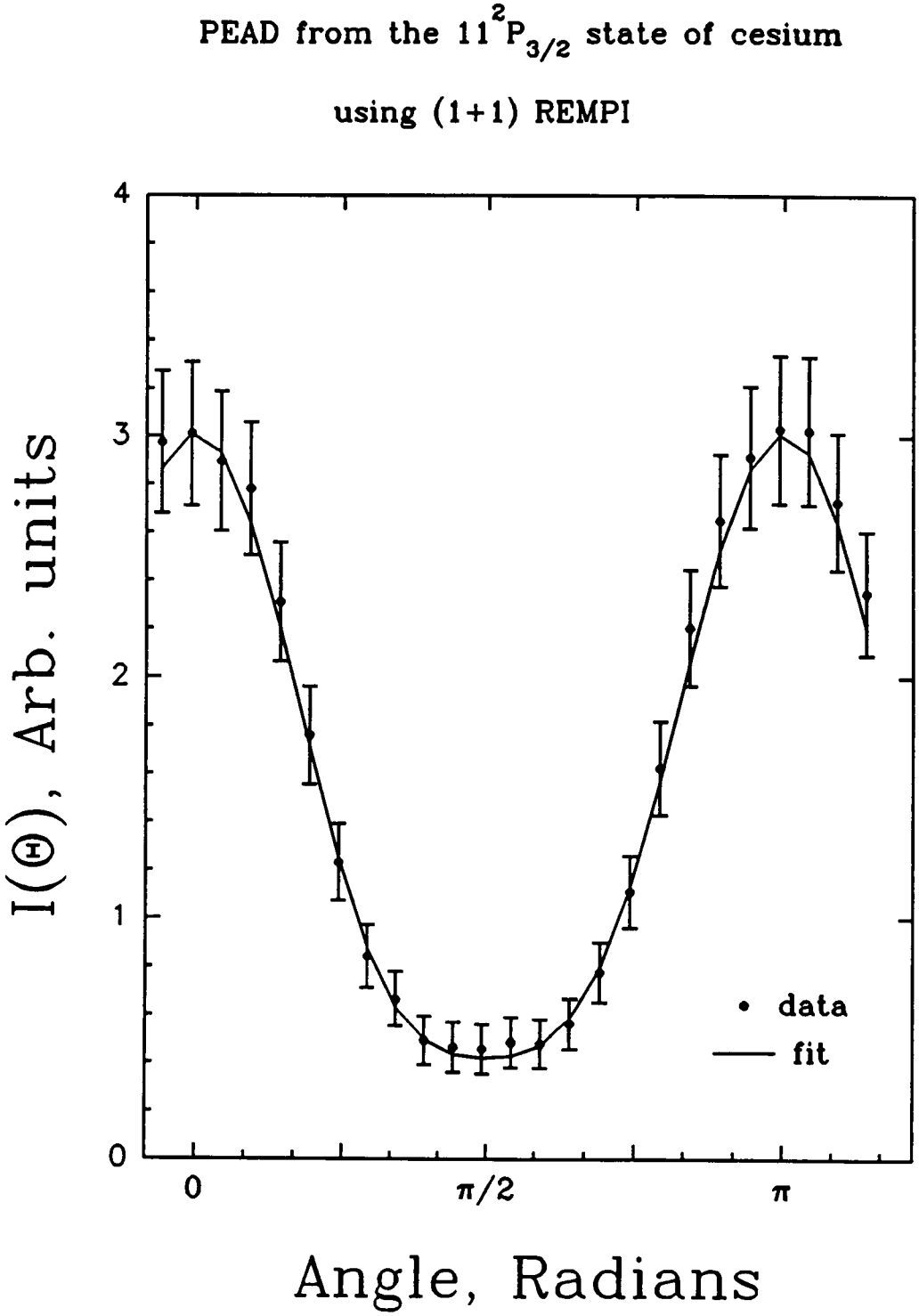

Fig. 4.19 PEAD for the $11^2P_{3/2}$ state of cesium. Standard deviation correspond to the average of 4 scans, each consisting of 100 laser pulses per each angle, minus an average of the PEAD of the background noise.

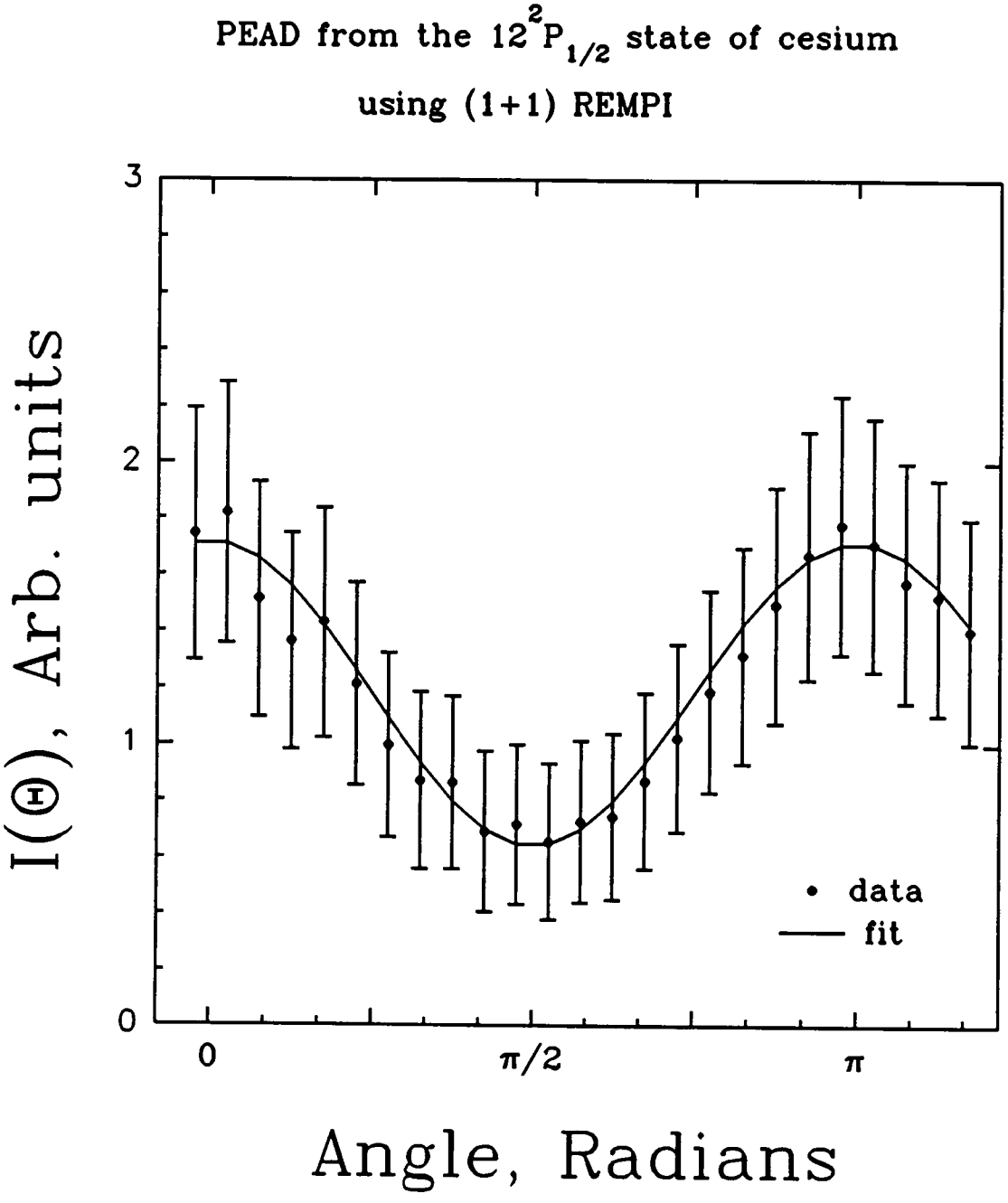

Fig. 4.20 PEAD from the $12^2P_{1/2}$ state of cesium. Standard deviations correspond to the average of 6 scans, each consisting of 100 laser pulses per angle, minus removal of the average of the background noise PEAD.

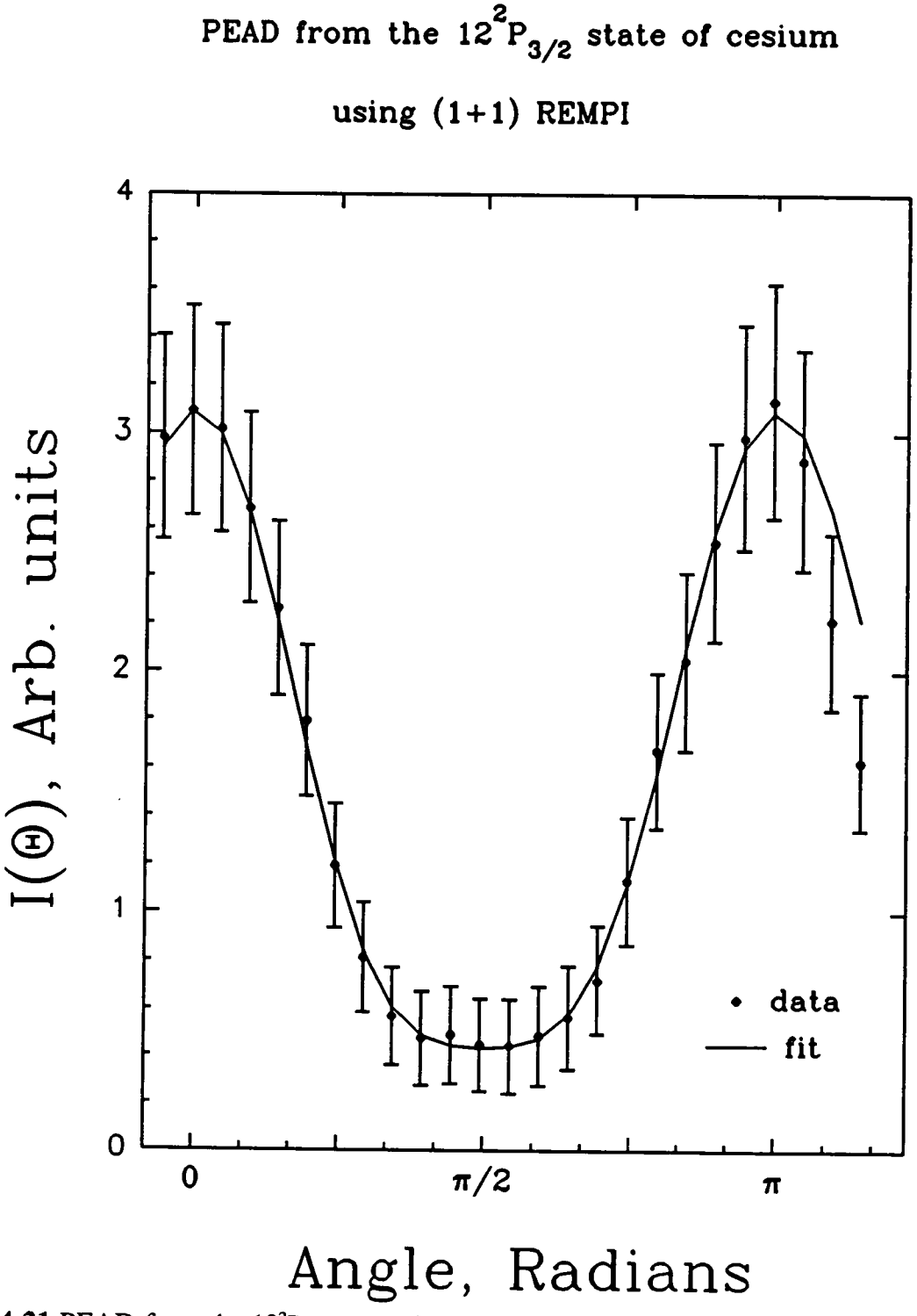

Fig. 4.21 PEAD from the $12^2P_{3/2}$ state of cesium. Standard deviations correspond to the average of 6 scans, each consisting of 100 laser pulses per angle, minus the background noise PEAD standard deviations.

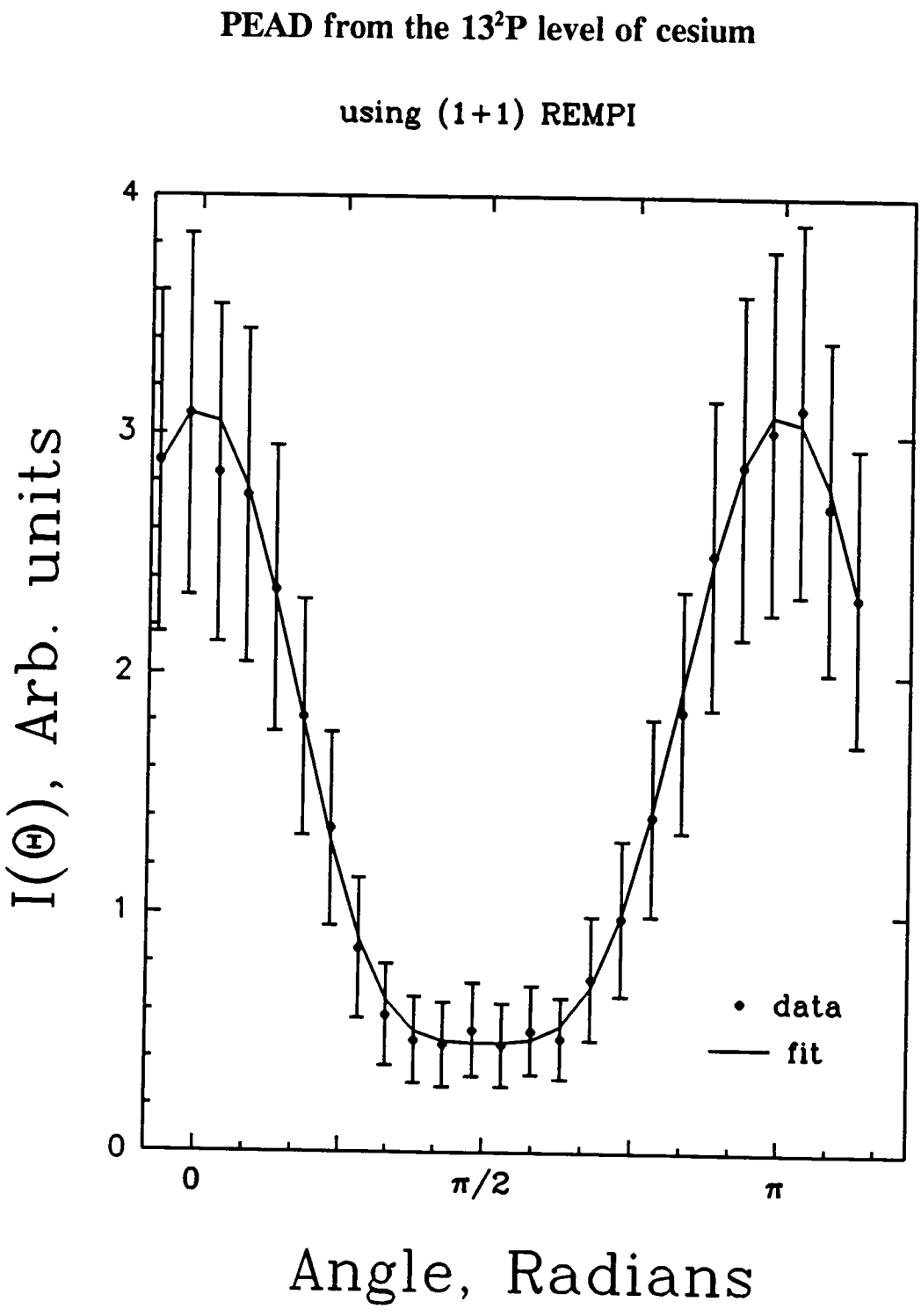

Fig. 4.22 PEAD from the 13^2P level of cesium. Standard deviations correspond to the average of 6 scans, each consisting of 100 laser pulses per angle, minus the standard deviation of the background noise.

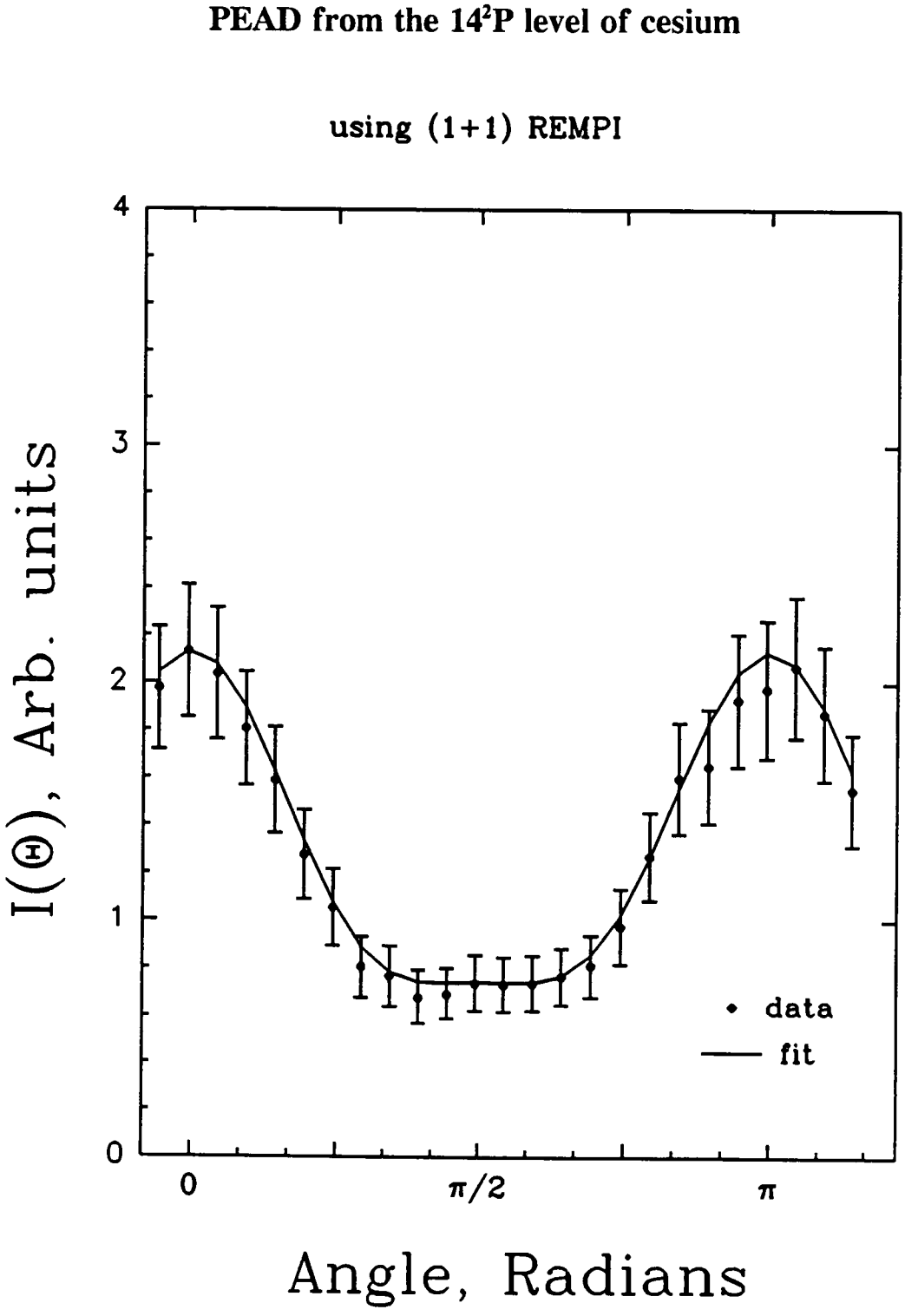

Fig. 4.23 PEAD from the 14^2P state of cesium. Standard deviations correspond to the average of 6 scans, each consisting of 100 laser pulses per angle. Includes a background noise subtraction.

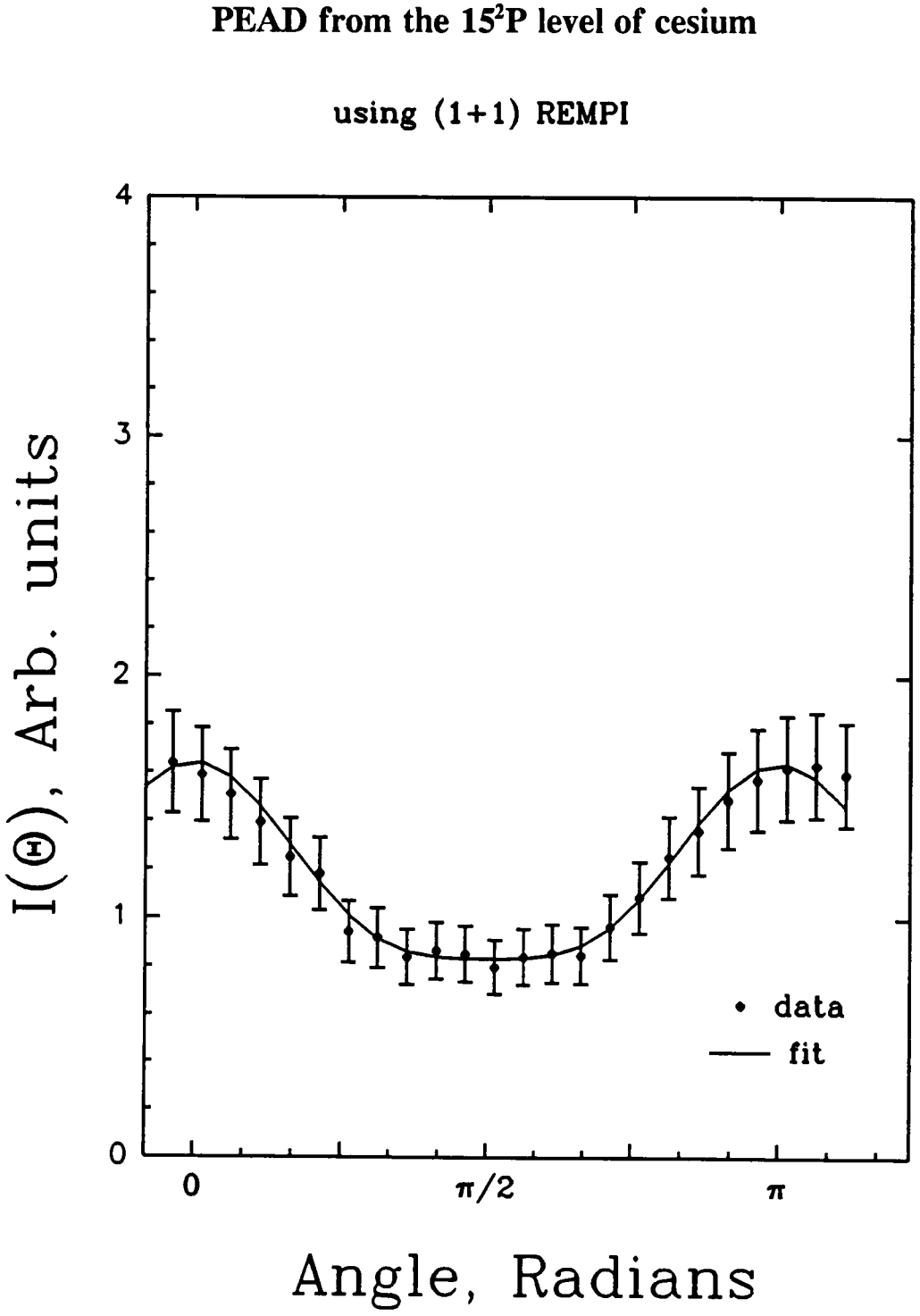

Fig. 4.24 PEAD from the 15^2P state of cesium. Standard deviations correspond to the average of 6 scans, each consisting of 100 laser pulses for each angle. Includes a subtraction of a PEAD of the background noise.

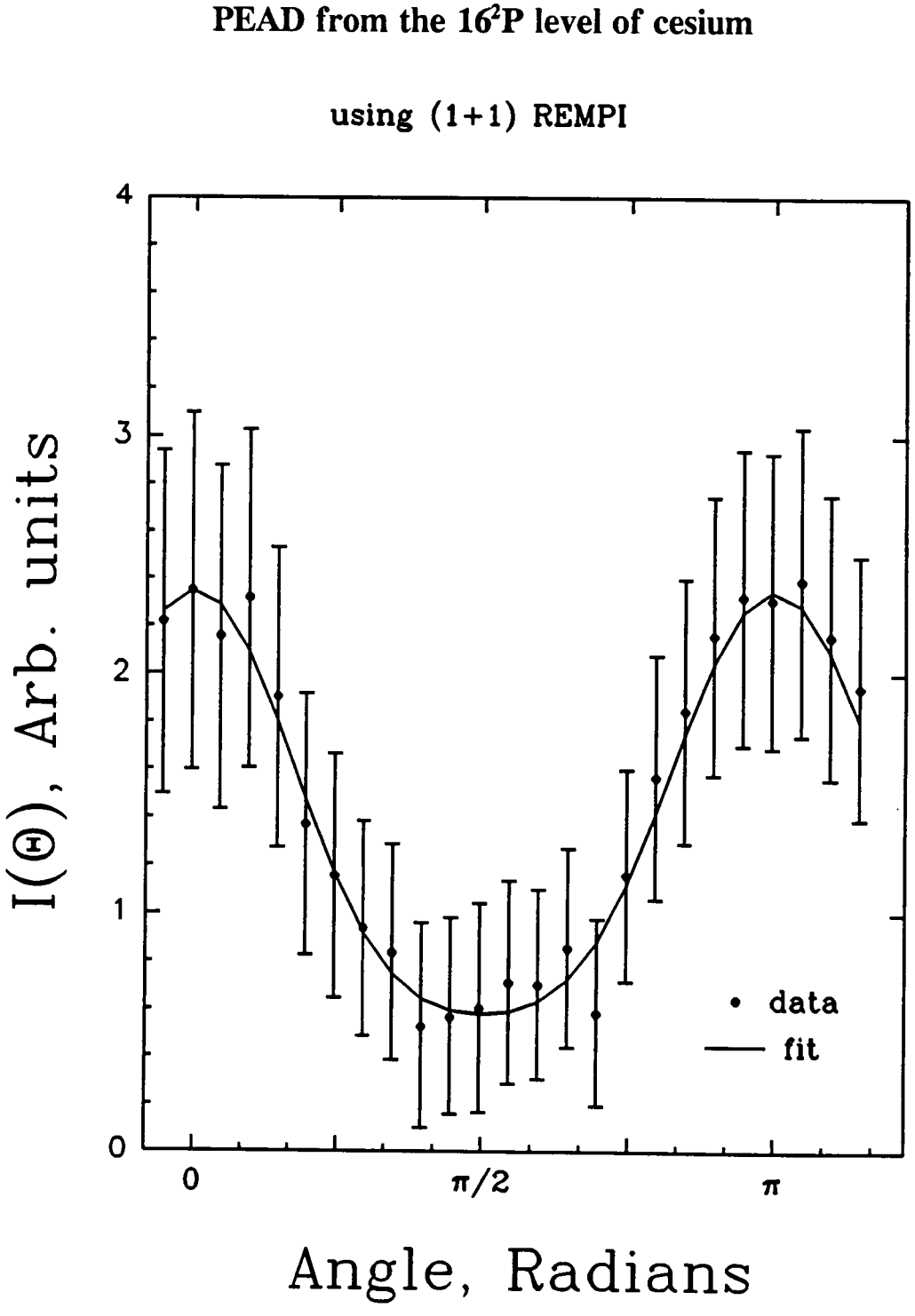

Fig. 4.25 PEAD from the 16^2P state of cesium. Standard deviations correspond to the average of 4 scans, each consisting of 100 laser sweeps for each angle. A PEAD of the background has been subtracted.

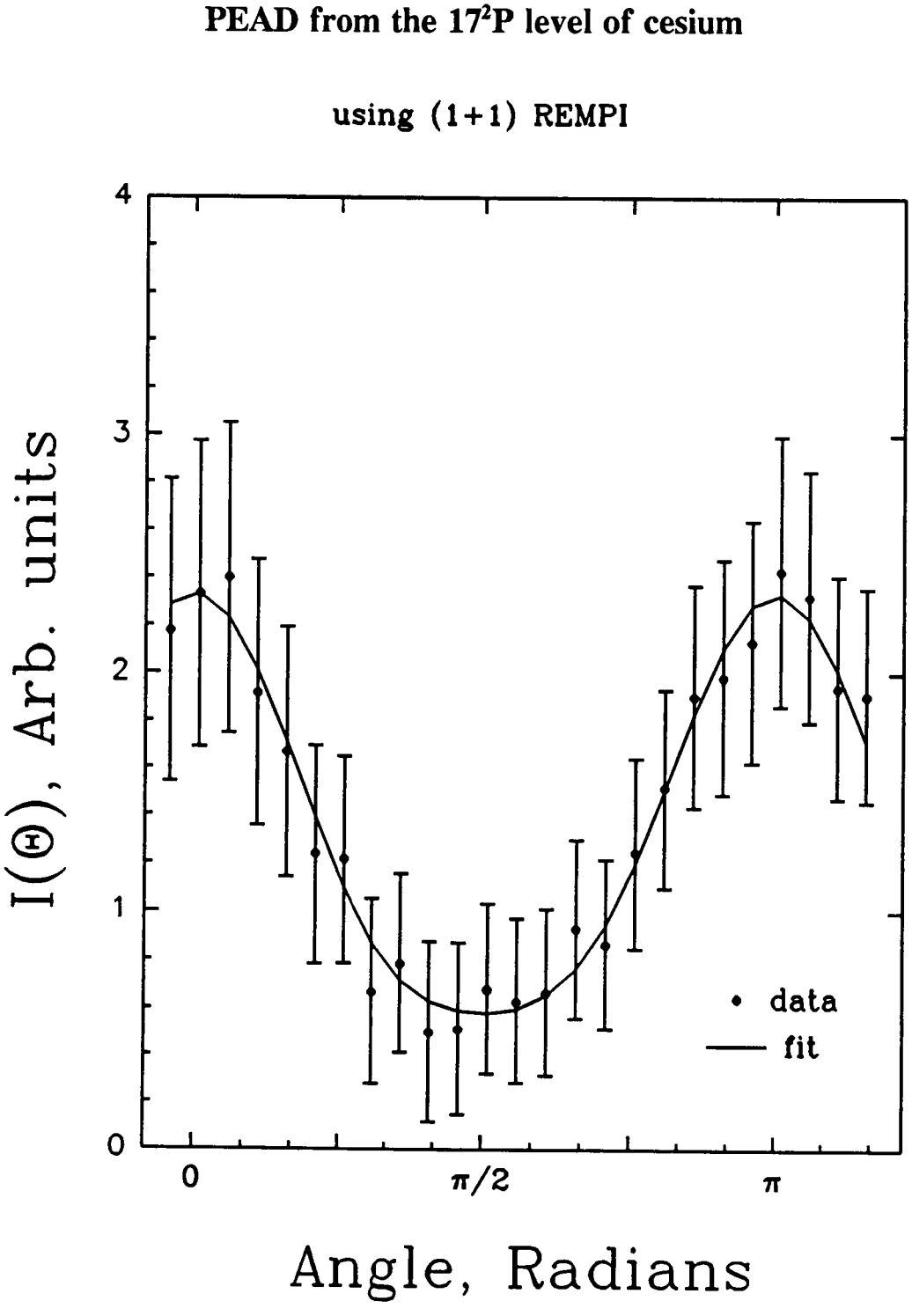

Fig. 4.26 PEAD from the 17^2P state of cesium. Standard deviations correspond to the average of four scans, each consisting of 100 laser sweeps for each angle. Includes a subtraction of the background noise.

(a)

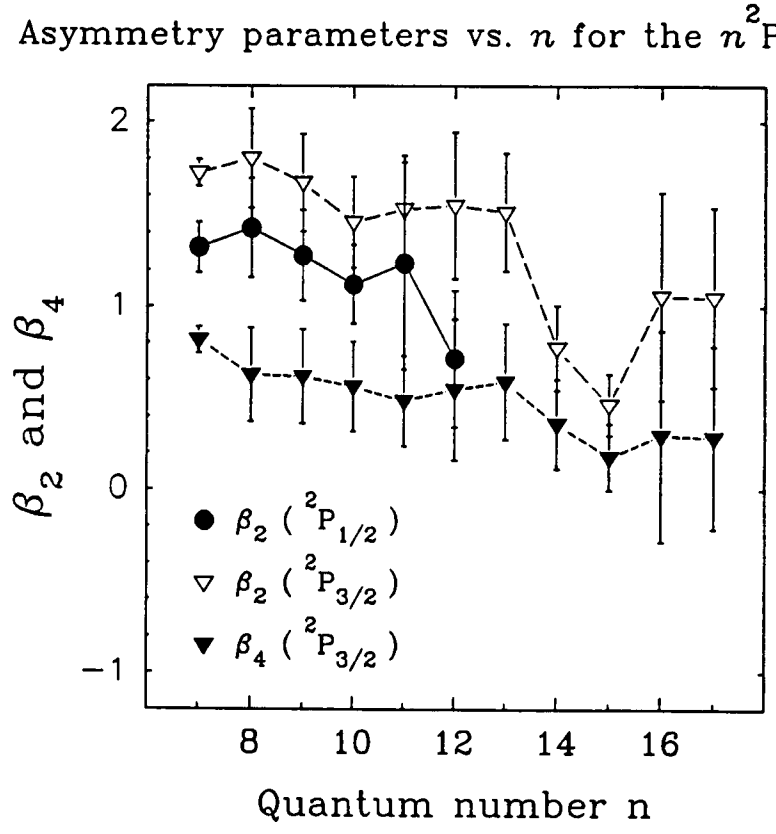

(b)

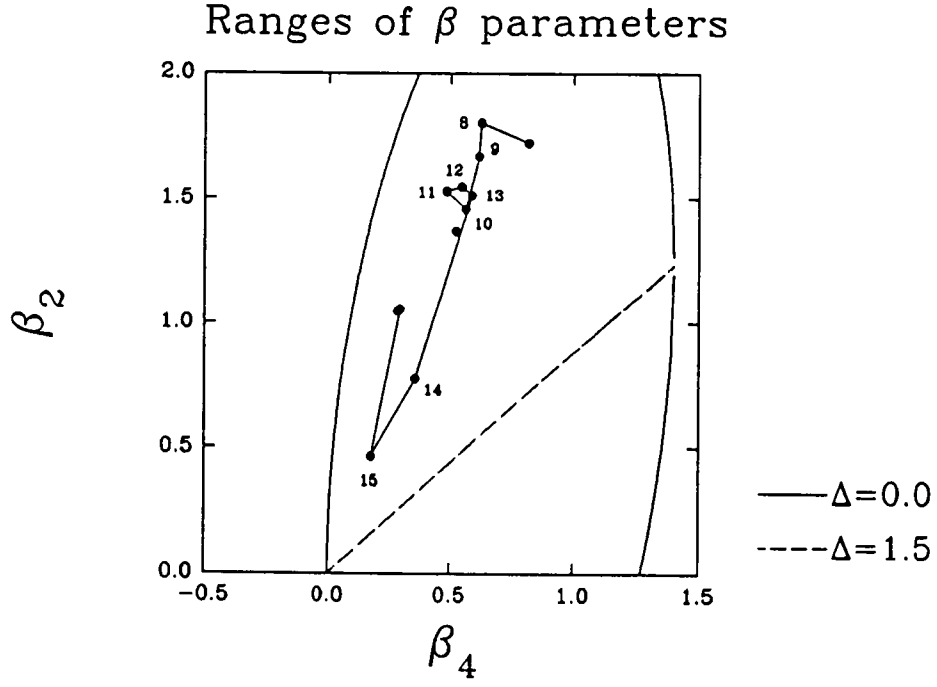

Fig. 4.27. (a) Asymmetry parameters β_2 and β_4 versus quantum number for $n^2P_{3/2}$. (b) β_2 versus. β_4 and their location within the ranges .

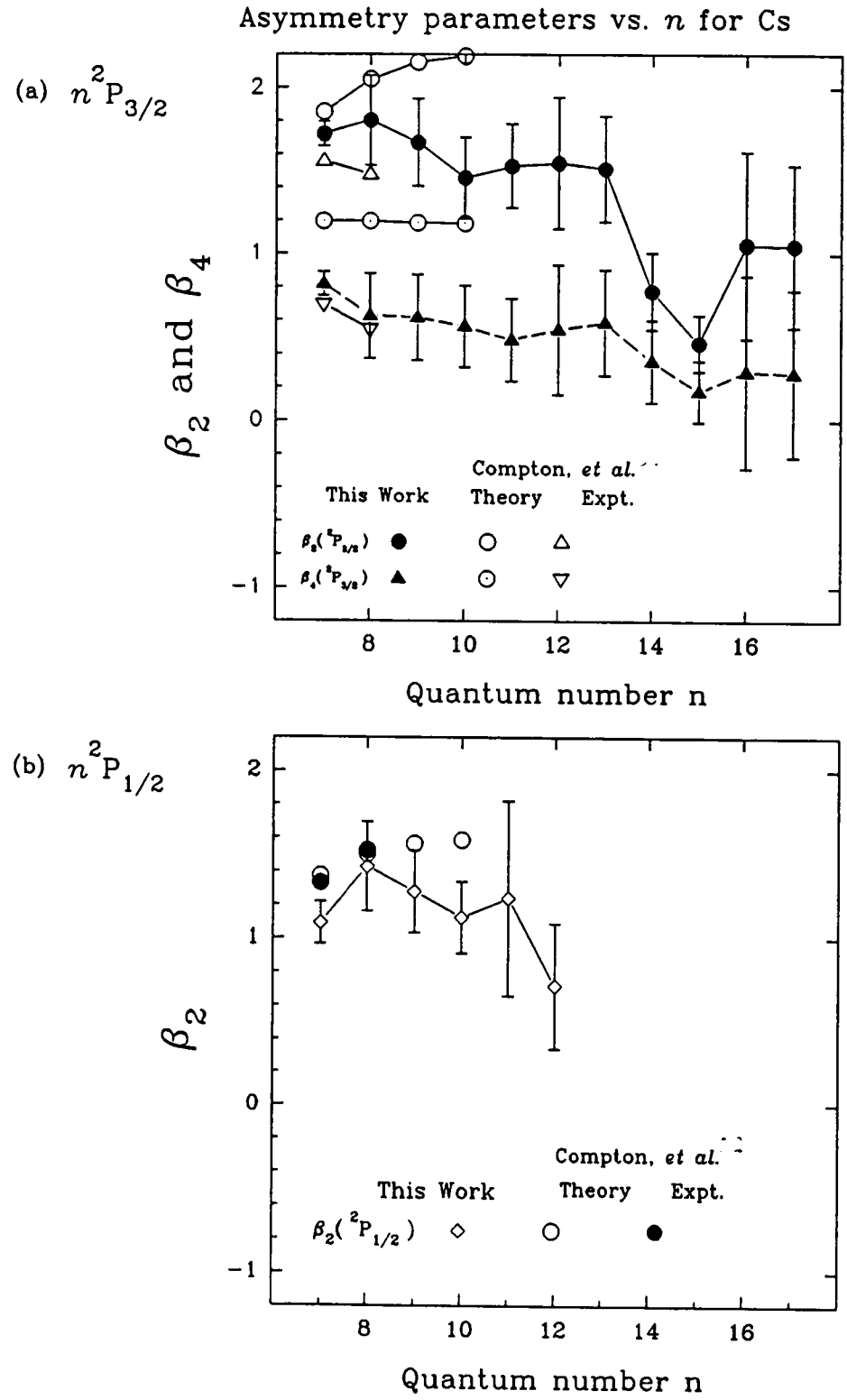

Fig. 4.28 Comparison of the asymmetry parameters for the PEAD of the *np* states of cesium obtained by Compton, *et al.*[32] and those in this work. (a) $n^2P_{3/2}$, (b) $n^2P_{1/2}$.

$n^2P_{1/2}$ were found to vary from 1.46 to 1.10. In contrast, the asymmetry parameter β_2 was found to vary from 1.80 to 0.465, while the β_4 did not vary significantly for the $n^2P_{3/2}$ states. This is attributed to the fact that the β_4 reflects alignment of the intermediate state, and depends only on the ratio of the matrix elements, and not at all on the difference of the phase shifts, as evident from equation (2-36c). Alignment of the intermediate state is given by equation (2-23.b), and it is independent on the quantum number n. For the np states using plane polarized light, alignment of the $n^2P_{1/2}$ states is zero, while alignment of the $n^2P_{3/2}$ is predicted to be $-2/5$. Alignment of an isotropic $n^2P_{3/2}$ is predicted to be zero.

A local maxima is predicted at 90° in the PEADs corresponding to the $n^2P_{3/2}$ states, due to the quadrupole moment of the population distribution of the excited state. These local maxima are not immediately observable in the data. The failure to observe them is attributed to depolarization of the angular momentum distribution of the resonant state due to hyperfine coupling. Hyperfine coupling introduces a time dependence to the alignment, making the photoelectron angular distribution dependent on the pulse width of the laser. As the laser intensity rises, photoionization can occur anytime during the entire pulse width, allowing for depolarization of the excited state. This notion is supported by the lower values of β_4, found by the least squares fits, than what were theoretically expected, suggesting a smaller quadrupole moment in the angular momentum polarization of the $n^2P_{3/2}$ states.

A summary of results of measurements of PEADs from n^2P_j states is listed in Table IV-2, including fundamental information about the resonant np states and the corresponding wavelengths used to excite the ground state, and the expected time-of-flight. The asymmetry parameters are obtained by performing a least squares fit of the data. The associated radial matrix element ratio $\chi = R_D/R_S$ and difference of the phase shifts $\Delta = \delta_0 - \delta_2$ were computed for comparison with theory,[32] and results are given in Table IV-3.

The experimental results vary slightly from the predictions given by equations (2-36.a-c) in that the asymmetry parameters for the $n^2P_{3/2}$ states seem to "dip" twice as

Table IV-2. Summary of the experimental results for the $n^2P_{3/2}$ and $n^2P_{1/2}$ states of cesium. Energy levels data were obtained from C. Moore[58].

State	Energy, cm^{-1}	λ, nm	TOF, ns	Experimental			
				β_2	β_4	χ	Δ^a
$7^2P_{1/2}$	21765.65	459.4	68.7	1.321 ± 0.137	-		
$8^2P_{1/2}$	25709.14	389.0	53.5	1.426 ± 0.267	-		
$9^2P_{1/2}$	27637.29	361.8	49.0	1.277 ± 0.246	-		
$10^2P_{1/2}$	28727.09	348.1	46.9	1.122 ± 0.214	-		
$11^2P_{1/2}$	29403.68	340.1	45.7	1.236 ± 0.291	-		
$12^2P_{1/2}$	29852.85	335.0	45.0	0.716 ± 0.372	-		
$7^2P_{3/2}$	21946.66	455.7	67.7	1.723 ± 0.073	0.819 ± 0.072	1.130	1.320
$8^2P_{3/2}$	25791.78	387.7	53.3	1.803 ± 0.269	0.626 ± 0.257	0.856	1.410
$9^2P_{3/2}$	27681.96	361.3	48.9	1.670 ± 0.263	0.617 ± 0.258	0.845	1.403
$10^2P_{3/2}$	28753.93	347.8	46.9	1.457 ± 0.245	0.563 ± 0.246	0.781	1.409
$11^2P_{3/2}$	29421.10	339.9	45.7	1.529 ± 0.253	0.484 ± 0.248	0.692	1.444
$12^2P_{3/2}$	29864.72	334.8	45.0	1.548 ± 0.397	0.546 ± 0.388	0.761	1.422
$13^2P_{3/2}$	30174.51	331.4	44.5	1.513 ± 0.319	0.588 ± 0.318	0.810	1.403
$14^2P_{3/2}$	30399.49	329.0	44.2	0.776 ± 0.231	0.357 ± 0.245	0.557	1.438
$15^2P_{3/2}$	30567.98	327.1	43.9	0.465 ± 0.168	0.177 ± 0.181	0.362	1.488
$16^2P_{3/2}$	30697.52	325.8	43.7	1.055 ± 0.564	0.294 ± 0.576	0.491	1.484
$17^2P_{3/2}$	30799.15	324.7	43.6	1.049 ± 0.488	0.284 ± 0.499	0.480	1.487

[a] Using the negative solution for χ, we obtain $\pi - \Delta$.

Table IV-3. Comparison of experimental results of this work for $n^2P_{3/2}$ states of cesium with Compton, *et al.*[32] Their β parameters were transformed to our convention.

n	Experiment (this work)				Theory[32]				Experiment[32]	
	β_2	β_4	χ	Δ	β_2	β_4	χ	Δ^a	β_2	β_4
7	1.723	0.819	1.130	1.320	1.854	1.197	-2.35	0.957	1.559	0.694
8	1.803	0.626	0.856	1.410	2.050	1.196	-2.29	0.747	1.479	0.545
9	1.670	0.617	0.845	1.403	2.153	1.186	-2.23	0.637	-	-
10	1.457	0.563	0.781	1.409	2.188	1.181	-2.21	0.597	-	-

[a] Have subtracted 2π.

a function of the energy, instead of only once. This difference may be due to the detail that equations (2-36) were calculated in the LS coupling scheme, and did not take into consideration spin-orbit effects in the continuum. At the time of this writing there are no theoretical calculations for the asymmetry parameters that take into consideration relativistic effects in PEADs for aligned states to substantiate this conclusion.

AC Stark effects on the *np* levels were examined by studying the shape, or profile, of the resonance as a function of photon energy. Figure 4-29 depicts averages of the digitized resonant photoelectron signal corresponding to electrons ejected parallel to the polarization of the photons, *i.e.* 0°, for the 17*p* state of cesium. Each curve corresponds to the average of 100 digitized samples of the electronic pulse of the time-of-flight spectrometer taken at several positions around, and at the energy of the resonance. The dye laser counter was operated at fourth order, and the dye beam was frequency doubled to 324.68 nm using the WEX. Figure 4-29(a) shows the digitized signal as a function of time, and wavelength, and figure 4-29(b) shows the peak heights at channel 17, corresponding to a 170 ns time offset.

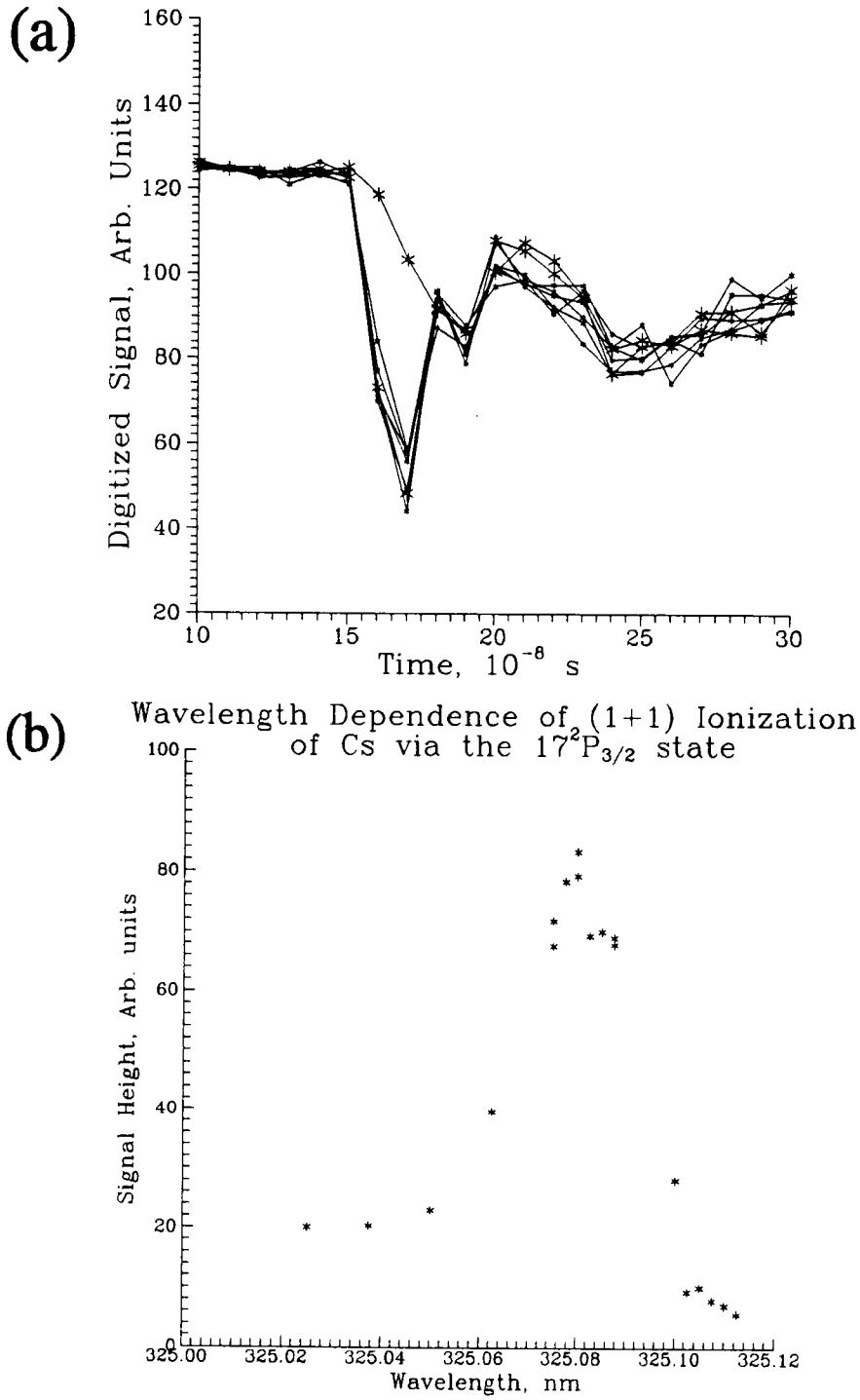

Fig. 4.29 Profile of the 17P photoelectron signal corresponding to the axis of quantization. (a) Digitized signal versus. time for different wavelengths, showing signal noise; (b) signal height vs. wavelength.

A-3 *n*P States Of Rubidium

The (1+1) resonantly enhanced photoelectron angular distribution for the $n^2P_{1/2}$ and $n^2P_{3/2}$ (n = 6, 7) states of rubidium were also measured using a similar experimental arrangement as that depicted in figure 3.3. Two key differences were the placement of the alkali beam source at right angles to the laser beam, the collimation scheme depicted in figure 3.10(b), and the absence of the lower plate in the interaction region. PEAD measurements were taken using the data acquisition software that averaged several digitized signal sweeps and also calculated the standard deviation for each digitized channel.

The (1+1) REMPI angular distributions for the $n^2P_{1/2}$ and $n^2P_{3/2}$ states are characterized, respectively, by only a β_2, or by a β_2 and a β_4 asymmetry parameters. The observed photoelectron angular distributions for these states, and respective fits using equation (4-1), are shown in figures 4.30-33. A brief summary of the results for the studies of the *np* states of rubidium is given in Table IV-4, listing the wavelengths used.

The expected peak at 90° is more noticeable in the PEADs of rubidium than they were in the PEADs of cesium. This may be due to a smaller degree of depolarization by hyperfine coupling, since for ^{85}Rb the hyperfine levels have maximum separation of

Table IV-4. Summary of the experimental results for the studies on the *np* states of Rubidium. Energy levels were obtained from C. Moore.[58]

States, n, j	Energy, cm^{-1}	λ, nm	β_2	β_4
6, 1/2	23715.23	421.67	1.118 ± 0.067	-
6, 3/2	23792.53	420.30	1.303 ± 0.083	1.129 ± 0.082
7, 1/2	27834.99	359.26	1.564 ± 0.065	-
7, 3/2	27869.90	334.81	1.549 ± 0.090	1.082 ± 0.075

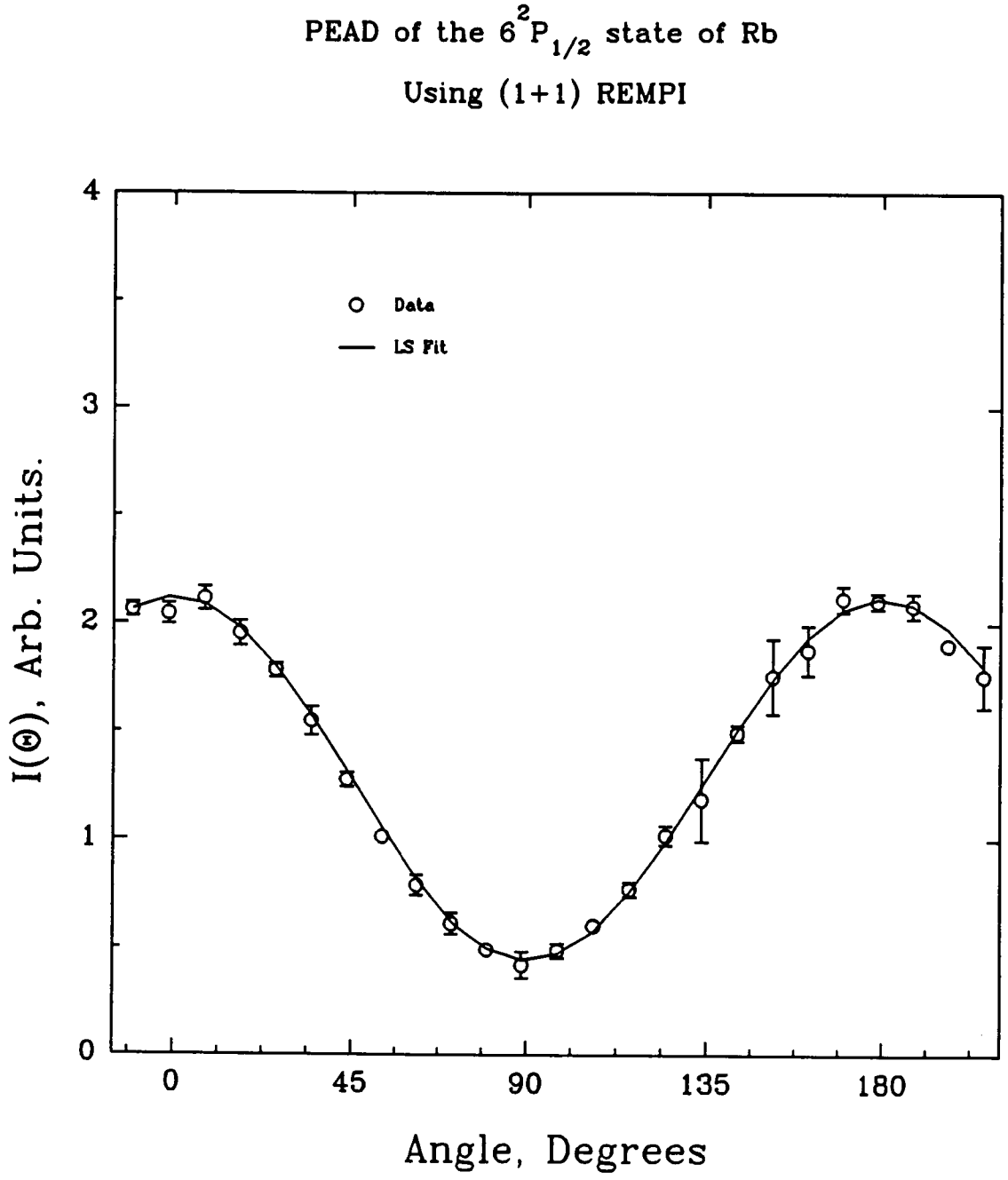

Fig. 4.30. PEAD from the $6^2P_{1/2}$ state of rubidium. Standard deviations correspond to the average of 3 scans, each consisting of 100 laser pulses per angle.

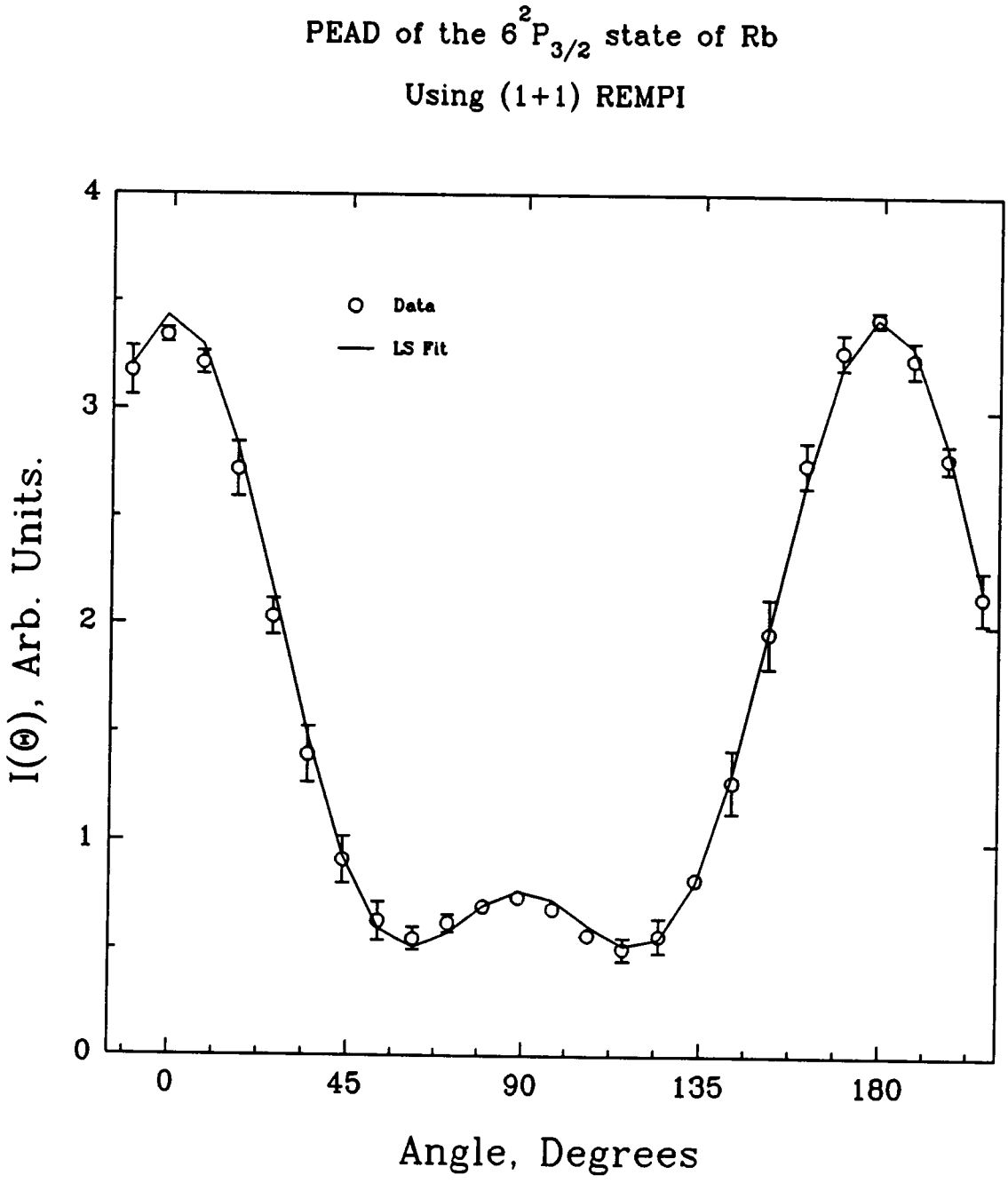

Fig. 4.31. PEAD for the $6^2P_{3/2}$ state of rubidium. Standard deviations correspond to the average of 4 scans, each consisting of 100 laser pulses per angle.

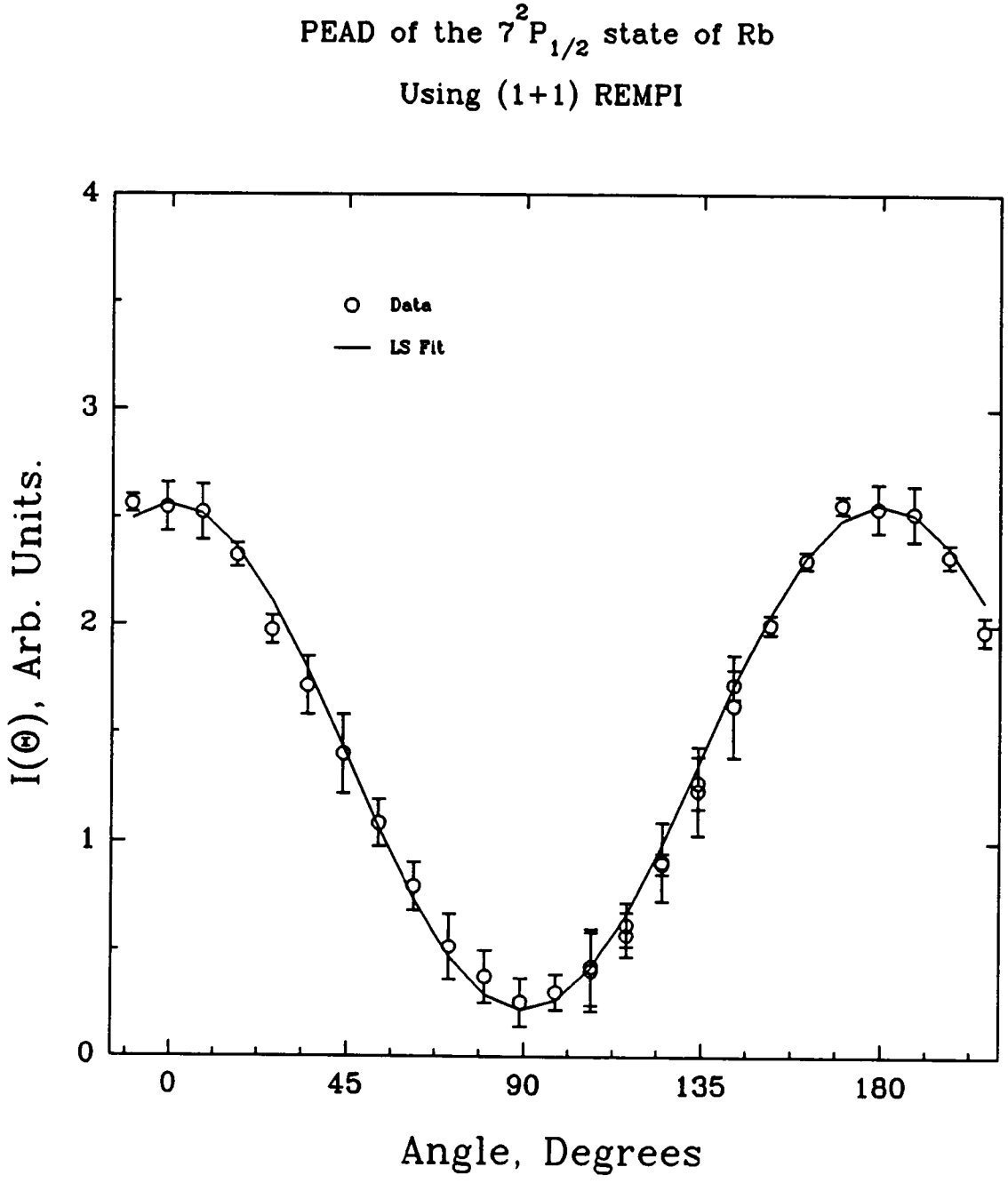

Fig. 4.32. PEAD for the $7^2P_{1/2}$ state of rubidium. Standard deviations reflect the averaging of 4 scans, each consisting of 100 laser pulses per angle.

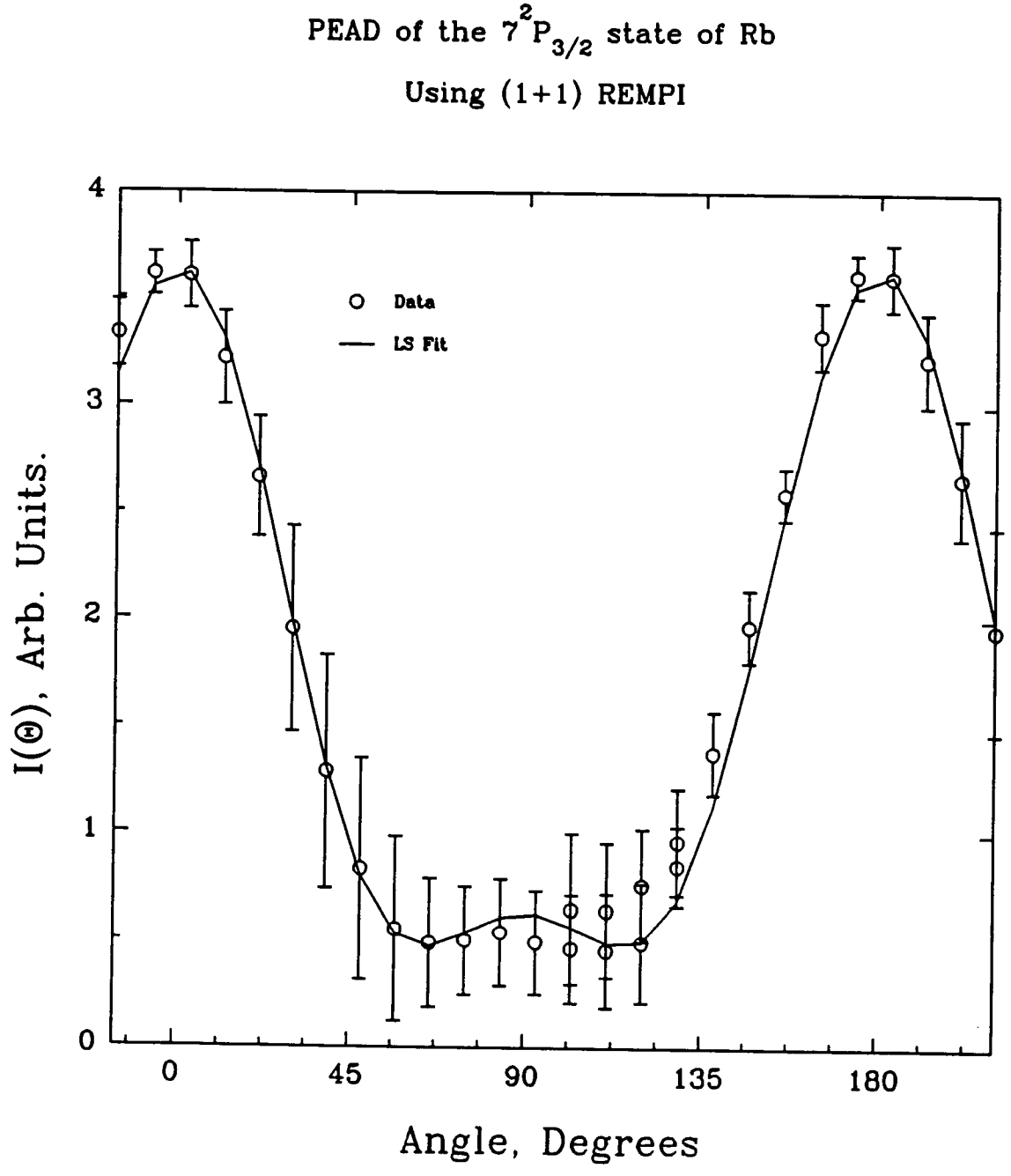

Fig. 4.33. PEAD from the $7^2P_{3/2}$ state of rubidium. Standard deviations correspond to the average of 4 scans, each consisting of 100 laser pulses per angle.

ΔE_{HF} = 69.93 MHz (14.3 ns) for the $6^2P_{3/2}$ state, and ΔE_{HF} = 31.73 MHz (31.52 ns) for the $7^2P_{3/2}$ state. In contrast, the hyperfine levels of the second ($7^2P_{3/2}$) and third ($8^2P_{3/2}$) excited *p* states of cesium have, respectively, maximum separations of ΔE_{HF} = 199.3 MHz (5 ns) and ΔE_{HF} = 91.00 MHz (11 ns).

A-4 *n*D States Of Cesium

The photoelectron angular distribution for $9^2D_{3/2}$ and $9^2D_{5/2}$ using (2 + 1) REMPI were also measured to investigate the performance of the experimental apparatus. Angular distributions from *nd* states of cesium have been previously measured extensively by Compton, *et al.*[32]. Measurements are included in this dissertation only to further validate the experimental methods employed. We remark that the results of Compton, *et al.*[32], were obtained using an electrostatic energy analyzer, which can provide a much greater angular and energy resolution than the time-flight-spectrometer.

The expected photoelectron angular distributions are given by equation (2-30) with j = 3/2 and 5/2, and thus are characterized respectively by two and three asymmetry parameters. Two of the measured PEADs from the $9^2D_{5/2}$ and $9^2D_{3/2}$ are shown in figures 4.34 and Fig. 4.35, together with least squares fits using equation (2-31).

The cross sections for photoionization for the n^2D states were relatively large compared with that for $n^2S_{1/2}$ states, and did not require as much laser power to observe. Interestingly, as a consequence of the relatively high vapor pressure of cesium at room temperature, sufficient cesium was available inside the vacuum chamber after operation of the experimental apparatus for several hours to permit the measurement of PEADs from resonant n^2D_j states using full laser power available. Fig. 4.36 depicts the results of measuring the PEAD for the $9^2D_{3/2}$ and $9^2D_{5/2}$ states of cesium with full laser power (~50 mJ/pulse at 694.7 nm) and the alkali beam turned off. The data is shown unnormalized to show the relative intensities of the signals. The PEADs for the same states measured with only the Nd:YAG oscillator on (~20 mJ/pulse at 694.7 nm) and

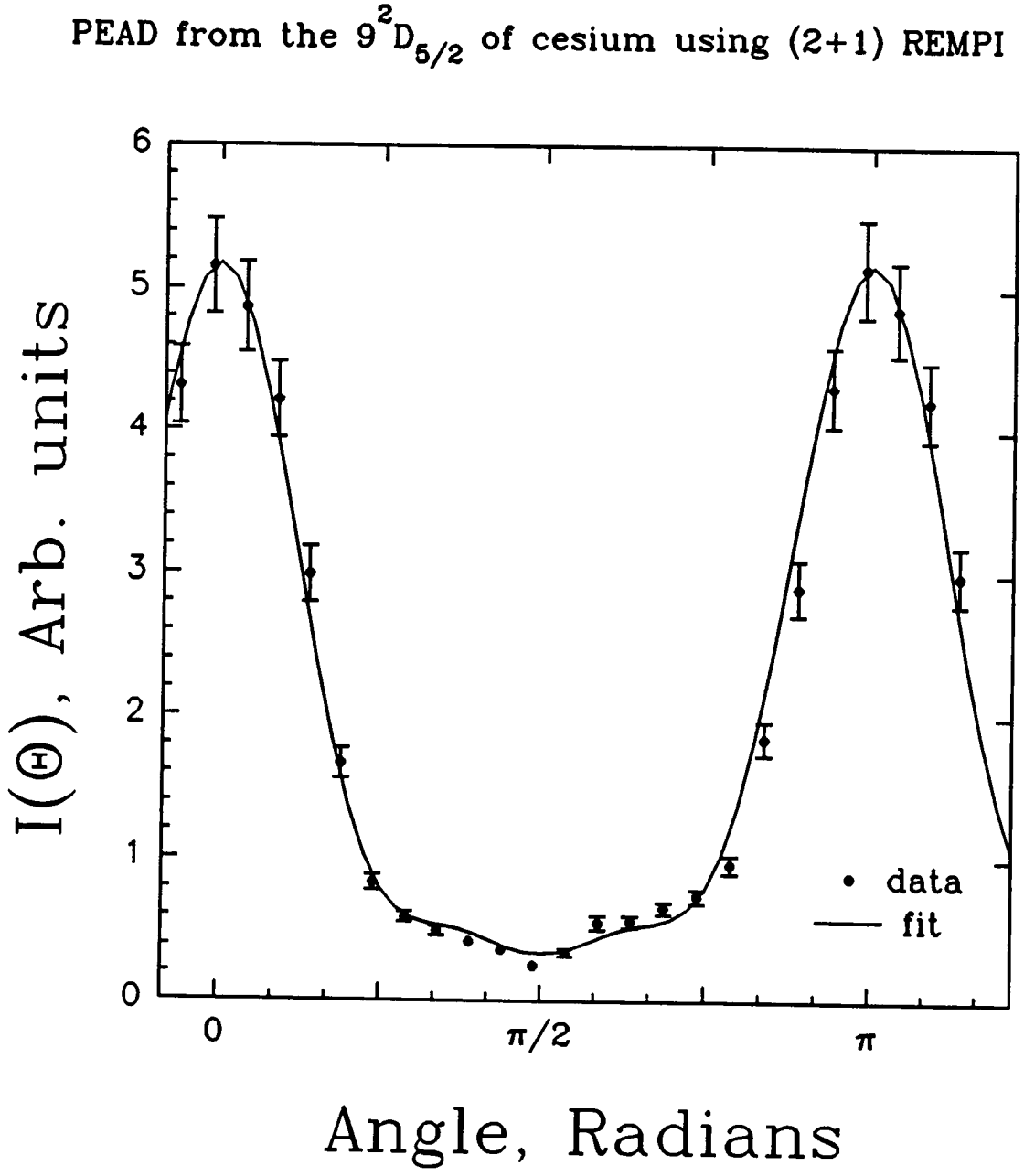

Fig. 4.34. Photoelectron angular distribution from the $9^2D_{5/2}$ state of cesium, using (2 + 1) REMPI.

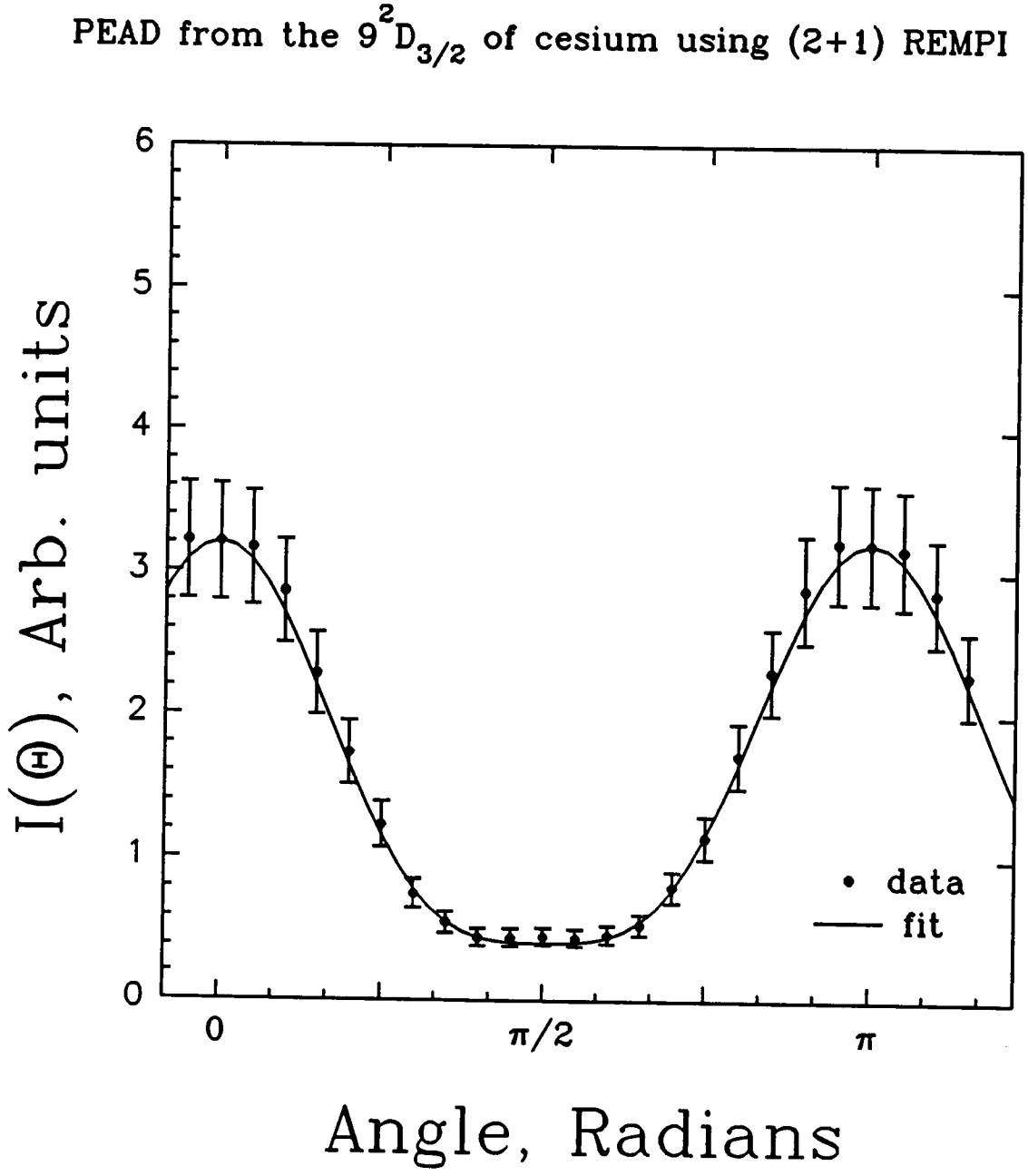

Fig. 4.35. Photoelectron angular distribution from the $9^2D_{3/2}$ state of cesium using (2 + 1) REMPI.

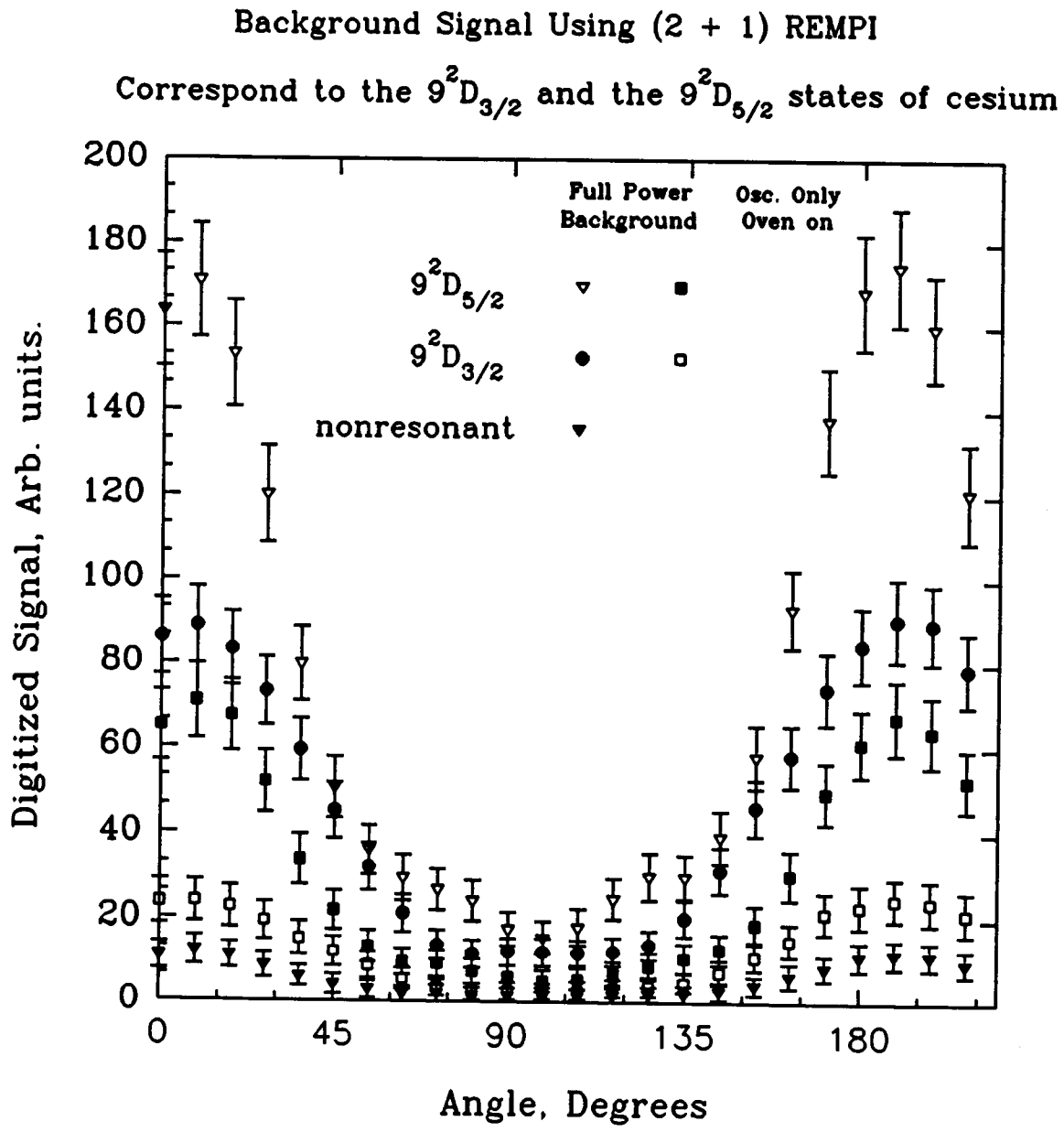

Fig. 4.36. (2 + 1) PEAD from the $9^2D_{3/2}$ and $9^2D_{5/2}$ states with the alkali oven source turned off (on) and using full laser (oscillator only) power. Each set consists of 1 run, averaging 100 laser pulses per angle.

the alkali beam on are also shown for comparison. These PEADs provide an idea of the resolution of the true time-of-flight detector, as well as giving an idea of nonresonant background contributions to the PEAD.

B. CIRCULAR DICHROISM IN THE ANGULAR DISTRIBUTIONS (CDAD)

B-1. *n*P STATES OF CESIUM

The results for circular dichroism in the angular distributions (CDAD) reported in this thesis represent the first measurements of CDAD in an atomic system. The (1 + 1′) REMPI CDAD for the $7^2P_{3/2}$ and the $8^2P_{3/2}$ states of cesium were measured using the apparatus depicted in figure 3.4. Similar experiments were also carried out on the $7^2P_{1/2}$ and the $8^2P_{1/2}$ for contrast, and to help in the diagnostics of the experimental apparatus.

The n^2P_j resonant state was populated employing one photon absorption by cesium atoms in the ground state ($6s$, $j = 1/2$, $m_j = \pm 1/2$) using plane polarized light. Due to the selection rules for dipole transitions, the magnetic sublevels of the $n^2P_{3/2}$ state ($m_j = \pm 3/2, \pm 1/2$) were not equally populated, only the $m_j = \pm 1/2$ sublevels became occupied with the same probability, thus initially creating pure alignment of the resonant state. The alignment was probed employing one photon ionization using both left and right circularly polarized light. In contrast, the one photon excitation to the $n^2P_{1/2}$ state produced an isotropic population distribution. Photoionization from isotropically populated states produces isotropic PEADs when circularly polarized light is used in the ionization step.

The tunable plane polarized photon beam output of the PDL-2 dye laser was used in the initial excitation step, and its polarization was rotated using a double Fresnel rhomb mounted on an optical bench. Any photon wavelength with enough energy to

ionize the atom could have been used in the probe step, and the second harmonic of the Nd:YAG (532 nm) was chosen for both its readily availability and its relatively high power. The polarization of the 532 nm laser beam was manipulated using the optical setup depicted in figure 3.5.

Figure 4.37 depicts the observed CDAD of the $7^2P_{3/2}$ state of cesium with theoretical calculations by Dubs, Dixit and McKoy[74] specifically performed for this work. The discrepancy is attributed to depolarization of the resonant state due to hyperfine coupling. The angular momentum polarization, in this case alignment, prepared by the absorption of plane polarized light was defined in the LS coupling scheme, and the population distribution of the excited state was specified in terms of the populations distribution $\rho(m_j)$ of the magnetic sublevels. The m_j is no longer a good quantum number in the hyperfine coupling scheme. As the total angular momentum vector $\vec{\mathbf{F}}$ precesses about the axis of quantization, $\vec{\mathbf{J}}$ precesses about $\vec{\mathbf{F}}$, and the magnetic projections m_j are constantly changing. Thus, the population distribution, and consequently the alignment, expressed in terms of the magnetic quantum numbers become time dependent. The initial created alignment in the excitation step will thus exhibit a time dependence given by equation (2-44). For our experiments, this can be verified by calculating the long-time limit depolarization factor using the methodology of Green and Zare[5] and the data of Arimondo, *et al.*[33] from equation (2-52) to be

$$\lim_{\omega_{F'F}\to\infty} \bar{g}^{(k)} = 0.219 \qquad \textbf{(4-5)}$$

The theoretical calculation by Dubs, Dixit and McKoy[74] was multiplied by this factor, and plotted with the experimental data in figure 4.37 as well. Reasonable agreement between theory and experiment is thus obtained.

Figure 4.38 shows the observed CDAD of the $8^2P_{3/2}$ state of cesium. At this time, theoretical calculations are not available, but are soon expected to be available from Professor Cherepkov. If depolarization of the resonant state by hyperfine coupling is presumed, calculation of the long-time limit using equation (2-52) yields the same result

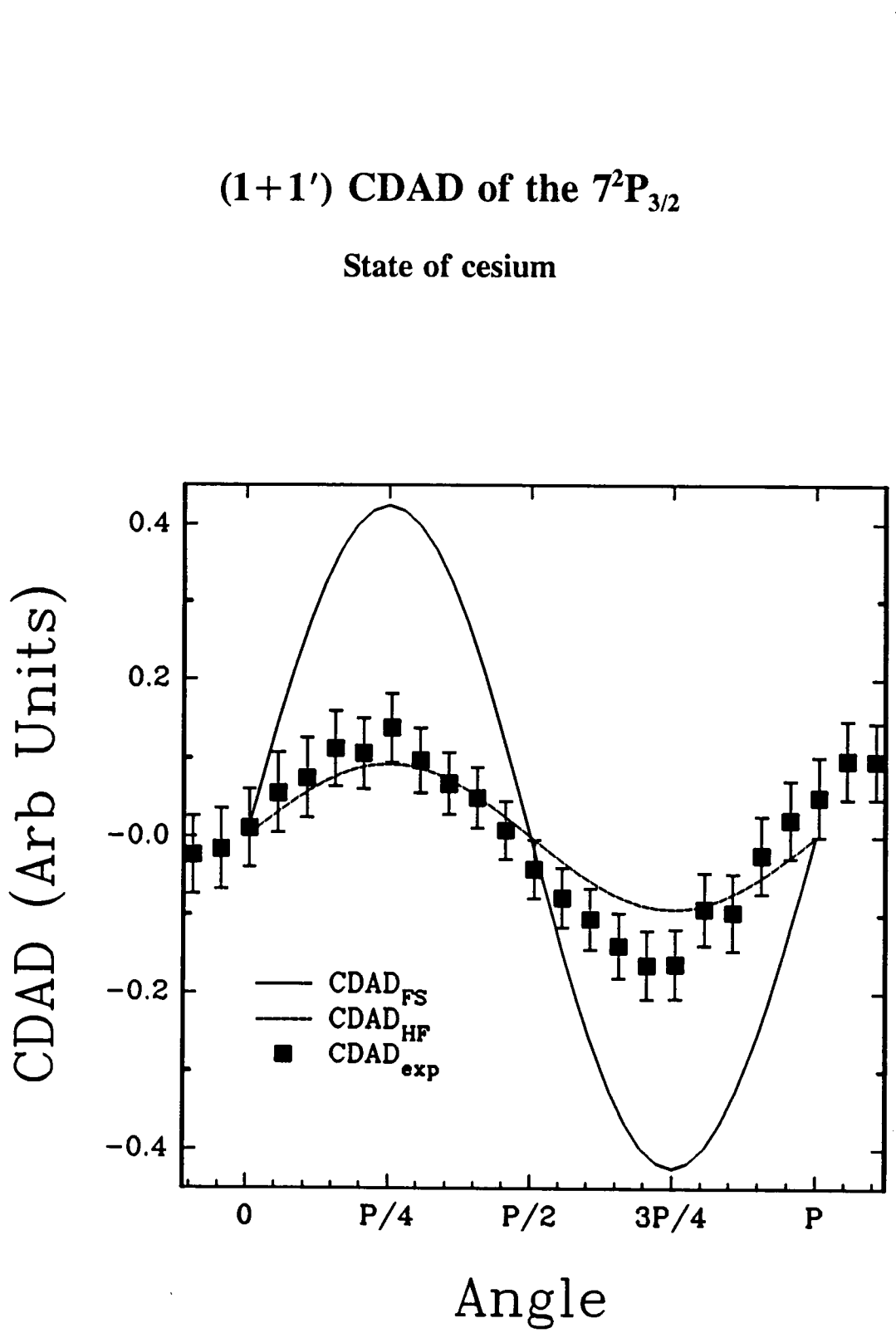

Fig. 4.37. Observed CDAD of the $7^2P_{3/2}$ state of cesium. Theoretical calculations by Dubs, *et al.*[74] Dashed curve is the long time limit using the model of Greene and Zare.[5]

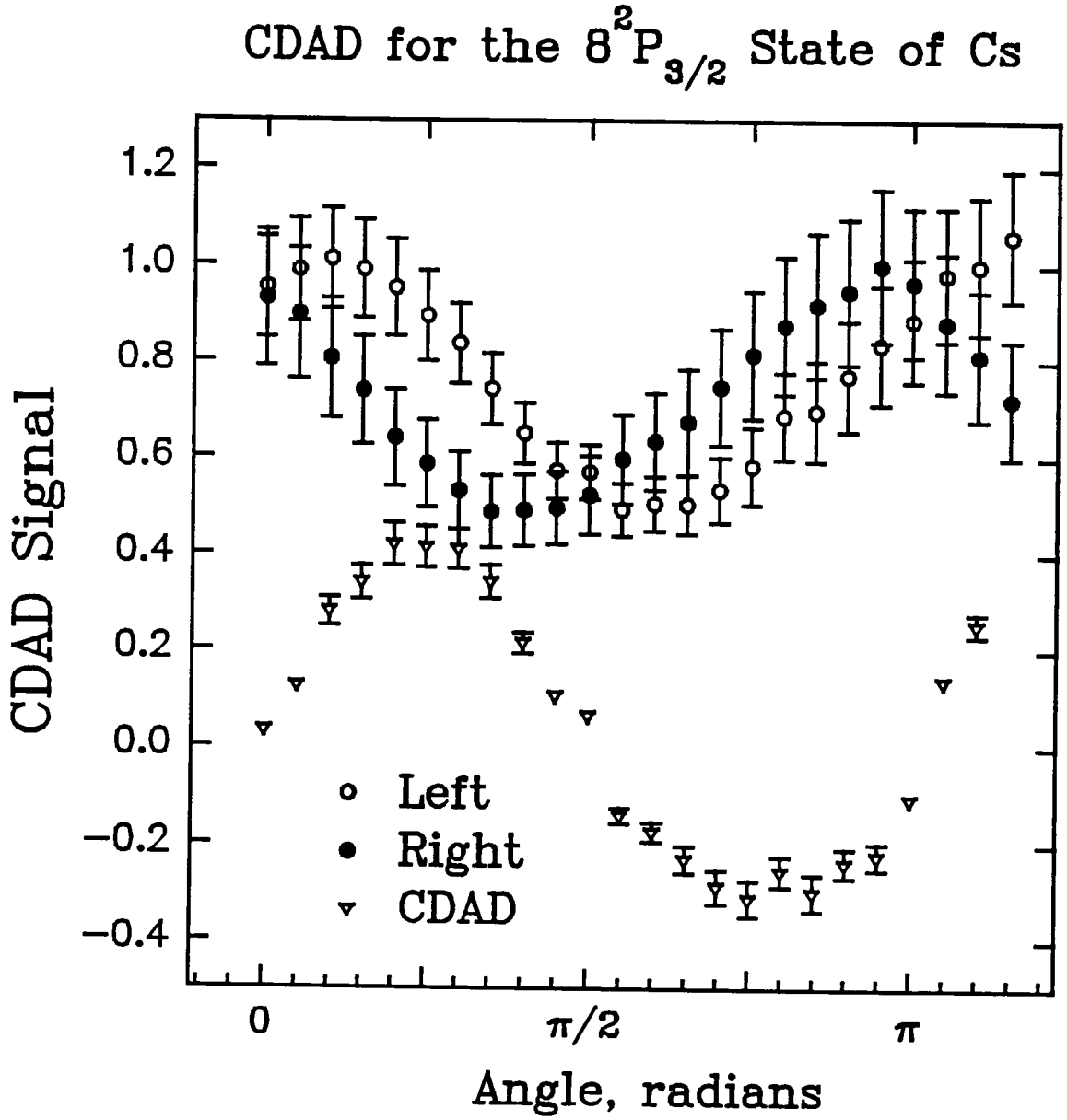

Fig. 4.38. Observed PEADs and CDAD of the $8^2P_{3/2}$ state of cesium.

given by equation (4-4), since the calculation involves similar angular momentum quantum numbers F, I, and J, and is independent of n. A calculation of the time dependence of the relative alignment of the $8^2P_{3/2}$ using the equations of Greene and Zare[5] and the experimental data cited by Arimondo, *et al.*[33] is shown in figure 4.39. A similar calculation of the time dependence for the $7\,^2P_{3/2}$ state was shown in figure 2.4. From these figures we determine that if there is a significant delay between excitation and ionization, the alignment created during the excitation will evolve and can be completely destroyed within 5 ns (for the $7\,^2P_{3/2}$) or within 10 ns (for the $8^2P_{3/2}$).

If we ignore hyperfine depolarization and assume that the created alignment, given by equation (2-23.b), is a constant of the system, then for the one photon excitation of a state with $j = 1/2$ to a state with $j = 3/2$ using plane polarized light, we have

$$A_0 = \left\langle \frac{3J_z^2 - \vec{J}^2}{2\vec{J}^2} \right\rangle = 2 \times \frac{1}{2} \frac{3\left(\pm\frac{1}{2}\right)^2 - \frac{3}{2}\cdot\frac{5}{2}}{2\cdot\frac{3}{2}\cdot\frac{5}{2}} = -\frac{2}{5}, \qquad (4\text{-}6)$$

and proceeding with a data analysis of the experimental results we find

$$I_{CDAD}(\theta=\tfrac{\pi}{4}) = A_0\,\bar{\bar{\beta}}_2 \approx 0.12 \quad \textit{for the } 7\,^2P_{3/2} \textit{ state,} \qquad (4\text{-}7)$$

$$A_0\,\bar{\bar{\beta}}_2 \approx 0.40 \quad \textit{for the } 8\,^2P_{3/2} \textit{ state.}$$

Thus for the above alignment, $\bar{\bar{\beta}}_2 \approx -0.30$, for the $7^2P_{3/2}$ state and $\bar{\bar{\beta}}_2 \approx -1.0$, for the $8^2P_{3/2}$ state.

For diagnostics of the beam alignment, angular distributions of the $7^2P_{1/2}$ and $8^2P_{1/2}$ using similar pump-probe methods were also measured, and as expected, no CDAD effects were observed. The PEADs from the $7^2P_{1/2}$ using both left and right circularly polarized light are shown in figure 4.40. There was no difference between probing the resonant state with either left or right circularly polarized light. For completion, the PEADs from the $8^2P_{1/2}$ using both left and right circularly polarized light are shown in figure 4.41. Again, no difference between the two PEADs was observed, as expected.

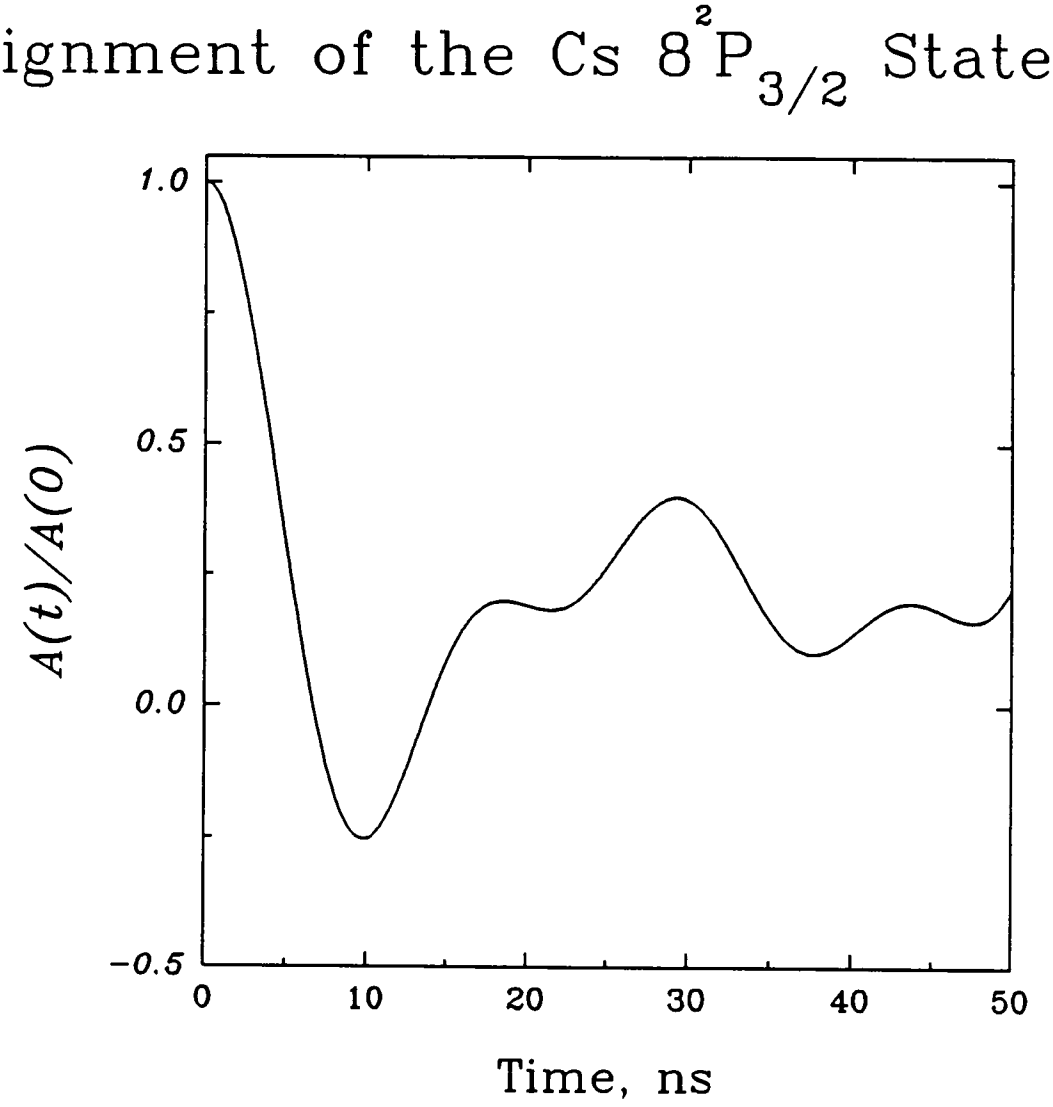

Fig. 4.39. Time dependence of the alignment for the $8^2P_{3/2}$ state. Calculated using the model of Green and Zare[5] and the experimental data cited by Arimondo, *et al.*[33]

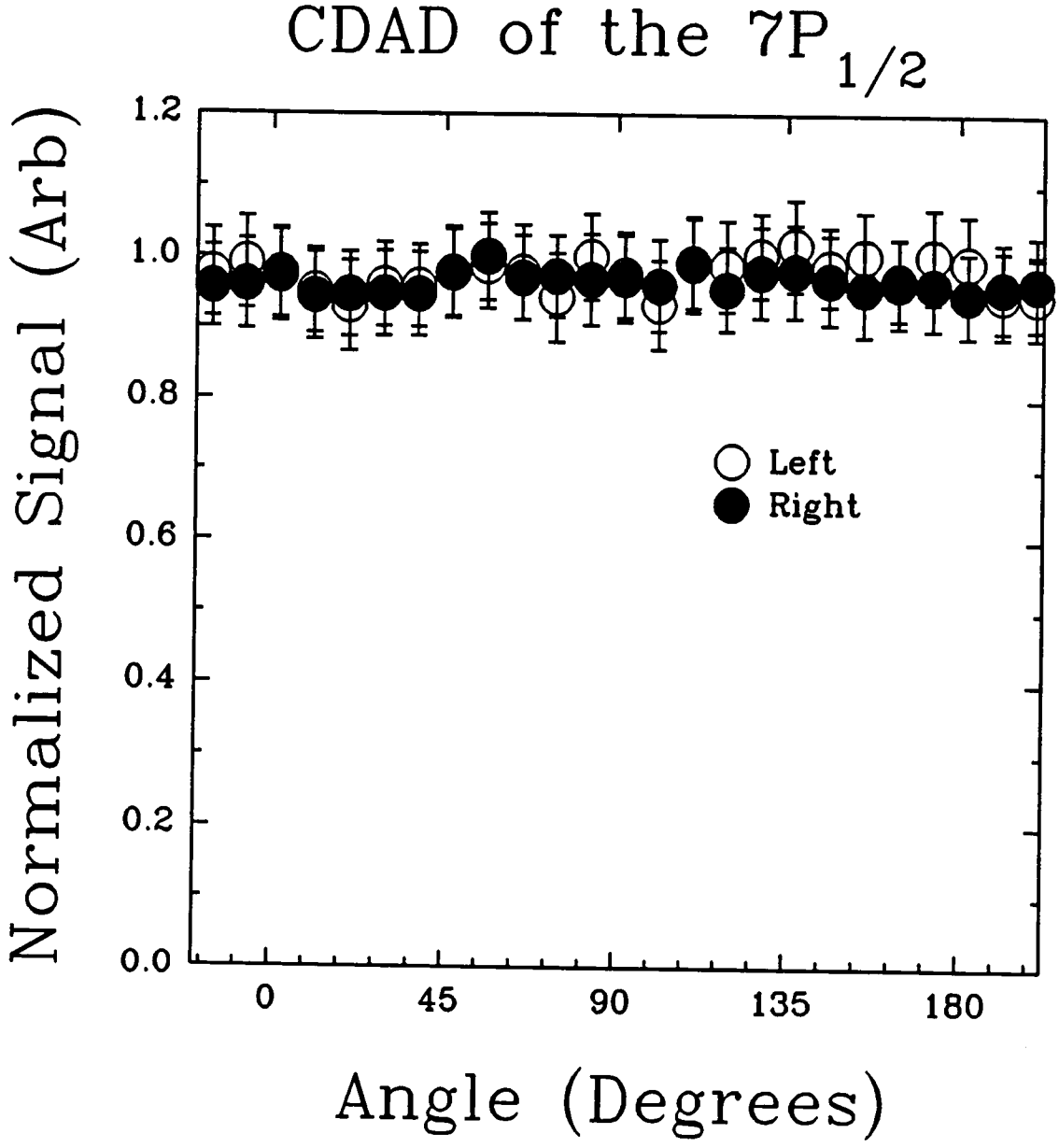

Fig. 4.40. Photoelectron angular distributions from the $7^2P_{1/2}$ state of cesium using both left and right circular polarized light.

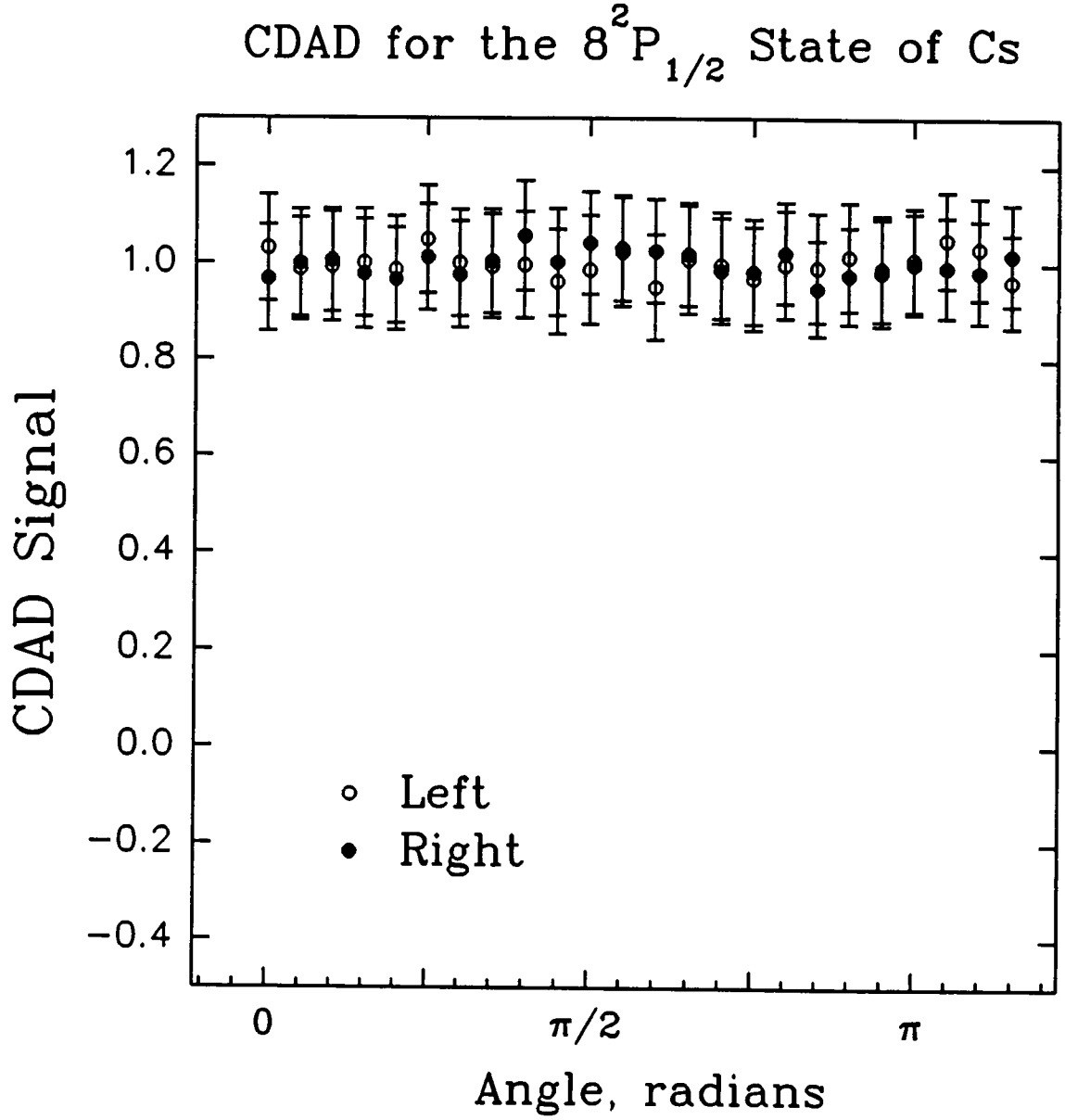

Fig. 4.41. PEADs from the $8^2P_{3/2}$ state of cesium using $\nu_2 = 532$ nm.

B-2. *n*P STATES OF RUBIDIUM

The (1 + 1′) resonantly enhanced photoelectron angular distributions of the $n^2P_{3/2}$ (n = 5, 6) states of rubidium using both left, and right circularly polarized photons were also measured using the experimental setup depicted in figure 3.4. The experiments on the $n^2P_{3/2}$ states were done using the tunable output of the dye laser to resonantly excite the state, and the third harmonic (λ = 355 nm) to ionize the atom.

The results of these measurements are shown in figures 4.42-43. An analysis of these CDAD measurements yields

$$I_{CDAD}(\theta=\tfrac{\pi}{4}) = A_0 \bar{\bar{\beta}}_2 \approx 0.25 \quad \textit{for the } 5^2P_{3/2} \textit{ state,} \qquad \textbf{(4-8)}$$

$$A_0 \bar{\bar{\beta}}_2 \approx 0.20 \quad \textit{for the } 6^2P_{3/2} \textit{ state.}$$

This gives a $\bar{\bar{\beta}}_2 \approx$ -0.62 for the $5^2P_{3/2}$ and $\bar{\bar{\beta}}_2 \approx -0.50$ for the $6^2P_{3/2}$.

At this time there are no theoretical calculations that predict the magnitude of the circular dichroism in the photoelectron angular distribution from state in rubidium, although we may expect that the CDAD in the states of rubidium be of the same order of magnitude as that predicted for the resonant states of cesium without considering hyperfine depolarization. As discussed in section (IV.A-3), rubidium states exhibit a relatively smaller hyperfine splitting with corresponding longer decoupling times, and are therefore less affected by hyperfine depolarization. The time dependence of the $5^2P_{3/2}$ state is show in figure 4.44. The comparison of the time dependence of the alignment of the $6^2P_{3/2}$ state of rubidium with that of the $7^2P_{3/2}$ of cesium is shown in Figure 4-45.

For comparison, angular distributions using the same experimental setup were measured on the $n^2P_{1/2}$ states, and as expected, no significant difference was observed between the PEADs obtained using left circularly polarized light, and the PEADs obtained using right circularly polarized. We omit presentation of these results.

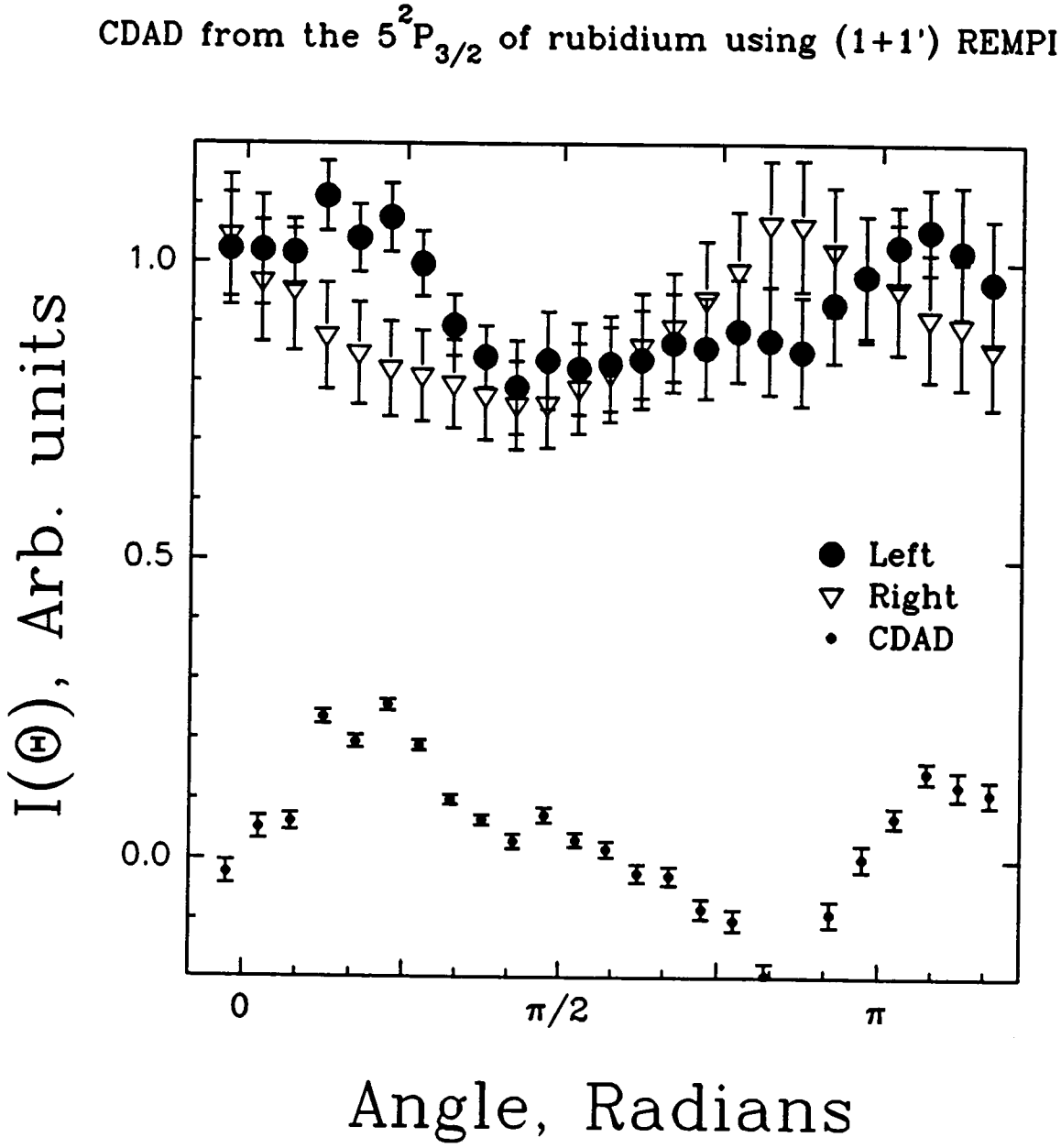

Fig. 4.42. CDAD of the $5^2P_{3/2}$ state of rubidium, using (1 + 1') REMPI. Ionization with 355 nm.

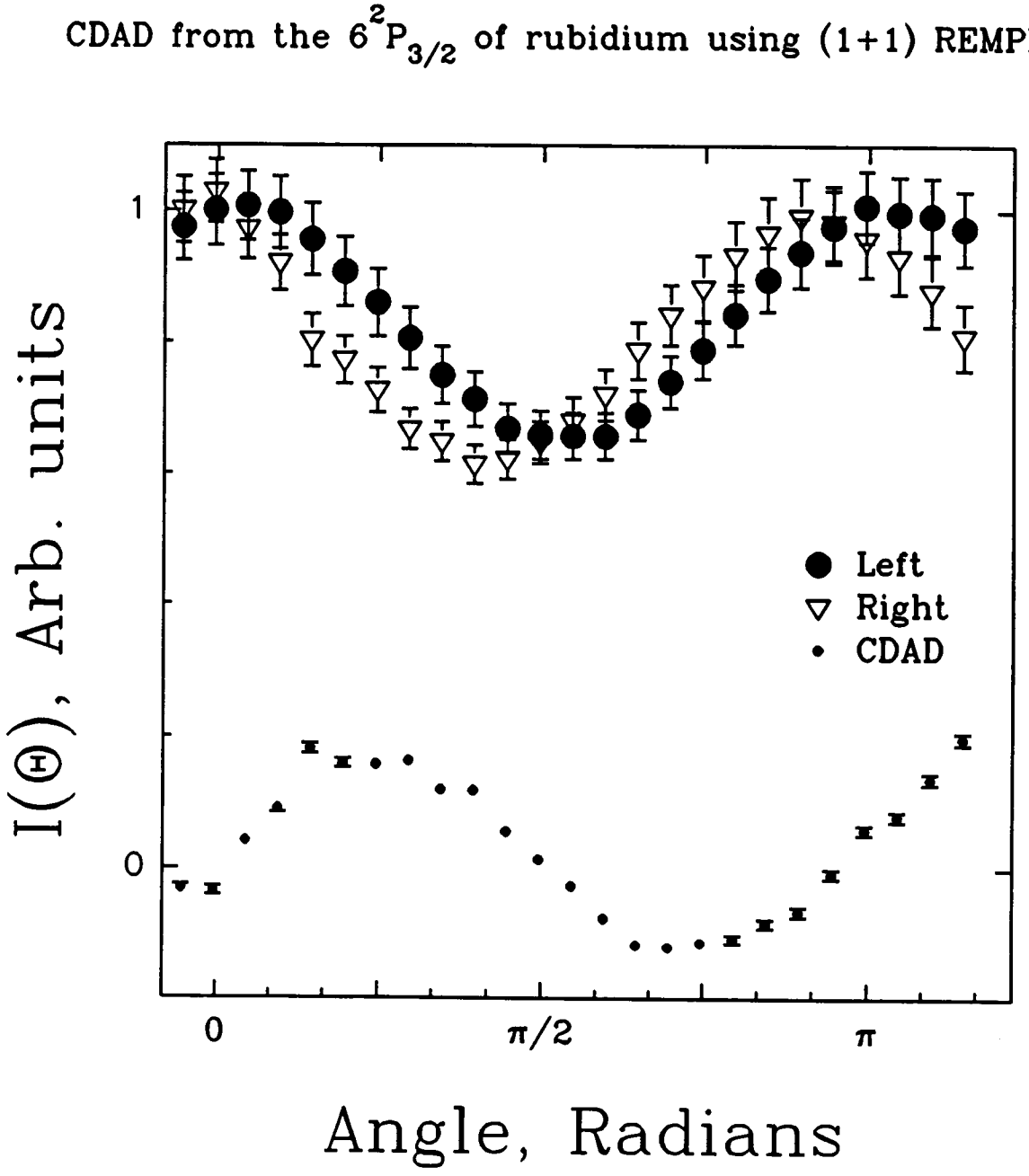

Fig. 4.43. CDAD of the $6^2P_{3/2}$ state of rubidium, using (1 + 1′) REMPI. Ionization with 355 nm.

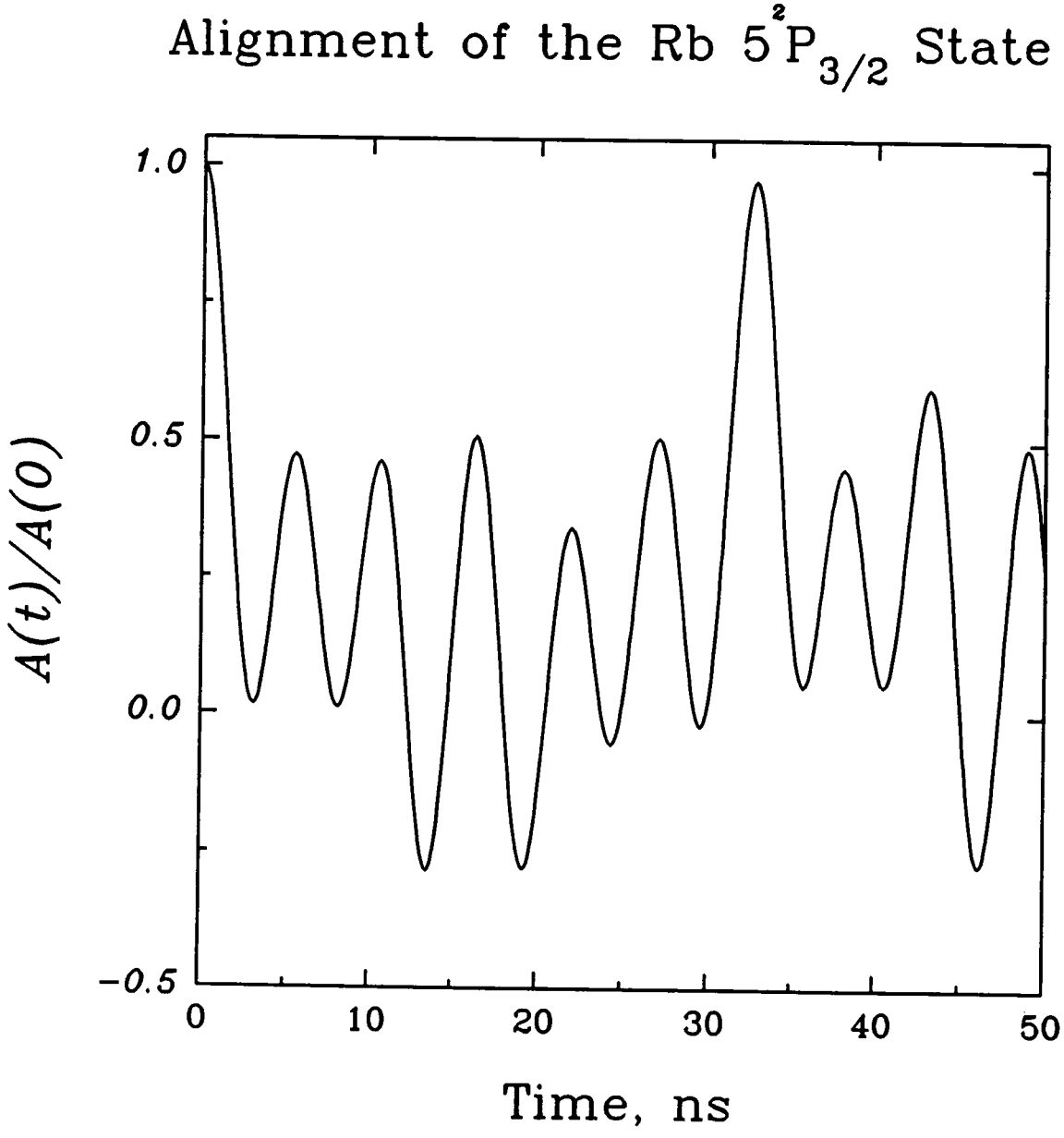

Fig. 4.44. Time dependence of the alignment of the $5^2P_{3/2}$ state of rubidium.

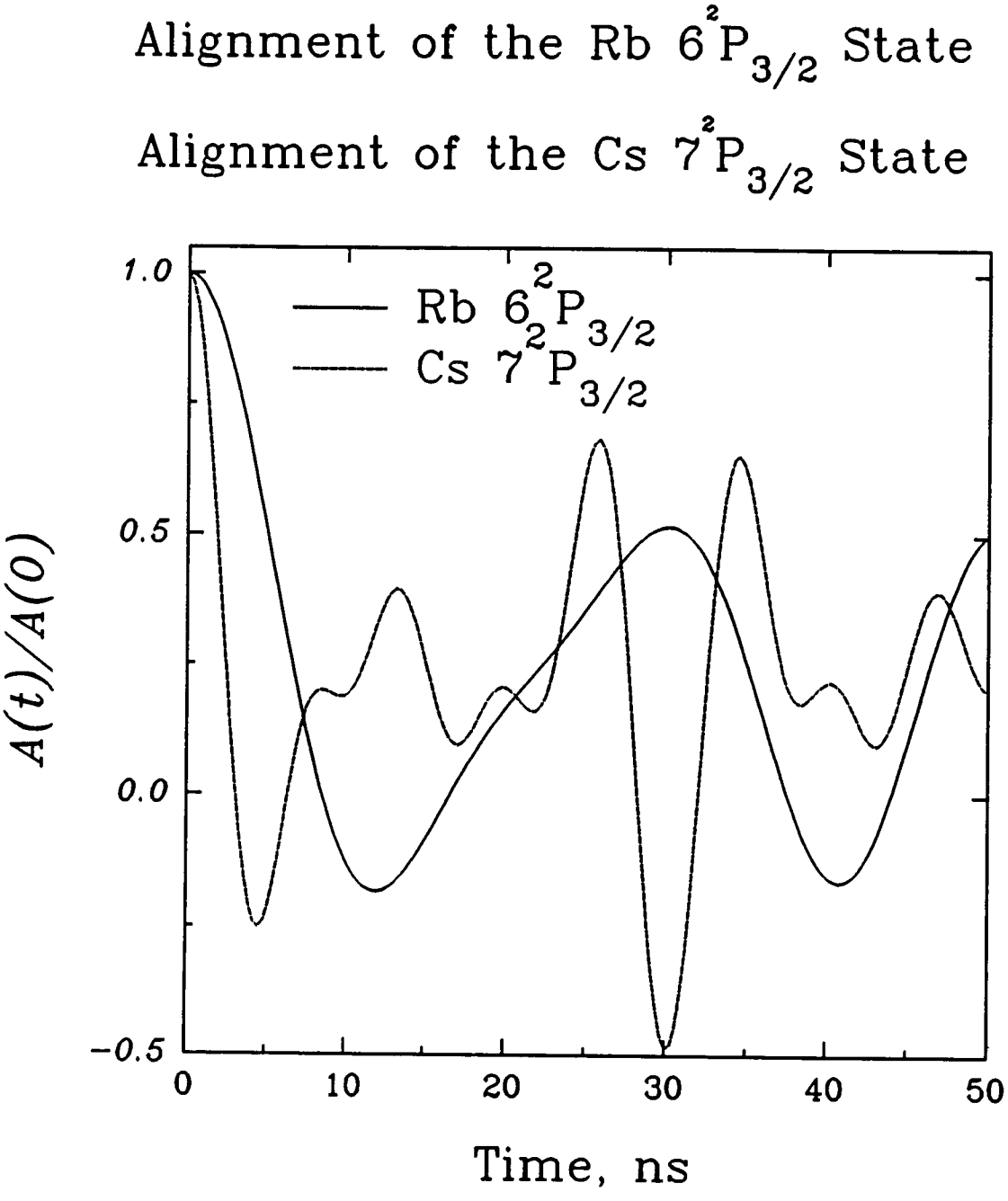

Fig. 4.45. Comparison of the time dependence of the alignment of the second p state of rubidium and cesium.

CHAPTER V

SUMMARY

The photoelectron angular distributions of several excited states of cesium and rubidium were measured using resonantly enhanced multiphoton ionization techniques. The (2 + 1) PEADs for the *ns* states of cesium verified the variation of the asymmetry parameter β_2 from the constant value of two (2) predicted by including relativistic (spin-orbit) coupling in the continuum. The asymmetry parameters β_2 were found to vary from $+1.23$ for the $8s$ state to about -0.5 for the $12s$ state, in good agreement with theoretical calculations by Pindzola.[31] Relativistic effects are also thought to be observed in the (1 + 1) PEADs of *np* states of cesium, although presently there are no theoretical calculations to substantiate this hypothesis.

Comparison of experiment and theory for the (1 + 1) and (1 + 1′) PEADs for the *np* states of cesium and rubidium demonstrated the effects of depolarization of the alignment of the intermediate state due to hyperfine coupling. Depolarization of the alignment due to hyperfine coupling of the intermediate state was also examined by studies of circular dichroism on the photoelectron angular distributions (CDAD). Alignment of the $7^2P_{3/2}$ and $8^2P_{3/2}$ states of cesium and the $5^2P_{3/2}$ and $6^2P_{3/2}$ states of rubidium, created by resonant excitation of the ground state with plane polarized light, was probed using left and right circularly polarized light in the ionization step and CDAD. The observed CDAD of the $7^2P_{3/2}$ was smaller than that predicted by theoretical calculations.[74] However, better agreement between experiment and theory was obtained by multiplying the theoretical calculations by Dubs, *et al.*[74] by the long time depolarization limit of hyperfine coupling for the $7^2P_{3/2}$ state based on the hyperfine depolarization model of Greene and Zare.[5] The observed CDAD effects for the $8^2P_{3/2}$ state of cesium and the $5^2P_{3/2}$ and $6^2P_{3/2}$ states of rubidium could not be directly compared to theory due to nonexistence of theoretical calculations. These experimental results were the first observation of circular dichroism effects on the photoelectron angular distributions in an atomic system.

BIBLIOGRAPHY

BIBLIOGRAPHY

1. Joseph Berkowitz, "Photoabsorption, Photoionization, and Phoelectron Spectroscopy", Academic Press, New York (1979).

2. S. L. Chin and P. Lambropoulos, "Multiphoton Ionization of atoms" , Academic Press, Orlando, Florida (1984).

3. J. Cooper and R. N. Zare "Lectures in Theoretical Physics" (S. Geltman, K. T. Mahanthapa, and W. E. Brittin, eds.), Vol. **XI-C**, pp. 317-337. Gordon and Breach, New York (1969).

4. S. J. Smith, G. Leuchs, *Advances in Atomic and Molecular Physics*, **24**, 157-221, Academic Press, Inc. (1988).

5. C. H. Greene and R. N. Zare, *American Review Physical Chemistry*, **33** 119-150 (1982).

6. R. L. Dubs, S. N. Dixit, and V. McKoy, *Physical Review Letters*, **54**, 1249 (1985).

7. R. L. Dubs, S. N. Dixit, and V. McKoy, *Journal of Chemical Physics*, **85**, 6267 (1986).

8. R. L. Dubs, S. N. Dixit, and V. McKoy, *Journal of Chemical Physics*, **85**, 656 (1986).

9. M. A. Chaffee, *Physics Review*, **37**, 1233 (1931).

10. Yi-Yian, D. S. Elliot, *Physical Review A*, **45**, 281 (1992); **46**, 1339 (1992).

11. Kurt Gottfried, "Quantum Mechanics: *Volume I: Fundamentals*", W.A. Benjamin, Inc., Reading, Massachusetts (1966).

12. A. F. Starace, "Handbuch der Physik, Band XXXI" (W. Mehlhorn, ed.), p. 1, Springer-Verlag, Berlin (1982).

13. Robert D. Cowan, "The Theory of Atomic Structure and Spectra", University of California Press, Berkeley (1981).

14. Robert N. Compton and John C. Miller, "Laser Applications in Physical Chemistry", 221-306, Marcel Dekker, Inc., New York and Basel (1989).

15. C. K. Jen, "Encyclopedia of Physics", 1121, Addison-Wesley Publishing Company, Inc. Reading, Massachusetts (1981).

16. J. E. Bjorkholm and P.F. Liao, *International Conference on Laser Spectroscopy* **43**, 176-185 (1975).

17. D. C. Hanna, M. A. Yuratich, and D. Cotter, "Nonlinear Optics of Free Atoms and Molecules", 51-55, 181-185 (1979).

18. Richard N. Zare, "Angular Momentum, Understanding Spatial Aspects in Chemistry and Physics", 226-238, John Wiley & Sons, Inc. (1988).

19. L. C. Biedenharn, J. D. Louck, Peter A. Carruthers, "Angular Momentum in Quantum Physics, Theory and Application", Addison-Wesley Publishing Company, Reading, Massachusetts (1981).

20. G. Laplanche, M. Jaouen, and A. Rachman, *Journal of Physics B: Atomic and Molecular Physics*, **19** 79-100 (1986).

21. C. N. Yang, *Physics Review.* **74**, 764 (1948).

22. D. Dill, S. T. Manson, and A. F. Starace, *Physical Review Letters*, **32** 971 (1974).

23. A. F. Starace, R. H. Rast, and S. T. Manson, *Physical Review Letters*, **38** 1522 (1977).

24. E. S. Chang and K. T. Taylor, *Journal of Physics B*, **11**, L507 (1978).

25. S. Shahabi, *Physics Letters*, **72A**, 212 (1979).

26. V. Jacobs, *Journal of Physics B*, **5**, 2257 (1972).

27. T. E. H. Walker and J. T. Waber, *Physical Review Letters*, **30**, 307 (1973); *Journal of Physics B*, **6**, 1165 (1973); **7**, 674 (1974).

28. G. V. Marr, *Journal Physics B*, **7**, L47 (1974).

29. W. Ong and S. T. Manson, *Physics Letters*, **66A**, 17 (1978).

30. K.-N. Huang and A. F. Starace, *Physical Review A*, **19**, 2335 (1979).

31. M. S. Pindzola, *Physical Review A*, **32**, 1883 (1985).

32. R. N. Compton, J. A. D. Stockdale, C. D. Cooper, X. Tang, P. Lambropoulos, *Physical Review A*, **30**, 1766-1774 (1984).

33. E. Arimondo, M. Inguscio, and P. Violino, *Reviews of Modern Physics*, **49**, 31 (1977).

34. K. Smith and J. W. Stephenson, Argonne National Laboratory Reports ANL-5776 (1957) and ANL-5860 (1958).

35. S. H. Koozekanani, "9j Symbols", Engineering Publications, Ohio State University, Columbus (1972).

36. N. A. Cherepkov, *Chemical Physics Letters*, **87**, 344 (1982).

37. R. Parzyński, *Acta. Phys. Pol. A*, **57**, 49 (1980).

38. B. Ritchie, *Physical Review A.*, **12**, 567 (1975).

39. B. Ritchie, *Physical Review A*, **13**, 1411 (1976).

40. B. Ritchie, *Physical Review A.* **14**, 359 (1976).

41. N. A. Cherepkov, *Journal of Physics B.*, **16**, 1543 (1983).

42. J. R. Appling, M. G. White, *J. Chem. Phys.*, **85**, 6803 (1986).

43. S. N. Dixit and P. Lambropoulos, *Physics Review A*, **27**, 861 (1983).

44. L. Cuéllar, C. S. Feigerle, H. S. Carman, Jr. and R. N. Compton, *Physical Review A.*, **43**, 6437 (1991).

45. H. A. Bethe, and E. E. Saltpeter, "Quantum Mechanics of One and Two Electron Systems", Springer-Verlag, Berlin, (1957).

46. D. W. Walker, *Adv. Phys.*, **20**, 260, (1971).

47. J. J. Matese, and W. R. Johnson, *Physical Review A*, **140**, 1 (1965).

48. U. Fano, *Physical Review*, **178**, 131 (1969); **184**, 250 (1969).

49. D. W. Norcross, *Physical Review A*, **7**, 606 (1973).

50. L. E. Cuéllar, R. N. Compton, H. S. Carman, C. S. Feigerle, *Physical Review Letters*, **65**, 163 (1990).

51. H. Kaminski, J. Kessler, and K. J. Kollath, *Physical Review Letters*, **45**, 1161 (1980).

52. Eugene Hecht, "Optics, Second Edition", Addison-Wesley Publishing Company, Reading, Massachusetts, 1987.

53. Varian VacSorb Operating Manual and Instructions.

54. Kent R. Wilson and R. J. Ivanetich, Lawrence Radiation Laboratory AES Contract W-7405-eng-48, (1964); Howard A. Jones and Irving Langmuir, *General Electric Review*, **30**, 310-320, 356-361, and 408-412 (1927).

55. Stephen K. O'Brien, "Turbo Pascal: Advanced Programmer's Guide", Borland • Osborne/McGraw • Hill Programming Series, Osborne McGraw-Hill, Berkeley (1988).

56. Hugh D. Young, "Statistical Treatment of Experimental Data", McGraw-Hill Book Company, Inc., New York, (1962).

57. Phillip R. Bevington, "Data Reduction and Error Analysis for the Physical Sciences", McGraw-Hill Book Company, New York, (1969).

58. Charlotte E. Moore, "Atomic Energy Levels", Circular of the National Bureau of Standards 467, Washington, D. C. (1992).

59. K.-H. Weber and Craig J. Sansonetti, *Physical Review A*, **35**, 4650 (1987).

60. A. Niehaus and M. W. Ruf, *Zeitschrieft fur Physiks*, **252**, 84 (1972).

61. J. L. Dehmer and D. Dill, *Physics Review Letters*, **37**, 1049 (1976).

62. W. Ong and S. T. Manson, *Journal of Physics B*, **11**, L65 (1978).

63. W. R. Johnson and K. T. Cheng, *Physics Review Letters*, **40**, 1167 (1978); *Physics Review A*, **20**, 978 (1979).

64. N. A. Cherepkov, *Physics Letters*, **66A**, 204 (1978).

65. M. G. White, S. H. Southworth, P. Kobrin, E. D. Poliakoff, R. A. Rosenberg, and D. A. Shirley, *Physics Review Letters*, **43**, 1661 (1979).

66. K.-N. Huang and A. F. Starace, *Physics Review A*, **21**, 697 (1980).

67. A. Fahlman, T. A. Carlson, and M. O. Krause, *Physics Review Letters*, **50**, 1114 (1983).

68. A. Fahlman, M. O. Krause, and T. A. Carlson, *Journal Physics B*, **17**, L217 (1984).

69. H. Derenbach and V. Schmidt, *Journal Physics B*, **16**, L337 (1983).

70. H. Derenbach and V. Schmidt, *Journal Physics B*, **17**, 83 (1984).

71. J. Tulkki, *Physics Review Letters*, **62**, 2817 (1989).

72. J. A. R. Samson (unpublished); (private communication to R. N. Compton).

73. F. Rasetti. *Zeitschrift fur Physik*, **59**, 680-686 (1930).

74. R. L. Dubs, S. N. Dixit, and V. McKoy, private communication.

APPENDICES

APPENDIX A

RANGES OF THE β PARAMETERS

β_2 VS. β_4

Calculation of the ranges of the β parameters for the PEAD in the case j=3/2..

Computation carried out both manually and using Maple V Release 2.0.

Reset system.

```
> restart;
```

Define the Legendre Polynomials:

```
> p2:=orthopoly[P](2,x); p4:=orthopoly[P](4,x); p6:=orthopoly[P](6,x);
```

$$p2 := \frac{3}{2}x^2 - \frac{1}{2}$$

$$p4 := \frac{35}{8}x^4 - \frac{15}{4}x^2 + \frac{3}{8}$$

$$p6 := \frac{231}{16}x^6 - \frac{315}{16}x^4 + \frac{105}{16}x^2 - \frac{5}{16}$$

Define the expressions for the angular distributions:

```
> i2:=1+p2*b2;  i4:= i2+ p4*b4;  i6:=i4+p6*b6;
```

$$i2 := 1 + \left(\frac{3}{2}x^2 - \frac{1}{2}\right) b2$$

$$i4 := 1 + \left(\frac{3}{2}x^2 - \frac{1}{2}\right) b2 + \left(\frac{35}{8}x^4 - \frac{15}{4}x^2 + \frac{3}{8}\right) b4$$

$$i6 := 1 + \left(\frac{3}{2}x^2 - \frac{1}{2}\right) b2 + \left(\frac{35}{8}x^4 - \frac{15}{4}x^2 + \frac{3}{8}\right) b4$$

Define b2, b4, and b6 as constants, and x as a the variable:

```
> D(b2) := 0;  D(b4) := 0; D(b6) := 0; D(x):=1;
```

$$D(b2) := 0$$

$$D(b4) := 0$$

$$D(0) := 0$$

$$D(x) := 1$$

Recalculate with b6=0.

Compute the derivative of the angular distribution:

```
> g:=factor(D(subs(b6=0,i6)));
```

$$g := \frac{1}{2} x \left(35\, b4\, x^2 + 6\, b2 - 15\, b4\right)$$

Find the zeros of the derivative of the distribution in terms of the variable x:

```
> s:=solve(g=0,x);
```

$$s := 0, \frac{1}{35}\frac{\sqrt{105}\sqrt{5\, b4 - 2\, b2}}{\sqrt{b4}}, -\frac{1}{35}\frac{\sqrt{105}\sqrt{5\, b4 - 2\, b2}}{\sqrt{b4}}$$

We know that D(cos(theta)) produces sin(theta), and thus we also have sin(theta)=0.

```
> x1:=1;  x2:=s[1];  x3:=s[2];  x4:=s[3];
```

$$x1 := 1$$

$$x2 := 0$$

$$x3 := \frac{1}{35}\frac{\sqrt{105}\sqrt{5\, b4 - 2\, b2}}{\sqrt{b4}}$$

$$x4 := -\frac{1}{35}\frac{\sqrt{105}\sqrt{5\, b4 - 2\, b2}}{\sqrt{b4}}$$

In the angular distribution expression we only have even terms.

```
> r1:= x3^2;   r3:=x3^4;
```

$$r1 := \frac{3}{35}\frac{5\, b4 - 2\, b2}{b4}$$

$$r3 := \frac{9}{1225}\frac{(5\, b4 - 2\, b2)^2}{b4^2}$$

(Others give rise to the same conditions, except in the case b6 < > 0).

These solutions must correspond to the cosines of real angles, thus 0 <= ri <= 1.

```
> r10:= 0<=r1 ; r11:=  r1<=1;
```

$$r10 := 0 \le \frac{3}{35}\,\frac{5\,b4 - 2\,b2}{b4}$$

$$r11 := \frac{3}{35}\,\frac{5\,b4 - 2\,b2}{b4} \le 1$$

These inequalities give rise to bounds on the β parameters, that hold only when the minima is given by x3 or x4.

```
> b4<>0; l1:= solve(r1=0,b2); l2:= solve(r1=1,b2);
```

$$b4 \neq 0$$

$$l1 := \frac{5}{2}\,b4$$

$$l2 := -\frac{10}{3}\,b4$$

The angular distribution must be nonnegative for all of the minima. Thus,

```
> b6:= 0; h[1]:=subs(x=x1,i6); h[2]:=subs(x=x2,i6); h[3]:=simplify(subs(x=x3,i6));
```

$$b6 := 0$$

$$h_{[1]} := 1 + b2 + b4$$

$$h_{[2]} := 1 - \frac{1}{2}\,b2 + \frac{3}{8}\,b4$$

$$h_{[3]} := -\frac{1}{70}\,\frac{-70\,b4 - 10\,b4\,b2 + 9\,b2^2 + 30\,b4^2}{b4}$$

Also obtain h[3] using x=x4.

h[1], h[2] and h[3] give rise to bounds on the β parameters.

```
> plane1 := solve(h[1]=0,b2); plane2:= solve(h[2]=0,b2); surf1:=
> solve(factor(h[3])=0,b2);
```

$$plane1 := -1 - b4$$

$$plane2 := 2 + \frac{3}{4}\,b4$$

$$surf1 := \frac{5}{9}\,b4 + \frac{1}{9}\sqrt{35}\,\sqrt{-7\,b4^2 + 18\,b4},\ \frac{5}{9}\,b4 - \frac{1}{9}\sqrt{35}\,\sqrt{-7\,b4^2 + 18\,b4}$$

Define functions to plot. We use the ones we have derived above. First, find where the functions cross.

```
> cross:=simplify(solve(plane1=surf1[1],b4)),
> simplify(solve(plane2=surf1[2],b4)),solve(plane1=plane2,b4),
> solve(surf1[1]=surf1[2],b4);
```

$$cross := \frac{3}{7}, \frac{8}{7}, \frac{-12}{7}, 0, \frac{18}{7}$$

We define the following functions to be used in the procedures w and v (below).

```
> f1:= subs(b4=x,plane1);   f2:= subs(b4=x, plane2);
> f3:= subs(b4=x,surf1[1]); f4:=subs(b4=x,surf1[2]);
```

$$f1 := -1 - x$$

$$f2 := 2 + \frac{3}{4}x$$

$$f3 := \frac{5}{9}x + \frac{1}{9}\sqrt{35}\sqrt{-7x^2 + 18x}$$

$$f4 := \frac{5}{9}x - \frac{1}{9}\sqrt{35}\sqrt{-7x^2 + 18x}$$

Unfortunately, we were not able to use variables in the procedures below. Type in.

```
> w:=proc(x) if (x<=cross[1]) then -1-x else
> 5*x/9-1/9*sqrt(35)*sqrt(-7*x^2+18*x)  fi end;
  w := proc(x)
           if x <= cross[1] then -1-x
           else 5/9*x-1/9*sqrt(35)*sqrt(-7*x^2+18*x)
           fi
       end
```

```
> v:=proc(x) if (x<=cross[2]) then 2+3*x/4 else
> 5*x/9 + 1/9*sqrt(35)*sqrt(-7*x^2+18*x)  fi end;
  v := proc(x)
           if x <= cross[2] then 2+3/4*x
           else 5/9*x+1/9*sqrt(35)*sqrt(-7*x^2+18*x)
           fi
       end
```

We thus obtain the plot (b2 is the vertical axis, and b4 is the horizontal axis)

```
> plot({w,v},cross[3]..cross[5]);
```

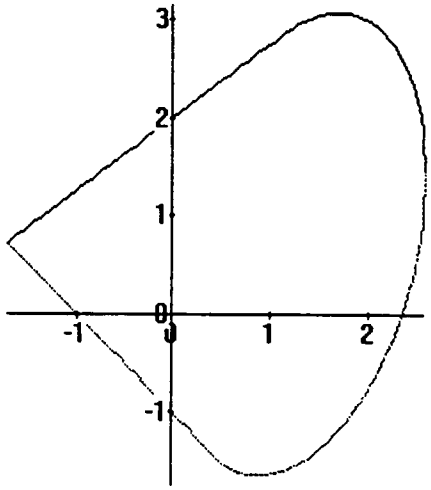

>

Fig. A.1. Limits of β_2 vs. β_4.

APPENDIX B

SIMION STUDIES OF THE TIME-OF-FLIGHT SPECTROMETER

The following pages describe the results of studying the performance of the time-of-flight spectrometer using the SIMION Ions lens program. The "Fast-Adjust" option was used, since the geometry of the spectrometer isn't changed, only the applied voltages to the lower plate, and to the microchannel detector. Grid units correspond to millimeters, so that the plate separation in the interaction region corresponds to 1 inch, at drawing scale approximately of 2:1. Unless otherwise noted, the starting position was about halfway between the plates, or coordinates x=15, y=0 (*x* axis is parallel to the axis of the TOF). The initial electron or ion momentum is considered to be along the axis of the TOF, except in the angular studies for electrons, where the initial direction is changed by 1°. Ions were assumed to have an initial kinetic energy of 0.1 eV, and have a velocity vector perpendicular, *i.e.*, along the *y*-axis, to the axis of the TOF. Ions trajectories are 1 mm apart. Electrons were assumed to have a kinetic energy of 1.61 eV, corresponding approximately to the case of REMPI through the $7^2P_{3/2}$ state of cesium. Low energy electrons were assumed to have a kinetic energy of 0.1 eV.

The studies for ions were conducted by assuming an applied voltage of −2000 V for the front end of the detector, and grounding of the anodes. The studies for electrons were carried out grounding of the front end of the detector, and applying +2000 V to the anodes. The effect of the pushing voltage was studied by varying the voltage in the case of ions from +1000 V to +300 V, and in the case of electrons from 0 V up to −100 V. The time-of-flight tube was grounded for all SIMION calculations. These contidions reflect standard operating conditions for our time-of-flight.

The figures below are representative, but not exclusive of the studies done using SIMION. The results included correspond strictly to last version of the TOF. These studies were used to aid in the understanding of the operation of the time-of-flight

detector. Modifications to the TOF detector used for the experiments were made based on the results of these studies.

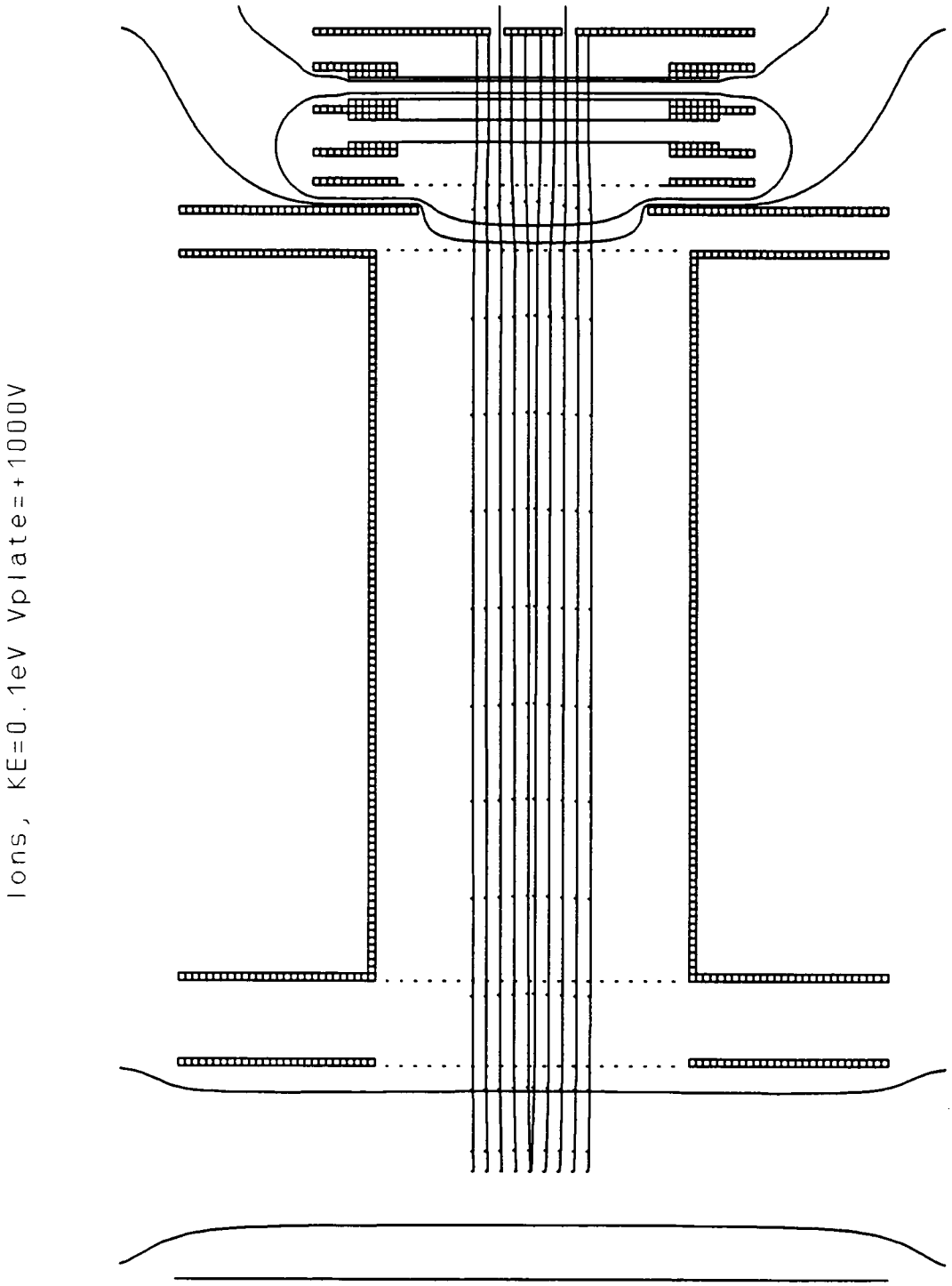

Fig. B.1. Ion trajectories, pushing voltage $V_{plate} = +1000$ V. Contours shown for potential surfaces of +750 V, +125 V, −250 V, −750 V. Tick marks are 0.5 μs apart. Lower plate is the single line at the bottom.

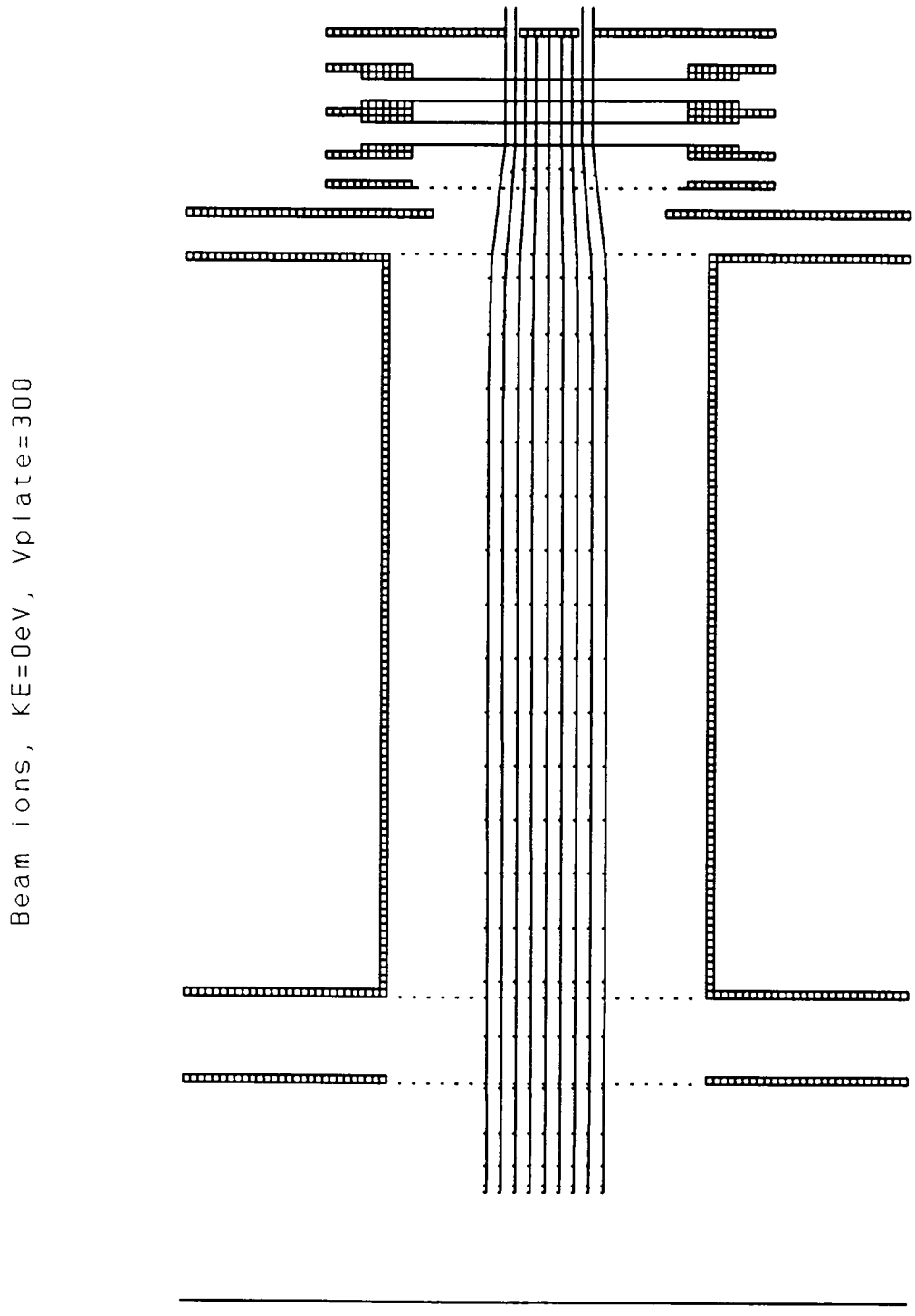

Fig. B.2. Ion trajectories, pushing voltage V_{plate} = +300 V. Tick marks are 500 ns apart. This model provided an idea of the effect of introducing a second grid at the entrance to the microchannel plates.

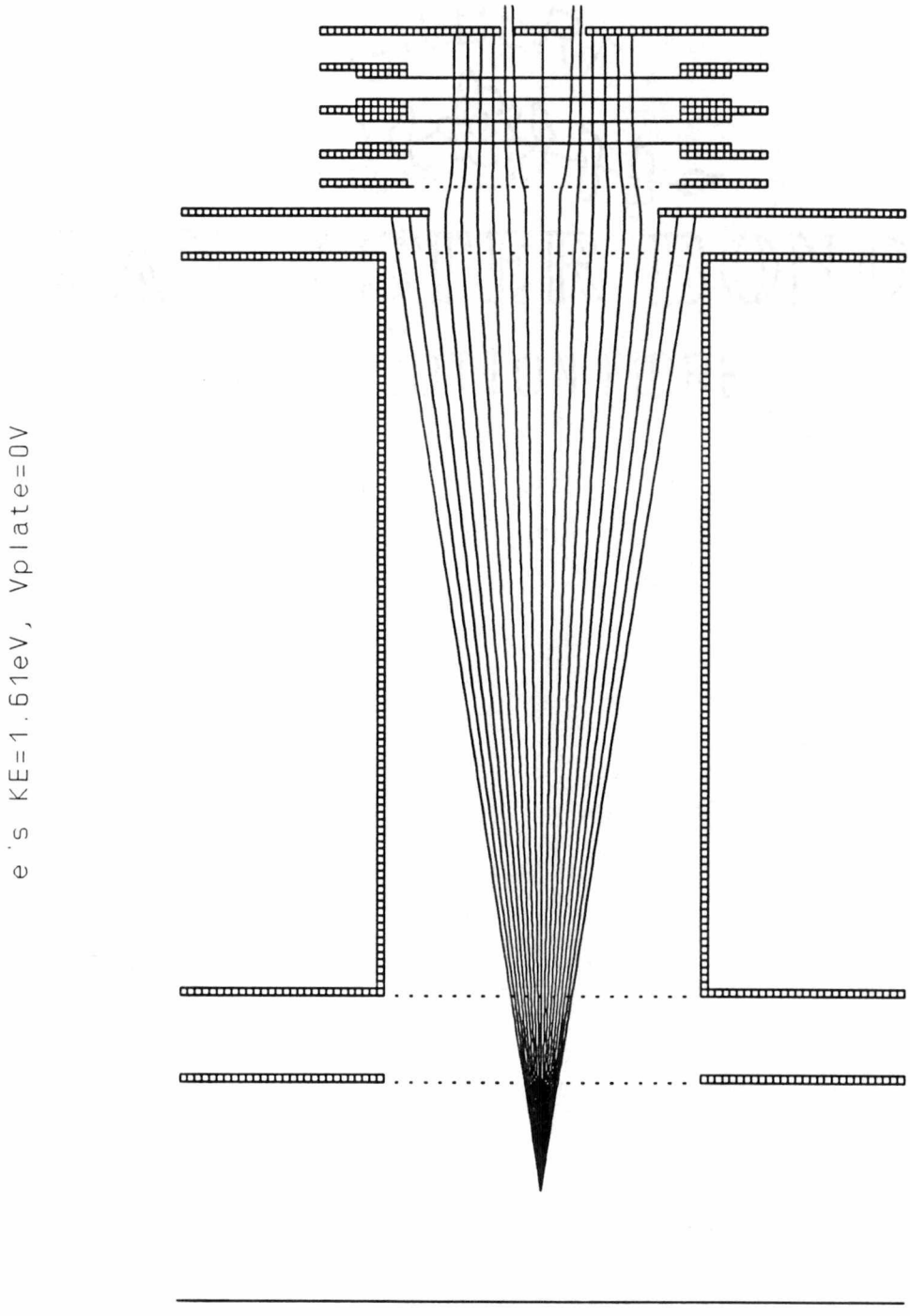

Fig. B.3. Trajectories of electrons with a K.E. of 1.61 eV. $V_{plate} = 0$ V. Trajectories are 1° apart, ranging from -10° to +10°. This model provided information on the effect of installing a second grid.

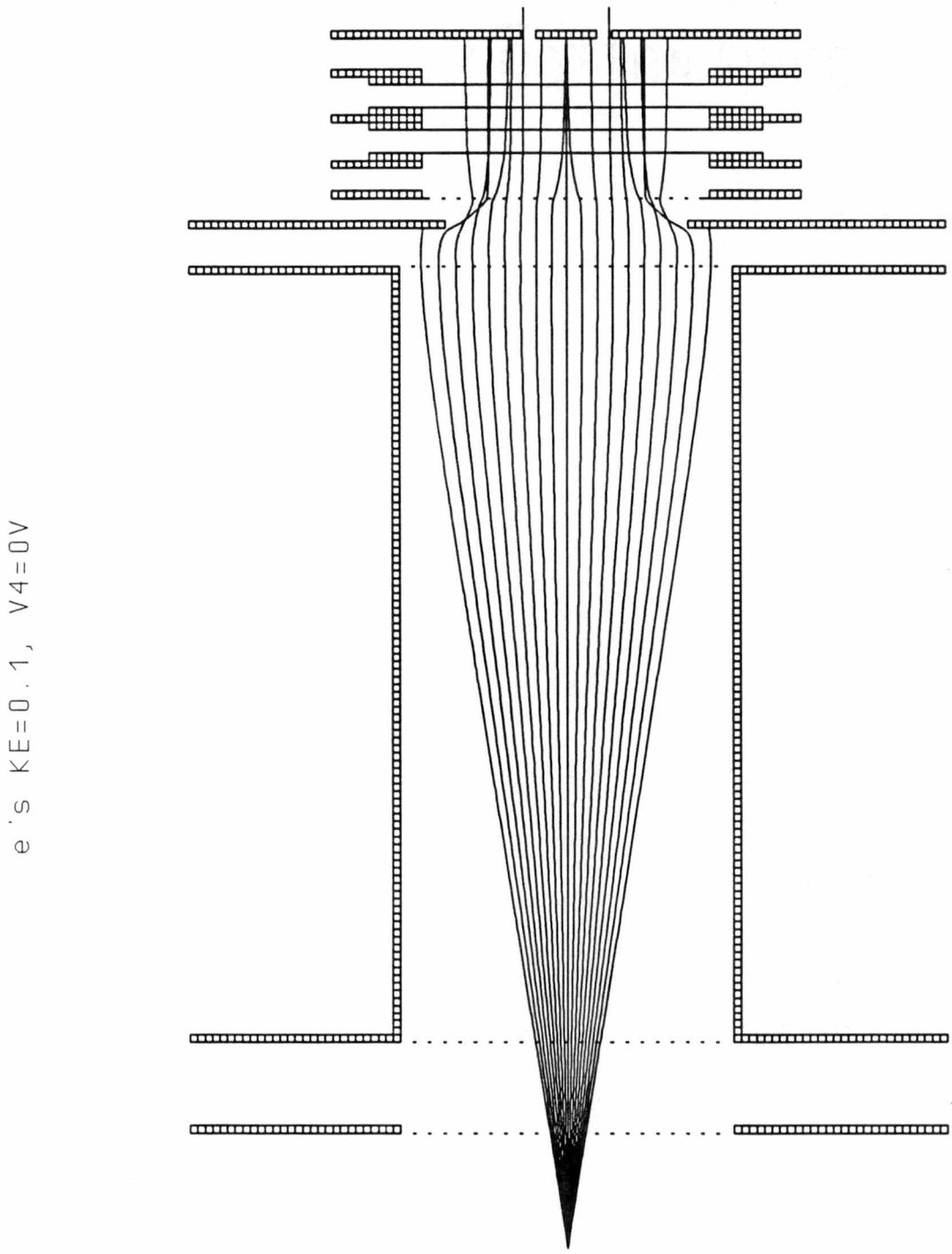

Fig. B.4. Trajectory for 0.1 eV electrons. $V_{plate} = 0$ V. Trajectories are 1° apart, and spanned ±10°.

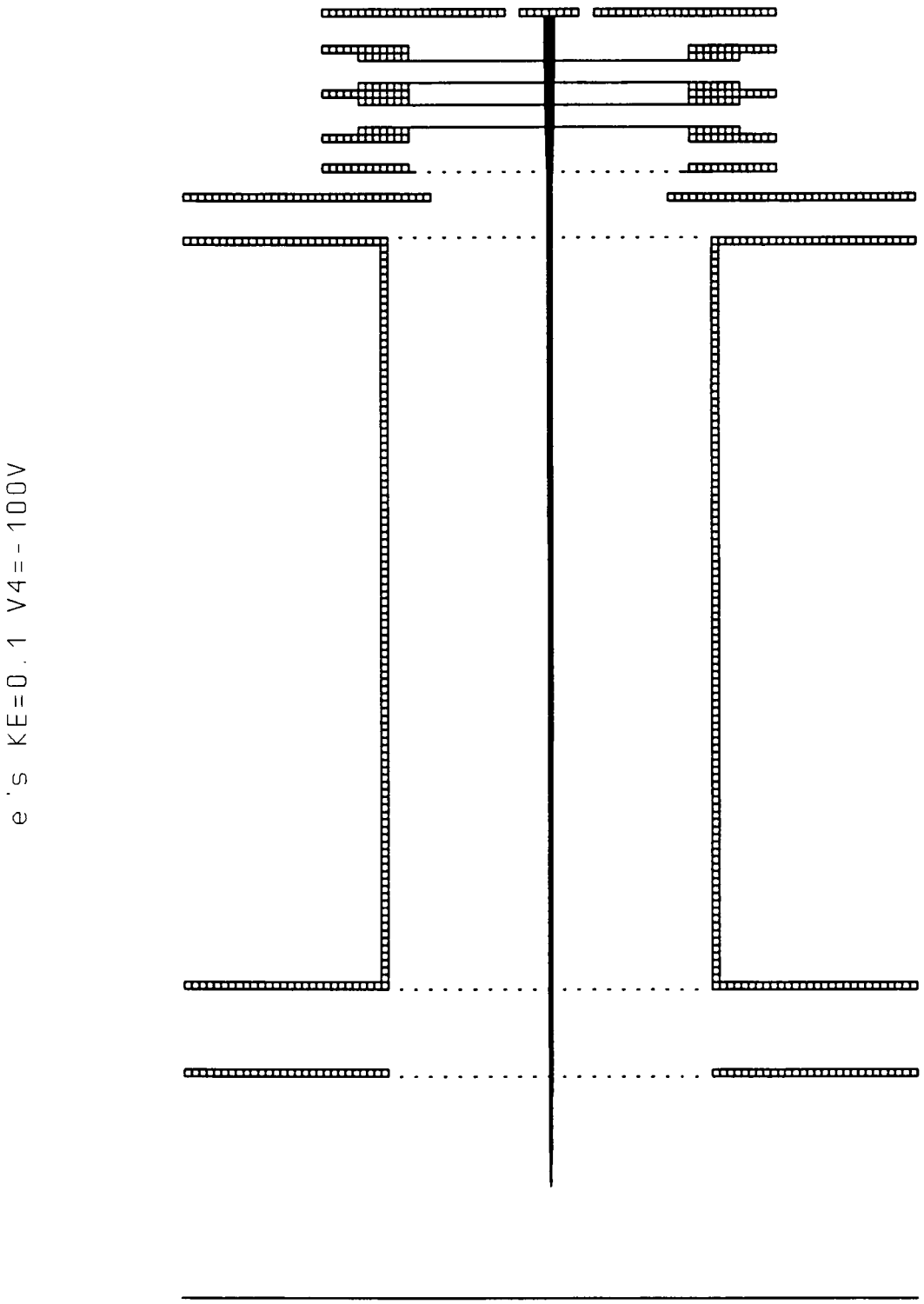

Fig. B.5. Trajectories for 0.1 eV electrons. $V_{plate} = -100$ V. Initial trajectories are 1° apart, and spanned ± 10.

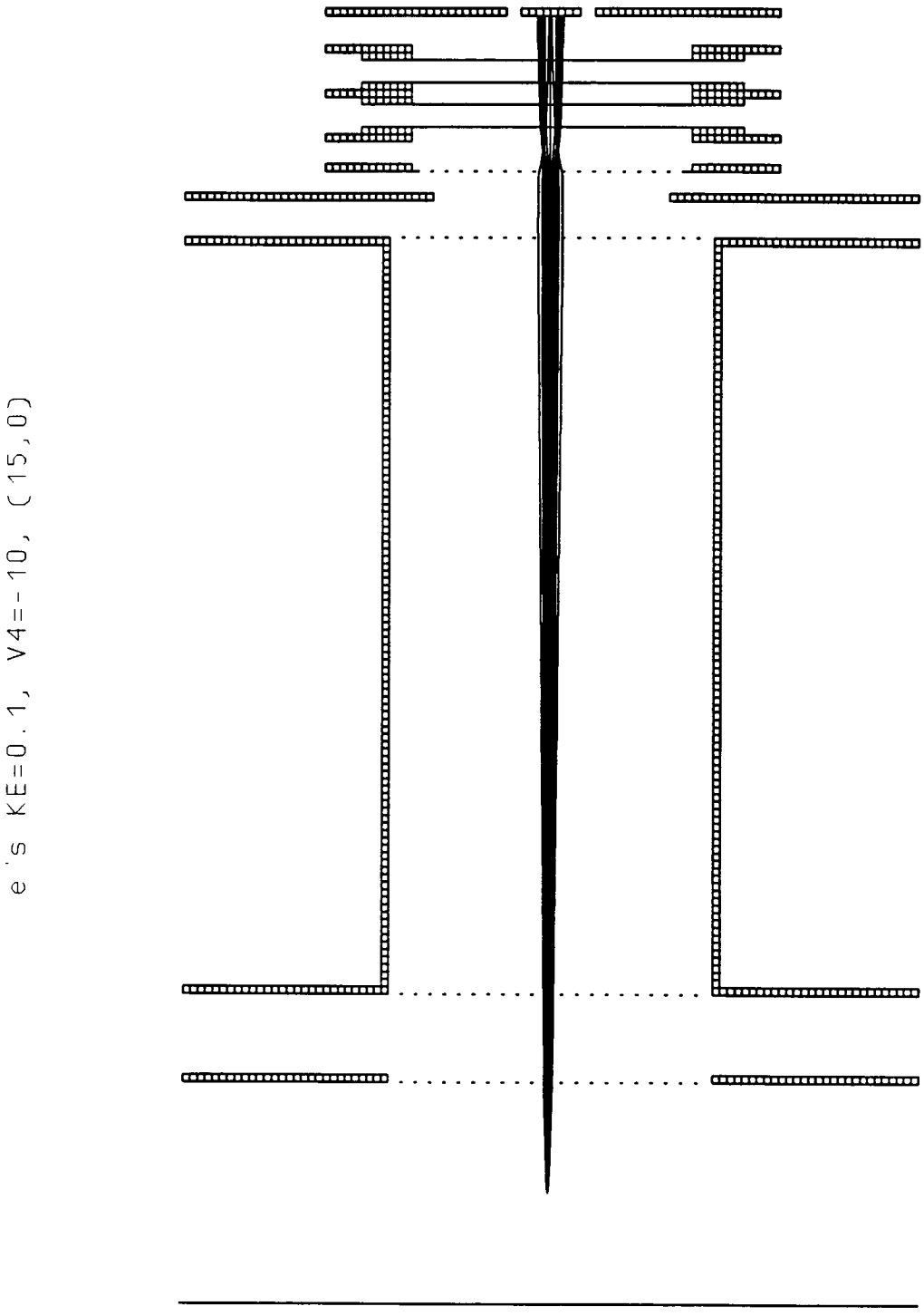

Fig. B.6. Trajectory for 0.1 eV electrons, V_{plate} = -10 V. Initial directions are 1° apart, spanning ±10°.

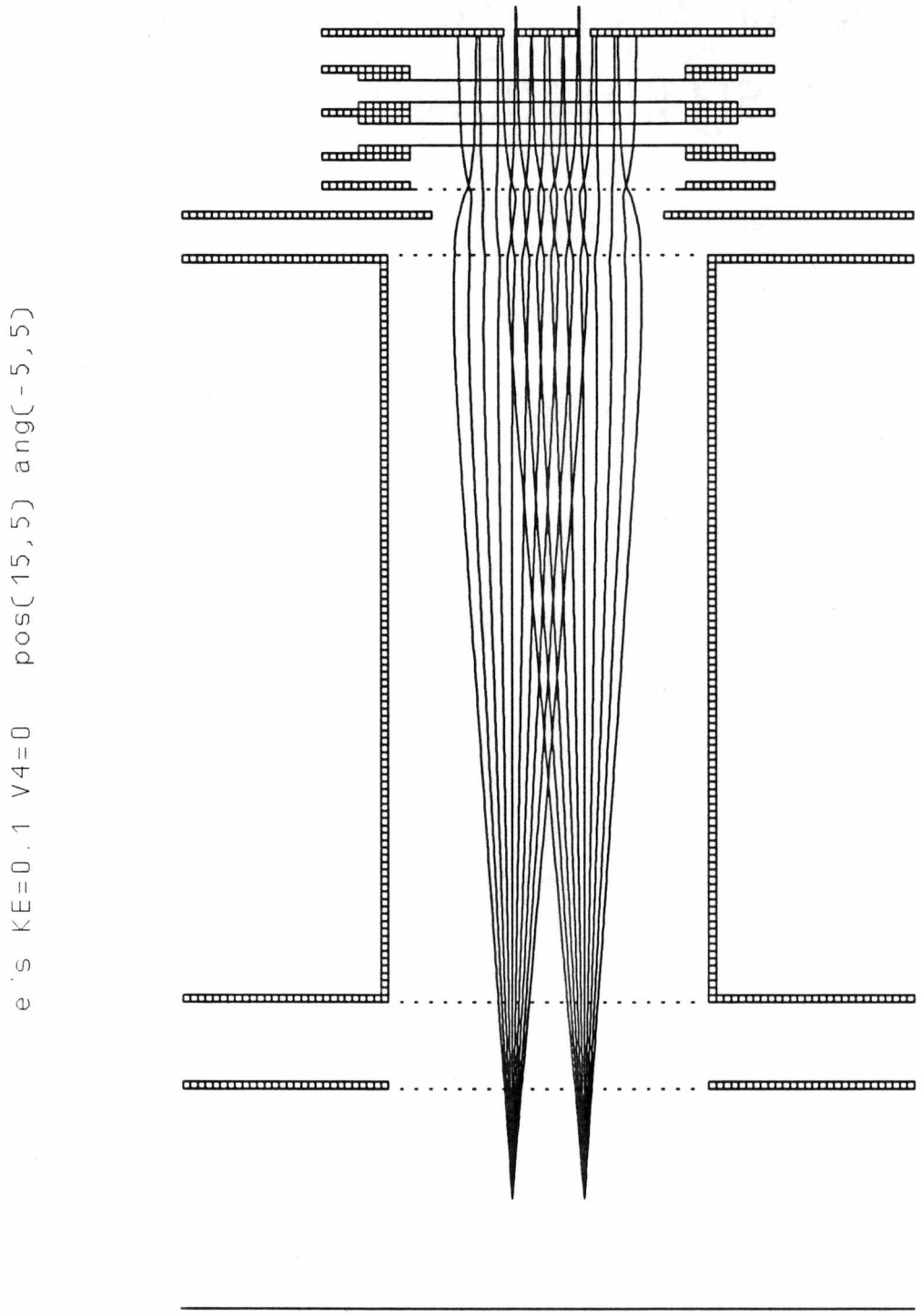

Fig. B.7. Trajectory for 0.1 eV electrons, V_{plate} = 0 V. Starting position is 15, 5. Trajectories are 1° apart. This model explores the effects of off center focusing of the laser beam.

VITA

Luis Edgardo Cuéllar was born in Santa Ana, El Salvador, on August 18th 1965. He attended school at Liceo San Luis in Santa Ana until the ninth grade, when at the age of 15, moved to Baton Rouge, Louisiana. He graduated with academic honors from Baton Rouge Magnet High School, on May, 1983.

In June 1983 he started his undergraduate career at the Louisiana State University and A&M College, in Baton Rouge. In the fall of 1983 he was admitted to the College of Basic Sciences, and obtained a Bachelor of Science Degree in Physics and Mathematics in August 1986, also with academic honors. Mr. Cuéllar spent a year doing graduate work in the Louisiana State University Department of Mathematics, however, he quickly discovered his preference of Physics.

He accepted an offer by the Department of Physics at University of Tennessee of a Science Alliance assistantship on the Spring of 1987. In the Fall quarter of 1987 he began his graduate career at the University of Tennessee. He joined the research groups of Robert N. Compton and Charles Feigerle on May 1988. During the following five years, Mr. Cuéllar worked measuring photoelectron angular distributions of cesium and rubidium, and in the summer of 1993, he obtained his Doctor of Philosopy Degree in Physics at the University of Tennessee, Knoxville.